Influence of gravitational waves on Earth normal modes

Josipa Majstorović

UNIVERSITÉ DE STRASBOURG

ÉCOLE DOCTORALE 413

SCIENCE DE LA TERRE ET ENVIRONNEMENT

Institut de Physique du Globe de Strasbourg

THÈSE

présentée par :

Josipa MAJSTOROVIĆ

soutenue le : **16 septembre 2019**

pour obtenir le grade de:
Docteur de l'Université de Strasbourg

Discipline/ Spécialité : SCIENCES DE LA TERRE / GEOPHYSIQUE

Influence des ondes gravitationnelles sur les modes propres de la Terre

THÈSE dirigée par :

Mme ROSAT Séverine	Chargée de recherche, CNRS/Université de Strasbourg
M. ROGISTER Yves	Maître de conférence, Université de Strasbourg

RAPPORTEURS :

M. WIDMER-SCHNIDRIG Rudolf	Chercheur, Universität Stuttgart
M. BARSUGLIA Matteo	Directeur de recherche, CNRS/Université Paris Diderot

AUTRES MEMBRES DU JURY :

Mme GREFF-LEFFTZ Marianne	Professeur, Institut de Physique du Globe de Paris
M. LOGNONNÉ Philippe	Professeur, Institut de Physique du Globe de Paris
M. HARMS Jan	Professeur associé, Gran Sasso Science Institute

Uvik ka bi Einstein izmišlja one šeme
prvo i glavno bi svratija do mene.
*"U redu, Alberte, ovo je u redu, al koji je ovo k****, donesi kredu.*
Da ti nacrtan na ploči, jednom za svagda,
neš ništa postić bez puno rada.
Učiti, učiti i samo učiti,
jer jedino tako možeš razlučiti šta je dobro, a šta nije,
šta se smi uvrstit, a šta ne smije.
Sve se mora dobro promatrat.
Evo, npr., na "c" ti fali kvadrat.
Ostalo je dobro, manje više, i Alberte zapamti:
Alles ist relativische!"

The Beat Fleet

Acknowledgements

After three years of the intense emotional and professional period, here I humbly present you my work. There is so much more about these three years that go above and beyond this manuscript. I am grateful for each moment and every opportunity that brought me here.

I want to express my gratitude to my supervisor Séverine Rosat who initially accepted me as a master student and then further encouraged me to pursue a PhD. Throughout the years I have always appreciated her pleasant and positive personality that helped me to express and build my critical opinion. I would also like to thank Yves Rogister who supported my work on a daily basis, Sophie Lombotte who wholeheartedly shared her code with me, Jan Harms who enthusiastically welcomed me at the Gran Sasso Science Institute and helped with the gravitational part of my thesis, Rudolf-Widmer Schnidrig who generously invited me to the Black Forest Observatory and assisted me with my thesis writing.

My social life wouldn't be existing without these unique people: Alice, Agnes, Agneza, Baptiste, Bérénice, Catalina, Clara, Dalija, Damian, Diane, Emily, Emmanuel, Guillaume, Iva, Javier, Jelica, Jean-Rémi, Lena, Marta, Mechthild, Minghe, Nolwenn, Quentin, Thifhelimbilu, Romain, Roman ... They made me feel that I belong here and I am grateful I met each one of them. I hope our paths will cross in future again.

Neizmjerno sam zahvalna mojoj obitelji majci Marici, ocu Darku i sestri Ani koji me bezuvjetno i godinama podržavaju u svemu. Također želim zahvaliti i mojoj novoj obitelji Pavici, Vitomiru, Andreju i Andreji, na prihvaćanju u njihovu obitelj i brizi koju gaje prema meni i Benjaminu.

I na kraju moj svemir, Benjamin, za kojeg su riječi suvišne...

Extended Abstract

The gravitational waves (GWs) detection has a long history that culminated with the actual detection on September 14, 2015 (Abbott et al., 2016). The detected transient signal is an indisputable proof of the theory of general relativity published by Albert Einsten in 1916 (Einstein, 1916, 1918). The event consisted of signal with the peak strain of 1.1×10^{-21} which frequency increased with time (chirp) from 35 to 250 Hz in 0.15 s. It matched the predicted waveform for the inspiral and merger of a pair of black holes and the ringdown of the resulting signal black hole. This event, not only being remarkable by itself, encouraged other existing theories to be reconsidered again. One of them is studying how the GWs from the astrophysical sources interact with the elastic bodies, since it has been shown that the GWs are capable of exciting their vibrations. The first idea came from Weber (1959), who proposed to use Earth as a large detector of the GWs. Later on, Dyson (1969) was the first one to develop a response of a Earth to the incoming GWs using a flat-Earth model. In this study he showed that in the isotropic homogeneous elastic medium the GWs interact only with the discontinuities in the shear-modulus profile. This leads to the important fact that the GWs are for Earth ever-existing vibrational triggers since the shear-modulus jump at the free-surface is always present. Next important study was the one done by Ben-Menahem (1983) who calculated the response of a radially heterogeneous non-rotating Earth model in terms of toroidal and spheroidal normal modes. He showed that for this model the only spheroidal modes that are being excited are the quadrupole ones. In the terms of the actual detection both studies provided the estimates of expected horizontal displacement, for their different Earth models, to be $2 \cdot 10^{-19}$ m and 10^{-9} m, respectively. These results are remarkable and thus a bit doubtful, hence by reconsideration of these results again we might get new insight into the GW detection. Therefore, the main aim of this dissertation is to reconsider what has been done in terms of the GW detection using Earth as a large detector and to extend these studies by accounting for more complex and realistic Earth models and the GW sources.

The goal of this dissertation is to revisit and develop an analytical model of an induced Earth spheroidal response to the emitted GWs from the astrophysical sources in terms of Earth's normal modes. There are three common sources of the GWs. The first class are transient sources such as burst sources which includes, for example, the final coalescence

of the compact binary star systems. The second class are the narrow-band sources that includes rotation of single asymmetrical stars or radiation from a binary star systems far from the coalescence. And the third class are the stochastic backgrounds. There are two sources of stochastic backgrounds: the ones created by the superposition of a large number of the independent sources that cannot to be detected separately and the ones that formed at the earliest moments of the universe shortly after the Big Bang. Each class of these sources is associated with different part of the GW spectrum and hence for each source there is a different detection strategy (see Fig. 1). For us the most interesting part of the GW spectrum is the low frequency band defined from 10^{-4} Hz to 0.1 Hz, since this is a range to which the normal modes of the Earth belong as well. In this frequency range there has not been a detection, however the future mission Laser Interferometer Space Antenna (LISA) should successfully operate in this range.

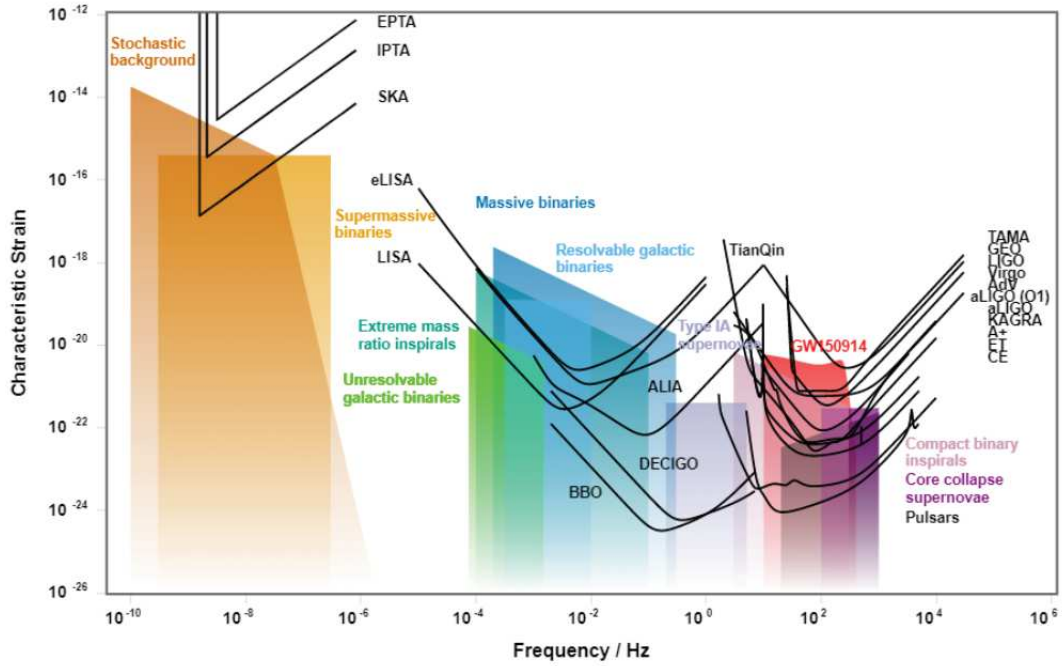

Fig 1: GW frequency spectrum versus the characteristic strain for the GW detectors and sources (From Moore et al. (2015).)

Studying Earth response in terms of the normal modes in natural choice since normal modes are Earth's vibrational states after any trigger. They are actually standing waves whose properties (such as the frequency, the decay rate, the amplitude) depend on the Earth's interior. One can obtain normal modes as solutions to the linearized equations and boundary conditions for the spherically symmetric, non-rotating, perfectly elastic and isotropic model (SNREI model). There are two types of these modes or oscillations,

spheroidal ones, which alter the external shape and internal density of the Earth and toroidal modes, which are purely tangential and zero divergence, thus they leave the radial density shape and distribution intact. Spheroidal and toroidal modes of the spherical symmetric model have degenerate eigenfrequencies which span the $(2l+1)$-dimensional space since the dependency upon azimuthal order m is removed. Also, for each angular order l there are infinitive number of spheroidal and toroidal eigenfrequencies denoted with n, the overtone order. The $(2l+1)$ oscillations is usually referred to as a multiplet, denoted as ${}_{\mathrm{n}}\mathrm{S}_{\mathrm{l}}$ for the spheroidal modes or ${}_{\mathrm{n}}\mathrm{T}_{\mathrm{l}}$ for the toroidal modes. Each individual oscillations within the multiplet is called singlet and is denoted with the order m. Effects of the Earth's rotation, hydrostatic ellipticity and lateral heterogeneity remove the eigenfrequency degeneracy and cause each multiplet to split and couple. To model this one can use the normal-mode perturbation theory, where the aforementioned effects are regarded as slight perturbations from the equilibrium state. There are different approximation how the perturbations, governing the splitting of and coupling between modes, are calculated. One way is to define a splitting matrix for an isolated multiplet (the self-coupling approximation), a group of multiplet in the narrow frequency band (the group-coupling approximation) and a group of multiplet in the wide frequency band (the full-coupling approximation). A splitting matrix is a operator that defines an ordinary eigenvalue problem for the complex frequency perturbations. Once defined one can calculate the split and coupled eigenfrequencies. Naturally, theory of the splitting and coupling help us to put constraints to the velocity and density profiles inside the Earth by studying how the normal modes split and couple. In terms of the GW detection to understand more thoroughly what will happen with the Earth when the GW passes it is important to go beyond 1D Earth model such as SNREI. That implies studying models that involve rotation, ellipticity and lateral heterogeneities.

The advantage of studying response in terms of the normal modes is that we can place constrains on the GW detection in the mHz frequency band. Two models are considered. One is the revisited model developed by Ben-Menahem (1983) for a radially heterogeneous non-rotating Earth and the other the newly developed model one for a radially heterogeneous elliptical rotating model with lateral heterogeneities. For both models the gravitational field is considered to be weak, hence the metric is decomposed into the Minkowski metric and a small perturbation. The metric perturbation is taken to be ≤ 1, therefore we can chose that it satisfies the transverse-traceless gauge condition where the metric perturbation is considered to be spatial, trace free and divergence free. In this gauge we can express the metric perturbation as plane waves defined by the propagating vector. Also, there are only two independent non-zero components in the transverse-traceless gauge, conventionally called "+" and "×" polarizations. If the wave is traveling perpendicularly to

xy-plane, the "+" polarization distorts particles by stretching and contracting of x and y axis. This configuration rotated for 45° represent "×" polarization. Moreover, for the weak gravitational wave field one can use the linearized theory of gravity. In the linearized gravitational theory Dyson (1969) showed that interaction between the GW and the elastic solid can be described by defining the force term containing the shear modulus discontinuities. This is further used in the two considered models.

Revisiting Ben-Menahem's analytical model yielded some inconsistencies that were not completely straightforward, therefore the full model is derived again but this time using modern formalism defined in the book by Dahlen and Tromp (1998). The usefulness of his approach, kept also for the newly developed model, is defining the induced displacement as a double integral of the convolution between Green tensor, representing the impulse response of a given Earth model, and the force term. Several other hypotheses are also included: firstly, GWs are monochromatic waves described by a source scalar value, a polarization tensor and a propagating vector; secondly, the Earth is a non-rotating and anelastic body; thirdly, the derivation is conducted in the Earth's reference system. Additionally to the right-hand polarized GW waves, the linearly polarized solution is also considered. The derivation and analysis have shown that in both cases, for the right-hand and linearly polarizes waves, due to the fact that the GW tensor is traceless and symmetric the only spheroidal normal modes that couple with the GW are the quadrupole ones, therefore confirming the Ben-Menahem result. Furthermore, it is shown that specific configuration of the GW's angles excite specific singlets within the quadrupole modes. Special consideration is also given to the resonant and off-resonant excitations. It is shown that the low-frequency resonant modes have larger response than the high-frequency modes and clearly the contributions of the low-frequency modes could be used exclusively in the computation of the induced displacement. With the newly derived analytical model the horizontal displacement has a value of $2.5 \cdot 10^{-14}$ m and radial $6.9 \cdot 10^{-17}$ m. If we want to put this into perspective what does this estimate means for a detection, let's consider the following example. The minimal envelope of the environmental seismic noise may be represented by the widely used New Low Noise Model (NLNM) (Peterson, 1993).

By integrating this model over the frequency band of ${}_0S_2$ multiplet width, a rough estimate of the noise standard deviation is $\sigma_{NLNM} = 1.1390 \cdot 10^{-10}\mathrm{m/s^2}$ (-151.88 dB). In Fig. 2 we show the power spectral density of the signal obtained by stacking 209 synthetic resonances computed at stations from seismometer and superconducting gravimeter networks for ${}_0S_2$ and $m = -2$. Signal at each station depends on the station colatitude and longitude, the GW amplitude which is set to $h_0 = 10^{-21}$ and is obtained for 19 days with $\Delta t = 60$ s. The noise level is primarily set to the value estimated above, $\sigma_{NLNM} = 1.1390 \cdot 10^{-10}\mathrm{m/s^2}$.

Since, this high noise level completely prevails the signal, we start reducing the noise till our signal emerges from the noise. In the mentioned configuration the emerged signal is reached with $\sigma_{NLNM} = 3.6018 \cdot 10^{-18}\mathrm{m/s}^2$, seven orders of magnitude smaller than the first value. It is clear that the GW signal is far below the detection level. In the next example, showed on the same figure, we calculate the stacked signal with the noise standard deviation $\sigma_{NLNM} = 1.1390 \cdot 10^{-10}\mathrm{m/s}^2$, and we increase the GW source amplitude h_0 until the signal emerges from the noise. This is finally reached with $h_0 = 10^{-14}$ for 19 day long signals. A cataclysmic event generating the GWs of amplitude of order 10^{-14} would emerge clearly from the noise. Such an event is however not very realistic, since the expected maximum for h_0 would be of the order $h_0 = 10^{-17}$ at these frequencies (see Fig.1). This revisited model and its solutions give us a foundation for studying interaction between Earth and GWs, however further upgrade is needed to be able to consider different sources of astrophysical origin.

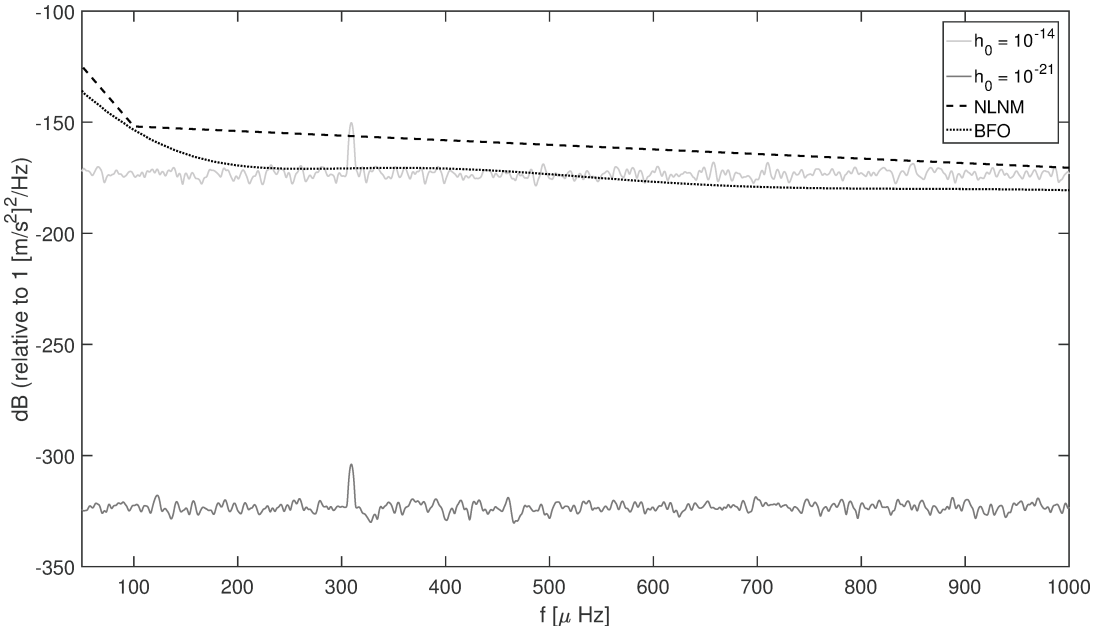

Fig 2: Comparison in terms of power spectral densities between NLNM model, observed acceleration signal at the BFO (Germany) station and synthetic noisy signals (4.74) obtained by stacking 209 stations for ${}_0S_2$ and m=-2. Dark grey signal is obtained for $h_0 = 10^{-21}$ and with the standard deviation of injected white noise adjusted to allow for the signal to emerge from the noise. It was achieved with the rms value of NLNM model integrated over the frequency band of ${}_0S_2$ multiplet width, but reduced by seven orders of magnitude. Light grey signal is obtained for the level of the noise set to match rms value of NLNM model. The value of h_0 is increased until the signal emerges from the noise. That is achieved for $h_0 = 10^{-14}$.

The upgraded model consists in the analytical development of the induced response

for a radially heterogeneous elliptical rotating model with lateral heterogeneities. This time we consider the realistic astrophysical GW source. The most promising GW sources in the mHz frequency band are the white dwarf binary systems. These sources vastly outnumber other compact binary sources in mHz band and are the fairest the simplest objects and therefore represent good sources for modeling. Since this time we are using the realistic astrophysical sources in the celestial reference system, the attention is given to the transformation matrix of the metric perturbation from a celestial reference frame to the rotating terrestrial reference frame. For the rotating Earth model the Green tensor is obtained using the normal mode summation and the perturbation theory. Hence, the effects of the splitting of and coupling between normal modes are introduced by defining the splitting matrix. For the purpose of this study the splitting matrices are defined for the group-coupling approximation. The first important alteration, using the binary systems as the GW sources, introduces dependency of the induced solution on many binary parameters, such as the masses of two stars, the orbital angular frequency (the GW source frequency), the right ascension, the declination, the distance from the source, the inclination and the polarization angles. Moreover, the GW frequencies are now defined by the angular orbital velocity of the binary stars. Meaning they do not match the normal mode eigenfrequencies, hence we are restricted to the off-resonance regime. The second important alternation concerns using a rotating model. The effect of the rotation is manifested through the patter functions. This functions define which singlets are going to be excited depending on the inclination and polarization angles. Also, they define the splitting of the GWs frequencies. For this model we also obtain that the only excited spheroidal modes are quadrupole ones. For the GWs sources we used a verification catalog of the binary stars for the future LISA (Laser Interferometer Space Antenna) space mission. LISA is a space mission that will consist of a huge 2.5 million km arm length laser interferometer, compared to a few kilometers long one on Earth, consisting of the three spacecraft that will follow the Earth in its orbit. Estimated radial induced spheroidal responses for 14 GW sources are shown in Fig. 3 and their maximum spectral amplitude are show in Tab. 1. We see that the maximal radial response for the new model is $8.1 \cdot 10^{-17}$ m. This is the same order of magnitude as the radial response for the revisited model, even though this is for the off-resonance regime. In the resonance regime this value is two orders of magnitude larger than in the off-resonance regime due to the source-time function. The source-time function depends on the GW source frequency and the normal mode eigenfrequencies. By calculating the relative ratio between the source-time functions for the revisited (the non-rotating model) and the new model (the rotating model) we obtain that the maximum difference between functions of these two models is of the order of the Q-factor. This

explains two orders of magnitude difference between two models in the resonance regime. Also, it implies that we can expect higher response amplitudes for the GWs that have frequencies close to the normal mode eigenfrequencies and that have high Q-values.

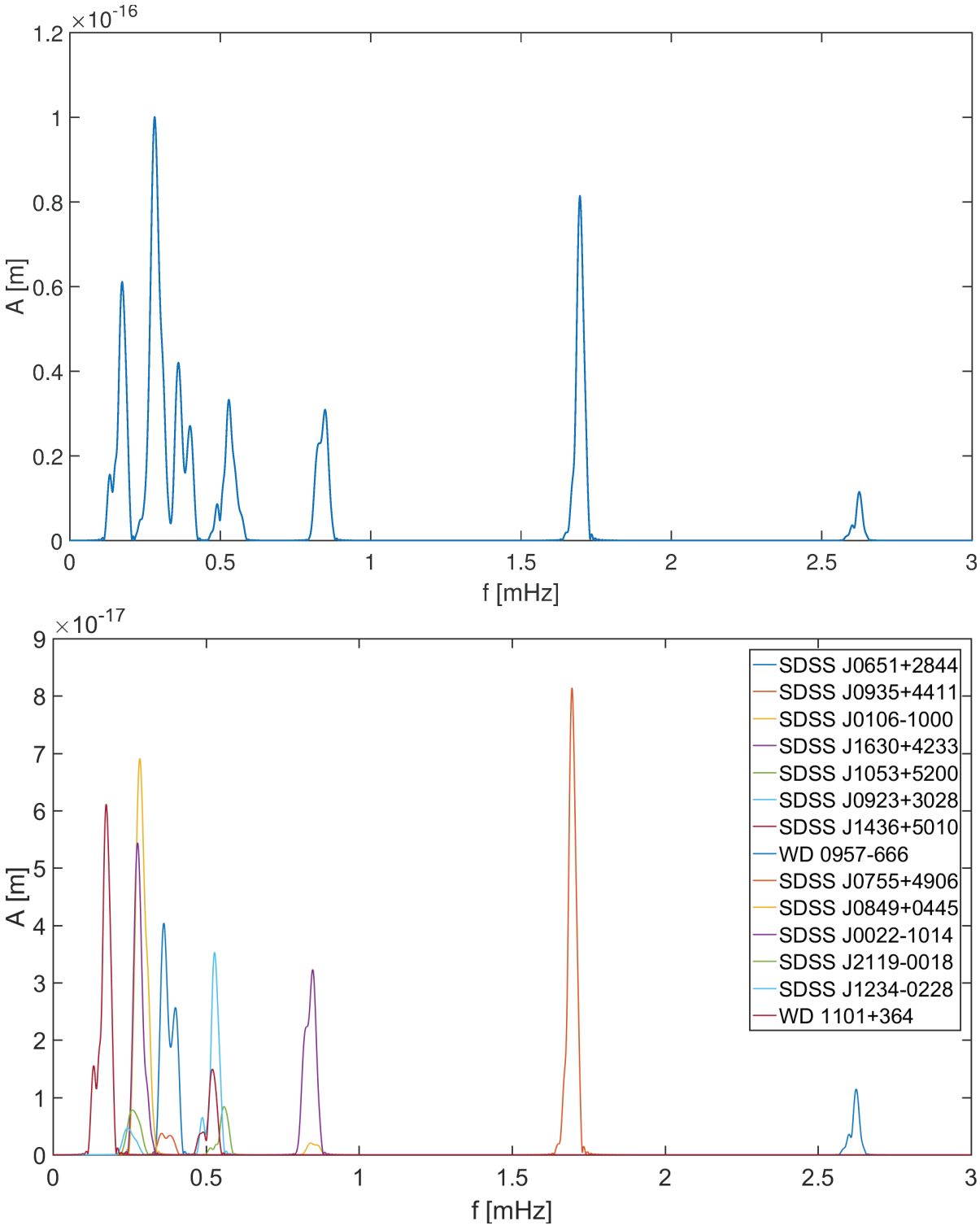

Fig 3: Induced spheroidal response for 14 GW sources when all responses are summed together (up) and when each response is plot individually (down) for one day long signals.

Tab 1: Maximum spectral amplitudes of the induced spheroidal response for 14 GW sources.

Name	A $[\cdot 10^{-18}\mathrm{m}]$	A $[\cdot 10^{-22}\mathrm{m/s^2}]$
SDSSJ0651+2844	11.47999	30.94457
SDSSJ0935+4411	81.43515	91.11686
SDSSJ0106-1000	2.04780	0.58756
SDSSJ1630+4233	32.30985	8.93221
SDSSJ1053+5200	8.42014	0.98185
SDSSJ0923+3028	35.31244	3.69649
SDSSJ1436+5010	14.95197	1.50795
WD0957-666	40.41132	2.29791
SDSSJ0755+4906	3.72761	0.19854
SDSSJ0849+0445	69.10639	2.36004
SDSSJ0022-1014	54.40300	1.80340
SDSSJ2119-0018	7.80692	0.21934
SDSSJ1234-0228	4.63214	0.11721
WD1101+364	61.13572	0.61757

Once when the analytical model is developed, the next step is to study how one can search for this signal in data. The considered sources, the white-dwarf binaries, are in the inspiral phase meaning that they present nearly periodic sources that should be constantly present in the measurements (at least longer than the existence of the active network of sensors on the Earth). The best way to perform the search of the newly developed signal in data is to utilize the matched filter technique (also commonly used for the detection of the GWs from the interferometers data of the LIGO type (Feller, 1950; Allen and Romano, 1999; Allen, 2004; Allen et al., 2012)). The matched filtering technique can simultaneously tell us if there is a signal and when it started. It is performed by calculating the correlation between data and a template of the signal, that should resemble the target signal at some level of accuracy. Our induced response depends on the white-dwarf binary parameters and on the associated parameters' standard deviations. The question that is imposing itself if whether these standard deviations form the binary stars could deteriorate the matched filtering performance. That is, if we perform the search for a signal using template that its not generated with same binary star parameters as a target signal, could we still detect it. To approach this problem several steps are undertaken. First, using the standard deviations of the binary star parameters (the mass, the inclination angle, the declination angle, the

right ascension, the distance, the polarization angle, the GW source frequency) we define range of values for each parameter around some default value. For each parameter and for each value in its defined range we calculate the template to generate something called the bank of templates. The generated bank of templates are used to preform the sensitivity tests. These test help us understand which parameters are the best constrained and the most sensitive. Tests have finally shown that the GW source frequency is the best one constrained (the standard deviations are small enough so that the differences between templates are also small in terms of the relative errors) and also the most sensitive one (a small change between the templates is generating the largest difference scale-wise compared to other parameters). Further, to answer the question at the beginning of this paragraph we need to understand how the standard deviations or the individual templates in bank of templates are affecting the match filtering technique. The two hypotheses are studied, one where there is just a noise in the data, H_0, and the other where within the noise the signal is also present, H_1. The results are represented in terms of the probability density functions (PDFs). When the PDFs of the two hypothesis are well separated it means that there is a good probability that we will detect signal within the current noise level. Next we perform the experiments for each parameter separately. We keep the same noise level (thus keeping the PDF of the hypothesis H_0 the same) and for each template within the bank of template we calculate the PDF. This means that the target signal and the template we perform the matched filtering are the same. Comparing the two PDFs for the two edge templates for the GW source frequency parameter is shown in Fig. 4. We can see that performing a matched filtering with the template that is obtained for the parameter smaller than the default parameter there is smaller probability of the detection than in the case when the analysis is performed using a template obtained by the parameter bigger than the default one. This is expected, since the response amplitude is larger for the second case.

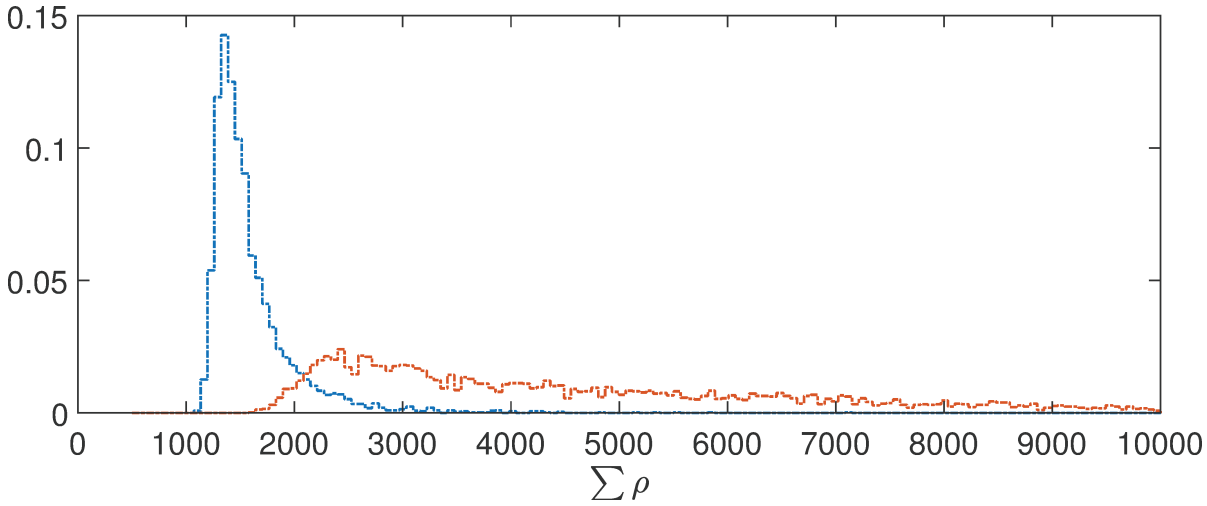

Fig 4: Two PDFs for the H_1 hypothesis calculated for the edge templates (blue for the parameter smaller than the default parameter and orange for opposite) in the bank of templates for the GW source frequency parameter.

In the next set of the experiments we also want to obtain the PDFs for each template within the bank of templates, but this time the target signal and the template we perform the matched filtering are not the same. This means that we fix a template used in the matched filtering. The results for the GW source frequency are shown in Fig. 5. We can see that the PDFs functions are the same for all templates within the bank of templates. This implies that even if we perform the search where the target signal and the template do not match, we have the same probability to detect signal even if they do match. This is valid only if the differences between the target signal and the template are within the standard deviations of the GW source frequency. The same conclusion is valid for all other parameters. Our synthetic tests have therefore shown that the matched filtering technique is not sensitive to the uncertainties present in the catalog of the binary systems. In other words, the uncertainties are too small to significantly impact the shape of our response signal so that they correlate very well with the target signal even if the template we use to perform the matched filtering is not equal.

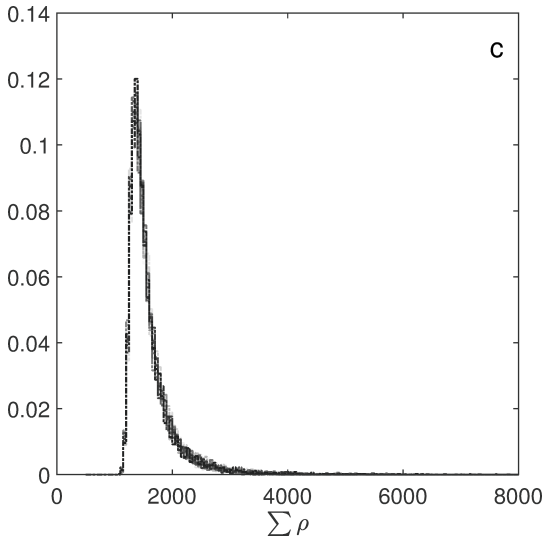

Fig 5: PDFs calculated for each template from the bank of templates for the case when the target signal the template we perform the matched filtering do not match. The results are for the GW source frequency parameter.

Synthetic test also showed that current noise levels from gravimetric data needs to be 10 orders of magnitude smaller to be able to detect the modelled radial induced response. We tested this by inserting a target synthetic signal in the data obtained for the most quiet station in the world, the Black Forest Observatory. We considered one year of data for the year 2012 where all the earthquakes has been removed and only those days that has a power spectral density below 25th percentile were accepted. The remaining days formed a data set that we further recall as the observational noise. Our analysis showed that the matched filtering technique has a same performance when the synthetic signal is inserted into data set containing the white Gaussian noise or the observational noise. The result is showed in Fig. 6.

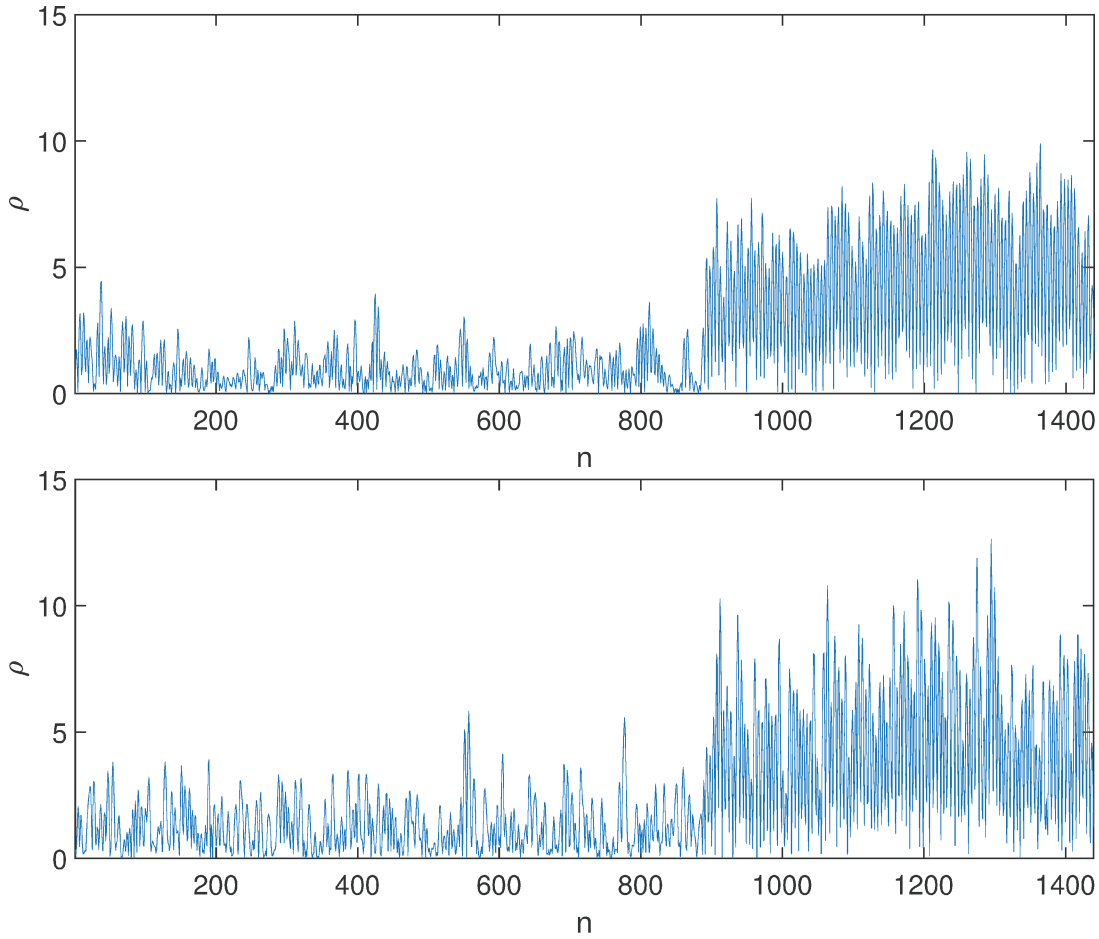

Fig 6: Matched filter output for the synthetic signal inserted into white noisy time series with $\sigma_N = 7.5 \cdot 10^{-21}$ m/s^2 (above) and the same synthetic signal inserted into observational noisy time series scaled with scalar $1.2 \cdot 10^{10}$ (below).

The last part of this dissertation deals with the normal modes measurements only in order to gain a complete concept of biases that one can introduce by using a normal modes as tools in modeling. The normal modes studies have long provided some of the essential constraints and contributed to building spherically symmetric Earth models as well as 3D models of lateral heterogeneities by performing the measurements of normal modes eigenfrequencies. Despite many developed methods inconsistency in measurements still exists and it is difficult to understand which results are more precise, that is which methods introduce less systematic biases in measurements. Therefore, the main goal of this study is to test the performances of typically used techniques in normal mode studies (which also came out as best according to previously published studies) and to test their performances in the eigenfrequency and Q-factors measurements. Three techniques are implemented: optimal sequence estimation (OSE) (Ding and Shen, 2013a), autoregressive method in frequency domain (ARFD80) (Chao and Gilbert, 1980) and phasor walkout method (Zürn and Ry-

delek, 1994) with R^2-test. The phasor walkout is a graphical representation of the Fourier transform at the desired frequency. The OSE method is the stacking method used to enchain weak signals buried in noise based on the assumption that the displacement at the Earth's surface is decomposed in spherical harmonics. The measurement of eigenfrequencies is performed using ARFD80 method, which linearizes the non-linear problem of estimating the singlets complex frequencies using the Prony technique for extracting exponential signals from time-series. Once measured, the complex eigenfrequency estimates are validated graphically by using the phasor walkout method. These methods are tested on synthetically generated data and on observations. The synthetic tests are performed for a global 3-D Earth density and velocity model using only one source mechanism and one multiplet chain at the time. The focus is set to the low-frequency modes, where one can use the group-coupling approximation over full-coupling one. The synthetic tests have two main parts: gradually increasing noise levels and decreasing the number of stations in stacking. Furthermore, once when the eigenfrequencies are estimated, they are used to retrieve the splitting function coefficients based on a perturbation theory of the first order. Synthetic experiments have shown that when noise is gradually added, the signal-to-noise ratio (SNR) of the stacked signals decreases and standard deviations of estimated frequencies and Q-factors increase, being overall more scattered around the true synthetic value (see Fig. 7). Results are foremost when more records are included in the stacking. More importantly it has been shown that OSE method is sensitive to different station distributions under the noise influence. Furthermore, the performances of ARFD80 method become deteriorated when the stacking signal is obtained with the less excited signals, that is when the input signals have SNR ≤ 2. However, even for those cases the estimates are within the standard deviations. Moreover, it turns out that the standard deviations calculated with the bootstrap method are not sufficient to include all biases introduced with the methods, that is to say our standard deviations are for most cases underestimated. Thus, even though we have a good precision on our estimates, the accuracy can be poor. This analysis showed that we do not need a priori model to estimate structure coefficients, but results may be biased. Synthetic tests are also compared with the measurements obtained in the observations. The study shows that these kinds of tests are crucial in understanding and scrutinizing the obtained values and their associated standard deviations. Any kind of measurement in the normal mode studies should be considered within the context of used data (e.g. number of stations in stacking) and the performances of used techniques.

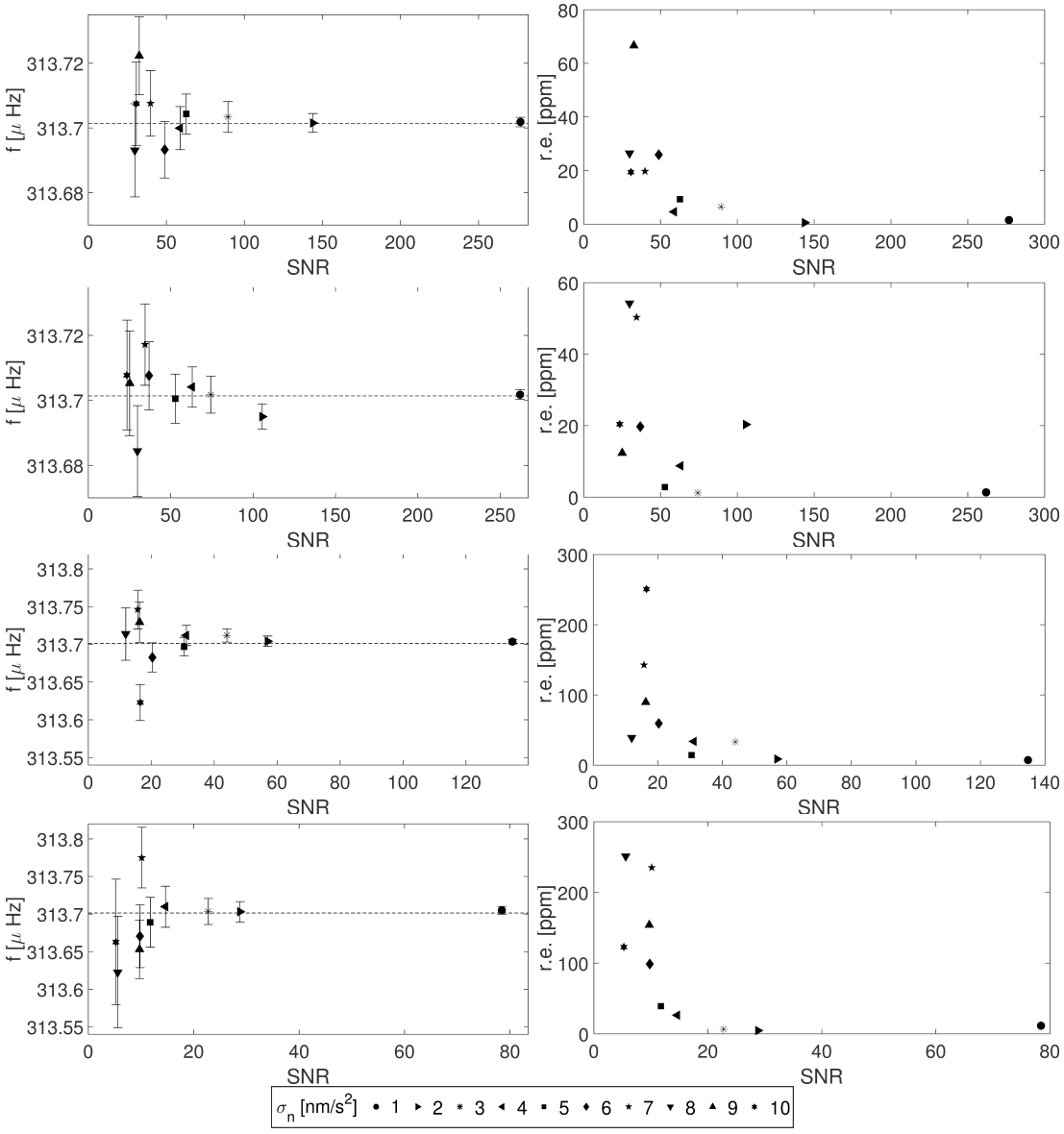

Fig 7: Synthetic experiments for ${}_0S_2^1$ singlet conducted for four station distributions: 1) full (the first row), 2) northern (the second row), 3) southern (the third row), 4) selected (the fourth row) networks. Figures on the left represent the estimated frequencies versus SNR for ten different noise levels. Figures on the right represent the relative errors of frequencies with regard to synthetic value (dashed line) versus SNR for ten noise levels. Be careful, the vertical scales of the left-side figures are optimized, thus the full and the northern networks have the same scale and the southern and the selected networks too.

In conclusion, we have revisited and develop a new model of the interaction between the GWs and the Earth in terms of the normal modes. We have reevaluated the induced resonance amplitude for a spherical and radially stratified terrestrial model which turns out to be several orders of magnitude lower than the initially proposed by Ben-Menahem (1983) but higher than proposed by Dyson (1969) for a flat Earth model. The newly developed

model consist in the analytical development of the induced response for a rotating elliptical model with lateral heterogeneities. This time the GW sources are the double white-dwarf binaries. These GW sources generate the amplitude of the order 10^{22} - 10^{-23}, two order of magnitude smaller than the event detected by LIGO in 2015 that was generated by the coalescence of two black holes. The time scales for the two are different, since the considered GW sources have frequencies in the mHz band and the emission of these sources are continuous. Therefore, the excitation of the quadrupole normal modes by the white-dwarf binaries is also continuous. However, the detection of these signal in gravimetric and seismological data using the matched filter technique is very difficult due to the noise amplitude present in the data. Finally, we have highlighted some limitations of the data analysis techniques of the weak signals and some biases introduced by the station distribution on the surface of the globe within the normal mode studies.

This work gives a new contribution to the GW studies and sets a new limit on their detection. Detection of the GWs by their resonance with the Earth's normal modes in the milihertz frequency band is therefore not possible today. Technological limitations but also the environmental noise present in the observations are still limiting factors. The normal mode approach in this thesis could be extended to other planets, particular Mars where a seismometer was recently deployed as part of the Mars Insight mission. A correlation technique between lunar seismometric data with terrestrial data has been proposed by Coughlin and Harms (2014c) resulting in a better constraint on the GW energy density at frequencies below 1 Hz. In the future, Martian seismometer data may offer promising perspectives in this context and thus bring new constraints on cosmological models.

Résumé Étendu

La quête des ondes gravitationnelles a connu une longue histoire jusqu'à leur première observation directe le 14 septembre 2015 grâce aux données de l'interféromètre LIGO (Abbott et al., 2016). Le signal transitoire détecté constitue une preuve supplémentaire de la validité de la théorie de la relativité générale publiée par Albert Einstein en 1916 (Einstein, 1916, 1918). L'événement gravitationnel ainsi observé présentait un pic d'amplitude 10^{-21} en déformation avec une fréquence augmentant de 35 à 250 Hz en 0.15 s. Ce signal concorde avec les différentes phases prédites de la coalescence de deux trous noirs : phase spiralante, fusion, puis déclin du trou noir résultant. Cet évènement nous encourage donc à reconsidérer certaines idées développées pour la détection d'ondes gravitationnelles par des moyens indirects. L'une d'elles est l'étude de l'interaction des ondes gravitationnelles d'origine astrophysique avec les corps élastiques tels que les planètes : les ondes gravitationnelles correspondent à la propagation d'une perturbation de la métrique de l'espace-temps. Elles vont, lors de leur passage à travers un corps élastique, déclencher les vibrations propres de ce corps. L'idée pionnière a été proposée par Weber (1959). Puis, Dyson (1969) a été le premier à développer les équations de la réponse de la Terre aux ondes gravitationnelles dans le cadre d'un modèle de Terre plate. Il a montré que dans un milieu élastiquement isotrope et homogène, les ondes gravitationnelles interagissent avec les discontinuités du module de cisaillement. Cela mène au fait important que les ondes gravitationnelles constituent forcément une source de vibrations puisque le saut du module de cisaillement est présent à la surface libre de la Terre. L'étude importante qui a suivi est celle de Ben-Menahem (1983) qui a calculé la réponse d'un modèle de Terre sphérique et radialement stratifié en termes de modes propres sphéroïdaux et toroïdaux. Il a montré que pour un tel modèle de Terre, les seuls modes sphéroïdaux excités sont ceux de forme quadripolaire, correspondant au degré harmonique deux. Dyson (1969) et Ben-Menahem (1983) ont estimé un déplacement horizontal de l'ordre de $2 \cdot 10^{-19}$ et 10^{-9} m pour leurs modèles de Terre respectifs et pour une même amplitude de la perturbation de la métrique de l'espace-temps de 10^{-21} en déformation. Ces deux résultats très différents démontrent la nécessité de réévaluer ces amplitudes dans le cadre d'une modélisation plus réaliste. L'objectif principal de cette thèse est donc de considérer la possibilité d'utiliser la Terre comme détecteur d'ondes gravitationnelles dans le cadre d'un modèle plus réaliste et pour des sources d'ondes gravitationnelles bien

définies. Une réévaluation des amplitudes attendues permettra ainsi de discuter la possibilité de détecter les ondes gravitationnelles via leurs interactions avec les modes propres de la Terre à des fréquences non atteintes par les détecteurs terrestres actuels.

Le but premier de ce travail est de développer un modèle analytique de la réponse sphéroïdale de la Terre aux ondes gravitationnelles émises par des sources astrophysiques en utilisant le formalisme des modes propres. Il y a typiquement trois types de sources d'ondes gravitationnelles. La première sorte sont les sources transitoires telles que des sources explosives qui incluent par exemple la phase finale de la coalescence de systèmes d'étoiles binaires compactes. Les secondes sont les sources à bande fréquentielle étroite qui incluent la rotation d'étoiles seules mais asymétriques ou la radiation émise par des systèmes binaires d'étoiles éloignés de la phase de coalescence. Enfin, la troisième sorte constitue le fond stochastique d'onde gravitationnelle. On distingue deux types de fond stochastique : celui d'origine cosmologique produit peu de temps après le Big-Bang (pendant la phase d'inflation cosmique) et celui d'origine astrophysique qui est la superposition des signaux plus récents provenant d'un très grand nombre de sources qu'il est impossible de détecter séparément.

Chacune de ces catégories de sources émet des ondes gravitationnelles dans différentes bandes spectrales, ainsi, suivant les fréquences considérées, la stratégie de détection sera différente (cf. Fig. 8). Pour nous, la partie du spectre des ondes gravitationnelles qui nous intéresse est la bande basse-fréquences définie de 10^{-4} Hz à 0.1 Hz, puisqu'il s'agit de la bande fréquentielle contenant les modes propres sismiques de la Terre. A ces fréquences, aucune détection d'onde gravitationnelle n'a encore eu lieu. Cependant la future mission LISA (Laser Interferometer Space Antenna) devrait apporter de nouveaux résultats prometteurs dans cette gamme de fréquences.

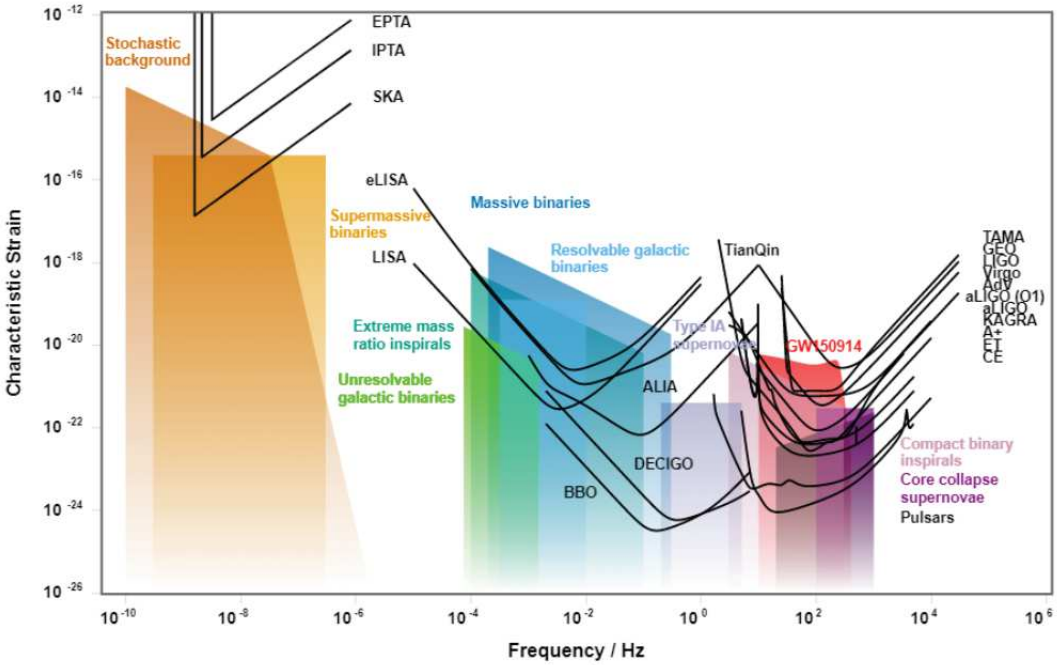

Fig 8: Amplitude spectrale en déformation des ondes gravitationnelles en fonction des sources. Les courbes de sensibilité des détecteurs sont également indiquées (d'après Moore et al. (2015).)

Etudier la Terre en termes de modes propres est un choix naturel puisque les modes propres constituent les états de vibration de la Terre après une quelconque excitation. Les modes propres correspondent à des ondes stationnaires dont les propriétés (fréquences propres, temps d'amortissement et fonctions propres) ne dépendent que de la structure interne de la Terre. Les modes propres peuvent être obtenus à partir des équations linéarisées de la gravito-élasticité et les conditions aux limites qui gouvernent les oscillations libres d'un modèle de Terre de type SNREI à symétrie sphérique, sans rotation, parfaitement élastique et isotrope. Il existe deux sortes de modes propres, les modes sphéroïdaux qui altèrent la forme externe et la densité interne de la Terre, et les modes toroïdaux qui possèdent des déplacements purement tangentiels et une divergence nulle; ils laissent donc la forme et la distribution en densité radiale de la Terre intactes. Les modes propres sphéroïdaux et toroïdaux d'un modèle à symétrie sphérique ont des fréquences propres dégénérées avec un espace propre associé de dimension $(2l + 1)$; la dépendance sur l'ordre azimutal m est supprimée. Pour chaque degré l il y a une infinité de fréquences propres identifiées avec le nombre n, l'ordre harmonique. Les $(2l + 1)$ oscillations sont appelées multiplet, dénoté par ${}_{n}S_{l}$ pour les modes sphéroïdaux ou ${}_{n}T_{l}$ pour les modes toroïdaux. Chaque oscillation individuelle dans un multiplet est appelée singlet et est désigné par son ordre m. Les effets de la rotation de la Terre et son ellipticité hydrostatique ainsi que les hétérogénéités latérales

soulèvent la dégénérescence en éclatant le multiplet en $(2l+1)$ fréquences (« splitting ») et couplent les modes (« coupling ») entre eux. Afin de modéliser ces effets, il est possible d'utiliser une théorie de la perturbation des modes propres pour laquelle ces effets sont considérés comme des petites perturbations de l'état d'équilibre. Il existe différents niveaux d'approximation afin de calculer les perturbations dues au splitting et coupling des modes. Un moyen est de définir une matrice de splitting pour un multiplet isolé (approximation dite « self-coupling »), pour un groupe de multiplets dans une bande fréquentielle étroite (approximation dite « group-coupling ») ou pour un groupe de multiplets dans une bande fréquentielle large (approximation dite « full-coupling »). Une matrice de splitting est un opérateur qui définit un problème classique aux valeurs propres pour les perturbations sur la fréquence complexe du mode. Une fois définie, il est possible de calculer les fréquences propres éclatées et couplées. Inversement, la théorie des modes propres et en particulier l'étude du splitting et coupling des modes propres nous permet d'apporter des contraintes sur les profils de vitesses et de densité dans la Terre. Pour comprendre la réponse de la Terre aux ondes gravitationnelles, nous verrons par la suite qu'il est nécessaire de prendre en compte une théorie complète des modes propres en tenant compte de du « splitting » et du couplage des modes qui apparaissent pour une Terre elliptique en rotation à variations latérales de densité.

L'avantage d'étudier la réponse de la Terre à une excitation par les ondes gravitationnelles en termes de modes sismiques est d'apporter des contraintes sur la détection des ondes gravitationnelles dans la bande fréquentielle du millihertz. Deux modèles sont considérés. Le premier consiste à revisiter le modèle développé par Ben-Menahem (1983) pour une Terre sans rotation et radialement hétérogène. Le second est un nouveau développement que nous proposons pour un modèle de Terre elliptique en rotation radialement stratifié et à hétérogénéités latérales. Pour ces deux modélisations, le champ gravitationnel est considéré faible, ainsi la métrique peut être décomposée comme la somme de la métrique de Minkowski et une petite perturbation. La perturbation de la métrique est prise inférieure ou égale à 1, ainsi nous pouvons la choisir de sorte à ce qu'elle satisfasse à la condition de gauge dite « transverse-traceless » pour laquelle la perturbation de la métrique est spatiale, à trace nulle et à divergence nulle. Dans cette condition, la perturbation de la métrique peut être représentée par des ondes planes définies par un vecteur de propagation. Il existe seulement deux types de polarisations indépendantes et non nulles dans cette condition de gauge « transverse-traceless » conventionnellement appelées polarisations "+" et "×". Si l'onde se propage perpendiculairement au plan (x, y), la polarisation "+" déforme les particules en étirant et contractant selon les axes x et y. Cette configuration est tournée de 45 degrés pour représenter la polarisation "×". En outre, pour un champ gravitationnel faible,

on peut utiliser une théorie linéarisée. Dans une théorie linéarisée de la gravitation, Dyson (1969) a montré que l'interaction entre les ondes gravitationnelles et un corps élastique peut être décrite en définissant un terme de force qui contient les discontinuités du module de cisaillement. Nous utilisons cette description du forçage dans nos modélisations.

En reprenant le travail de Ben-Menahem (1983), nous avons noté quelques incohérences aussi nous avons repris son développement analytique mais avec un formalisme moderne défini dans le livre de Dahlen and Tromp (1998). Nous avons suivi sa démarche basée sur le calcul du déplacement de surface par la convolution entre le tenseur de Green, représentant la réponse impulsionnelle d'un modèle de Terre donné, et le terme de force, représentant l'action de l'onde gravitationnelle. Différentes hypothèses sont utilisées: les ondes gravitationnelles sont des ondes monochromatiques décrites par une valeur scalaire source, un tenseur de polarisation et un vecteur de propagation; la Terre est sphérique sans rotation et anélastique; les équations sont écrites directement dans un système de référence terrestre. Par ailleurs, nous considérons la solution dans le cas d'une polarisation linéaire des ondes gravitationnelles, en plus du cas d'ondes à polarisation circulaire droite. La dérivation et l'analyse des équations dans ces deux cas de polarisation ont montré que comme le tenseur des déformations associé aux ondes gravitationnelles est symétrique à trace nulle, les seuls modes sphéroïdaux capables d'être excités par les ondes gravitationnelles sont ceux de forme quadripolaire, confirmant les résultats de Ben-Menahem (1983). Nous montrons de plus que pour certaines configurations angulaires des ondes gravitationnelles dans le système terrestre, seulement certains termes azimutaux sont excités au sein d'un mode, apportant ainsi de l'information sur la source d'ondes gravitationnelles dans le ciel. Une considération particulière est apportée à l'excitation de modes à la résonance mais aussi en dehors de la fréquence de résonance des modes sismiques. Nous montrons que le déplacement de surface induit par les ondes gravitationnelles est plus important à résonance avec les modes les plus graves qu'avec les modes à fréquences plus élevées. A partir de notre modèle analytique, le déplacement horizontal de surface est de $2.5 \cdot 10^{-14}$ m et le déplacement radial de $6.9 \cdot 10^{-17}$ m. Pour une mise en perspectives en termes de détection à la surface de la Terre, considérons le modèle de bruit bas (NLNM) de Peterson (1993) couramment utilisé pour représenter le niveau de bruit environnemental sur Terre.

Par intégration de ce modèle sur la largeur fréquentielle du mode ${}_0S_2$, l'écart-type estimé est de l'ordre de $\sigma_{NLNM} = 1.1390 \cdot 10^{-10}\mathrm{m/s^2}(\approx$ -152 dB). Sur la Fig. 9 nous avons représenté la densité spectrale de puissance du signal obtenu après sommation de 209 séries temporelles synthétiques calculées aux stations sismologiques et gravimétriques des réseaux mondiaux, pour le singlet m = -2 du mode ${}_0S_2$. Le signal à chaque station dépend de la latitude et longitude du site, de l'amplitude de l'onde gravitationnelle fixée à $h_0 = 10^{-21}$.

Il est généré sur 19 jours avec un pas d'échantillonnage temporel $\Delta t = 60$ s. Le bruit blanc injecté est initialement fixé à la valeur définie précédemment, soit $\sigma_{NLNM} = 1.1390 \cdot 10^{-10}\mathrm{m/s^2}$. Puisque ce niveau de bruit est trop élevé et masque complètement le signal des ondes gravitationnelles, nous diminuons l'amplitude du bruit graduellement jusqu'à ce que le signal émerge du bruit. Dans la configuration mentionnée plus haut, le signal émerge du bruit lorsque $\sigma_{NLNM} = 3.6018 \cdot 10^{-18}\mathrm{m/s^2}$, soit sept ordres de grandeur de moins que la valeur initiale. Il est clair que le signal des ondes gravitationnelles est largement en dessous du seuil de détection. Dans l'exemple suivant, illustré sur la même figure, nous calculons le signal stacké avec $\sigma_{NLNM} = 1.1390 \cdot 10^{-10}\mathrm{m/s^2}$ et nous augmentons l'amplitude source h_0 de l'onde gravitationnelle jusqu'à l'émergence du signal au-dessus du bruit. La valeur ainsi atteinte est $h_0 = 10^{-14}$ pour des signaux de durée 19 jours. Un évènement cataclysmique générant des ondes gravitationnelles d'amplitude de l'ordre 10^{-14} en déformation émergerait clairement du bruit. Un tel évènement n'est cependant pas très réaliste, puisque le maximum attendu pour h_0 serait de l'ordre de 10^{-17} à ces fréquences (cf. Fig. 8).

Bien que ce modèle nous donne les fondations pour l'étude de l'interaction entre la Terre et les ondes gravitationnelles, des améliorations sont nécessaires afin de traiter tout type de sources astrophysiques et cosmologiques.

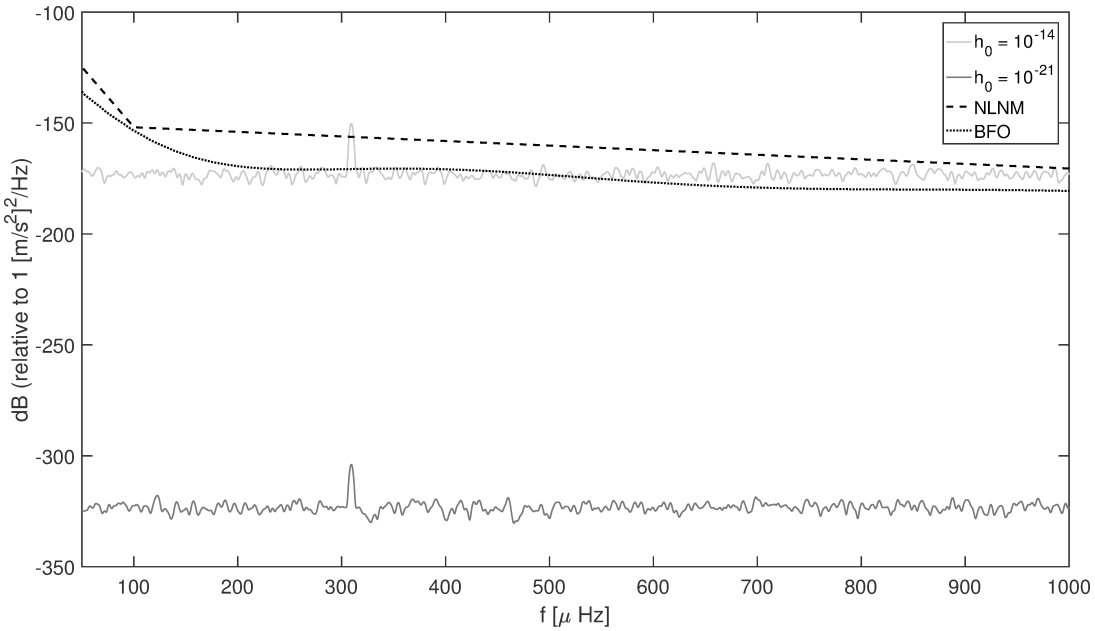

Fig 9: Comparaison en termes de densités spectrales de puissance (PSD) du modèle de bruit bas NLNM, avec le niveau de PSD observé à la station BFO (Black Forest Observatory, Allemagne) et avec les signaux synthétiques bruités obtenus en sommant les séries temporelles générées à 209 stations pour le singlet m=-2 du mode ${}_0S_2$. Le niveau de PSD en gris foncé est obtenu pour $h_0 = 10^{-21}$ et avec un bruit blanc injecté ajusté de sorte que son écart-type permette au signal résultant du stacking d'émerger au-dessus du bruit. Ceci est atteint pour une valeur de RMS réduite de sept ordres de grandeur par rapport au NLNM par intégration de ce modèle sur la largeur fréquentielle du mode ${}_0S_2$. Le niveau de PSD en gris clair correspond au niveau de bruit du NLNM à la fréquence de ${}_0S_2$. Un signal périodique d'amplitude h_0 y a été ajouté avec une valeur h0 augmentée jusqu'à dépasser du bruit. Ce niveau de détectabilité est atteint pour $h_0 = 10^{-13}$.

Nous développons par la suite une modélisation analytique de la réponse de la Terre à des sources astrophysiques d'onde gravitationnelle bien définies. Le calcul est réalisé dans le cas d'un modèle de Terre elliptique, en rotation et à hétérogénéités latérales. Les sources d'onde gravitationnelle les plus prometteuses dans la bande du millihertz sont les systèmes binaires de naines blanches. Ces sources surpassent en nombre les autres sources de binaires compacts à ces fréquences et sont des objets relativement aisés à modéliser en tant que source lointaine. Lorsque nous considérons des sources astrophysiques définies dans un système de référence céleste, il est nécessaire d'appliquer un changement de repère via une matrice de transformation permettant de passer d'une définition de la perturbation du tenseur métrique dans un système de référence céleste à une définition de cette perturbation dans un repère terrestre tournant. Le tenseur de Green pour un modèle de Terre en rotation et à hétérogénéités latérales est quant à lui obtenu par sommation des modes propres dans le cadre d'une théorie linéarisée des perturbations (Dahlen and Tromp, 1998). Ainsi les effets

de « splitting » (éclatement en fréquences) et de couplage des modes sont introduits en définissant les matrices de « splitting ». Nous utilisons une approximation de type « group-coupling ». L'expression de l'amplitude de la perturbation du tenseur métrique associée à un système double de naines blanches dépend de caractéristiques propres aux deux étoiles (masses, rayons), de leurs paramètres orbitaux et de la distance à laquelle on se place pour estimer la perturbation (ici la distance par rapport à la Terre). Un fait très important dans ce type de source est que la fréquence de l'onde gravitationnelle est désormais définie par la vitesse angulaire orbitale du système binaire. Cette fréquence étant généralement différente de celle des modes sismiques, nous sommes dans un régime hors résonance. Une autre différence importante par rapport au cas d'un modèle de Terre non tournant est que l'effet de la rotation se manifeste à travers des fonctions géométriques qui déterminent quels singlets sont excités selon les angles d'inclinaison et de polarisation de l'onde gravitationnelle émise. Elles définissent aussi le splitting des fréquences des ondes gravitationnelles. Dans cette modélisation, les seuls modes sphéroïdaux excités sont également les modes quadripolaires.

Nous avons utilisé un catalogue de sources validé pour la future mission spatiale LISA (Laser Interferometer Space Antenna). LISA est une mission spatiale qui consistera en un immense interféromètre laser de longueur de bras 2.5 million km, à comparer aux quelques kilomètres des observatoires sur Terre, formé de trois engins spatiaux qui suivront la Terre sur son orbite. Les réponses sphéroïdales en terme de déplacement radial à la surface de la Terre pour ces quatorze sources sont représentées sur la Fig. 10. Leurs amplitudes spectrales maximales sont résumées dans la Table 2. Nous voyons que le déplacement radial maximum est de $8.1 \cdot 10^{-17}$ m, soit du même ordre de grandeur que dans le cas de la modélisation sans rotation. Si nous considérons une fréquence de l'onde gravitationnelle égale à celle d'un mode propre, c'est-à-dire si nous nous plaçons dans un régime à résonance, ces amplitudes sont alors deux ordres de grandeur supérieures. En comparant les réponses respectives d'un modèle de Terre avec et sans rotation, à résonance, alors le rapport correspond à la valeur du facteur de qualité du mode propre considéré. La contribution du splitting des modes est donc conséquente. Il serait également intéressant de pouvoir identifier des sources d'onde gravitationnelle de fréquence proche des modes propres quadripolaires peu amortis.

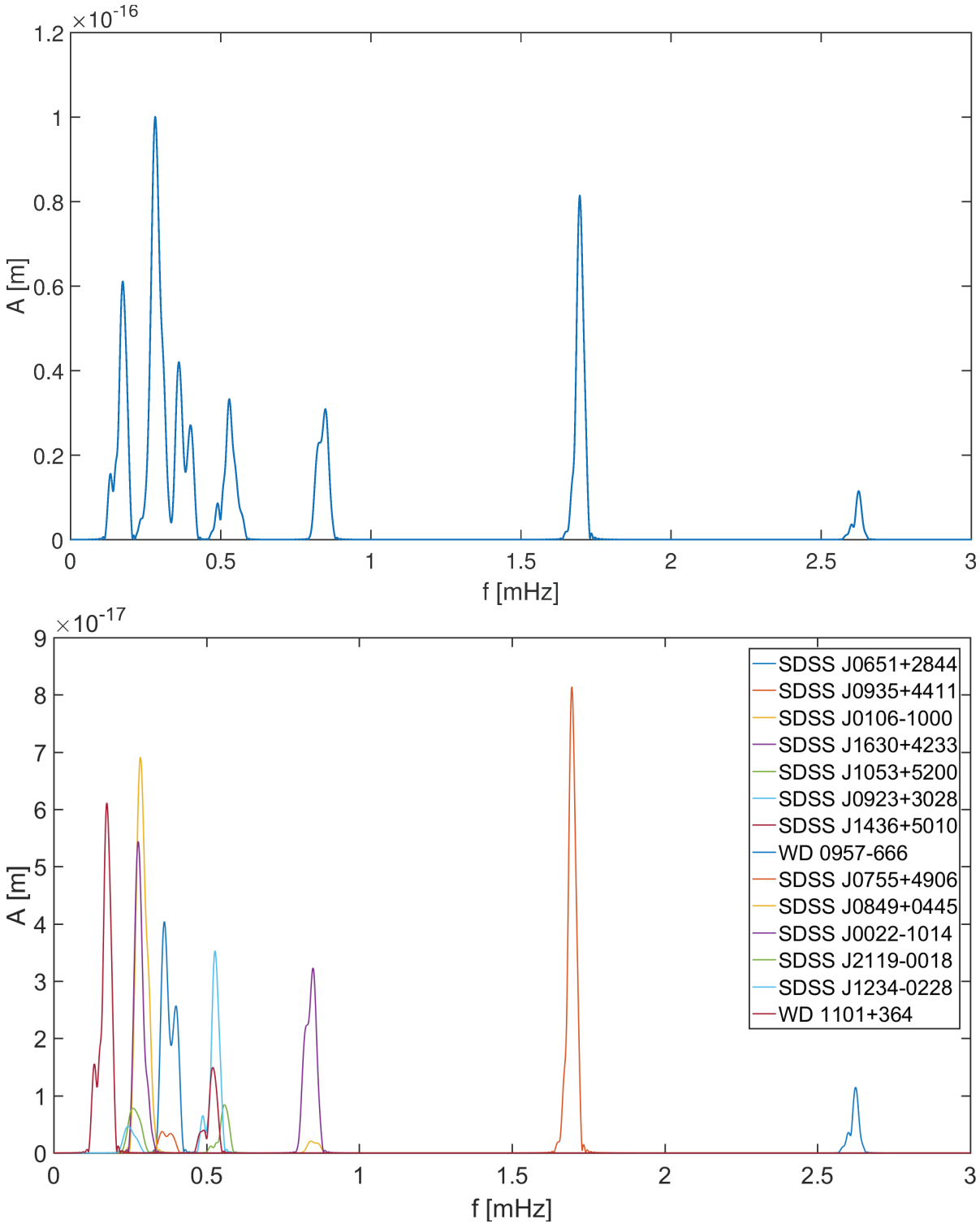

Fig 10: Déplacement radial à la surface de la Terre induit par les modes sphéroïdaux excités par 14 sources d'ondes gravitationnelles lorsque toutes les réponses individuelles sont sommées (en haut) et pour chaque réponse individuelle (en bas). Le spectre d'amplitude est calculé sur des signaux synthétiques d'une journée.

Tab 2: Amplitudes spectrales maximales de la réponse sphéroïdale induite pour les 14 sources d'ondes gravitationnelles du catalogue.

Name	A $[\mathrm{m} \cdot 10^{-18}]$	A $[\mathrm{m/s^2} \cdot 10^{-22}]$
SDSSJ0651+2844	11.47999	30.94457
SDSSJ0935+4411	81.43515	91.11686
SDSSJ0106-1000	2.04780	0.58756
SDSSJ1630+4233	32.30985	8.93221
SDSSJ1053+5200	8.42014	0.98185
SDSSJ0923+3028	35.31244	3.69649
SDSSJ1436+5010	14.95197	1.50795
WD0957-666	40.41132	2.29791
SDSSJ0755+4906	3.72761	0.19854
SDSSJ0849+0445	69.10639	2.36004
SDSSJ0022-1014	54.40300	1.80340
SDSSJ2119-0018	7.80692	0.21934
SDSSJ1234-0228	4.63214	0.11721
WD1101+364	61.13572	0.61757

Connaissant la réponse analytique de la Terre à une perturbation de la métrique de l'espace-temps, il est alors possible de chercher à détecter ce signal dans des données d'observations. Les sources considérées, les naines-blanches binaires, sont des sources stables en phase spiralante qui émettent continument des signaux quasi périodiques. Le signal est donc constamment présent dans les données, du moins à l'échelle de temps des détecteurs terrestres. Une technique de filtrage adaptatif appelée « matched filtering » s'avère être un outil pertinent pour chercher ce type de signal dans les données bruitées. Ce type de filtrage permet de détecter si un tel signal est présent dans les données et quand il a commencé. Le « matched filtering » consiste à calculer la corrélation entre les données et un signal-modèle (« template ») qui ressemble plus ou moins au signal cherché. Cette technique est d'ailleurs couramment utilisée pour la détection des ondes gravitationnelles à partir des interféromètres de type LIGO par exemple (Feller, 1950; Allen and Romano, 1999; Allen, 2004; Allen et al., 2012).

Le catalogue de sources que nous avons utilisé contient quatorze systèmes binaires de naines blanches dont les paramètres sont entachés d'une certaine incertitude. Aussi nous avons effectué des tests de sensibilité du signal gravitationnel modélisé à ces paramètres

et généré une banque de « templates » qui sera ensuite utilisée pour le filtrage adaptif. Nous avons ainsi vérifié que la fréquence de l'onde gravitationnelle est le paramètre le mieux contraint mais aussi le plus sensible pour définir des « templates ». Autrement dit, une faible modification de la fréquence génère de grandes différences sur les templates par rapport aux autres paramètres.

De plus, il est important de vérifier si le résultat du « matched filtering » va être influencé par des templates générés à partir de paramètres légèrement erronés. Nous allons donc faire varier les valeurs de ces paramètres sur un intervalle de valeurs défini par les incertitudes données dans le catalogue de sources. Nous testons ainsi deux hypothèses. La première H_0 correspond à la présence de bruit uniquement et H_1 à la présence d'un signal dans le bruit. Les résultats sont présentés sous forme de fonctions de densité de probabilité (PDFs). Lorsque les PDFs des deux hypothèses sont bien séparées, cela signifie qu'il y a une forte probabilité que l'on puisse détecter le signal avec le niveau de bruit présent. Nous testons ensuite une série d'expériences dans lesquelles nous faisons varier un paramètre à la fois tout en gardant le même niveau de bruit (la PDF de l'hypothèse H_0 ne change pas). Pour chaque « template », nous calculons ensuite la PDF. Le signal cherché et le template utilisé pour le filtrage sont pour l'instant identiques. Une comparaison des PDFs obtenues pour des templates générés à partir des deux valeurs extrêmes (c'est-à-dire la fréquence par défaut plus ou moins l'incertitude donnée dans le catalogue) de la fréquence de la source est représentée Fig. 11. Nous voyons qu'un template généré à partir d'une valeur du paramètre plus petite que celle par défaut (celle utilisée pour le signal cherché) nous conduit à une probabilité plus faible de détecter le signal que dans le cas où le template est généré à l'aide d'une valeur plus grande que la valeur par défaut. Ce qui est attendu, étant donné qu'alors l'amplitude de la déformation est plus grande.

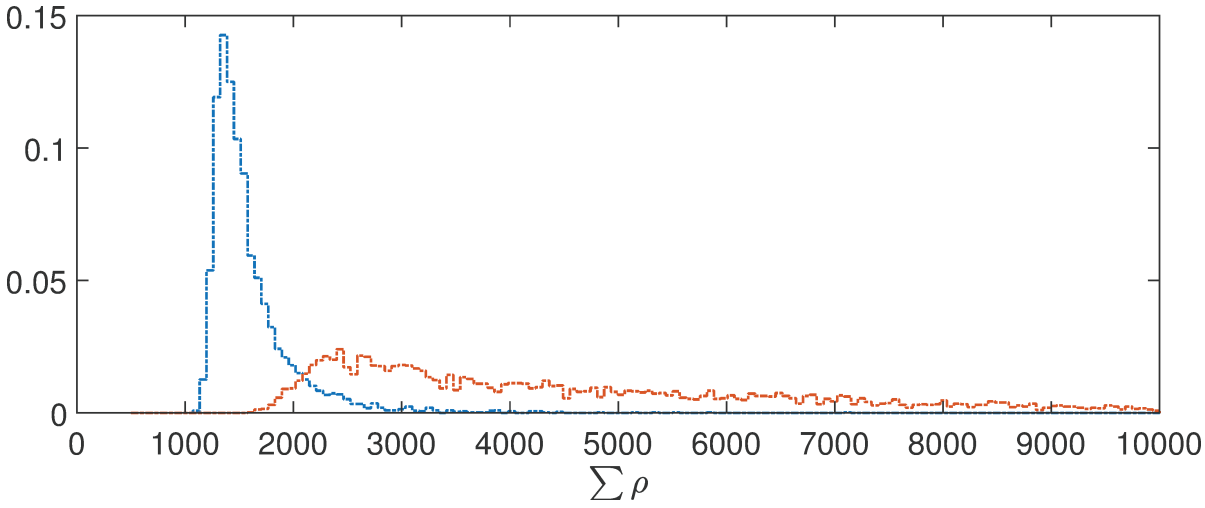

Fig 11: Fonctions densité de probabilité (PDFs) pour l'hypothèse H_1 lorsque le matched filtering est utilisé avec des templates générés à partir des valeurs extrêmes des paramètres source (en bleu pour des valeurs plus petites et en orange pour des valeurs plus grande que la valeur par défaut du paramètre). Ici nous avons représenté un exemple pour la fréquence source de l'onde gravitationnelle.

Dans les expériences suivantes, le signal cherché et le template utilisé pour le matched filtering ne sont pas forcément identiques. Le résultat dans le cas d'une modification de la fréquence source de l'onde gravitationnelle est représenté sur la Fig. 12. Nous voyons que les PDFs sont les mêmes pour tous les templates générés. Cela signifie que si nous appliquons le filtrage adaptatif avec un template légèrement différent du signal cherché (dans les limites de l'incertitude sur le paramètre considéré, ici la fréquence), nous obtenons la même probabilité de détection du signal. Cette conclusion est valide pour tous les paramètres que nous avons testés.

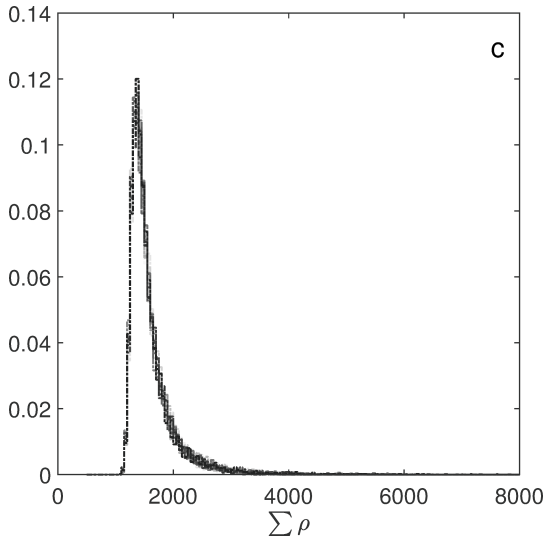

Fig 12: Fonctions densité de probabilité pour chaque template lorsque le template utilisé pour le matched filtering est légèrement différent du signal cherché. Ici nous avons représenté un exemple pour la fréquence source de l'onde gravitationnelle.

Nos tests synthétiques ont donc démontré que le « matched filtering » n'est pas sensible aux incertitudes présentes dans le catalogue de systèmes binaires. En d'autres termes, les incertitudes sur les paramètres des naines blanches doubles sont trop faibles pour impacter significativement la forme de nos signaux-modèles de sorte qu'ils se corrèlent très bien avec le signal cherché même si la superposition n'est pas parfaite.

La technique de « matched filtering » est désormais testée sur un signal synthétique injecté dans des vraies données gravimétriques. Les données utilisées sont celles enregistrées à BFO (Allemagne), qui est l'une des stations les moins bruitées dans la bande sismique considérée. Nous avons considéré un an de données enregistrées en 2012 dans lesquelles nous avons enlevé les journées comprenant des séismes. Nous avons ensuite sélectionné les jours pour lesquels le niveau de densité spectrale de puissance est inférieur au $25^{\text{ème}}$ percentile. La technique de « matched filtering » est finalement appliquée à ces données d'observation. Le résultat est représenté sur la Fig. 13. Afin de pouvoir détecter le signal injecté, le bruit des données a été artificiellement réduit en le divisant par un facteur d'amplitude $1.2 \cdot 10^{10}$ de sorte à avoir le même niveau de bruit que dans le cas d'un bruit blanc synthétique d'écart-type $\sigma_N = 7.5 \cdot 10^{-21}$ m/s^2. La Fig. 13 démontre qu'avec un bruit blanc synthétique la probabilité de détection est la même qu'avec un vrai bruit d'observations. Ce n'est pas surprenant, puisqu'à ces fréquences les PSDs observées sont constantes (cf. Fig. 9), ce qui est caractéristique d'un bruit blanc. Enfin, ce test montre que les niveaux de bruit actuels des données gravimétriques nécessitent d'être 10 ordres de grandeur plus petits afin de pouvoir détecter la réponse radiale induite par les ondes gravitationnelles émises par les

binaires de naines blanches.

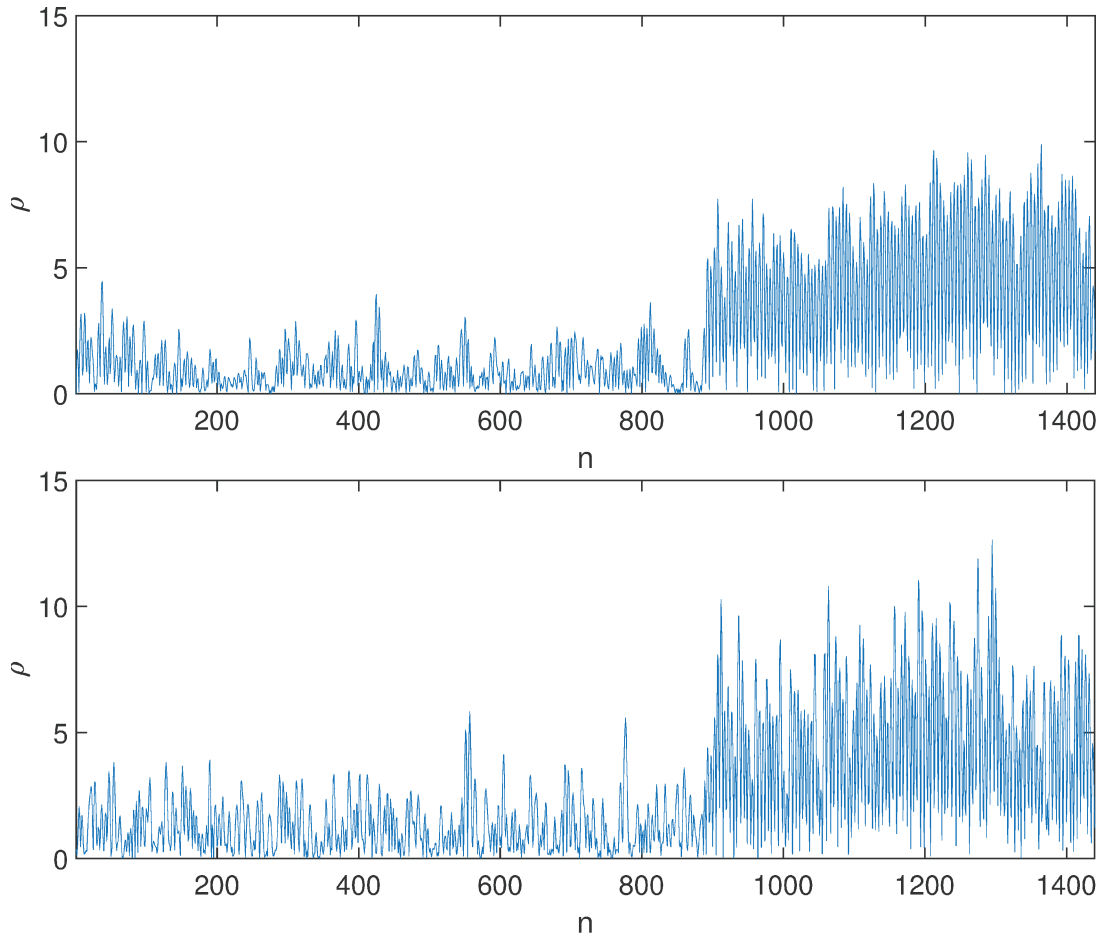

Fig 13: Résultat du matched filtering appliqué pour détecter un signal synthétique injecté dans (en haut) du bruit blanc d'écart-type $\sigma_N = 7.5 \cdot 10^{-21}$ m/s^2 et (en bas) dans des données enregistrées à la station BFO, pour lesquelles nous avons artificiellement réduit le bruit observé d'un facteur $1.2 \cdot 10^{10}$.

La dernière partie de ce travail de thèse concerne l'analyse des modes propres et en particulier souligne les éventuels biais qui peuvent être introduits par des méthodes de sommation de données. L'étude des modes sismiques apporte des contraintes essentielles sur notre connaissance de l'intérieur de la Terre et a largement contribué à la construction des modèles de référence, aussi bien des modèles radiaux de type PREM que des modèles tomographiques 3D. Malgré les nombreux outils d'analyses développés, des différences dans les mesures des paramètres (fréquences et facteurs de qualité) des modes sismiques existent encore soulignant la possible présence de biais inhérent à chaque méthode. Nous avons donc testé les performances de certaines techniques d'analyse couramment utilisées dans l'étude des modes propres et qui ont été proposées comme étant les plus adaptées. Nous avons ainsi implémenté trois méthodes qui ont été utilisées en complémentarité, à savoir : une

méthode de sommation dite OSE (Optimal Sequence Estimation) proposée par (Ding and Shen, 2013a), une méthode auto-régressive d'analyse fréquentielle (ARFD80) développée par (Chao and Gilbert, 1980) et une méthode appelée « phasor walkout » suggérée par (Zürn and Rydelek, 1994) basée sur la représentation d'un diagramme des phases d'une transformée de Fourier discrète d'un signal à une fréquence test donnée. La méthode OSE est une méthode de sommation permettant d'extraire des signaux de faible amplitude noyés dans du bruit. Cette méthode est basée sur le développement en harmoniques sphériques et suppose donc que le signal recherché est harmonique. La mesure de la fréquence propre d'un mode est effectuée à l'aide de la méthode ARFD80 qui repose sur la linéarisation du problème de l'estimation d'une fréquence complexe à l'aide de la technique de Prony permettant d'extraire des signaux exponentiels d'une série temporelle. Une fois mesurée, la fréquence propre complexe d'un mode est validée graphiquement à l'aide du « phasor walkout ». Ces trois méthodes ont été testées sur des sismogrammes synthétiques et sur des données gravimétriques et sismologiques. Les tests synthétiques sont effectués pour un modèle de Terre 3D à variations latérales de densité et de vitesse, pour un mécanisme de source sismique et en ne considérant qu'une chaîne de multiplets à la fois. Nous nous concentrons sur les modes basse-fréquence, là où l'approximation en « group-coupling » n'introduit que très peu d'erreur par rapport à l'approche en « full-coupling ». Nous avons conduit deux tests indépendants : augmenter progressivement le niveau de bruit d'une part et diminuer le nombre de stations utilisées dans le stacking d'autre part. L'influence sur les valeurs estimées des fréquences propres est quantifiée, ainsi que sur les coefficients de la fonction de splitting obtenue à partir de ces fréquences dans le cadre d'une théorie de la perturbation du premier ordre. Nos expériences synthétiques ont ainsi démontré que lorsque le bruit augmente, le rapport signal sur bruit (SNR) des signaux stackés diminue et les écarts-types des fréquences et facteurs de qualité Q estimés augmentent, et surtout les valeurs obtenues sont de plus en plus dispersées autour de la valeur de référence (cf. Fig. 14). Nous avons en particulier montré que la méthode OSE devient sensible à la distribution des stations sous l'influence du bruit. En outre, les performances de la méthode auto-régressive ARFD80 se détériorent lorsque le signal stacké est obtenu avec des signaux faiblement excités, c'est-à-dire lorsque les signaux d'entrée ont un rapport signal sur bruit inférieur ou égal à 2. Cependant, même dans ces cas, les estimations obtenues restent dans les barres d'erreur. Nos incertitudes calculées à l'aide d'une méthode itérative de « bootstrap » ne tiennent pas compte des biais identifiés précédemment. Par conséquent, même si la précision semble bonne, l'exactitude des estimations peut être mauvaise. Finalement, estimer les coefficients de structure à partir des fréquences, présente l'avantage d'avoir une détermination indépendante d'un modèle a priori, mais un biais peut alors être introduit.

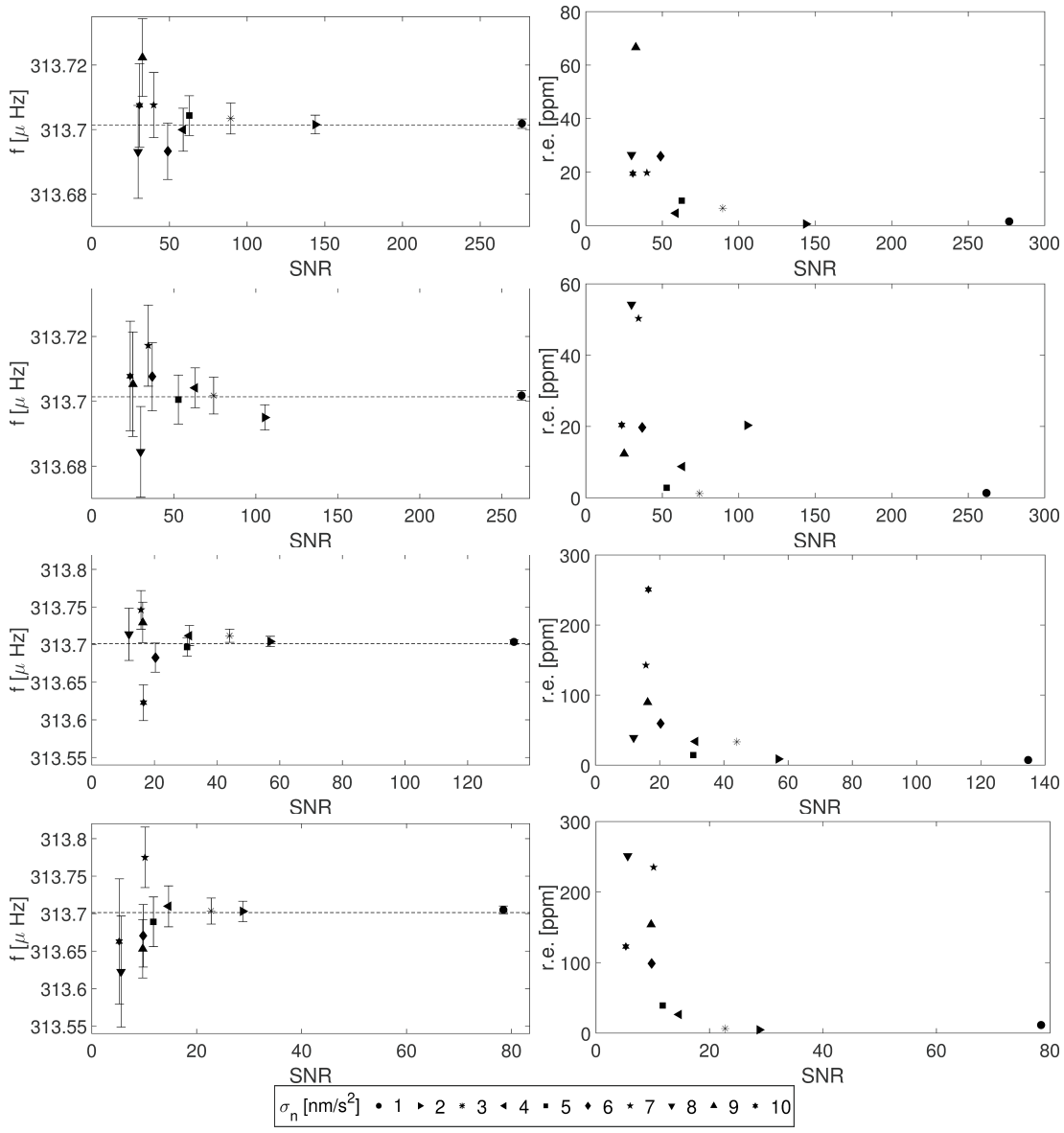

Fig 14: Expériences synthétiques pour le singlet m=1 du mode ${}_0S_2$ pour quatre distributions de stations différentes: 1) réseau complet (1ère ligne), 2) stations de l'hémisphère nord uniquement (2ème ligne), 3) stations de l'hémisphère sud uniquement (3ème ligne), 4) une sélection de stations (4ème ligne). Les figures sur la gauche représentent les fréquences estimées versus le SNR pour dix niveaux de bruit différents. Les figures sur la droite représentent les écarts relatifs des fréquences obtenues par rapport à la valeur synthétique de référence (valeur indiquée en line pointillée) en fonction du SNR pour les dix niveaux de bruit considérés. A noter que les échelles verticales des figures de gauche sont optimisées de sorte que celles pour le réseau complet et le réseau du Nord sont les mêmes, et celles du réseau du Sud et du réseau sélectionné sont les mêmes.

En conclusion, nous avons réécrit les équations modélisant l'effet des ondes gravitationnelles d'origine astrophysique sur les modes propres de la Terre. Nous avons réévalué l'amplitude à résonance pour un modèle de Terre sphérique et radialement stratifié du dé-

placement induit qui s'avère être plusieurs ordres de grandeur plus faible qu'initialement proposé par Ben-Menahem (1983) mais plus élevé que proposé par Dyson (1969) pour un modèle de Terre plate. Nous avons ensuite considéré la solution pour une Terre elliptique en rotation et à variations latérales de densité pour des sources d'ondes gravitationnelles que sont les systèmes doubles de naines blanches. Les amplitudes en déformation de ces ondes gravitationnelles émises sont de l'ordre de 10^{-22}-10^{-23}, soit deux ordres de magnitude plus faible que l'évènement détecté par LIGO en 2015 et provenant de la coalescence de deux trous noirs. Les échelles de temps en jeu sont cependant beaucoup plus longues puisque les fréquences considérées sont de l'ordre du millihertz et l'émission de ces ondes est continue dans le temps. L'excitation des modes sismiques de degré deux par les systèmes doubles de naines blanches est donc continue. La recherche dans les données gravimétriques et sismologiques à l'aide d'une technique de filtrage adaptatif est cependant rendue très difficile par l'amplitude du bruit présent dans les données. Enfin, nous avons mis en évidence certaines limites des techniques de combinaison et d'analyse de données dans la recherche et la caractérisation de faibles signaux et certains biais introduits par la distribution des réseaux de stations à la surface du globe.

Ce travail apporte une nouvelle contribution à l'étude des ondes gravitationnelles et pose de nouvelles limites sur leur détection. Détecter les ondes gravitationnelles par leur résonance avec les modes propres de la Terre dans la bande fréquentielle du millihertz n'est donc pas envisageable aujourd'hui de par les limites technologiques mais aussi à cause de la difficulté de réduire le bruit environnemental présent sur les observations terrestres. L'approche par modes propres proposée dans le cadre de cette thèse pourrait être étendue à d'autres planètes, en particulier Mars où un sismomètre a été récemment déployé dans le cadre de la mission Mars Insight. Une technique de corrélation entre les données sismométriques lunaires avec des données terrestres a été proposée par Coughlin and Harms (2014c) aboutissant à une meilleure contrainte sur la densité d'énergie d'ondes gravitationnelles émises dans l'univers aux fréquences inférieures à 1 Hz. Dans le futur les données du sismomètre martien pourront offrir des perspectives prometteuses dans ce contexte et apporter ainsi de nouvelles contraintes sur les modèles cosmologiques.

Contents

Acknowledgements

Extended Abstract

Résumé Étendu

List of Figures iii

List of Tables xv

1 Introduction 1

2 Detection of Gravitational Waves 3

2.1 Sources . . . 3

2.2 Detectors and Frequency Ranges . . . 5

2.3 Elastic Bodies as Detectors . . . 11

3 Earth Normal Modes 17

3.1 Spherical Non-rotating Elastic Isotropic Earth (SNREI) . . . 17

3.2 Rotating Anelastic Heterogeneous Earth . . . 20

3.2.1 The Splitting of an Isolated Multiplet . . . 20

3.2.2 The Mode Coupling . . . 22

3.2.3 The Splitting Function Coefficients . . . 24

3.3 Green tensor . . . 25

4 Normal Modes Excited By Gravitational Waves 27

4.1 Force Term in Flat Space-Time Approximation . . . 27

4.2 Terrestrial Reference System and Elastic, Non-rotating Earth Model . . . 29

4.2.1 Metric Perturbation Defined as Plane-wave . . . 30

4.2.2 Green tensor . . . 31

4.2.3 Induced spheroidal response . . . 32

4.2.4 Discussion . . . 38
4.2.5 Conclusion . . . 56
4.3 Celestial Reference System and Anelastic, Rotating Earth Model . . . 57
4.3.1 Rotation matrix from Celestial to Terrestrial Reference System . . . 57
4.3.2 Metric perturbation for the binary star system . . . 63
4.3.3 Green tensor . . . 65
4.3.4 Induced spheroidal response . . . 66
4.3.5 Discussion . . . 72
4.3.6 Conclusion . . . 96

5 Search for Gravitational Waves Using Matched Filtering 99
5.1 Introduction . . . 99
5.2 Synthetic tests . . . 100
5.3 Observations . . . 119
5.4 Conclusion . . . 124

6 Uncertainties in Normal Mode Studies 127
6.1 Introduction . . . 127
6.2 Synthetic Experiments . . . 130
6.3 Observations . . . 143
6.4 Conclusions . . . 149

7 Conclusion and Perspectives 151

A Greenwich Sidereal Time 155

B Matched Filter And Detection Statistics 159

C Autoregressive Method in Frequency Domain 165

D Optimal Sequence Estimation 169

E Phasor Walkout 173

Bibliography 181

List of Figures

1 GW frequency spectrum versus the characteristic strain for the GW detectors and sources (From Moore et al. (2015).) . . . . . .

2 Comparison in terms of power spectral densities between NLNM model, observed acceleration signal at the BFO (Germany) station and synthetic noisy signals (4.74) obtained by stacking 209 stations for ${}_0S_2$ and m=-2. Dark grey signal is obtained for $h_0 = 10^{-21}$ and with the standard deviation of injected white noise adjusted to allow for the signal to emerge from the noise. It was achieved with the rms value of NLNM model integrated over the frequency band of ${}_0S_2$ multiplet width, but reduced by seven orders of magnitude. Light grey signal is obtained for the level of the noise set to match rms value of NLNM model. The value of h_0 is increased until the signal emerges from the noise. That is achieved for $h_0 = 10^{-14}$. . . . . .

3 Induced spheroidal response for 14 GW sources when all responses are summed together (up) and when each response is plot individually (down) for one day long signals. . . . . .

4 Two PDFs for the H_1 hypothesis calculated for the edge templates (blue for the parameter smaller than the default parameter and orange for opposite) in the bank of templates for the GW source frequency parameter. . . . . .

5 PDFs calculated for each template from the bank of templates for the case when the target signal the template we perform the matched filtering do not match. The results are for the GW source frequency parameter. . . . . .

6 Matched filter output for the synthetic signal inserted into white noisy time series with $\sigma_N = 7.5 \cdot 10^{-21}$ m/s^2 (above) and the same synthetic signal inserted into observational noisy time series scaled with scalar $1.2 \cdot 10^{10}$ (below).

7 Synthetic experiments for ${}_0S_2^1$ singlet conducted for four station distributions: 1) full (the first row), 2) northern (the second row), 3) southern (the third row), 4) selected (the fourth row) networks. Figures on the left represent the estimated frequencies versus SNR for ten different noise levels. Figures on the right represent the relative errors of frequencies with regard to synthetic value (dashed line) versus SNR for ten noise levels. Be careful, the vertical scales of the left-side figures are optimized, thus the full and the northern networks have the same scale and the southern and the selected networks too.

8 Amplitude spectrale en déformation des ondes gravitationnelles en fonction des sources. Les courbes de sensibilité des détecteurs sont également indiquées (d'après Moore et al. (2015).) . . . . . .

9 Comparaison en termes de densités spectrales de puissance (PSD) du modèle de bruit bas NLNM, avec le niveau de PSD observé à la station BFO (Black Forest Observatory, Allemagne) et avec les signaux synthétiques bruités obtenus en sommant les séries temporelles générées à 209 stations pour le singlet m=-2 du mode ${}_0S_2$. Le niveau de PSD en gris foncé est obtenu pour $h_0 = 10^{-21}$ et avec un bruit blanc injecté ajusté de sorte que son écart-type permette au signal résultant du stacking d'émerger au-dessus du bruit. Ceci est atteint pour une valeur de RMS réduite de sept ordres de grandeur par rapport au NLNM par intégration de ce modèle sur la largeur fréquentielle du mode ${}_0S_2$. Le niveau de PSD en gris clair correspond au niveau de bruit du NLNM à la fréquence de ${}_0S_2$. Un signal périodique d'amplitude h_0 y a été ajouté avec une valeur h0 augmentée jusqu'à dépasser du bruit. Ce niveau de détectabilité est atteint pour $h_0 = 10^{-13}$. . . . . .

10 Déplacement radial à la surface de la Terre induit par les modes sphéroïdaux excités par 14 sources d'ondes gravitationnelles lorsque toutes les réponses individuelles sont sommées (en haut) et pour chaque réponse individuelle (en bas). Le spectre d'amplitude est calculé sur des signaux synthétiques d'une journée. . . . . .

11 Fonctions densité de probabilité (PDFs) pour l'hypothèse H_1 lorsque le matched filtering est utilisé avec des templates générés à partir des valeurs extrêmes des paramètres source (en bleu pour des valeurs plus petites et en orange pour des valeurs plus grande que la valeur par défaut du paramètre). Ici nous avons représenté un exemple pour la fréquence source de l'onde gravitationnelle. . . . . .

12 Fonctions densité de probabilité pour chaque template lorsque le template utilisé pour le matched filtering est légèrement différent du signal cherché. Ici nous avons représenté un exemple pour la fréquence source de l'onde gravitationnelle. . . . . .

13 Résultat du matched filtering appliqué pour détecter un signal synthétique injecté dans (en haut) du bruit blanc d'écart-type $\sigma_N = 7.5 \cdot 10^{-21}$ m/s^2 et (en bas) dans des données enregistrées à la station BFO, pour lesquelles nous avons artificiellement réduit le bruit observé d'un facteur $1.2 \cdot 10^{10}$. . . . . .

14 Expériences synthétiques pour le singlet m=1 du mode ${}_0S_2$ pour quatre distributions de stations différentes: 1) réseau complet (1$^{\text{ère}}$ ligne), 2) stations de l'hémisphère nord uniquement (2$^{\text{ème}}$ ligne), 3) stations de l'hémisphère sud uniquement (3$^{\text{ème}}$ ligne), 4) une sélection de stations (4$^{\text{ème}}$ ligne). Les figures sur la gauche représentent les fréquences estimées versus le SNR pour dix niveaux de bruit différents. Les figures sur la droite représentent les écarts relatifs des fréquences obtenues par rapport à la valeur synthétique de référence (valeur indiquée en line pointillée) en fonction du SNR pour les dix niveaux de bruit considérés. A noter que les échelles verticales des figures de gauche sont optimisées de sorte que celles pour le réseau complet et le réseau du Nord sont les mêmes, et celles du réseau du Sud et du réseau sélectionné sont les mêmes. . . . . .

2.1 Light from the laser first pass through the power recycling mirror and then is split by passing though the beam splitter. From the beam splitter light is sent along two arms, where these arms form cavities between near and far mirrors (the near mirrors are almost fully reflecting). After light leaves the cavities it returns back to the beam splitter to be recombined. If the recombined beam has a destructive interference it goes further to the photodetector; it is dark if GW is not present. Otherwise, if the recombined beam is constructive interference beam it is returned back to the laser. There the beam enters the power recycling mirror and is being reflected back into the interferometer in phase with the new incoming laser beam. All the mirrors and beam splitter are suspended to filter out mechanical vibrations. This scheme is not to scale, since arms are, for example, 4 km long like in LIGO experiment and all mirrors (except far mirrors) with beam splitter and photodetector are contained in a single building. (Adopted from Schutz (2009).) 8

2.2 Different models of the resonant mass detectors: two masses connected by the spring (up left), a bar (up right), multi-spring mass detector (down left), spherical detector formed with six transducers located with dots (down right). (From Ju et al. (2000).) 10
2.3 GW frequency spectrum versus the characteristic strain for GW detectors and source (From Moore et al. (2015).) 11
2.4 Historical chart representing the progress of the utilization of Earth as a detector of GWs (•). Additionally, the studies utilizing general elastic sphere (+) and astrophysical bodies (×) are also shown. Abbreviations stands for: $\rho_P(\omega)$ - power spectrum of the gravitational-radiation mass density, f - frequency/frequency range, u - displacement, u_h - horizontal displacement, Ω_{GW} - upper limit on energy density, S_E - spectral energy density, F - flux density. 15

4.1 Cartesian coordinate system $\mathcal{O}$, where its origin coincides with the center of mass of the Earth and $\hat{\mathbf{e}}_z$-axis points to the North, $\hat{\mathbf{e}}_x$-axis toward the Greenwich Meridian and $\hat{\mathbf{e}}_y$-axis is perpendicular to the $\hat{\mathbf{e}}_z\hat{\mathbf{e}}_x$-plane. 30
4.2 Function $f^m(e, \lambda, \nu)$ depending on e and λ angles when $\nu = 0$ from left to right and up to down corresponding to azimuth order $m = \{-2, -1, 0, 1, 2\}$, respectively. 37
4.3 Comparison in terms of power spectral densities between NLNM model, observed acceleration signal at the BFO (Germany) station and synthetic noisy signals (4.74) obtained by stacking 209 stations for ${}_0\mathrm{S}_2$ and m=-2. Dark grey signal is obtained for $h_0 = 10^{-21}$ and with the standard deviation of injected white noise adjusted to allow for the signal to emerge from the noise. It was achieved with the rms value of NLNM model for frequency band-width 20 μHz (see Tab. 4.4), but reduced by seven orders of magnitude. Light grey signal is obtained for the level of the noise set to match rms value of NLNM model. The value of h_0 is increased until the signal emerges from the noise. That is achieved for $h_0 = 10^{-14}$. 49
4.4 Resonance excitation of the Earth's normal modes due to monochromatic GW passing through Earth. Each frequency spike represent a resonance for a different radial order of a quadrupole mode. The light grey lines represent the normal mode frequency as a function of the radial order n indicated above the figure. 52

4.5 Absolute amplitude values for resonance and off-resonance modes. Each row on y-axis labelled by n represents the radial order of ${}_{n}S_2$ mode in resonance, for which $\omega_g =_0 \omega_2$, while each column on x-axis also labelled by n represents modes that are in the off-resonance regime. Each row is normalized with the largest value in that row. The black color represent the normal mode with the largest contribution. 53

4.6 Values for ${}_{n}Q_2$-factors (up), ${}_{n}U_2(r = a)$ eigenfucntions at the free surface (middle) and ${}_{n}\zeta_2$ functions (bottom) for $n = 0, ..., 99$ radial orders and $l = 2$. 54

4.7 Celestial reference system where CNP stands for Celestial Northern Pole and CSP for Celestial Southern Pole. On left, E stands for Earth and S for star system. The right ascension α and declination δ angles are marked, together with three vectors $\hat{\boldsymbol{k}}$, $\hat{\boldsymbol{i}}$, $\hat{\boldsymbol{j}}$ that form the orthogonal basis in the celestial reference system. On right, the same orthogonal basis in side view. The vector $\hat{\boldsymbol{k}}$ points from a star system to the center of the celestial reference system, $\hat{\boldsymbol{i}}$ is parallel to the celestial equator and point in the direction of decreasing right ascension. 58

4.8 Rotation of the natural polarization unit vectors $\hat{\boldsymbol{l}}$ and $\hat{\boldsymbol{m}}$ respect to the reference polarization unit vectors $\hat{\boldsymbol{i}}$ and $\hat{\boldsymbol{j}}$ via (4.83). The polarization angle ψ is measured from $\hat{\boldsymbol{i}}$ to $\hat{\boldsymbol{l}}$, counter-clockwise around $\hat{\boldsymbol{k}}$. (From Whelan (2013)). 59

4.9 Relationship between the Earth-fixed system $\{\hat{\boldsymbol{e}}_1^*, \hat{\boldsymbol{e}}_2^*, \hat{\boldsymbol{e}}_3^*\}$ and the inertial system $\{\hat{\boldsymbol{e}}_1, \hat{\boldsymbol{e}}_2, \hat{\boldsymbol{e}}_3\}$ where $\hat{\boldsymbol{e}}_3^* = \hat{\boldsymbol{e}}_3$. Angle γ between these two systems is Greenwich Sidereal Time. Vector $\hat{\boldsymbol{e}}_q$ is the projection of the vector $\hat{\boldsymbol{k}}$ into the equatorial plane. (From Whelan (2013)). 60

4.10 Projection of the unit vector $\hat{\boldsymbol{k}}$ into the equatorial plane represented by the vector $\hat{\boldsymbol{e}}_q$. This vector point to the Celestial Equator with the right ascension α, while vector $\hat{\boldsymbol{e}}_3$ points to Celestial North Pole. (From Whelan (2013)). . 61

4.11 Equatorial plane viewed from the top where the unit vectors $\{\hat{\boldsymbol{e}}_1^*, \hat{\boldsymbol{e}}_2^*, \hat{\boldsymbol{e}}_3^*\}$ are associated with the Earth-fixed system and the unit vectors $\{\hat{\boldsymbol{e}}_1, \hat{\boldsymbol{e}}_2, \hat{\boldsymbol{e}}_3\}$ with the inertial star system. Vector $\hat{\boldsymbol{e}}_q$ is projection of the unit vector $\hat{\boldsymbol{k}}$ into the equatorial plane and it points to Celestial Equator. Vectors $\hat{\boldsymbol{i}}$ and $\hat{\boldsymbol{j}}$ together with $\hat{\boldsymbol{k}}$ define the orthogonal basis defined by the right ascension α and the declination δ angles. γ is Greenwich Sidereal Time. 62

4.12 Split and coupled eigenfrequencies relative errors calculated for five models of the shear-velocity variations in Earth's mantle and two multiplet chains ${}_0S_2$ - ${}_0T_2$ - ${}_2S_1$ - ${}_0S_3$ (up) and ${}_2S_0$ - ${}_7S_2$ (bottom). Model S40RTS model is the referent one. y-axis stand for the relative error function. 78

4.13 Split and coupled eigenfrequencies relative errors between full- and group-coupling approximations for two multiplet chains ${}_0S_2$ - ${}_0T_2$ - ${}_2S_1$ - ${}_0S_3$ (up) and ${}_2S_0$ - ${}_7S_2$ (bottom), with group coupling values as referent ones. Both set of frequencies (for full and group coupling) are calculated for S40RTS model. y-axis stand for the relative error function. 79
4.14 Induced spheroidal radial response for 14 GW sources from Tab. 4.5 when all responses are summed together (up) and when each response is plot individually (bottom) for one day long signals. 83
4.15 Induced spheroidal radial response of the GW source SDSS J0651+2844 split into five singlets. 85
4.16 Pattern function $f_+^m(\gamma(t), \alpha, \delta, \psi)$ values for the declination δ versus the polarization ψ angles where Greenwich Sidereal Angle and the right ascension angle are set to zero ($\gamma(t) = 0, \alpha = 0$). From up to down each row stands for five azimuthal orders $m = -2, -1, 0, 1, 2$, respectively. From left to right each column stand for absolute, real and imaginary part of the function, respectively. 86
4.17 Same as Fig. 4.16 just for pattern function $f_\times^m(\gamma(t), \alpha, \delta, \psi)$. 87
4.18 Normalized response amplitudes for SDSS J0651+2844 source frequency 2.61 mHz for all quadrupole modes and their singlets used for building the complete response for this particular source. The rows represent quadrupole modes ${}_nS_2$ where $n = 0$ is the first row and $n = 23$ is the last row. Each column represents one azimuthal order, from left to right $m = -2, -1, 0, 1, 2$, respectively. 89
4.19 Comparison of the quadrupole modes frequencies for ${}_nS_2$, $n = 0, 1, 2, 3, 4, 5, 6, 7$ with the orbital frequencies of the binary systems listed in Tab. 4.5. 90
4.20 Amplitudes of the source-time functions $\bar{g}_+(t, \Omega, \omega_k)$ (left) and $\bar{g}_\times(t, \Omega, \omega_k)$ (right) with $t = 0$ and for SDSS J0651+2844 source. The rows represent quadrupole modes ${}_nS_2$ where $n = 0$ is the first row and $n = 23$ is the last row. Each column represents one azimuthal order, from left to right $m = -2, -1, 0, 1, 2$, respectively. 90
4.21 Amplitudes in terms of jointly contributions from displacement eigenfunction and model dependent functions ζ_k for all quadrupole modes ${}_nS_2$, where $n = 0$ is the first row and $n = 23$ is the last row. Each column represents one azimuthal order, from left to right $m = -2, -1, 0, 1, 2$, respectively. 91
4.22 Same as Fig. 4.18 but for sources A) SDSS J0935+4411, B) SDSS J0106-1000, C) SDSS J1630+4233, D) SDSS J1053+5200, E) SDSS J0923+3028, F) SDSS J1436+5010 from left to right and up to bottom, respectively. . . 92

4.23 Same as Fig. 4.18 but for sources A) WD 0957-666, B) SDSS J0755+4906, C) SDSS J0849+0445, D) SDSS J0022-1014, E) SDSS J2119-0018, F) SDSS J1234-0228 from left to right and up to bottom, respectively. 93
4.24 Same as Fig. 4.18 but for source WD 1101+364. 94
4.25 Density, horizontal and vertical P-velocity, horizontal and vertical S-velocity profiles (left) and shear modulus profile (right) of the PREM model. 96

5.1 Bank of the acceleration templates for the mass (up), the inclination angle (middle) and the declination angle (bottom) parameter. The bank of templates for the mass parameter is defined by the standard deviations from the catalog of the binaries, for the inclination angle the full range of non-repeating angles is considered and for the declination angle we artificially set standard deviation to be 5°. The result is for SDSS J0935+4411 source. . . 103
5.2 Bank of the acceleration templates for the right ascension angle (up), the distance (middle) and the polarization angle (bottom) parameter. The bank of templates for the right ascension parameter is defined by the standard deviations artificially set to be 5°. For the distance the standard deviations from the catalog of the binaries is used. For the polarization angle the full range of non-repeating angles is considered. The result is for SDSS J0935+4411 source. 104
5.3 Bank of the acceleration templates for the GW source frequency parameter defined by the frequency standard deviations from the catalog of binaries. The result is for SDSS J0935+4411 source. We show all templates plot together (up) and the first 14 (middle) and last 6 templates (bottom) separately. 105
5.4 Sensitivities to the mass (up left), the inclination angle (up right), the declination (down left) and the right ascension angle (down right) parameters of the GW source. The default template is indicated with the zero relative error percentage, except for the inclination angle where zero indicates the value of the angle for which the template is calculated. The result is for SDSS J0935+4411 source. 106
5.5 Same as Fig. 5.4 for the distance (up left), polarization angle (up right) and the GW source frequency (bottom) parameters. For polarization angle the same argument is valid as for the inclination angle. The result is for SDSS J0935+4411 source. 107

5.6 Synthetic data $d(t)$ of length $M = 5$ days consisting of white noise $n(t)$ of equal length and GW signal $w(t)$ for the SDSS J0935+4411 source of length $N \approx 9.5$ h. Indicated is also the template length of 5 periodic cycles $L < 1$ h and length of the window for which the matched filtering is performed of size $K = 2$ days. 108
5.7 Protocol expressed by the relations (5.3). From up to down: the first row, the synthetic signal $w(t)$ of length $N = 1$ day inserted into the noisy time series $\sigma_N n(t)$ of the standard deviation $\sigma_N = 5.1 \cdot 10^{-21}$ m/s^2 and length $M \approx 145$ days constitute data $d(t)$ of length M; the second row, data $d(t)$ is separated in $k = 145$ smaller data sets of length $K = 1$ day; the third row, represent the two matched filter outputs ρ_w of length K for window when there is a signal and when there is no signal present; the fourth row, the PDFs for the two hypotheses H_0 (blue) and H_1 (orange) for 2500 randomly generated signals (left) and the ROC curve for these two probabilities (right). 111
5.8 PDFs for the two hypotheses H_0 (blue) and H_1 (orange) (left) and the ROC curves (right) for the three different noise standard deviations σ_N: $1.3 \cdot 10^{-20}$ m/s^2 (up), $2.0 \cdot 10^{-20}$ m/s^2 (middle), $3.2 \cdot 10^{-20}$ m/s^2 (bottom). All the other parameters are the same as in Fig. 6.1. 112
5.9 PDFs for the two hypotheses H_0 (blue) and H_1 (orange) when template is one cycle long (background) and ten cycles long (foreground) with all the other parameters same as in Fig. 6.1. 113
5.10 PDFs for the two hypotheses H_0 (blue) and H_1 (orange) for $K = 1$ (background) and $K = 0.5$ day (foreground) and with all the other parameters same as in Fig. 6.1. 113
5.11 Two PDFs for the H_1 hypothesis calculated for the edge templates (the left edge, when parameter value is smaller than the default parameter is denoted by blue; the right edge, when parameter value is bigger than the default parameter is denoted by orange) in the bank of templates for the mass (up), the inclination angle (middle) and the declination angle (bottom) parameter. 115
5.12 Same as Fig. 5.11 just for the right ascension angle (up), the distance (middle) and the polarization angle (bottom) parameter. 116
5.13 Same as Fig. 5.11 just for the frequency parameter. 117
5.14 PDFs calculated for each template from the bank of templates for the case when the waveform $w(t)$ and the template $w_{template}(t)$ do not match for a) the mass, b) the inclination angle, c) the declination angle, d) the right ascension angle. 118

5.15 Same as Fig. 5.14 just for a) the distance, b) the polarization angle, c) the GW source frequency. 119
5.16 Distribution of the earthquakes of magnitude larger than 6.5 for year 2012 at the Black Forest Obsrvatory station, Germany $(43.33°, 8.33°)$. 120
5.17 PSDs of the one day long signals for year 2012 at BFO station with 1st, 25th, 50th and 75th percentile marked together with the NLNM. 121
5.18 Same as Fig. 5.17 just for 25th percentile only. 121
5.19 Synthetic signal inserted into white noisy time series with $\sigma_N = 7.5 \cdot 10^{-21}$ m/s^2 (above) and the matched filter output (below) for window where the signal is inserted. 123
5.20 Synthetic signal inserted into observational noisy time series scaled with scalar $1.2 \cdot 10^{10}$ (above) and the matched filter output (below) for window where the signal is inserted. 124

6.1 Diagram of the used protocol, where the input data are in yellow color, output data in blue and used methods in purple. The input data, the network of stations and noise level, are used to obtain response functions for specific normal mode described by radial n, angular l and azimuthal m order in the stacking process by OSE method. Further, from each function the complex frequency and Q-factor are estimated using ARFD80 method and phasor walkout is used to validate the estimated values. Finally, from the obtained singlets complex frequencies the splitting function coefficients are estimated. 130
6.2 Station database build from Global Seismograph Network, where 4 group of stations are: "full" network of 81 stations (circle mark), "northern" network with 53 stations in northern hemisphere (blue color), "southern" network with 23 stations in southern hemisphere (red color) and "selected" network which 10 stations (underlined). 131
6.3 Synthetic experiments for ${}_0S_2^1$ singlet conducted for four station distributions: 1) full (the first row), 2) northern (the second row), 3) southern (the third row), 4) selected (the fourth row) networks. Figures on the left represent the estimated frequencies versus SNR for ten different noise levels. Figures on the right represent the relative errors of frequencies with regard to synthetic value (dashed line) versus SNR for ten noise levels. Be careful, the vertical scales of the left-side figures are optimized, thus the full and the northern networks have the same scale and the southern and the selected networks too. 134

6.4 Synthetic experiments for ${}_0S_2^1$ singlet conducted for four station distributions: 1) full (the first row), 2) northern (the second row), 3) southern (the third row), 4) selected (the fourth row) networks. Figures on the left represent the estimated Q-factors versus SNR for ten different noise levels. Figures on the right represent the relative errors of Q-factors with regard to synthetic value (dashed line) versus SNR for ten noise levels. 135
6.5 Variability of the OSE resonance functions due to four different networks and ten noise levels for the ${}_0S_2$ mode. 136
6.6 Fourier Transform of OSE stacked signals (left) with associated phasor walkouts and applied R^2-test values (right) for five test frequencies with f_e being the estimated frequency of stacked signal on left and σ the standard deviation. Three cases are shown: full network with noise level $\sigma_n = 1$ nm/s^2(top), full network with $\sigma_n = 9$ nm/s^2 (middle) and selected network with $\sigma_n = 8$ nm/s^2 (bottom). Results are for ${}_0S_2^1$ singlet. 137
6.7 Estimated frequency bootstrap standard deviations (black line) and standard deviations estimated from frequency relative errors (gray line) versus SNRs for all experiments of ${}_0S_2$ multiplet. 138
6.8 Splitting function coefficient c_{20} inverted from eigenfrequencies estimated in synthetic experiments for ${}_0S_2$ multiplet considering four different station distributions and ten noise levels. 140
6.9 Fourier Transform of OSE signal (left) with associated phasor walkout and R^2-test values (right) for five test frequencies with f_e being the estimates frequency of stacked signal on left and σ the standard deviation. Results correspond to selected network with $\sigma_n = 1$ nm/s^2 for ${}_2S_1^{-1}$ singlet with SNR of 5.8. 141
6.10 Comparison between the synthetic resonance functions obtained for group coupling (solid line) and self coupling (dashed line) approximations for the singlets of ${}_1S_3$ multiplet. 142
6.11 ${}_2S_1$ and ${}_3S_1$ singlets obtained using the OSE stacking method applied on 7 and 12 days long time series, respectively. The amplitude values are 0.08, 0.05, 0.20 nm/s^2 for ${}_2S_1$ and 0.51, 0.25, 0.81 nm/s^2 for ${}_3S_1$. 145

B.1 Probability density functions for H_0 (blue) and H_1(orange) hypothesis (left column) and associated ROC curves (right column). AROC stand for the area under the ROC curves. 163

E.1 The result of the R^2-test for three different tested frequencies $\{f_e-\sigma, f_e, f_e+\sigma\}$, where f_e is truth frequency of tested signal, thus the R^2-test is the closest to 1. 175

E.2 The phasor walkout for a signal with two harmonic functions of frequencies $f_1 = 9$ mHz and $f_2 = 10.1$ mHz for several different cases. From a) to g) the tested frequency is $f_s = f_1$, while for b) to h) $f_s = f_2$. Cases a) and b) the starting signal is defined by (E.7) with $A_1 = A_2 = 1$ [nm/s^2], $\theta_1 = \theta_2 = 0$. In c) and d) phases are added $\theta_1 = 0.75$ and $\theta_2 = -0.75$ are added. In e) and f) phases are the same $\theta_1 = \theta_2 = 0.75$ and amplitudes are added with $A_1 = 10$ [nm/s^2] and $A_2 = 1$ [nm/s^2]. In g) and h) phases and amplitudes stay the same but a decay rate defined with $\exp\left(-\frac{\pi f_1}{100}\mathrm{i}\Delta t\right)$ is added. 177

E.3 Synthetic signals (left) and appropriate phasor walkouts (right) for the experiment setups a, b, c, d, e from Table E.1. In all setups the phasor walkout is calculated for the ${}_0\mathrm{S}_2^{-2}$ singlet. 179

E.4 Synthetic signals (left) and appropriate phasor walkouts (right) for the experiment setups f, g, h, i, j from Table E.1. In setups f and h the phasor walkout is calculated for the ${}_0\mathrm{S}_2^{0}$ singlet, in g and i for ${}_0\mathrm{S}_2^{-2}$ singlet and in j for ${}_0\mathrm{S}_2^{-1}$ singlet. 180

List of Tables

1 Maximum spectral amplitudes of the induced spheroidal response for 14 GW sources. . . . . .

2 Amplitudes spectrales maximales de la réponse sphéroïdale induite pour les 14 sources d'ondes gravitationnelles du catalogue. . . . . .

2.1 The summary of the existed, existing and planned ground-based laser interferometers. 7

2.2 The summary of the existed and existing resonant bar detectors. 10

3.1 Seismic Green tensor with and without rotation and anelasticity. Each of the sums is over all of the seismic normal modes with associated real or complex eigenfrequencies ω_k or $\nu_k = \omega + i\gamma_k$. 25

3.2 Displacement eigenfunction of a spherically symmetric Earth model in the presence or absence of rotation and anelasticity. The scalars U,V,W and the spherical harmonics $\mathcal{Y}_{lm}$ are real, whereas $\mathcal{U}, \mathcal{V}, \mathcal{W}$ and Y_{lm} are complex. The eigenfunctions of a non-rotating spherical Earth model are exact, whereas those of a rotating spherical Earth model are only correct to zeroth order in the angular rate of rotation, $\Omega = ||\mathbf{\Omega}||$. 26

4.1 Excited degree-2 azimuthal terms for different combinations of the $\{e, \lambda, \mu\}$ angles defining the incoming gravitational wave. 38

4.2 List of functions (spherical harmonics, associated Legendre functions, Green tensors, displacement eigenfunctions, normalization of displacement eigenfunctions, respectively) that are used to develop displacement for radially heterogeneous, anelastic self-gravitating, rotating Earth model for Ben-Menahem (1983) and Dahlen & Tromp (1998) formalism. Constants are $\Omega_{lm} = \frac{4\pi}{2l+1}\frac{(l-m)!}{(l+m)!}$ and $\kappa = \sqrt{(l(l+1))}$. Normalization of the displacement eigenfunction for Dahlen & Tromp (1998) is written for spherical non-rotating elastically isotropic Earth model, since the rotation is treated as a perturbation. 45

4.3 MINEOS normalized values of the eigenfunctions U, V, P at the Earth surface $r = a$, frequency ω, quality factor Q for ${}_0S_2$ and gravity value at the surface g. Used normalization for length is $R = 6371$ km, time $\frac{1}{\pi G \rho_a}$ and mass $\rho_a R^3$, where $G = 6.67408 \cdot 10^{-11}$ $m^3 kg^{-1} s^{-2}$ is the gravitational constant and $\rho_a = 5515.0$ kgm^{-3} is the average density. 46

4.4 Estimate of the noise standard deviations for the frequency band-width of entire multiplet and one singlet for ${}_0S_2$ mode and the fixed PSD value of the NLNM. 48

4.5 List of the double white dwarf binaries and their parameters: the orbital periods, the distances to the sources,the masses of the two stars, the inclination angle, the right ascension and the declination angle. Each parameter, except the right ascension and the declination, has associated uncertainties if they exist. The last column contains appropriate references. The table is based on link. 74

4.6 List of the double white dwarf binaries with their orbital frequencies and the associated relative errors and the metric perturbation strength for + and × terms. 75

4.7 List of the multiplet chains and their frequency ranges used in the group-coupling approximation for the splitting matrix calculation. Multiplet chains for ${}_nS_2, n = 0, \ldots, 7$ modes are adopted from Deuss and Woodhouse (2001). Multiplets from $n = 8$ to $n = 23$ are used to check the far off-resonance regime. 77

4.8 Split and coupled eigenfrequencies (in mHz) for 24 quadrupole modes calculated for S40RTS model. 81

4.9 Q-factors corresponding to the split and coupled eigenfrequencies for 24 quadrupole modes calculated for S40RTS model in Tab. 4.8. 82

4.10 Maximum spectral amplitudes of the induced spheroidal radial responses shown in Fig. 4.14. 84

6.1 Estimated eigenfrequencies (in μHz) and Q-factors with associated standard deviations, SNRs and number of stations N used in the stacking for ${}_0S_2$ and ${}_0S_3$ multiplets compared with published values. Methods applied: * Lorentzian fitting, $^\diamond$ nonlinear iterative least squares inversion, $^\circ$ multitapers, $^\triangledown$ ARFD80, $^\triangleleft$ ensemble empirical mode decomposition, $^\triangleright$ AR-spectrum and ARFD80. 146

6.2 Estimated eigenfrequencies (in μHz) and Q-factors with associated standard deviations, SNRs and number of stations N used in the stacking for ${}_2S_1$ triplet compared with published values. Methods applied: * Lorentzian fitting, $^\diamond$ nonlinear iterative least squares inversion, $^\times$ OSE and ARFD80, $^\triangledown$ ARFD80, $^\triangleleft$ ensemble empirical mode decomposition, $^\triangleright$ AR-spectrum and ARFD80, $^\otimes$ multi-station experiment technique, † spherical harmonic stacking and ARFD80. 147

6.3 Estimated eigenfrequencies (in μHz) and Q-factors with associated standard deviations, SNRs and number of stations N used in the stacking for ${}_3S_1$ triplet compared with published values. Methods applied: * Lorentzian fitting, $^\diamond$ nonlinear iterative least squares inversion, $^\times$ OSE and ARFD80, $^\triangledown$ ARFD80, $^\triangleleft$ ensemble empirical mode decomposition, $^\triangleright$ AR-spectrum and ARFD80, $^\otimes$ multi-station experiment technique, † spherical harmonic stacking and ARFD80. 148

6.4 Second order axisymmetric structure coefficients for ${}_0S_2$ compared with published values. The structure coefficients are computed from the singlet frequencies (*) or the nonlinear iterative least squares inversion ($^\diamond$). 148

E.1 Singlets parameters used to calculate signals, where f [μHz] is the frequency of the signal, Q the quality-factor and A [nm/s^2] amplitude. Amplitude marked with the asterisk points to the singlet which frequency is used as test frequency for obtaining the phasor walkout patters in Fig. E.3 and E.4. . . 178

Chapter 1

Introduction

On September 14, 2015 at 09:50:45 UTC for the first time in history the two detectors of the Laser Interferometer Gravitational-Wave Observatory (LIGO) simultaneously detected a gravitational wave (GW) from a binary hole merger (Abbott et al., 2016). This was an additional indisputable proof of the theory of general relativity published by Albert Einstein in 1916, who found transverse waves that travel at the speed of light as a solution for the weak-field equation of his theory. These waves are generated by the time variation of the mass quadruple moment of the sources (Einstein, 1916, 1918). The detection consisted of a transient GW signal with the peak strain of 1.1×10^{-21} whose frequency increased with time (chirp) from 35 to 250 Hz in 0.15 s. The signal matched the predicted waveform for the inspiral and merger of a pair of black holes and the ringdown of the resulting single black hole. After the main detection ten more followed, thus until today there are eleven successfully identified mergers, ten of stellar-mass binary black hole mergers and one binary neutron star (Abbott et al., 2018). Currently The Advanced LIGO (Aasi et al., 2015) and The Advanced Virgo (Acernese et al., 2014b) are in the third observation run, known as O3, which began 1st of April, 2019 and is scheduled for one calendar year. The updates on detectors statuses and GW Candidate Event Database can be followed on the website https://www.gw-openscience.org/about/.

This historical breakthrough is a marvel of human achievement. It is a catalyst of many new sciences and as well a motivation for the reconsideration of some earlier ideas on the GW detection. One of these ideas is the topic of this dissertation and that is detecting the GWs by observing the vibration of the elastic bodies due to the incident GWs. The elastic body in question is the Earth and its states of vibration, the normal modes. The study is based on the works by Dyson (1969) and Ben-Menahem (1983). We use these earlier works to develop a new interaction model between the GWs and Earth. We further use this model to determine a limit of the sensitivity that we must reach with our sensors on Earth to be able to detect GWs. The appealing thought is whether we could use the existing network

of sensors, so far used to improve our understanding of Earth, as an astrophysical device to explore our Universe.

This dissertation is organized as follow. Chapter 1 is about the GW detection in general, what kind of sources generate GWs, what is the frequency spectrum of the GWs sources and detectors and also a short revision about the interaction between GWs and elastic bodies. Chapter 2 deals with the theoretical background on the normal modes of the Earth in terms what are the normal modes, how we define the idealized Earth model and the perturbation to that model, what does this implies in terms of normal modes splitting and coupling and how we model that. In chapter 3 we present two models of the interaction between GWs and Earth. In chapter 4 we introduce the matched filtering technique and application of this technique to the model developed in previous chapter. Chapter 5 is focused on the measurement uncertainties within the context of the normal mode studies, such as measurement of the normal mode frequencies, Q-factors and splitting function coefficients. We finish with general conclusions and perspective how this work could be extended in the future.

Chapter 2

Detection of Gravitational Waves

The first direct detection of the GWs started an era of the gravitational-wave observational astronomy. Standard astronomy has traditionally relied on electromagnetic radiation, however since 96% of the mass-energy of the universe carries no charge, the large part of the universe remained non-visible within the electromagnetic spectrum (Sathyaprakash and Schutz, 2009). Electromagnetic waves strongly couple to charges, therefore they are easy to detect but are also easily scattered or absorbed by material between us and the source. Unlike electromagnetic waves, the GWs couple extremely weakly to matter, making them very hard to detect but allowing them to travel substantially unaffected by intervening matter. Last few decades many work has been done to understand what kind of sources generate the GWs and how one can detect them. In this chapter we give a short introduction into these two topics. In Section 2.2 we list some of the expected GW sources; in Section 2.1 we explain a bit further the GW spectrum and detectors associated with each GW frequency band; in Section 2.3 we touch upon some of the earliest studies on the GW detection using elastic bodies.

2.1 Sources

Due to the non-existence of the monopolar and dipolar gravitational radiation a spherical symmetric variation does not produce gravitational radiation. And this is true no matter how violent the explosion or a collapse is. Also, a rotation lacking contraction or expansion does not generate gravitational radiation because the quadrupolar and higher moments are changeless. The sources that actually produce gravitational radiation form a spectrum that is conventionally divided into three classes, according to the data processing methods and signal extraction (Ju et al., 2000).

The first class consist of very poorly modeled transient sources which are catastrophic burst sources: the final coalescence of the compact binary star systems (binary neutron

stars, black holes and neutron-star-black-hole binaries), formation of neutron stars and black holes in supernova events (gravitational collapse to a neutron star or black holes). The burst signals can produce very strong signals with very large amplitudes, however they are of the short duration and due to the lack of the detailed waveform, their detection is difficult. The search is normally performed using the time-frequency techniques. One needs to identify the excess of power in the data segments in the frequency domain (Abadie et al., 2012; Moore et al., 2015).

The second class are narrow-band sources. This includes a rotation of single nonaxisymmetric stars (pulsars and accreting neutron stars) and radiation from a binary star systems far from coalescence. Such systems are less stronger than the burst signals, however they are quasi-periodic and by tracking them over a long time period, in principle, one can extract their signal from noise. This implies that one needs to accurately model frequency modulation due to the binary motion and the Earth's orbital motion. During the orbital motion of the binary star system the energy radiation causes the orbit to shrink. The shrinking is causing the increase in the GW frequency in time, called a chirp. As the binary system evolves, the frequency and the amplitude of the GW grow and this cause the binary to evolve even more rapidly. The slow inspiral phase is ending when stars begin to merge or when the distance between stars reach the last stable orbit (for the compact binaries). After passing the last stable orbit the compact-object coalesces and this is called compact binary coalescences (Sathyaprakash and Schutz, 2009). The eleven confident detection of GWs belong to the class of the compact binary merges, ten binary black holes mergers and one binary neutron star signal (Abbott et al., 2018). At lower frequencies than the frequencies of the coalescing binaries the most promising source of GWs are the more abundant white-dwarf binaries. These binaries have a long lifetimes and since they are not as compact as neutron stars or black holes they never reach the last stable orbit. Their amplitude is several orders smaller than the amplitude of the neutron star or black binary hole coalescence at the same distance. Another type of second class sources are also supermassive black holes and extreme and intermediate mass-ratio inspiral sources.

The third class of the GW sources are the stochastic backgrounds, random GW fields produced from a superposition of the countless discrete systems and also from fundamental processes, such as the Big Bang. They can contain everything, from very weak periodic sources, very distant burst sources and as well cosmological processes existing in the early universe. Detection of the stochastic backgrounds is performed by cross-correlating two nearby detectors, because a random radiation is indistinguishable from the noise in a single detector. By doing so one expects to obtain nonzero output that is much larger than one

would obtain from the variance of the correlation of two statistically independent noise fields from the two detectors.

Each of these sources can be detected differently and in the next section we introduce more specifically individual parts of the GW spectrum and their associated detectors.

2.2 Detectors and Frequency Ranges

Detection of the GW has many different approaches for different part of the GW spectrum. Each frequency band is characterized by different operating detectors and different gravitational sources. There are four frequency bands of interest:

- extremely low frequency (ELF) band from $\sim 10^{-15}$ to $\sim 10^{-18}$ Hz,
- very low frequency (VLF) band from $\sim 10^{-7}$ to $\sim 10^{-9}$ Hz,
- low frequency (LF) band from $\sim 10^{-4}$ to ~ 0.1 Hz,
- high frequency (HF) band from ~ 10 to $\sim 10^{3}$ Hz.

In the ELF band the GWs are sought via their imprint on the polarization of the cosmic microwave background (CMB) radiation, a relic of the early Universe. The expected sources are the quantum fluctuations in the gravitational field (space-time curvature) that emerged from the Big Bang's event (Thorne and Blandford, 2017).

In the VLF band radio astronomers search for small irregularities in the arrival times of the pulsar signals caused by the GWs. Pulsars are spinning neutron stars that emit strong radio waves due to their rotational energy. Their very high rotational energy generates electric field from the movement of the very strong magnetic field, which result in the acceleration of protons and electrons on the star surface and thus creation of the electromagnetic beam emanating from the poles of the magnetic field. Every time a magnetic pole points toward the Earth, the beamed emission is observed as a 'pulse' of radio waves. Therefore, each pulsar act as a regular clock. The measured pulse arrival time can be compared against a prediction, where residual times include the effects of the passing GW through the radio array (Schutz, 2009). Current pulsar timing arrays (PTAs) in operation are the European Pulsar Timing Array (EPTA[1]; Kramer and Champion (2013); the detector sensitivities in Babak et al. (2016)), the Parkes Pulsar Timing Array (PPTA[2]; Hobbs (2013)) in Australia and the North American Nanohertz Observatory for Gravitational Waves (NANOGrav[3],

[1] http://www.epta.eu.org/
[2] http://www.atnf.csiro.au/research/pulsar/ppta/
[3] http://nanograv.org/

McLaughlin (2013)). The International Puslar Timing Array (IPTA[4]; Manchester (2013)) is a consortium of consortia, comprised of EPTA, PPTA, NANOGrav, and its principal goal is to detect GWs using one single array of approximately 30 pulsars. The next detector prototype in the radio astronomy is the Square Kilometre Array (SKA[5]; Dewdney et al. (2009)), the world's largest radio telescope. It will be made up of arrays of antennas - SKA-mid observing mid to high frequencies and SKA-low observing low frequencies - spread approximately over one square kilometre. Having the receiving stations extending over the vast area it would provide the highest resolution images in all astronomy.

In the LF band a common method to detect GWs is interplanetary spacecraft tracking. This technique works on the principle of a general beam detector (Thorne and Blandford, 2017). Spacecraft carries transponders, radio receivers, that amplify and return the signal from the ground tracking stations. A measurement of the return time defines the position of the spacecraft and if this measurement is accurate enough, small changes in the return time of the radio signals might indicate existence of the GWs (Armstrong, 2006). Since it turned out that the sensitivity of these searches is not high, this technique will be supplanted by Laser Interferometer Space Antenna (LISA[6], Bender et al. (1995)) and eLISA[7] (Amaro-Seoane et al., 2012), rescoped version of the classic LISA mission. LISA is a space-based detector that consists of three satellites flying in a triangular constellation with arms of length 5×10^9 m in a 1 AU orbit around the Sun, trailing the Earth by 20°. Each satellite contains of two telescopes, two lasers and two free falling test masses arranged so that each satellite point at the other two. This forms Michelson-like interferometers, each centered on one of the satellites, with the test masses defining the ends of the arms. Therefore, LISA-like detectors use laser interferometry, however the laser beams are not contained in cavity and the beam travels only once along each arm, unlike in ground-based detectors. The distances between the satellites are precisely monitored and every distortions will be caused by the passing GWs. Each satellite is a zero-drag satellite, which effectively floats around test masses, maintaining themselves centered around the masses and monitoring their relative position to the spacecraft. Thus, using this principle all non-gravitational forces are eliminated. eLISA (evolved Laser Interferometer Space Antenna) is designed to probe the same frequency range as LISA and the main differences are the shorter arms (10^9 m), two laser arms instead of three and different orbit. Some of the potential sources for space-based detectors are massive black holes mergers at the centre of galaxies, massive black holes orbited by small compact objects, extreme mass ratio inspirals, binaries of compact

[4] http://www.ipta4gw.org/
[5] https://www.skatelescope.org/
[6] https://lisa.nasa.gov/
[7] https://www.elisascience.org/

stars in our Galaxy. Proposed successor to LISA are the Advanced Laser Interferometer Antenna (ALIA; Crowder and Cornish (2005)), Big Bang Observer (BBO; Crowder and Cornish (2005)) and Deci-hertz Interferometer GW Observatory (DECIGO; Takahashi and Nakamura (2003)). All successors are designed to probe the decihertz region of the GW spectrum. For overview of the GW detection in space the reader is referred to Ni (2016).

In the HF band GWs are detected by the ground-based laser interferometer detectors and the resonant-mass detectors. The laser interferometers utilize the principle of laser interferometry and a common configuration for optical interferometry is the Michelson interferometer. It consists minimally of one stable laser (source), a beam splitter (usually a partially reflecting mirror), two reflecting mirrors at the end of two arms and a detector (Fig. 2.1). In Michelson interferometer a single coherent light beam passes through a beam splitter, which sends half the light down one arms and other half down the orthogonal arm. The two beams have correlated phases. In the two arms beams are passing through an optical cavity and are being reflected by the mirrors at the end of the two arms. On their why back they are recombined to an interference pattern measured by detector. Any difference in the local space time creates a phase difference between the two beams and this effect is measured by observing the changing interference pattern. Therefore, if two arms have same proper length, beams will return in phase, interfering constructively. Otherwise, beams will return to the detector out of phase and they will interfere destructively. All mirrors and beam splitter are freely floating and suspended in order to filter out the mechanical vibration noise. The response of the detector to the incident GW depends upon the relative orientations of the detector and the incoming wave. The existed, existing and planned ground-based detector are listed in Tab. (2.1) with relevant references.

Tab 2.1: The summary of the existed, existing and planned ground-based laser interferometers.

Detector	Country	Arm length	Years active	Generation
GEO600 [8] (Grote, 2010)	Germany	600 m	2001 - present	First
TAMA300 [9] (Ando, 2002)	Japan	300 m	1995 - present	First
iLIGO (Abbott et al., 2009)	USA	4 km	2004 - 2010	First
Virgo (Accadia et al., 2012)	Italy	3 km	2007 - 2011	First
aLIGO [10] (Harry et al., 2010)	USA	4 km	2015 - present	Second
AdV [11] (Acernese et al., 2014a)	Italy	3 km	2016 - present	Second
KAGRA [12] (Somiya, 2012)	Japan	3 km	est. 2019	Second
ET [13] (Punturo et al., 2010)	-	10 km	est. 2025	Third

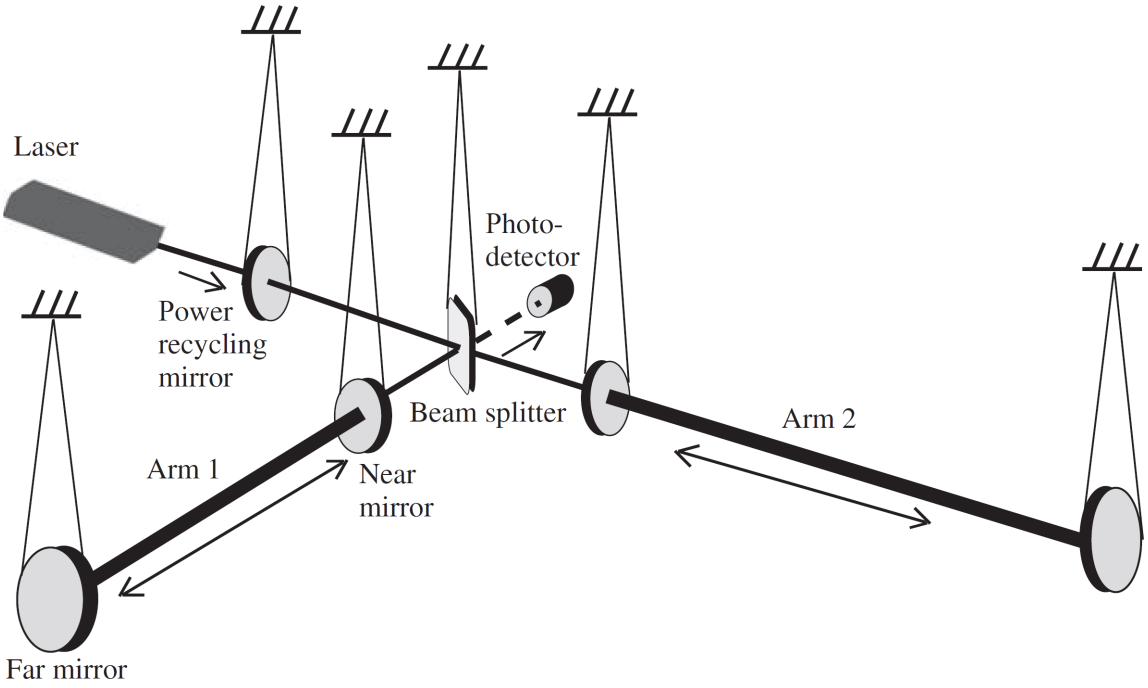

Fig 2.1: Light from the laser first pass through the power recycling mirror and then is split by passing though the beam splitter. From the beam splitter light is sent along two arms, where these arms form cavities between near and far mirrors (the near mirrors are almost fully reflecting). After light leaves the cavities it returns back to the beam splitter to be recombined. If the recombined beam has a destructive interference it goes further to the photodetector; it is dark if GW is not present. Otherwise, if the recombined beam is constructive interference beam it is returned back to the laser. There the beam enters the power recycling mirror and is being reflected back into the interferometer in phase with the new incoming laser beam. All the mirrors and beam splitter are suspended to filter out mechanical vibrations. This scheme is not to scale, since arms are, for example, 4 km long like in LIGO experiment and all mirrors (except far mirrors) with beam splitter and photodetector are contained in a single building. (Adopted from Schutz (2009).)

The other type of the HF band detector is the resonant mass detector. There are different types of this detector (see Fig. 2.2) and they all work on the principle of the absorption of the GW energy that manifest itself as the detector's vibrations. The very first GW detector was resonant bar detector developed by Weber (1959). It consisted of the two cylindrical aluminum bar detectors, each of mass $1.4 \cdot 10^3$ kg, length 1.5 m, resonant frequency 10^4 Hz and Q-factor of 10^5. The resonant mass detectors are non-free mass detectors (Aguiar, 2011). The atoms in the body are connected by the crystal structures

[8] http://www.geo600.org/
[9] http://gwpo.nao.ac.jp/en/
[10] https://www.ligo.caltech.edu/
[11] http://public.virgo-gw.eu/
[12] https://gwcenter.icrr.u-tokyo.ac.jp/en/
[13] http://www.et-gw.eu/

and when the GWs pass the atoms try to follow the geodesic trajectories produced by the space-time distortions. However, electrostatic connections between atoms prevent them for following this trajectories. That is, if the GW is traveling perpendicularly to the bar's axis it produces tidal forces that stretched and contracts the bar's length. And if the frequency of the GW is close to the frequency of the bar, there are better chances that this change in length will be detected. The sensitivity of the aforementioned resonant bar detectors is limited due to technical challenges. It depends on the wave's amplitude, length of the bar and the Q-value of the bar (Schutz, 2009). The practical bars cannot be larger than few meters, otherwise it is difficult to isolate bar from the external disturbances. However, this limits the size of tidal stretching excited by the GW (compare this with four kilometer long arms used in LIGO). Further, the resonant bars require very high Q-values due to several effects. First, it will continue to oscillate long after the GW has passed, as it remembers the effect of the GW (Ju et al., 2000). And second effect is based on the fluctuation-dissipation theorem: the lower the dissipation the lower the fluctuation, that is the thermal noise level. Therefore, a high-Q bar approaches a idealized harmonic oscillator whose motion becomes predictable. If there is a high level of predictability small deviation from the harmonic sinusoidal behavior can be resolved. Therefore, the highest the Q-value the better, but this is limited by the crystal structure of the material. The resonant bars also encounter the difficulty of detecting broadband signals that are very far from their resonant frequencies (although it is possible in principle). Their resonant frequencies usually lay above 600 Hz and since the most of the strong GW sources are at lower frequencies, this represent a big challenge. Next problem, concerns reaching the sensitivity around 10^{-21}. This implies that bars need to be able to detect below quantum limit, since at these small excitation the energy transferred to the bar from the wave is below one quantum of excitation of the resonant mode energy (Schutz, 2009). And the detection below quantum limit has not been met in practice. All modern-day resonant detectors use cryogenic techniques since these reduce the thermal noise and enable the use of high-sensitivity superconducting transducers. In Tab. 2.2 we enlisted some of the existed and still operational bar detectors. All detectors are bar ones, expect MiniGRAIL and Mario Schenberg which are spherical resonant detectors.

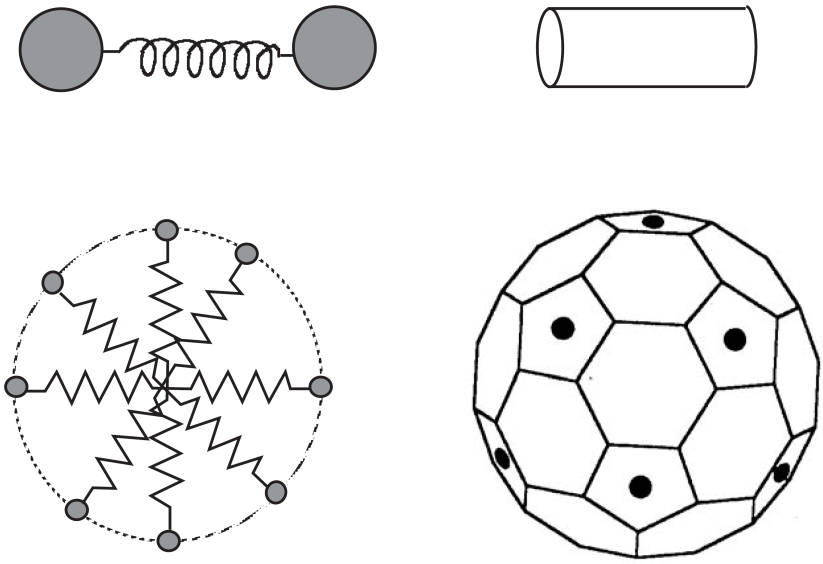

Fig 2.2: Different models of the resonant mass detectors: two masses connected by the spring (up left), a bar (up right), multi-spring mass detector (down left), spherical detector formed with six transducers located with dots (down right). (From Ju et al. (2000).)

Tab 2.2: The summary of the existed and existing resonant bar detectors.

Detector	Country	Years active	Frequency [Hz]	Strain sensitivity
ALLEGRO [14] (Mauceli et al., 1996)	Louisiana	1991-2007	900	$7 \cdot 10^{-19}$
EXPLORER [15] (Astone et al., 1993)	CERN	1990-2010	900	$7 \cdot 10^{-19}$
NIOBE (Heng et al., 1996)	Australia	1993-2001	700	$5 \cdot 10^{-19}$
NAUTILUS [16] (Astone et al., 1997)	Italy	1995-present	900	$6 \cdot 10^{-19}$
AURIGA (Conti et al., 2001)	Italy	1997-present	900	$3 \cdot 10^{-19}$
MiniGRAIL [17] (Waard et al., 2003)	Netherlands	2004-present	3250	$1.5 \cdot 10^{-20}$
Mario Schenberg (Aguiar et al., 2002)	San Paulo	2006-present	3000 - 3400	$4 \cdot 10^{-20}$

[14] http://www.auriga.lnl.infn.it/welcome.html
[15] http://www.roma1.infn.it/rog/rogmain.html
[16] http://www.roma1.infn.it/rog/rogmain.html
[17] http://www.minigrail.nl/

The extensive summary of the GW detectors and sources is shown in Fig. 2.3 versus the characteristic strain (plot is created using interactive tool on the website http://gwplotter.com/).

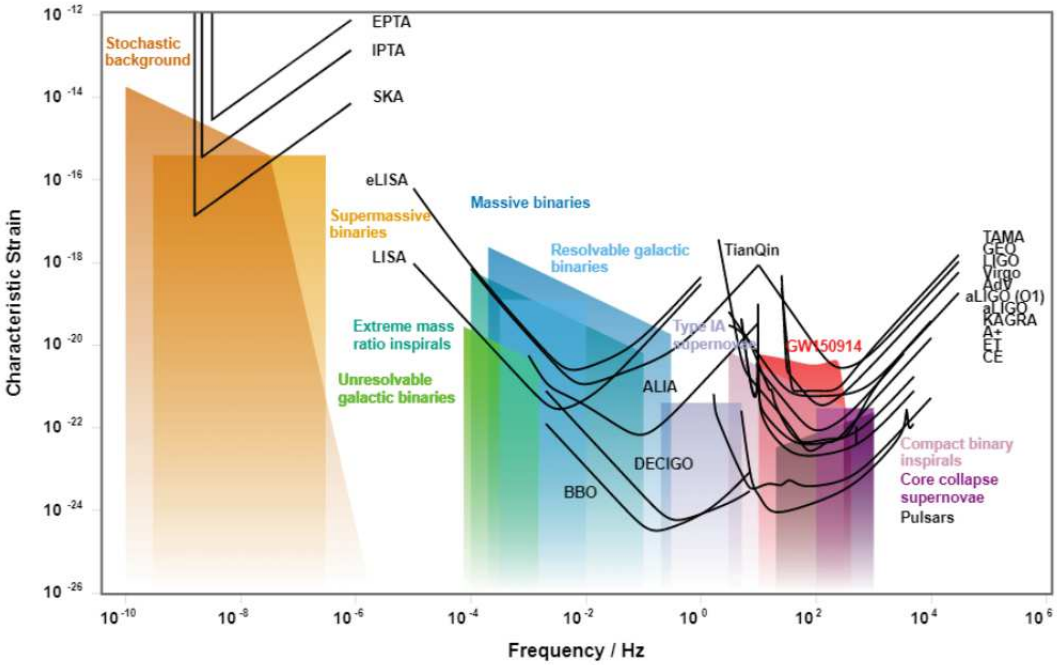

Fig 2.3: GW frequency spectrum versus the characteristic strain for GW detectors and source (From Moore et al. (2015).)

Utilizing of the Earth as a detector of the GWs has a long history and this is a topic of next section.

2.3 Elastic Bodies as Detectors

Around the same time when the first idea about the ground-based detector was established, the idea that GWs could excite the vibrations of elastic bodies, and therefore Earth too, was developed (Pirani, 2009; Weber, 1959). Weber (1959) proposed methods for the interstellar gravitational radiation detection using the fact that the relative motion of mass points are driven by second spatial derivatives of the gravitational fields. He proposed an experiment where the Earth is considered as a block of material representing the GW antenna, a resonant body, for which the normal modes of the Earth are expected as a response to the excitation. He also discussed generation and detection of GW in the laboratory. Forward et al. (1961) were the first to calculate the upper bound of the GW energy passing through the Earth using the strain data from the seismograph at Isabella, California. They computed the strain magnitude induced by the Riemann tensor in a longitudinally vibrating rod (Weber, 1959). Next, Weber (1967) provided the first upper limit on the gravitational-radiation

flux using a mechanical gravimeter in vicinity of normal mode periods. Tuman (1971, 1973) first claimed a GW detection using the Earth's normal modes observed in cryogenic gravity meter records. He interpreted a higher energy content in the power spectra of the even harmonic degrees as the normal modes harmonics excited by gravitational radiation. His finding was criticized due to a lack of more convincing statistical proof (Flinn, 1971). An important study was done by Dyson (1969) who was the first to calculate the response of a flat-Earth model to an incident GW, where effects of sphericity and rotation were added to the flat stationary Earth solution. The calculated response was in the 1-Hz band where seismic wavelengths are small compared to the Earth's radius and large compared to lateral density heterogeneities. Dyson (1969) showed that the GWs, in such a set-up, are absorbed only by irregularities in the shear-modulus, with the strongest absorption at free surface. De Sabbata et al. (1970) proposed detecting GWs by the observation of Earth's free oscillations. Their apparatus consisted of laser interferometer which allows to measure the soil deformations. They proposed that distinction of the seismic (free oscillations) from the gravitational signals could be accomplished by considering a long interval of time, to look at the Fourier components at the presumed frequencies and consider the decay time of the oscillations. Mast et al. (1974) performed the search for gravitational radiation from pulsars using a seismometer on the Earth. Even though no signal was found, they estimated an upper limit on the Earth motion due to such signal from 10^{-11} m near 1 Hz to 10^{-14} m near 125 Hz. Extensive work on the reception of GW by an elastic self-gravitating spherical detector was done by Ashby and Dreitlein (1975). The equations of motion of a detector are presented in the coordinate system of Fermi, where the GW field appears as a classical driving force, and exact analytic solutions are modeled for the homogeneous isotropic elastic sphere as well as self-stress sphere, where stress on the body due to its own gravitational field causes radial variations in density and elastic moduli in equilibrium state. The elastic response was calculated for monochromatic waves in the range 10^{-4} Hz to 1 Hz. Similar work was done by Linet (1984), where he modeled the equations governing the interaction between non-rotating elastic self-gravitating sphere and GWs. Based on Dyson (1969), Jensen (1979) analysed the absorption of GW in the 1-Hz band by the layered crust of a realistic Earth model, developing the interaction between GWs and the elastic continuum. Jensen (1979) showed that discontinuities in the elastic modulus in a layered model significantly enhance the response of Earth to GWs at specific frequencies. The complete response of the radially heterogeneous rotating and self-gravitating Earth in terms of induced toroidal and spheroidal motions was then developed by Ben-Menahem (1983). He showed that in the long-wavelength regime for the induced spheroidal vibration the most significant response corresponds to quadrupole modes. More recently, Coughlin and

Harms (2014a,b,c) revisited Dyson's and Ben-Menahem's formalism of the Earth response to incident GW for the calculation of the upper limit of GW energy density. In the first paper (Coughlin and Harms, 2014a) they used a global network of broadband seismometers and they considered isotropic stochastic GW background integrated over one year in the frequency range 0.05-1 Hz. In the second paper (Coughlin and Harms, 2014b) they used data from a superconducting gravimeter network in the frequency range 0.035-0.15 Hz. In the third paper (Coughlin and Harms, 2014c) they used Apollo-era seismic data integrated over one year in the frequency range 0.1-1 Hz.

Besides Weber and Dyson, who were pioneers in considering the Earth as a detector of GW, many papers that followed studied the interaction of GW and elastic solids in the general relativity context. One of the first studies modeled a concept of the perfectly elastic solid in the high-pressure elasticity theory (condition that occurs in the interiors of neutron stars) for the purpose of scrutinizing the interaction of gravitational radiation with planetary bodies (Carter and Quintana, 1972). Also, for the fist time the strain-curvature equation for an elastic test body interacting with a GW was formulated in general relativistic systems (Glass and Winicourt, 1972). Further, the interaction problem was also solved in the gravito-inertial system of reference (Dozmorov, 1976a,b). In the later paper (Dozmorov, 1976b), it was emphasized the existence of the superposition of two different elastic waves, those with the phase velocity equal to the speed of light and those with the phase velocity equal to the seismic velocity.

The first two papers to consider absorption of GW by astrophysical objects were Zimerman and Hellings (1980) and Walgate (1983). Boughn and Kuhn (1984) were the first one to use realistic Earth and Sun models to calculate their responses to the homogeneous isotropic gravitational radiation considering coupling of GW to a spherically symmetric body. Thus, they put upper limits on the stochastic gravitational background from the observed solar oscillations. Khosroshahi and Sobouti (1997) studied the excitation possibility of the polytropic stars normal modes. They showed that the interaction is achieved through the irrotational component of the displacement vector field. Siegel and Roth (2010, 2011, 2012, 2014) published four articles on the topic of the non-relativistic stars excitation by arbitrary external GW fields starting from the full field equations of general relativity. In Siegel and Roth (2010), it was shown that GWs solely couple to quadrupole spheroidal eigenmodes. In their next paper (Siegel and Roth, 2011), they developed a hydrodynamic model of the excited normal modes for any non-relativistic star and arbitrary external GW fields, allowing them to use realistic current solar and stellar models. They studied two types of radiation, either from a particular astrophysical source or from a stochastic background. In the third and fourth papers (Siegel and Roth, 2012, 2014), based on their earlier theoretical

work, they showed that asteroseismology can place upper bounds on the amplitude of a stochastic background of GWs in the mHz and μHz frequency range. Recently, Lopes and Silk (2014, 2015, 2017) and Lopes (2017) published studies on the stars quadrupole acoustic modes. They showed that GWs with a strain spectral amplitude in the range 10^{-20} - 10^{-17} can lead to the excitation of Sun's low order quadrupole acoustic modes (Lopes and Silk, 2014). They also argued that stars in general form a natural set of detectors over a large spectral frequency range, from 10^{-7} to 10^{-2} Hz, and that their stellar configuration is ideal for GW search. Unlike experimental detectors this kind of network of stars allow to study the progression of GWs throughout space (Lopes and Silk, 2015). Lopes (2017) calculated that impact of GWs on low-order quadrupole modes is not above the current observational threshold of detectability, however he concluded it may be reached with the next generation of near infrared observatories and asteroseismology satellite missions. Among others, the studies about the absorption of GW by stars near black holes and white-dwarfs (McKernan et al., 2014) and red giant stars (Campante et al., 2015) also exist. A historical summary of all papers is presented in the chart in Fig. 2.4.

In next chapter we will further give a basic introduction into the normal mode theory in terms of different Earth models.

Earth	General spherical bodies	Astrophysical bodies
• **Pirani (1956)** • **Weber (1959)** GW antenna		
• **Forward *et al.* (1961)** First upper limit on Riemann tensor power 10^{-75} cm^{-4} (rad/sec) • **Weber (1967)** Upper limit on ρ_p (ω) < $2{\cdot}10^{-25}$ g cm^{-3} rad^{-1} sec • **Dyson (1969)** Flat model, f = 1 Hz, u_h = $2{\cdot}10^{-17}$ m		
• **Sabbata *et. al.* (1970)** • **Tuman (1971)** First claimed detection using free oscillations • **Tuman (1973)** • **Mast *et. al.* (1974)** u = 10^{-11} m (1 Hz) – 10^{-14} m (125 Hz) • **Ashby *et. al.* (1975)** Spherical self-gravitating model, f = 10^{-4} – 1 Hz • **Jensen (1979)** Layered/crustal model, f =0.1–10 Hz, u = $5{\cdot}10^{-20}$ m	+ **Carter & Quintana (1972)** + **Glass & Winicourt (1972)** + **Dozomorov (1976)**	
• **Ben-Menahem (1983)** Radially Heterogeneous Rotating SG, f = <10 mHz, u_h = 10^{-9} m	+ **Linet (1984)**	× **Zimmerman & Hellings (1980)** S_E = 10^{-3} ergs cm^{-3} Hz (10^{-4} – 10^{-3} Hz) × **Walgate (1983)** × **Boughn & Kuhn (1984)** F = 10^9 - 10^7 erg/s/cm^2/Hz (10^{-4} - 10^{-1} Hz)
		× **Khosroshahi & Sobouti (1997)** Excitation of polytropic stars
• **Coughlin & Harms (2014)** Ω_{GW} = 0.039 (0.3 mHz) – 0.12 (4.8 mHz)		× **Siegel & Roth (2010, 2011, 2012, 2014)** Solar g-mode rms surface velocities 10^{-5} -10^{-3} mm/sec; Ω_{GW} < $3.0{\cdot}10^{-3}$ (0.17 mHz) × **Lopes & Silk (2014, 2015, 2017)** Set of stars as GW detector × **McKernan *et. al.* (2014)** Stars as resonant absorbers × **Campante *et. al.* (2015)** × **Lopes (2017)**

Fig 2.4: Historical chart representing the progress of the utilization of Earth as a detector of GWs (•). Additionally, the studies utilizing general elastic sphere (+) and astrophysical bodies (×) are also shown. Abbreviations stands for: $\rho_P(\omega)$ - power spectrum of the gravitational-radiation mass density, f - frequency/frequency range, u - displacement, u_h - horizontal displacement, $\Omega_{\rm GW}$ - upper limit on energy density, S_E - spectral energy density, F - flux density.

Chapter 3

Earth Normal Modes

A short introduction to normal modes of a spherically symmetric, non-rotating, perfectly elastic Earth model and compared with a rotating, anelastic, laterally heterogeneous Earth model is presented below. For a detailed and more complete overview the reader is refeered to Dahlen and Tromp (1998).

3.1 Spherical Non-rotating Elastic Isotropic Earth (SNREI)

A SNREI Earth model stands for the spherically symmetric, non-rotating, perfectly elastic and isotropic model. Isotropic in this case means that the initial stress is isotropic, so there is no deviatoric stress $\tau = 0$, and that the fourth-order elastic tensor $\mathbf{\Gamma}$ is isotropic, defined as

$$\Gamma_{ijkl} = \left(\kappa - \frac{2}{3}\mu\right)\delta_{ij}\delta_{kl} + \mu(\delta_{ik}\delta_{jl} + \delta_{il}\delta_{jk}), \tag{3.1}$$

where κ stands for isentropic incompressibility or bulk modulus and μ for rigidity or shear modulus. Incompressibility and rigidity may be specified as radial variations of the compressional-wave speed $\alpha = \sqrt{(\kappa + \frac{4}{3})/\rho}$ and shear-wave speed $\beta = \sqrt{\mu/\rho}$, where ρ is mass density. The most well known and used SNREI 1D Earth model is the Preliminary Reference Earth Model, henceforth referred as PREM (Dziewonski and Anderson, 1981). The model is polynomial in nature, hence it provides formulas for the seismic velocities, α and β, density and quality factors Q as a function of radius for various regions of the Earth. The original version is transversely isotropic (only 220 km in the outer mantle) as well as anelastic.

The linearized equations and boundary conditions governing the free oscillations of a SNREI Earth model can be obtained for a non-rotating, hydrostatic model ($\tau^0 = 0$). The frequency-domain equation in terms of the displacement $\mathbf{s}$ and the incremental gravitational

potential ϕ is defined as

$$\begin{aligned} -\omega^2\rho\mathbf{s} - \left(\kappa + \frac{1}{3}\mu\right)\nabla(\nabla\cdot\mathbf{s}) - \mu\nabla^2\mathbf{s} - \left(\partial_r\kappa - \frac{2}{3}\partial_r\mu\right)(\nabla\cdot\mathbf{s})\hat{\mathbf{r}} \\ -2\partial_r\mu\left[\partial_r\mathbf{s} + \frac{1}{2}\hat{\mathbf{r}}\times(\nabla\times\mathbf{s})\right] + (4\pi G\rho^2 s_r)\hat{\mathbf{r}} + \rho\nabla\phi \\ +\rho g\left[\nabla s_r - (\nabla\cdot\mathbf{s} + 2r^{-1}s_r)\hat{\mathbf{r}}\right] = 0, \end{aligned} \tag{3.2}$$

where the vector Laplacian is $\nabla^2\mathbf{s} = \nabla(\nabla\cdot\mathbf{s}) - \nabla\times(\nabla\times\mathbf{s})$. The kinematic boundary conditions require the displacement to be continuous everywhere except on the fluid-solid boundaries, where tangential slip is allowed. The dynamical boundaries are

$$\hat{\mathbf{r}}\cdot\mathbf{T} = 0 \ \text{ on } \ \partial_\otimes, \tag{3.3}$$

$$[\hat{\mathbf{r}}\cdot\mathbf{T}]^+_- \ \text{ on } \ \Sigma_{\text{SS}}, \tag{3.4}$$

$$[\hat{\mathbf{r}}\cdot\mathbf{T}]^+_- = 0 \ \text{ on } \ \Sigma_{\text{FS}}, \tag{3.5}$$

where $\partial_\otimes$ stand for boundaries at the exterior surface, Σ_{SS} for the union of internal solid-solid discontinuities and Σ_{FS} for the union of fluid-solid discontinuities. The incremental Cauchy stress $\mathbf{T}$ is given by the isotropic relation

$$\mathbf{T} = \kappa(\nabla\cdot\mathbf{s})\mathbf{I} + 2\mu\mathbf{d} \tag{3.6}$$

where $\mathbf{d} = \frac{1}{2}\left[\nabla\mathbf{s} + (\nabla\mathbf{s})^{\text{T}}\right] - \frac{1}{3}(\nabla\cdot\mathbf{s})\,\mathbf{I}$ is the deviatoric strain. Outside and inside of the boundary are marked as $+$ and $-$ sides of the boundary. The Eulerian perturbation of the gravitational potential in the spherically symmetric Earth takes the form

$$\nabla^2\phi = -4\pi G(\rho\nabla\cdot\mathbf{s} + \partial_r\rho s_r). \tag{3.7}$$

The potential must be continuous everywhere, including the boundaries where we have $[\phi]^+_- = 0$. Additionally, we have

$$[\partial_r\phi + 4\pi G\rho s_r]^+_- = 0, \tag{3.8}$$

on all boundaries. The eigenfrequencies and eigensolutions of a SNREI Earth model, ω, $\mathbf{s}$, ϕ, are found by solving the equation (3.2) for all solid regions in the Earth and equation (3.7) for all space respecting the boundary conditions (3.3) - (3.5) and (3.8). This is accomplished by converting these equations and boundaries into an equivalent system of coupled scalar equations. One approach is a straightforward brute-force approach, where a system of spherical polar coordinates r, θ, ϕ is used. The separable solutions are defined in the form

$$\mathbf{s} = U\mathbf{P}_{lm} + V\mathbf{B}_{lm} + W\mathbf{C}_{lm}, \quad \phi = P\mathcal{Y}_{lm}, \tag{3.9}$$

where the radial eigenfunctions $U(r), V(r), W(r)$ and $P(r)$ are function of radius only. The real spherical harmonics $\mathcal{Y}_{lm}$ of degree $0 \leq l \leq \infty$ and order $-l \leq m \leq l$ are defined as

$$\mathcal{Y}_{lm}(\theta,\phi) = \begin{cases} \sqrt{2}X_{l|m|}(\theta)\cos m\phi & \text{if} \quad -l \leq m < 0 \\ X_{l0}(\theta) & \text{if} \quad m = 0 \\ \sqrt{2}X_{lm}(\theta)\sin m\phi & \text{if} \quad 0 < m \leq l \end{cases} \tag{3.10}$$

with

$$X_{lm} = (-1)^m \sqrt{\frac{2l+1}{4\pi}} \sqrt{\frac{(l-m)!}{(l+m)!}} P_{lm}(\cos\theta), \tag{3.11}$$

and $P_{lm}(\cos\theta)$ as associated Legendre functions defined as

$$P_{lm}(\cos\theta) = (-1)^m \frac{1}{2^l l!}(1-\cos^2\theta)^{m/2} \left(\frac{d}{d\cos\theta}\right)^{l+m} (\cos^2\theta - 1)^l. \tag{3.12}$$

The vector spherical harmonics $\mathbf{P}_{lm}, \mathbf{V}_{lm}, \mathbf{C}_{lm}$ are defined as

$$\begin{aligned} \mathbf{P}_{lm} &= \hat{\mathbf{r}}\mathcal{Y}_{lm}(\theta,\phi), \\ \mathbf{B}_{lm} &= (\sqrt{l(l+1)})^{-1}\nabla_1 \mathcal{Y}_{lm}(\theta,\phi), \\ \mathbf{C}_{lm} &= -(\sqrt{l(l+1)})^{-1}(\hat{\mathbf{r}} \times \nabla_1)\mathcal{Y}_{lm}(\theta,\phi), \end{aligned} \tag{3.13}$$

with the surface gradient $\nabla_1 = \hat{\theta}\partial_\theta + \hat{\phi}(\sin\theta)^{-1}\partial_\phi$ and the surface curl $\hat{\mathbf{r}} \times \nabla_1 = -\hat{\theta}(\sin\theta)^{-1}\partial_\phi + \hat{\phi}\partial_\theta$ on the unit sphere Ω. Substituting expressions (3.9) into (3.2), (3.7), (3.3) - (3.5) and (3.8) gives the system of equations for obtaining the eigensolutions for SNREI Earth model (full expressions in Dahlen and Tromp (1998)).

Every spherically symmetric, non-rotating Earth model consists of two types of free oscillations - spheroidal oscillations, which alter the external shape and internal density of the Earth, defined with the displacement of the form $U\mathbf{P}_{lm} + V\mathbf{B}_{lm}$ and toroidal oscillations, which are purely tangential and zero divergence, of the form $W\mathbf{C}_{lm}$. The spherical symmetry of the model removes the oscillations' dependency upon the azimuthal order m, thenceforth every spheroidal and toroidal eigenfrequency ω is degenerate spanning the $(2l+1)$-dimensional space defined with the real spherical harmonics. It is important to emphasize that for each spherical-harmonic degree l there will be an infinite number of spheroidal and toroidal eigenfrequencies, ${}_n\omega_l^{\mathrm{S}}$ and ${}_n\omega_l^{\mathrm{T}}$, since $n \to \infty$ where n is the overtone number. Further, for each l there are $(2l+1)$ oscillations collectively referred to as a multiplet, denoted as ${}_{\mathrm{n}}\mathrm{S}_{\mathrm{l}}$ for spheroidal modes or ${}_{\mathrm{n}}\mathrm{T}_{\mathrm{l}}$ for toroidal modes and associated with eigenfrequencies ${}_n\omega_l^{\mathrm{S}}$ or ${}_n\omega_l^{\mathrm{T}}$, respectively. Each individual oscillation within the multiplet is called a singlet and is denoted with the azimuthal order m, for spheroidal modes as ${}_{\mathrm{n}}\mathrm{S}_{\mathrm{l}}^{\mathrm{m}}$ and toroidal ${}_{\mathrm{n}}\mathrm{T}_{\mathrm{l}}^{\mathrm{m}}$. Therefore, there are $(2l+1)$ singlets spanning the multiplet. Any departure from the spherically symmetric Earth model removes the eigenfrequency degeneracy and causes each multiplet, ${}_n\omega_l^{\mathrm{S}}$ or ${}_n\omega_l^{\mathrm{T}}$, to split and couple. This is the topic of the next chapter.

3.2 Rotating Anelastic Heterogeneous Earth

In most global seismological applications effects of Earth's rotation, hydrostatic ellipticity and lateral heterogeneity can be regarded as slight perturbations from the equilibrium state. Usually in those applications, the normal-mode perturbation theory is used to calculate the singlet eigenfrequencies and associated eigenfunctions of the perturbed Earth. The basic problem to start with is finding the perturbation to a non-degenerate eigenfrequency of a mode that is well isolated in the seismic spectrum. In the first-order perturbation theory one wants to find the eigenfrequency perturbation $\delta\omega$ without solving simultaneously for the perturbations in the associated eigenfunctions $\delta\mathbf{s}$. Solutions to this classical problem serves as a basis for the degenerate and quasi-degenerate perturbations problem, where we cannot treat modes as perfectly isolated in the normal-mode spectrum. As mentioned before, the real eigenfrequencies of spherically non-rotating symmetric Earth model exist in $(2l+1)$ degenerate spheroidal and toroidal multiplets. This degeneracy is removed in a three-dimensional rotating Earth model and it is perceived as splitting of the multiplet eigenfrequencies and coupling between singlets within the multiplet and also between individual multiplets, if their unperturbed eigenfrequencies are in close proximity to each other for later case. In the splitting and coupling approaches the basis functions are the unperturbed multiplet eigenfunctions of the mode one wishes to investigate, and the perturbed singlet eigenfunctions are of the form $\mathbf{s} = \sum_k q_k \mathbf{s}_k$, where q_k are expansion coefficients to be determined and $\mathbf{s}_k$ are the singlet eigenfunctions on a SNREI Earth model. Theoretically, all eigenfunctions form the basis set, however since it is impossible to incorporate $n \to \infty$ modes into the computation, one needs to truncate the number of studied multiplets, hence the term quasi-degenerate multiplets. The split eigenfrequencies are treated as small perturbation away from positive reference or fiducial frequency ω_0 .

3.2.1 The Splitting of an Isolated Multiplet

In the isolated-multiplet approximation the splitting of and self-coupling between singlets within the target multiplet, due to the rotation, ellipticity and lateral heterogeneity, is governed by a splitting matrix defined as

$$\mathbf{H} = \mathbf{W} + (2\omega_0)^{-1}\left[\mathbf{V}^{\text{ell+cen}} + \mathbf{V}^{\text{lat}} + i\,\mathbf{A} - \omega_0^2(\mathbf{T}^{\text{ell}} + \mathbf{T}^{\text{lat}})\right], \tag{3.14}$$

where $\mathbf{W}$ is rotating matrix, which contains the first-order perturbations of the Earth's rotation without the centrifugal potential and without associated ellipticity perturbations. Further, the combined effects of rotation and hydrostatic ellipticity are represented by matrices $(2\omega_0)^{-1}(\mathbf{V}^{\text{ell+cen}} - \omega_0^2\mathbf{T}^{\text{ell}})$ with $\mathbf{T}^{\text{ell}}$ being the kinetic-energy matrix and $\mathbf{V}^{\text{ell+cen}}$

the elliptical-plus-centrifugal potential energy matrix. Non-hydrostatic lateral heterogeneity perturbations are contained in $(2\omega_0)^{-1}(\mathbf{V}^{\text{lat}} - \omega_0^2\mathbf{T}^{\text{lat}})$ matrices and $\mathbf{A}$ is the matrix of anelastic perturbations. Therefore, the matrices $\mathbf{W}$, $\mathbf{V}^{\text{ell+cen}}$, $\mathbf{V}^{\text{lat}}$, $\mathbf{T}^{\text{ell}}$ and $\mathbf{T}^{\text{lat}}$ contain all deviations from the SNREI Earth model, so they are also called the perturbation matrices. The perturbation splitting matrix $\mathbf{H}$ is fundamentally an operator defining an ordinary eigenvalue problem for the complex eigenfrequency perturbations. In the isolated-multiplet approximation the size of the matrix is $(2l+1)\times(2l+1)$, therefore the coupling between adjacent multiplets is ignored. The elements of this complete $(2l+1)\times(2l+1)$ self-coupling matrix are given by

$$H_{mm'} = \omega_0[ibm\delta_{l-l'} + (a+cm^2)\delta_{mm'}] + \omega_0 \sum_{st}(c_{st} + i\psi_{st}) \int_\Omega \mathcal{Y}_{lm}\mathcal{Y}_{st}\mathcal{Y}_{lm'}d\Omega, \tag{3.15}$$

where aforementioned rotation and elliptical effects are defined with parameter b due to the first-order effect of the Coriolis force, whereas a and c are due to ellipticity and the second-order rotational effects (Dahlen and Sailor, 1979). Further, $\delta_{mm'}$ is the Kronecker delta symbol defined as

$$\delta_{ij} = \begin{cases} 0 \text{ if } i \neq j \\ 1 \text{ if } i = j \end{cases}, \tag{3.16}$$

Values c_{st} are called the splitting function coefficients and are linearly related to the perturbations of the spherical structure due to lateral heterogeneity in terms of bulk modulus κ, shear modulus μ, density ρ and boundaries d perturbations. They are defined as

$$c_{st} = \frac{1}{2}\omega_0^{-2}\Big\{ \int_0^a [\delta\kappa_{st}V_\kappa + \delta\mu_{st}V_\mu + \delta\rho_{st}(V_\rho - \omega_0^2 T_\rho)]r^2dr + \sum_d d^2\delta d_{st}[V_d - \omega_0^2 T_d]_-^+\Big\}. \tag{3.17}$$

where s is the degree of the heterogeneity. For the explicit expressions of kernels V_κ, V_μ, $V_\rho - \omega_0^2 T_\rho$, $V_d - \omega_0^2 T_d$ reader is referred to the Appendix D.4.2 in Dahlen and Tromp (1998). Additionally, the real integrals satisfy the selection rules

$$\int_\Omega \mathcal{Y}_{lm}\mathcal{Y}_{st}\mathcal{Y}_{lm'}d\Omega = 0 \quad \text{unless} \quad \left\{ \begin{array}{l} s \text{ is even} \\ 0 \leq s \leq 2l \\ t = m - m' \end{array} \right\}, \tag{3.18}$$

consequently defining the kind of structure a specific isolated multiplet is sensitive to (Woodhouse, 1980; Ritzwoller et al., 1986; Dahlen and Tromp, 1998). For example, the first rule requires that the splitting of an isolated multiplets depends only upon the even-degree structure of the Earth. Coefficients ψ_{st} belong to the the anelastic perturbation matrix $\mathbf{A}$ and are given by

$$\psi_{st} = \frac{1}{2}\omega_0^{-2}\int_0^a (\kappa_0 q_{\kappa,st}V_\kappa + \mu_0 q_{\mu,st}V_\mu)r^2dr \tag{3.19}$$

where $\delta\kappa \to \delta\kappa + i\kappa_0 q_\kappa$ and $\delta\mu \to \delta\mu + i\kappa_0 q_\mu$ with expansion coefficients defined as

$$q_\kappa = \sum_{s=1}^{s_{max}} \sum_{t=-s}^{s} q_{\kappa,st}\mathcal{Y}_{st}, \qquad q_\mu = \sum_{s=1}^{s_{max}} \sum_{t=-s}^{s} q_{\mu,st}\mathcal{Y}_{st}. \tag{3.20}$$

To calculate the first-order eigenfrequency perturbations one needs to diagonalize the splitting matrix $\mathbf{H}$ by similarity transformations, under conditions that $\mathbf{H}$ is non-defective,

$$\mathbf{Z}^{-1}\mathbf{Z} = \mathbf{I}, \qquad \mathbf{Z}^{-1}\mathbf{H}\mathbf{Z} = \Delta. \tag{3.21}$$

Matrix $\Delta = \mathrm{diag}\,[\cdots \delta\nu_j \cdots]$, contains complex eigenfrequency perturbations. The columns of the transformation matrix $\mathbf{Z}$ and the rows of its inverse $\mathbf{Z}^{-1}$ contain singlet eigenvectors. Eigenvectors are further used to modify receiver r and source s vectors. For example, in case of the acceleration $a(t)$ of an isolated multiplet

$$a(t) = A_0(t)\mathrm{e}^{i\omega_0 t - \gamma_0 t}, \tag{3.22}$$

that consists of the sum of $2l+1$ varying complex exponential functions where the modulation function is

$$A_0(t) = \tilde{\mathsf{r}}^{\mathrm{T}}\mathrm{e}^{i\Delta t}\tilde{\mathsf{s}} = \sum_j A_j \mathrm{e}^{i\delta\omega_j + \delta\gamma_j t} \tag{3.23}$$

with $A_j = \tilde{r}_j \tilde{s}_j$. The renormalized receiver $\tilde{\mathsf{r}}$ and source $\tilde{\mathsf{s}}$ vectors are related to their SNREI counterparts by

$$\tilde{\mathsf{r}} = \mathbf{Z}^{\mathbf{T}}\left(\mathbf{I} - \frac{1}{2}\mathbf{T}^{\mathrm{ell}} - \frac{1}{2}\mathbf{T}^{\mathrm{lat}} - \frac{1}{2}\omega_0^{-1}\mathbf{W}\right)\mathsf{r}, \tag{3.24}$$

$$\tilde{\mathsf{s}} = \mathbf{Z}^{-1}\left(\mathbf{I} - \frac{1}{2}\mathbf{T}^{\mathrm{ell}} - \frac{1}{2}\mathbf{T}^{\mathrm{lat}} - \frac{1}{2}\omega_0^{-1}\mathbf{W}\right)\mathsf{s}, \tag{3.25}$$

where tilde symbol is characterizing the receiver and source vectors where the effects of rotation and lateral heterogeneities are considered. In the absence of laterally heterogeneous anelasticity matrix $\mathbf{A} = 0$, the diagonalizing transformation matrix becomes unitary $\mathbf{Z}^{-1} = \mathbf{Z}^{\mathrm{H}}$.

3.2.2 The Mode Coupling

The isolated-multiplet approximation is not suitable for the overlapping modes or modes whose degenerate eigenfrequencies are in close vicinity to each other. To account for the possibility of coupling between multiplets, one needs to treat target multiplets within a single quasi-degenerate super-multiplet. Therefore, the splitting of and coupling between several multiplets is governed by the super-version of (3.14)

$$\mathbf{H} = \mathbf{N} - \nu_0\mathbf{I} + \mathbf{W} + (2\omega_0)^{-1}\left[\mathbf{V}^{\mathrm{ell+cen}} + \mathbf{V}^{\mathrm{lat}} + i\mathbf{A} - \omega_0^2(\mathbf{T}^{\mathrm{ell}} + \mathbf{T}^{\mathrm{lat}})\right], \tag{3.26}$$

where the additional matrix $\mathbf{N} = \text{diag}[\cdots \nu_k \cdots]$ is the diagonal matrix of complex degenerate eigenfrequencies, $\nu_0 = \omega_0 + i\gamma_0$ is a complex fiducial or reference frequency and is typically chosen to be one of the degenerate frequencies ν_k. The dimension of this matrix is determined by the number of multiplets we are considering, hence one has $\sum_k(2l_k+1) \times \sum_k(2l_k+1)$ dimension where l_k denotes the degree of kth multiplet and where index k denotes the quadruplet $\{n, l, m, \text{S or T}\}$. For better visual clarity let's say there are five multiplets in the super-multiplet, the matrix (3.26) can be written as

$$\begin{pmatrix} \mathbf{H}_{1,1} & \mathbf{H}_{1,2} & \mathbf{H}_{1,3} & \mathbf{H}_{1,4} & \mathbf{H}_{1,5} \\ \mathbf{H}_{2,1} & \mathbf{H}_{2,2} & \mathbf{H}_{2,3} & \mathbf{H}_{2,4} & \mathbf{H}_{2,5} \\ \mathbf{H}_{3,1} & \mathbf{H}_{3,2} & \mathbf{H}_{3,3} & \mathbf{H}_{3,4} & \mathbf{H}_{3,5} \\ \mathbf{H}_{4,1} & \mathbf{H}_{4,2} & \mathbf{H}_{4,3} & \mathbf{H}_{4,4} & \mathbf{H}_{4,5} \\ \mathbf{H}_{5,1} & \mathbf{H}_{5,2} & \mathbf{H}_{5,3} & \mathbf{H}_{5,4} & \mathbf{H}_{5,5} \end{pmatrix}. \tag{3.27}$$

where matrices with the same subscripts, $\mathbf{H}_{k,k}$, are the self-coupling matrices and matrices with combination of different subscripts, $\mathbf{H}_{k,k'}$, represent the coupling matrices between two different multiplets. Therefore, if k denotes a basis multiplet of spherical-harmonic degree l, and k' denotes a basis multiplet of spherical-harmonic degree l' then the matrix $\mathbf{H}_{k,k'}$ is a $(2l+1) \times (2l'+1)$ submatrix. The acceleration due to this super-splitting matrix is the same as (3.22) only the dimensions of each matrix change.

The coupling between modes is particularly strong if their frequencies are close and if their radial and geographical displacement fields are similar. There are a few selection rules defining how the two modes are coupled and these are (Laske and Widmer-Schindrig) :

- Coriolis force introduces coupling between spheroidal and toroidal (S-T) modes that differ by a single angular degree $|l - l'| = 1$;
- Earth's ellipticity causes the same coupling as above for $|l - l'| = 1$ and also same type coupling (S-S or T-T) for $|l - l'| = 0$ and $|l - l'| = 2$;
- the rotation causes same type coupling for $|l - l'| = 0$;
- lateral heterogeneity of degree s causes S-T coupling if $|l - l'| + 1 \leq s \leq l + l' + 1$ and $l + l' + s$ is odd;
- lateral heterogeneity of degree s causes same type coupling if $m - m' + t = 0$, $l + l' + s$ is even and $|l - l'| \leq s \leq l + l'$.

Calculation of the splitting matrix for multiplets in narrow frequency band governed by these specific selection rules is called the group-coupling approximation. This is different

from the full-coupling approximation where a large groups of multiplets in a broad frequency band are considered.

3.2.3 The Splitting Function Coefficients

As stated earlier, the degenerate frequencies of a spherically symmetric non-rotating Earth models are split by rotation, ellipticity and lateral heterogeneities. In most studies, rotation and ellipticity are known and lateral heterogeneities, which are represented by velocity and density perturbations, are the quantities to be estimated. Since lateral heterogeneities are described by the splitting function coefficients, c_{st}, to measure them we actually need to measure the splitting function coefficients. Estimation of the splitting function coefficients is a highly non-linear inverse problem which is commonly performed iteratively from a starting model in the spectral domain (Ritzwoller et al., 1986, 1988; Giardini et al., 1987, 1988; Li et al., 1991). This procedure has been frequently used in the past several years specially for building a catalog of c_{st} coefficients (Resovsky and Ritzwoller, 1998; Deuss et al., 2011, 2013; Koelemeijer et al., 2013). Besides, Ritzwoller et al. (1986) and Widmer et al. (1992) proposed retrieving information about splitting function coefficients directly from the estimated normal mode eigenfrequencies. This approach is based on a first-order perturbation theory for isolated multiplets and the assumption that the lateral heterogeneity is predominantly zonal which is also valid for some isolated multiplets (Woodhouse and Dahlen, 1978; Woodhouse, 1980; Dahlen and Tromp, 1998). Moreover, for multiplets below 1 mHz where the splitting is dominated by the effect of rotation it is known that the dominant heterogeneity sensed is axisymmetric (Widmer et al., 1992). All listed assumptions are valid only for the low-frequency modes.

For an isolated multiplet we can write the splitting matrix (3.15) in more simple form as

$$H_{mm'} = \bar{\omega}_k(a + mb + m^2c)\delta_{mm'} + \sum_{\substack{s=0 \\ s \text{ even}}}^{2l} \sum_{t=-s}^{s} \gamma_{st}^{mm'} c_{st} \tag{3.28}$$

Obtaining the splitting matrix, calculating its eigenvalues and adding them to the multiplet degenerate eigenfrequency $\bar{\omega}_k$, one can calculate the singlet split eigenfrequencies, ω_m, within the multiplet. In the special case where (3.28) is diagonal, resulting in a singlet being sensitive only to rotation, ellipticity and even degree axisymmetric aspherical structure ($t = 0$), equation (3.28) simplifies to

$$H_{mm} = \bar{\omega}_k(a + mb + m^2c) + \sum_{\substack{s=0 \\ s \text{ even}}}^{2l} \gamma_{s0}^{mm} c_{s0}, \tag{3.29}$$

which leads us to the expression of the split eigenfrequency

$$\omega_m = \bar{\omega}_k(1 + a + mb + m^2 c) + \sum_{\substack{s=0 \\ s \text{ even}}}^{2l} \gamma_{s0}^{mm} c_{s0}. \tag{3.30}$$

Relation (3.30) shows that if one measures the split eigenfrequencies ω_m and further subtracts the first term on the right-hand side, calculated for a given Earth model, from the left-hand side one can estimate axisymmetric splitting function coefficients sensitive to even degree structures.

3.3 Green tensor

The Earth's response to any source which excites free oscillations or traveling body and surface waves, can be expressed in terms of the second-order Green tensor $\mathbf{G}(\mathbf{r}, \mathbf{r}'; t)$. It represents a displacement response at location $\mathbf{r}$ and time t to a force acting at location $\mathbf{r}'$ at time 0. Therefore, the displacement $\mathbf{s}(\mathbf{r}, t)$ produced by the equivalent body force density $\mathbf{f}(\mathbf{r}, t)$ acting per unit volume and the equivalent surface force density $\mathbf{t}(\mathbf{r}, t)$ can be written as a convolution of the impulse response Green function $\mathbf{G}(\mathbf{r}, \mathbf{r}'; t)$ with the entire past history of the equivalent forces $\mathbf{f}(\mathbf{r}, t)$ and $\mathbf{t}(\mathbf{r}, t)$ as

$$\mathbf{s}(\mathbf{r}, t) = \int_{-\infty}^{t} \int_V \mathbf{G}(\mathbf{r}, \mathbf{r}'; t - t') \cdot \mathbf{f}(\mathbf{r}', t') dV' dt' + \int_{-\infty}^{t} \int_S \mathbf{G}(\mathbf{r}, \mathbf{r}'; t - t') \cdot \mathbf{t}(\mathbf{r}', t') d\Sigma' dt', \tag{3.31}$$

where the volume integral is carried throughout the Earth's volume and the surface integral over Earth's surface satisfying a dynamical free-surface boundary condition given by (3.3) for all surface. Definition of the Green tensor naturally changes with the Earth model used. In Tab (3.1) and (3.2) one can find four expressions of the Green tensor and the displacement eigenfucntions with and without rotation and anelasticity, respectively.

Tab 3.1: Seismic Green tensor with and without rotation and anelasticity. Each of the sums is over all of the seismic normal modes with associated real or complex eigenfrequencies ω_k or $\nu_k = \omega + i\gamma_k$.

Earth model	Green Tensor
Non-rotating elastic	$\mathbf{G}(\mathbf{r}, \mathbf{r}'; t) = \Re \sum_k \omega_k^{-1} \mathbf{s}_k(\mathbf{r}) \mathbf{s}_k(\mathbf{r}') \mathrm{e}^{i\omega_k t}$
Rotating elastic	$\mathbf{G}(\mathbf{r}, \mathbf{r}'; t) = \Re \sum_k (i\omega_k)^{-1} \mathbf{s}_k(\mathbf{r}) \mathbf{s}_k^*(\mathbf{r}') \mathbf{e}^{i\nu_k t}$
Non-rotating anelastic	$\mathbf{G}(\mathbf{r}, \mathbf{r}'; t) = \Re \sum_k (i\nu_k)^{-1} \mathbf{s}_k(\mathbf{r}) \mathbf{s}_k(\mathbf{r}') \mathrm{e}^{i\nu_k t}$
Rotating anelastic	$\mathbf{G}(\mathbf{r}, \mathbf{r}'; t) = \Re \sum_k (i\nu_k)^{-1} \mathbf{s}_k(\mathbf{r}) \bar{\mathbf{s}}_k(\mathbf{r}') \mathrm{e}^{i\nu_k t}$

Tab 3.2: Displacement eigenfunction of a spherically symmetric Earth model in the presence or absence of rotation and anelasticity. The scalars U,V,W and the spherical harmonics $\mathcal{Y}_{lm}$ are real, whereas $\mathcal{U}, \mathcal{V}, \mathcal{W}$ and Y_{lm} are complex. The eigenfunctions of a non-rotating spherical Earth model are exact, whereas those of a rotating spherical Earth model are only correct to zeroth order in the angular rate of rotation, $\Omega = ||\mathbf{\Omega}||$.

Spherical Earth model	Exact or Zeroth-Order Displacement Eigenfunction
Non-rotating elastic	$\mathbf{s} = U\hat{\mathbf{r}}\mathcal{Y}_{lm} + k^{-1}V\nabla_1\mathcal{Y}_{lm} - k^{-1}W(\hat{\mathbf{r}} \times \nabla_1\mathcal{Y}_{lm})$
Rotating elastic	$\mathbf{s} = U\hat{\mathbf{r}}Y_{lm} + k^{-1}V\nabla_1 Y_{lm} - k^{-1}W(\hat{\mathbf{r}} \times \nabla_1 Y_{lm})$
Non-rotating anelastic	$\mathbf{s} = \mathcal{U}\hat{\mathbf{r}}\mathcal{Y}_{lm} + k^{-1}\mathcal{V}\nabla_1\mathcal{Y}_{lm} - k^{-1}\mathcal{W}(\hat{\mathbf{r}} \times \nabla_1\mathcal{Y}_{lm})$
Rotating anelastic	$\mathbf{s} = \mathcal{U}\hat{\mathbf{r}}Y_{lm} + k^{-1}\mathcal{V}\nabla_1 Y_{lm} - k^{-1}\mathcal{W}(\hat{\mathbf{r}} \times \nabla_1 Y_{lm})$

In the definition of displacement eigenfunctions in Tab. (3.2) the complex spherical harmonics are defined as

$$Y_{lm}(\theta, \phi) = X_{lm}(\theta)\mathrm{e}^{im\phi}. \tag{3.32}$$

In the next chapter we further develop the interaction between the GWs and the Earth in terms of the normal modes.

Chapter 4

Normal Modes Excited By Gravitational Waves

Elastic bodies such as the Earth can serve as the GWs detectors and we have shown that this idea is not a new one (see Subsection 2.3). In this chapter we want to focus on Dyson (1969) and Ben-Menahem (1983) formalism to upgrade the analytical model of the interaction between the GWs and the radially heterogeneous non-rotating Earth model (further referred to 1D Earth model) and to derive a new analytical model for radially heterogeneous elliptical rotating model where lateral heterogeneities are also included (further referred to 3D Earth model). This chapter is divided in three sections. In the first section we define the mathematical background for the GWs. In the second one we revisit Ben-Menahem's spheroidal displacement. This solution is based on the metric perturbation defined in the terrestrial reference system and for the monochromatic GW source. In the last section, we derive a new analytical model, where the metric perturbation is defined for a binary star system in the celestial reference system.

4.1 Force Term in Flat Space-Time Approximation

Far away from any significant masses, space-time possesses no curvature. It is the flat space-time approximation, where we can idealize the waves as plane-fronted. The appropriate formalism for describing this approximation is a linearized theory of gravity, a consequence of considering the Newtonian limit (moving from a curved space-time to a flat one). In the Newtonian limit particles are moving slowly with respect to the speed of light, the gravitational field is weak and so it can be considered as a perturbation of flat space and the field is static. The weakness of the gravitational field is expressed as decomposition of the metric into the Minkowski metric plus a small perturbation

$$g_{\mu\nu} = \eta_{\mu\nu} + h_{\mu\nu}, \quad |h_{\mu\nu}| \ll 1, \tag{4.1}$$

where the metric tensor $g_{\mu\nu}$ is a function of the distribution of mass and energy in space and time, $\eta_{\mu\nu}$ takes its canonical form $\eta_{\mu\nu} = \mathrm{diag}(-1, 1, 1, 1)$ and $h_{\mu\nu}$ is the metric perturbation. The assumption $|h_{\mu\nu}| \ll 1$ allows us to ignore anything that is higher order than first order in the metric perturbation. In this assumption the metric perturbation can be chosen so as to satisfy a transverse-traceless gauge condition where $h_{\mu 0} = 0$ is purely spatial, $h_{mm} = 0$ trace free and $h_{mn;n} = 0$ divergence free. In this gauge all components $h_{\mu\nu}$ obey the wave equation

$$\left(-\frac{1}{c^2}\frac{\partial^2}{\partial t^2} + \nabla^2\right) h_{\mu\nu} = 0 \tag{4.2}$$

where the solutions are plane waves, which phase fronts are huge compared to the wavelength and the radius of the curvature of the space-time through which they propagate. Because the metric (4.1) is the Minkowski metric plus a small spatial perturbation, we can do all important calculation for the GWs in the vector notation in three-dimensional Euclidean space. The wave coming from a distant source can be treated as a plane wave propagating along vector $\hat{\boldsymbol{k}}$ which points from the source to the observer. We choose our coordinate axes so that this unit vector has components

$$\hat{\boldsymbol{k}} = (0, 0, 1), \tag{4.3}$$

thus defining a vector propagating in $\hat{\boldsymbol{e}}_z$ direction. Because of a transverse-traceless gauge there are only two independent non-zero components of the metric perturbation conventionally named h_+ and $h_\times$, therefore we can write the metric perturbation tensor as

$$\boldsymbol{h} = \begin{pmatrix} h_+ & h_\times & 0 \\ h_\times & h_+ & 0 \\ 0 & 0 & 0 \end{pmatrix}, \tag{4.4}$$

where components h_+ and $h_\times$ are functions of $(t - \hat{\boldsymbol{k}} \cdot \frac{r}{c})$. Expression (4.4) can also be written as

$$\boldsymbol{h} = h_+ \boldsymbol{e}_+ + h_\times \boldsymbol{e}_\times, \tag{4.5}$$

using polarization tensors defined as

$$\boldsymbol{e}_+ = \hat{\boldsymbol{l}}\hat{\boldsymbol{l}}^{\mathrm{T}} - \hat{\boldsymbol{m}}\hat{\boldsymbol{m}}^{\mathrm{T}} = \begin{pmatrix} 1 & 0 & 0 \\ 0 & -1 & 0 \\ 0 & 0 & 0 \end{pmatrix}, \qquad \boldsymbol{e}_\times = \hat{\boldsymbol{l}}\hat{\boldsymbol{m}}^{\mathrm{T}} + \hat{\boldsymbol{m}}\hat{\boldsymbol{l}}^{\mathrm{T}} = \begin{pmatrix} 0 & 1 & 0 \\ 1 & 0 & 0 \\ 0 & 0 & 0 \end{pmatrix}, \tag{4.6}$$

with

$$\hat{\boldsymbol{l}} = (1, 0, 0), \qquad \hat{\boldsymbol{m}} = (0, 1, 0). \tag{4.7}$$

We see that for the construction of $\boldsymbol{e}_+$ and $\boldsymbol{e}_\times$ tensors we first need to define vector $\hat{\boldsymbol{l}}$ in the plane perpendicular to $\hat{\boldsymbol{k}}$ and then vector $\hat{\boldsymbol{m}}$ is uniquely determined as $\hat{\boldsymbol{m}} = \hat{\boldsymbol{k}} \times \hat{\boldsymbol{l}}$. The metric perturbation defined as (4.5) is the linearly polarized metric perturbation (compared to, for example, a right-hand or a left-hand polarizations).

Dyson (1969) discussed that in the linearized gravitational theory to account for the interaction between GW and the elastic solid one needs to modify the Lagrangian of the elastic solid by replacing the strain tensor with the sum of the strain tensor and the metric perturbation (4.4). This modification alters the linear elastic equations by simply adding a force term (Dyson, 1969; Ben-Menahem, 1983)

$$\boldsymbol{f}(\boldsymbol{r}, t) = -\frac{\partial \mu}{\partial r} \hat{\boldsymbol{e}}_r \cdot \boldsymbol{h}(\boldsymbol{r}). \tag{4.8}$$

to the equations, where μ is the shear modulus distribution in the Earth and $\hat{\boldsymbol{e}}_r$ is the radial unit vector. This result is important, since it tells us that within the interior of an isotropic elastic medium a GW interacts only with the discontinuities in the shear modulus profile μ. When considering an Earth profile there are two major discontinuities in the shear-modulus profile: at the free-surface and at the core-mantle boundary. This implies that for the GW described by (4.8) the Earth is constantly exposed to the forcing motion. To define the response of the Earth to the GW we need to consider the force term (4.8) as a body force in the relevant linear elastic equations of motion. This approach is taken in next two sections for deriving a response of 1D (see Section 4.2) and 3D (see Section 4.3) Earth models to GWs.

4.2 Terrestrial Reference System and Elastic, Non-rotating Earth Model

Ben-Menahem (1983) obtained an analytical solution of the interaction between the GWs and the Earth in terms of toroidal and spheroidal normal modes. For his calculation he used a radially heterogeneous non-rotating elastic Earth model. He assumed that the GWs are plane waves defined by their scalar values, polarization tensors and the propagation vectors. The usefulness of his approach is defining the induced displacement as a double integral of the convolution between the Green tensor and the force term as defined in Subsection 3.3. In this section we revisit his analytical model using the same assumption and also including some new ones. One of the main alteration involves using a standard notation as used in the global seismology and defined in Chapter 3. The section is organized as follows: firstly, we define the metric perturbation, and its components, which constitute the force term (4.8); secondly, we define the Green tensor for a specific Earth model, because the force term together with the Green tensor define the displacement relation (3.31); thirdly, we

derive the induced spheroidal response for linearly polarized metric perturbation; fourthly, we calculate the induced spheroidal response for a right-hand polarized metric perturbation, present the comparison with Ben-Menahem's solution and recalculate radial and horizontal displacement values.

Results from this Section are published in Majstorović et al. (2019b) (link).

4.2.1 Metric Perturbation Defined as Plane-wave

The metric perturbation as a plane-wave source is expressed as

$$\boldsymbol{h} = \Re\{h_0 \boldsymbol{\epsilon} \mathrm{e}^{i(\omega_g t - \hat{\boldsymbol{k}}_g \cdot \boldsymbol{r})}\}, \tag{4.9}$$

where $\Re$ designates the real part, h_0 defines the intensity of the wave source, $\boldsymbol{\epsilon}$ is a polarization tensor, $\hat{\boldsymbol{k}}_g = \frac{\omega_g}{c}\hat{\boldsymbol{e}}_k$ is the wavenumber with ω_g as frequency, c the velocity of light and $\hat{\boldsymbol{e}}_k$ a unit vector normal to the wave front of the GW. The polarization tensor is defined by the configuration of the incoming GW propagating along a vector $\hat{\boldsymbol{k}}_g$ located in the Earth reference system. Vectors $\hat{\boldsymbol{k}}_g$, $\hat{\boldsymbol{l}}$, $\hat{\boldsymbol{m}}$ are determined in the Earth's Cartesian coordinate system $\mathcal{O}$, with the $\hat{\boldsymbol{e}}_z$-axis pointing toward North, the $\hat{\boldsymbol{e}}_x$ and $\hat{\boldsymbol{e}}_y$-axes perpendicular to $\hat{\boldsymbol{e}}_z$, and whose origin coincidences with the center of mass of the Earth. Unit vector $\hat{\boldsymbol{e}}_x$ points to the Greenwich meridian. The plane of polarization in the $\mathcal{O}$-system is specified by three angles $\{e, \lambda, \nu\}$, where e defines the rotation in $\hat{\mathbf{e}}_y\hat{\mathbf{e}}_z$-plane, λ in $\hat{\mathbf{e}}_x\hat{\mathbf{e}}_y$-plane and ν is the rotation angle about the unit vector $\hat{\mathbf{e}}_k$ (Fig. 4.1).

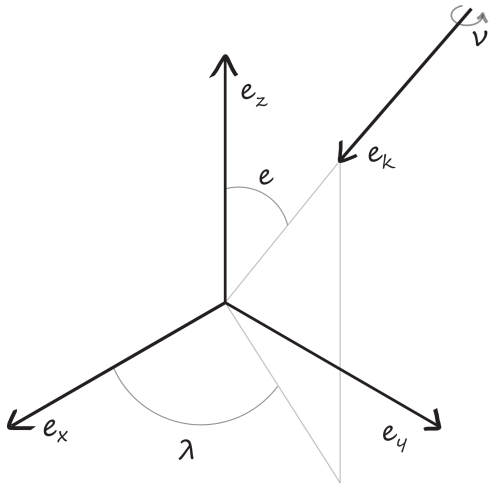

Fig 4.1: Cartesian coordinate system $\mathcal{O}$, where its origin coincides with the center of mass of the Earth and $\hat{\mathbf{e}}_z$-axis points to the North, $\hat{\mathbf{e}}_x$-axis toward the Greenwich Meridian and $\hat{\mathbf{e}}_y$-axis is perpendicular to the $\hat{\mathbf{e}}_z\hat{\mathbf{e}}_x$-plane.

Thus in the system $\mathcal{O}$ we have

$$\begin{aligned}\hat{\boldsymbol{e}}_e &= (\cos e\cos\lambda, \cos e\sin\lambda, -\sin e),\\ \hat{\boldsymbol{e}}_\lambda &= (-\sin\lambda, \cos\lambda, 0),\\ \hat{\boldsymbol{e}}_k &= (\sin e\cos\lambda, \sin e\sin\lambda, \cos e).\end{aligned} \tag{4.10}$$

Further, rotation about the GW-propagation axis gives us the unit vectors

$$\begin{aligned}\hat{\boldsymbol{l}} &= \cos\nu(-\hat{\boldsymbol{e}}_e) + \sin\nu(-\hat{\boldsymbol{e}}_\lambda),\\ \hat{\boldsymbol{m}} &= \sin\nu(\hat{\boldsymbol{e}}_e) + \cos\nu(-\hat{\boldsymbol{e}}_\lambda).\end{aligned} \tag{4.11}$$

Considering the definition of tensors tensors $\boldsymbol{e}_+$ and $\boldsymbol{e}_\times$ from equation (4.6) and using the linearly polarized configuration tensor $\boldsymbol{\epsilon}$ is defined as

$$\boldsymbol{\epsilon} = \hat{\boldsymbol{l}}\hat{\boldsymbol{l}}^{\mathrm{T}} - \hat{\boldsymbol{m}}\hat{\boldsymbol{m}}^{\mathrm{T}} + \hat{\boldsymbol{l}}\hat{\boldsymbol{m}}^{\mathrm{T}} + \hat{\boldsymbol{m}}\hat{\boldsymbol{l}}^{\mathrm{T}}. \tag{4.12}$$

whence, in terms of angles $\{e, \lambda, \nu\}$, we have (with the shorthand $\sin = s$ and $\cos = c$)

$$\boldsymbol{\epsilon} = \begin{bmatrix} b_1(c^2(e)c^2(\lambda) - s^2(\lambda)) - b_2c(e)s(2\lambda) & \frac{1}{2}b_1s(2\lambda)(c^2(e)+1) + b_2c(e)c(2\lambda) & -\frac{1}{2}b_1s(2e)c(\lambda) + b_2s(e)s(\lambda) \\ \frac{1}{2}b_1s(2\lambda)(c^2(e)+1) + b_2c(e)c(2\lambda) & b_1(c^2(e)s^2(\lambda) - c^2(\lambda)) + b_2c(e)s(2\lambda) & -\frac{1}{2}b_1s(2e)s(\lambda) - b_2s(e)c(\lambda) \\ -\frac{1}{2}b_1s(2e)c(\lambda) + b_2s(e)s(\lambda) & -\frac{1}{2}b_1s(2e)s(\lambda) - b_2s(e)c(\lambda) & b_1s^2(e) \end{bmatrix}, \tag{4.13}$$

with

$$\begin{aligned}b_1 &= \cos 2\nu - \sin 2\nu,\\ b_2 &= \cos 2\nu + \sin 2\nu.\end{aligned} \tag{4.14}$$

The metric perturbation defined with (4.9) is further used to define force term (4.8).

4.2.2 Green tensor

Next step is to chose appropriate definition of the Green tensor for the model we want to calculate the response. Therefore, taking into account that the elastic wave speed is much smaller than the speed of light, we consider that the whole Earth is simultaneously excited, therefore the effect of rotation is ignored (Mulargia and Kamenshchik, 2016). For this purpose we use a Green tensor for a non-rotating, anelastic Earth defined in Tab. 3.1

$$\mathbf{G}(\mathbf{r}, \mathbf{r}'; t) = \Re\sum_k (i\nu_k)^{-1}\mathbf{s}_k(\mathbf{r})\mathbf{s}_k(\mathbf{r}')\mathrm{e}^{i\nu_k t}, \tag{4.15}$$

with associated definition of eigenfunction from Tab. 3.2

$$\mathbf{s}_k(\mathbf{r}) = \mathcal{U}_k(r)\hat{\mathbf{e}}_r\mathcal{Y}_{lm}(\theta,\phi) + \kappa^{-1}\mathcal{V}_k(r)\nabla_1\mathcal{Y}_{lm}(\theta,\phi) - \kappa^{-1}\mathcal{W}_k(r)(\hat{\mathbf{e}}_r\times\nabla_1\mathcal{Y}_{lm}(\theta,\phi)), \tag{4.16}$$

where $\mathcal{Y}_{lm}(\theta,\phi)$ are real spherical harmonics defined as (3.10). Radial scalar functions $\mathcal{U}_k(r), \mathcal{V}_k(r), \mathcal{W}_k(r)$ are complex, however for practical reasons in the calculation of synthetic seismograms on a spherical Earth, only the effect of anelasticity upon the eigenfrequencies

is retained and the effect of the anleasticity upon the radial eigenfunctions is ignored. This implies that the displacement eigenfunction becomes

$$\mathbf{s}_k(\mathbf{r}) = U_k(r)\hat{\mathbf{e}}_r\mathcal{Y}_{lm}(\theta,\phi) + \kappa^{-1}V_k(r)\nabla_1\mathcal{Y}_{lm}(\theta,\phi) - \kappa^{-1}W_k(r)(\hat{\mathbf{e}}_r\times\nabla_1\mathcal{Y}_{lm}(\theta,\phi)), \quad (4.17)$$

where $U_k(r), V_k(r), W_k(r)$ are real functions. With the metric perturbation for the plane waves (4.9) and the Green tensor for a non-rotating, anelastic Earth (4.15) we are ready to calculate the induced displacement in the next subsection.

4.2.3 Induced spheroidal response

To obtain the solution for the spheroidal motion induced by a GW defined by the force term (4.8), we need to insert this term into displacement (3.31) and take into account the boundary condition (3.3) on the surface. Using the weak field linear approximation, the interaction between GW and an elastic solid can be taken into account by adding a term (Dyson, 1969; Ben-Menahem, 1983)

$$\mathbf{T}^{GW} = -\mu\mathbf{h} \quad (4.18)$$

into the stress tensor, which results in the gravitational tidal force in the equation of motion, shown elsewhere (Ashby and Dreitlein, 1975; Linet, 1984). Therefore, the boundary condition (3.31) is altered and the surface force density becomes

$$\mathbf{t} = \mu(a)\hat{\mathbf{e}}_r\cdot\mathbf{h}. \quad (4.19)$$

where $\mu(a)$ is the value of the shear modulus at the Earth's surface. Considering the above relation, equation (3.31) becomes

$$\begin{aligned}\mathbf{s}(\mathbf{r},t) = &-\int_{-\infty}^{t}\int_V \frac{\partial\mu}{\partial r}\mathbf{G}(\mathbf{r},\mathbf{r}';t-t')\cdot(\hat{\mathbf{e}}_r\cdot\mathbf{h})dV'dt' \\ &+\mu(a)\int_{-\infty}^{t}\int_S \mathbf{G}(\mathbf{r},\mathbf{r}';t-t')\cdot(\hat{\mathbf{e}}_r\cdot\mathbf{h})d\Sigma'dt'.\end{aligned} \quad (4.20)$$

and substituting (4.9) and (4.15) we have for a given seismic mode k

$$\begin{aligned}\mathbf{s}_k(\mathbf{r},t) = &-h_0\mathbf{s}_k(\mathbf{r})\bar{g}(t)\int_V \frac{\partial\mu}{\partial r}\mathbf{s}_k(\mathbf{r}')\cdot(\hat{\mathbf{e}}_r\cdot\boldsymbol{\epsilon}\mathrm{e}^{-i\hat{\boldsymbol{k}}_g\cdot\mathbf{r}'})dV' \\ &+\mu(a)h_0\mathbf{s}_k(\mathbf{r})\bar{g}(t)\int_S \mathbf{s}_k(\mathbf{r}')\cdot(\hat{\mathbf{e}}_r\cdot\boldsymbol{\epsilon}\mathrm{e}^{-i\hat{\boldsymbol{k}}_g\cdot\mathbf{a}'})d\Sigma',\end{aligned} \quad (4.21)$$

where we have extracted the source-time function

$$\bar{g}(t) = \int_{-\infty}^{t}(i\nu_k)^{-1}\mathrm{e}^{i\nu_k(t-t')}\mathrm{e}^{i\omega_g t'}dt'. \quad (4.22)$$

Convolution in the time domain is equivalent to multiplication in the frequency domain, that is $\mathcal{F}\{f(t)*g(t)\} = \mathcal{F}\{f(t)\}\cdot\mathcal{F}\{g(t)\}$, where $\mathcal{F}$ is Fourier transform. Using this theorem we obtain

$$\begin{aligned}\bar{g}(t) &= \frac{1}{2\pi}\int_{-\infty}^{+\infty}(i\nu_k)^{-1}\mathcal{F}\{f(t)\}\cdot\mathcal{F}\{g(t)\}\mathrm{e}^{i\omega t}d\omega \\ &= \frac{1}{2\pi}\int_{-\infty}^{+\infty}(i\nu_k)^{-1}\delta(\omega-\omega_g)\frac{1}{\gamma_k+i(\omega-\omega_k)}\mathrm{e}^{i\omega t}d\omega \\ &= \frac{1}{2\pi}(i\nu_k)^{-1}\frac{1}{\gamma_k+i(\omega_g-\omega_k)}\mathrm{e}^{i\omega_g t}.\end{aligned} \tag{4.23}$$

In the long-wavelength regime we expect $k_g a \ll 1$ (Linet, 1984; Ashby and Dreitlein, 1975; Khosroshahi and Sobouti, 1997), thus we simplify (4.21) into

$$\begin{aligned}\mathbf{s}_k(\mathbf{r},t) &= h_0\mathbf{s}_k(\mathbf{r})\bar{g}(t)\left[-\int_V\frac{\partial\mu}{\partial r}\mathbf{s}_k(\mathbf{r}')\cdot(\hat{\mathbf{e}}_r\cdot\boldsymbol{\epsilon})dV'+\mu(a)\int_S\mathbf{s}_k(\mathbf{r}')\cdot(\hat{\mathbf{e}}_r\cdot\boldsymbol{\epsilon})d\Sigma'\right] \\ &= h_0\mathbf{s}_k(\mathbf{r})\bar{g}(t)\boldsymbol{\epsilon}:\left[-\int_V\frac{\partial\mu}{\partial r}\mathbf{s}_k(\mathbf{r}')\hat{\mathbf{e}}_r dV'+\mu(a)\int_S\mathbf{s}_k(\mathbf{r}')\hat{\mathbf{e}}_r d\Sigma'\right].\end{aligned} \tag{4.24}$$

Substituting the definition of the displacement eigenfunction (4.17) for the spheroidal modes ($W=0$) we obtain

$$\begin{aligned}\mathbf{s}_k(\mathbf{r},t) = h_0\mathbf{s}_k(\mathbf{r})\bar{g}(t)\boldsymbol{\epsilon}:\Bigg[&\left(\mu(a)U_k(a)a^2-\int_r\frac{\partial\mu}{\partial r}U_k(r)r^2dr\right)\int_\Omega\hat{\mathbf{e}}_r\hat{\mathbf{e}}_r\mathcal{Y}_{lm}(\theta,\phi)d\Omega \\ &+\left(\mu(a)\kappa^{-1}V_k(a)a^2-\int_r\frac{\partial\mu}{\partial r}\kappa^{-1}V_k(r)r^2dr\right)\int_\Omega\hat{\mathbf{e}}_r\nabla_1\mathcal{Y}_{lm}(\theta,\phi)d\Omega\Bigg]\end{aligned} \tag{4.25}$$

where $d\Omega = \sin\theta d\theta d\phi$ with $0<\phi<2\pi$, $0<\theta<\pi$ and $\int_r$ is integral over radius from center ($r=0$) to surface ($r=a$). To solve integrals in (4.25) we need to define the unit vectors $\{\hat{\mathbf{e}}_r,\hat{\mathbf{e}}_\theta,\hat{\mathbf{e}}_\phi\}$ and their dyadic products $\{\hat{\mathbf{e}}_r\hat{\mathbf{e}}_r,\hat{\mathbf{e}}_r\hat{\mathbf{e}}_\theta,\hat{\mathbf{e}}_r\hat{\mathbf{e}}_\phi\}$. For this we use the expressions of the unit vectors $\{\hat{\mathbf{e}}_r,\hat{\mathbf{e}}_\theta,\hat{\mathbf{e}}_\phi\}$ in spherical coordinates

$$\begin{bmatrix}\hat{\mathbf{e}}_r\\ \hat{\mathbf{e}}_\theta\\ \hat{\mathbf{e}}_\phi\end{bmatrix} = \begin{bmatrix}\sin\theta\cos\phi & \sin\theta\sin\phi & \cos\theta\\ \cos\theta\cos\phi & \cos\theta\sin\phi & -\sin\theta\\ -\sin\theta & \cos\phi & 0\end{bmatrix}\begin{bmatrix}\hat{\mathbf{e}}_x\\ \hat{\mathbf{e}}_y\\ \hat{\mathbf{e}}_z\end{bmatrix} \tag{4.26}$$

and calculate dyadic products using definition $\mathbf{ab} = \sum_{j=1}^3\sum_{i=1}^3 a_i b_j\hat{\mathbf{e}}_i\hat{\mathbf{e}}_j$. The solutions are

$$\hat{\mathbf{e}}_r\hat{\mathbf{e}}_r = \begin{bmatrix}\sin^2\theta\cos^2\phi & \sin^2\sin\phi\cos\phi & \sin\theta\cos\theta\cos\phi\\ \sin^2\theta\sin\phi\cos\phi & \sin^2\theta\sin^2\phi & \sin\theta\cos\theta\sin\phi\\ \sin\theta\cos\theta\cos\phi & \sin\theta\cos\theta\sin\phi & \cos^2\theta\end{bmatrix}, \tag{4.27}$$

$$\hat{\mathbf{e}}_r\hat{\mathbf{e}}_\theta = \begin{bmatrix}\sin\theta\cos\theta\cos^2\phi & \sin\theta\cos\theta\sin\phi\cos\phi & -\sin^2\theta\cos\phi\\ \sin\theta\cos\theta\sin\phi\cos\phi & \sin\theta\cos\theta\sin^2\phi & -\sin^2\theta\sin\phi\\ \cos^2\theta\cos\phi & \cos^2\theta\sin\phi & -\sin\theta\cos\theta\end{bmatrix}, \tag{4.28}$$

$$\hat{\mathbf{e}}_r\hat{\mathbf{e}}_\phi = \begin{bmatrix} -\sin\theta\cos\phi\sin\phi & \sin\theta\cos^2\phi & 0 \\ -\sin\theta\sin^2\phi & \sin\theta\sin\phi\cos\phi & 0 \\ -\cos\theta\sin\phi & \cos\theta\cos\phi & 0 \end{bmatrix}. \tag{4.29}$$

The first integral in (4.25)

$$I_1 = \int_\Omega \hat{\mathbf{e}}_r\hat{\mathbf{e}}_r\mathcal{Y}_{lm}(\theta,\phi)d\Omega = \int_0^\pi\int_0^{2\pi} \hat{\mathbf{e}}_r\hat{\mathbf{e}}_r\mathcal{Y}_{lm}(\theta,\phi)\sin\theta d\theta d\phi \tag{4.30}$$

is a double integral over two arguments ϕ and θ over nine components of the dyadic product $\{\hat{\mathbf{e}}_r\hat{\mathbf{e}}_r\}$. The solution is

$$\begin{aligned} I_1 = \frac{2\sqrt{\pi}}{3}\delta_{l,0}\delta_{m,0}\begin{bmatrix} 1 & 0 & 0 \\ 0 & 1 & 0 \\ 0 & 0 & 1 \end{bmatrix} + \frac{2}{3}\sqrt{\frac{\pi}{5}}\delta_{l,2}\delta_{m,0}\begin{bmatrix} -1 & 0 & 0 \\ 0 & -1 & 0 \\ 0 & 0 & 2 \end{bmatrix} \\ + 2\sqrt{\frac{\pi}{15}}\delta_{l,2}\begin{bmatrix} \delta_{m,-2} & \delta_{m,2} & -\delta_{m,-1} \\ \delta_{m,2} & -\delta_{m,-2} & -\delta_{m,1} \\ -\delta_{m,-1} & -\delta_{m,1} & 0 \end{bmatrix}. \end{aligned} \tag{4.31}$$

Next, we derive the second integral in relation (4.25), which is

$$\begin{aligned} I_2 = \int_\Omega \hat{\mathbf{e}}_r\nabla_1\mathcal{Y}_{lm}(\theta,\phi)d\Omega = \int_0^\pi\int_0^{2\pi} \hat{\mathbf{e}}_r\hat{\mathbf{e}}_\theta\partial_\theta\mathcal{Y}_{lm}(\theta,\phi)\sin\theta d\theta d\phi \\ + \int_0^\pi\int_0^{2\pi} \hat{\mathbf{e}}_r\hat{\mathbf{e}}_\phi(\sin\theta)^{-1}\partial_\phi\mathcal{Y}_{lm}(\theta,\phi)\sin\theta d\theta d\phi. \end{aligned} \tag{4.32}$$

The two integrals in (4.32) also involve nine integrals due to $\{\hat{\mathbf{e}}_r\hat{\mathbf{e}}_\theta\}$ and $\{\hat{\mathbf{e}}_r\hat{\mathbf{e}}_\phi\}$ dyadic products and the final result is

$$I_2 = 2\sqrt{\frac{\pi}{5}}\delta_{l,2}\delta_{m,0}\begin{bmatrix} -1 & 0 & 0 \\ 0 & -1 & 0 \\ 0 & 0 & 2 \end{bmatrix} + 6\sqrt{\frac{\pi}{15}}\delta_{l,2}\begin{bmatrix} \delta_{m,-2} & \delta_{m,2} & -\delta_{m,-1} \\ \delta_{m,2} & -\delta_{m,-2} & -\delta_{m,1} \\ -\delta_{m,-1} & -\delta_{m,1} & 0 \end{bmatrix} \tag{4.33}$$

Finally, the expression (4.25) becomes

$$\begin{aligned} \mathbf{s}_k(\mathbf{r},t) = h_0\mathbf{s}_k(\mathbf{r})\bar{g}(t)\boldsymbol{\epsilon} : \Bigg\{ \frac{2\sqrt{\pi}}{3}\delta_{l,0}\delta_{m,0}\begin{bmatrix} 1 & 0 & 0 \\ 0 & 1 & 0 \\ 0 & 0 & 1 \end{bmatrix}\left(\mu(a)U_k(a)a^2 - \int_r \frac{\partial\mu}{\partial r}U_k(r)r^2dr\right) \\ + \left(\frac{2}{3}\sqrt{\frac{\pi}{5}}\delta_{l,2}\delta_{m,0}\begin{bmatrix} -1 & 0 & 0 \\ 0 & -1 & 0 \\ 0 & 0 & 2 \end{bmatrix} + 2\sqrt{\frac{\pi}{15}}\delta_{l,2}\begin{bmatrix} \delta_{m,-2} & \delta_{m,2} & -\delta_{m,-1} \\ \delta_{m,2} & -\delta_{m,-2} & -\delta_{m,1} \\ -\delta_{m,-1} & -\delta_{m,1} & 0 \end{bmatrix}\right) \\ \left(\mu(a)a^2\left(U_k(a) + \frac{3}{\sqrt{6}}V_k(a)\right) - \int_r \frac{\partial\mu}{\partial r}\left(U_k(r) + \frac{3}{\sqrt{6}}V_k(r)\right)r^2dr\right)\Bigg\}. \end{aligned} \tag{4.34}$$

However, since $\boldsymbol{\epsilon} : \mathrm{I} = 0$ (I is the identity matrix) the above expression reduces to

$$\mathbf{s}_k(\mathbf{r},t) = h_0 \mathbf{s}_k(\mathbf{r})\bar{g}(t)\delta_{l,2}\boldsymbol{\epsilon} : \left\{ \frac{2}{3}\sqrt{\frac{\pi}{5}}\delta_{m,0}\begin{bmatrix} -1 & 0 & 0 \\ 0 & -1 & 0 \\ 0 & 0 & 2 \end{bmatrix} + 2\sqrt{\frac{\pi}{15}}\begin{bmatrix} \delta_{m,-2} & \delta_{m,2} & -\delta_{m,-1} \\ \delta_{m,2} & -\delta_{m,-2} & -\delta_{m,1} \\ -\delta_{m,-1} & -\delta_{m,1} & 0 \end{bmatrix} \right\}$$
$$\left(\mu(a)a^2\left(U_k(a) + \frac{3}{\sqrt{6}}V_k(a)\right) - \int_r \frac{\partial \mu}{\partial r}\left(U_k(r) + \frac{3}{\sqrt{6}}V_k(r)\right) r^2 dr\right). \tag{4.35}$$

The complete contraction between $\boldsymbol{\epsilon}$ and matrices appearing in (4.35) yields the expression

$$\mathbf{s}_k(\mathbf{r},t) = h_0 \mathbf{s}_k(\mathbf{r})\bar{g}(t)\delta_{l,2} f^m(e,\lambda,\nu)\zeta_k, \tag{4.36}$$

with

$$\zeta_k = \mu(a)a^2\left(U_k(a) + \frac{3}{\sqrt{6}}V_k(a)\right) - \int_r \frac{\partial \mu}{\partial r}\left(U_k(r) + \frac{3}{\sqrt{6}}V_k(r)\right) r^2 dr, \tag{4.37}$$

and the function $f^m(e,\lambda,\nu)$ defined as

$$\begin{aligned} f^m(e,\lambda,\nu) = & \frac{2}{3}\sqrt{\frac{\pi}{5}}\delta_{m,0} b_1 \sin^2 e \\ & + \delta_{m,2}\frac{C}{2}\left[4b_2 \cos e \cos 2\lambda + b_1(3+\cos 2e)\sin 2\lambda\right] \\ & + \delta_{m,-2} C\left[b_1 \cos 2\lambda(\cos^2 e + 1) - 2b_2 \cos e \sin 2\lambda\right] \\ & + \delta_{m,1} 2C \sin e\left[b_2 \cos\lambda + b_1 \cos e \sin\lambda\right] \\ & - \delta_{m,-1} 2C \sin e\left[b_2 \sin\lambda - b_1 \cos e \cos\lambda\right], \end{aligned} \tag{4.38}$$

with $C = 2\sqrt{\frac{\pi}{15}}$. According to (4.36) the leading angular term for the induced spheroidal motion is $\delta_{l,2}$ and therefore associated azimuth terms are $\{m = -2,-1,0,1,2\}$ (Ben-Menahem, 1983; Boughn and Kuhn, 1984; Khosroshahi and Sobouti, 1997; Siegel and Roth, 2010; Maggiore, 2008). This result comes from the fact that in the general relativity $h_{\mu\nu}$ is traceless and symmetric (Maggiore, 2008). In Fig. 4.2 we show the values of function $f^m(e,\lambda,\nu)$ when $\nu = 0$, since this angle is usually a unknown. The displacement depends on the value of the scalar h_0 which is defined by the gravitational source, the displacement eigenfunction $\mathbf{s}_k$, the source-time function $\bar{g}(t)$, the function $f^m(e,\lambda,\nu)$ defining the incoming GW and a constant ζ_k which depends on the Earth model. The three components of the displacement (4.36) at $\mathbf{r}$ are

$${}_n s^m_{2,r} = h_0\ {}_n\zeta_2\ {}_n U_2\ \mathcal{Y}_{lm}(\theta,\phi)\ f^m(e,\lambda,\nu)\ \Re\{\bar{g}(t)\}, \tag{4.39}$$

$${}_n s^m_{2,\theta} = h_0\ {}_n\zeta_2\ \frac{1}{\sqrt{6}}{}_n V_2\ \partial_\theta \mathcal{Y}_{lm}(\theta,\phi)\ f^m(e,\lambda,\nu)\ \Re\{\bar{g}(t)\}, \tag{4.40}$$

$${}_n s^m_{2,\phi} = h_0\ {}_n\zeta_2\ \frac{1}{\sqrt{6}}{}_n V_2 (\sin\theta)^{-1}\ \partial_\phi \mathcal{Y}_{lm}(\theta,\phi)\ f^m(e,\lambda,\nu)\ \Re\{\bar{g}(t)\}, \tag{4.41}$$

with

$$\Re\left\{\bar{g}(t)\right\} = \frac{1}{2\pi}\frac{(\omega_k^2 - \omega_k\omega_g - \gamma_k^2)\cos\omega_g t - (\gamma_k\omega_g - 2\gamma_k\omega_k)\sin\omega_g t}{(\omega_k^2 + \gamma_k^2)\left[\gamma_k^2 + (\omega_g^2 - \omega_k^2)\right]}. \tag{4.42}$$

We see that the incident angles of the GW $\{e, \lambda, \mu\}$ determine which normal modes are being excited. In Table 4.1 we show excited azimuth terms of the radial displacement ${}_n s_{2,r}^m$ for different combinations of $\{e, \lambda, \mu\}$ angles.

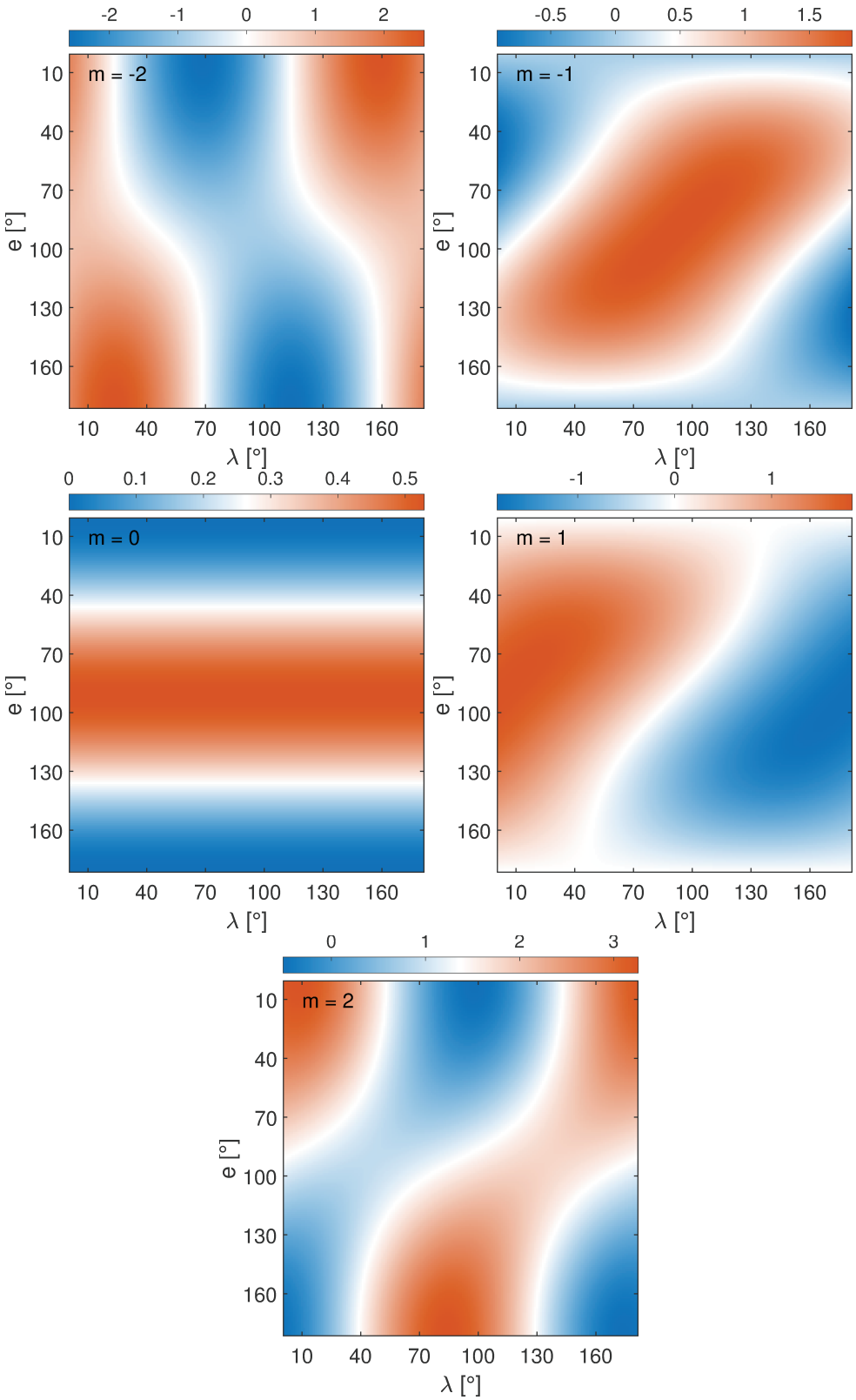

Fig 4.2: Function $f^m(e, \lambda, \nu)$ depending on e and λ angles when $\nu = 0$ from left to right and up to down corresponding to azimuth order $m = \{-2, -1, 0, 1, 2\}$, respectively.

Tab 4.1: Excited degree-2 azimuthal terms for different combinations of the $\{e, \lambda, \mu\}$ angles defining the incoming gravitational wave.

$\{e, \lambda, \mu\}$	m
$\{0,0,0\}$, $\{0,\frac{\pi}{2},0\}$, $\{0,0,\frac{\pi}{2}\}$, $\{0,\frac{\pi}{2},\frac{\pi}{2}\}$	-2,2
$\{\frac{\pi}{2},0,0\}$, $\{\frac{\pi}{2},0,\frac{\pi}{2}\}$	-2,1,0
$\{\frac{\pi}{2},0,0\}$, $\{\frac{\pi}{2},\frac{\pi}{2},0\}$, $\{\frac{\pi}{2},\frac{\pi}{2},\frac{\pi}{2}\}$	-2,-1,0

We emphasise that we are primarily interested in the Earth oscillatory motion continuously forced by a GW. We neglect the impulse reponse of the Earth to the initial excitation by the GW. We also neglect the transient motion that follows the initial excitation and decays before the oscillatory regime is reached.

4.2.4 Discussion

The relations (4.39)-(4.41) are essentially the same as relations [47]-[49] in Ben-Menahem (1983). However, differences exist since we used a different definition of spherical harmonics, different polarization of GW and Green tensor formalism from Dahlen and Tromp (1998). Next, we derive expression for the right-hand circularly polarized GW, defined as $\frac{1}{2}(\mathbf{e}_+ - i\mathbf{e}_\times)$, since this one was used in Ben-Menahem (1983). Therefore, the polarization tensor is defined as

$$\boldsymbol{\epsilon}_b = \frac{1}{2}\mathrm{e}^{2i\nu}\begin{bmatrix} (c(e)c(\lambda)+is(\lambda))^2 & -ic(e)c(2\lambda)+\frac{1}{2}(1+c^2(e))s(2\lambda) & -s(e)(c(e)c(\lambda)+is(\lambda)) \\ -ic(e)c(2\lambda)+\frac{1}{2}(1+c^2(e))s(2\lambda) & -(c(\lambda)+ic(e)s(\lambda))^2 & is(e)(c(\lambda)+ic(e)s(\lambda)) \\ -s(e)(c(e)c(\lambda)+is(\lambda)) & is(e)(c(\lambda)+ic(e)s(\lambda)) & s^2(e) \end{bmatrix}, \tag{4.43}$$

and corresponds to the polarization tensor of equation [15] in Ben-Menahem (1983). For the newly defined tensor the function $f^m(e,\lambda,\nu)$ from the displacement vector (4.36) becomes

$$\begin{aligned} f_b^m(e,\lambda,\nu) = &\sqrt{\frac{\pi}{5}}\delta_{m,0}\mathrm{e}^{2i\nu}\sin^2 e \\ &+ \delta_{m,-1}C\mathrm{e}^{2i\nu}\sin e\,[\cos e\cos\lambda + i\sin\lambda] \\ &+ \delta_{m,1}C\mathrm{e}^{2i\nu}\sin e\,[\cos e\sin\lambda - i\cos\lambda] \\ &+ \delta_{m,-2}\frac{C}{4}\mathrm{e}^{2i\nu}\,[3\cos 2\lambda + \cos 2e\cos 2\lambda + 4i\cos e\sin 2\lambda] \\ &+ \delta_{m,2}\frac{C}{4}\mathrm{e}^{2i\nu}\,[3\sin 2\lambda + \cos 2e\sin 2\lambda - 4i\cos e\cos 2\lambda]\,, \end{aligned} \tag{4.44}$$

with C defined above. The values in Table 4.1 are valid for the relation (4.44) too.

Considering this new expression the radial component of the induced spheroidal quadrupole response can be written as

$${}_n s^m_{2,r} = h_0\ {}_n\zeta_2\ {}_nU_2\ \mathcal{Y}_{lm}(\theta,\phi)\ \Re\{f_b^m(e,\lambda,\nu)\bar{g}(t)\}. \tag{4.45}$$

This expression is compared directly with the equivalent relation [47] from Ben-Menahem (1983) which is

$$
\begin{aligned}
{}_nu_r = (-1)^m \frac{2}{\sqrt{6}} h_{0n}\omega_2^2 \bar{g}_n(t) \left[y_{1n}(r) \frac{\mu(a)a^2(y_{1n}+3y_{3n}) - \int_0^a \frac{\partial \mu}{\partial r}(y_{1n}(r)+3y_{3n}(r))r^2 dr}{{}_n\omega_2^2 \int_0^a (y_{1n}^2(r)+6y_{3n}^2(r))r^2 dr} \right] \\
\Re\{ \mathrm{e}^{2i\nu} P_{2m}(\cos\theta) \sin^{2-m}\left(\frac{e}{2}\right) \cos^{2+m}\left(\frac{e}{2}\right) \mathrm{e}^{im(\phi+\lambda)} \}.
\end{aligned}
\tag{4.46}
$$

We rewrite the radial induced response (4.46) in terms that are comparable to relation (4.45) as

$$
{}_nu_r = h_0 \; {}_n\alpha_2^{\mathrm{BM83}} \; y_{1n}(r) \; Y_{lm}(\theta,\phi) \; \Re\{ f_b^{m;\mathrm{BM83}}(e,\lambda,\nu)\bar{g}(t) \},
\tag{4.47}
$$

where

$$
{}_n\alpha_2^{\mathrm{BM83}} = \frac{\mu(a)a^2(y_{1n}+3y_{3n}) - \int_0^a \frac{\partial \mu}{\partial r}(y_{1n}(r)+3y_{3n}(r))r^2 dr}{\int_0^a (y_{1n}^2(r)+6y_{3n}^2(r))r^2 dr},
\tag{4.48}
$$

and

$$
\begin{aligned}
f_b^{m;\mathrm{BM83}}(e,\lambda,\nu) = {} & \delta_{m,0} \frac{1}{2\sqrt{6}} \mathrm{e}^{2i\nu} \sin^2 e \\
& + \delta_{m,2} \frac{2}{\sqrt{6}} \mathrm{e}^{2i\nu} \cos^4\left(\frac{e}{2}\right) \mathrm{e}^{2im} \\
& + \delta_{m,-2} \frac{2}{\sqrt{6}} \mathrm{e}^{2i\nu} \sin^4\left(\frac{e}{2}\right) \mathrm{e}^{-2im} \\
& - \delta_{m,1} \frac{2}{\sqrt{6}} \mathrm{e}^{2i\nu} \sin\left(\frac{e}{2}\right) \cos^3\left(\frac{e}{2}\right) \mathrm{e}^{im} \\
& - \delta_{m,-1} \frac{2}{\sqrt{6}} \mathrm{e}^{2i\nu} \sin^3\left(\frac{e}{2}\right) \cos\left(\frac{e}{2}\right) \mathrm{e}^{-im}.
\end{aligned}
\tag{4.49}
$$

Therefore, by directly comparing (4.45) and (4.47), we see there are several differences. At the beginning, it should be emphasised that in these two relations the notations for the displacement eigenfunction are different, thus we have $U_k(r) = y_{1n}(r)$ and $V_k(r) = y_{3n}(r)$. Thus, the first difference concerns the model dependent functions (4.49) and (4.37), which are dissimilar due to the different normalization used for the displacement eigenfunctions that actually depends on the spherical harmonics normalization. In Dahlen and Tromp (1998) one uses the orthonormalized spherical harmonics and in Ben-Menahem (1983) the Schmidt semi-normalized spherical harmonics. The radial eigenfunctions in Dahlen and Tromp (1998) are orthonormal due to the general orthonormality of displacement eigenfunctions (see page 279 in Dahlen and Tromp (1998)). This is not the case for the formalism in Ben-Menahem and Singh (1981) and the reader is referred to page 379 for further details. The second difference concerns the used definition of the spherical harmonics. Beside a different normalization for the spherical harmonics, we use real spherical harmonics. This essentially affects the results of the two integrals (4.31) and (4.33). The integrals additionally generate a third difference and these are dissimilarities between functions (4.44)

and (4.49), a consequence of the contraction between the polarization tensor and integrals outputs.

Comparing the solutions from Ben-Menahem (1983) with ours is not completely straightforward because we do not use the same formalism. Also, when we rederive the solutions of Ben-Menahem (1983) we find some inconsistencies that we are going to be describe. In the following, the equations from Ben-Menahem (1983) are still inserted in square brackets. Ben-Menahem stated that he derived the induced spheroidal field by using his equations [28], [35] and [36]. For the sake of comparison we assume that those equations are correct and we perform the same calculations. Further, we adopt his notation and to distinguish f^m functions derived above from the ones below we change notation to f_m by changing the m from superscript to subscript. Thus, the result is

$$
{}_n\boldsymbol{u}_{m2}(\boldsymbol{r},t) = h_0\bar{g}_n(t){}_n\boldsymbol{Q}^*_{m2}(\boldsymbol{r}){}_n\wedge^{-1}_{m2}\frac{8\pi}{5\sqrt{6}}f_m\left[a^2\mu(a)(y_{1n}+3y_{3n}) - \int_0^a \frac{\partial\mu}{\partial r}(y_{1n}+3y_{3n})r^2dr\right], \tag{4.50}
$$

with function f_m being

$$
\begin{aligned}
f_m = &\frac{\sqrt{6}}{4}\sin^2(e)\,\mathrm{e}^{2i\nu}\delta_{m,0} \\
&+\cos^4\left(\frac{e}{2}\right)\mathrm{e}^{2i\lambda}\mathrm{e}^{2i\nu}\delta_{m,2} \\
&+\sin^4\left(\frac{e}{2}\right)\mathrm{e}^{-2i\lambda}\mathrm{e}^{2i\nu}\delta_{m,-2} \\
&-2\sin\left(\frac{e}{2}\right)\cos^3\left(\frac{e}{2}\right)\mathrm{e}^{i\lambda}\mathrm{e}^{2i\nu}\delta_{m,1} \\
&-2\sin^3\left(\frac{e}{2}\right)\cos\left(\frac{e}{2}\right)\mathrm{e}^{-i\lambda}\mathrm{e}^{2i\nu}\delta_{m,-1}.
\end{aligned} \tag{4.51}
$$

Substituting the normalization factor defined as

$$
{}_n\wedge_{m2} = \frac{4\pi}{5}\int_0^a (y_{1n}^2+6y_{3n}^2)\rho(r)r^2dr, \tag{4.52}
$$

into (4.50) we arrive at the expression

$$
{}_n\boldsymbol{u}_{m2}(\boldsymbol{r},t) = \frac{2}{\sqrt{6}}h_0\bar{g}_n(t){}_n\boldsymbol{Q}^*_{m2}(\boldsymbol{r})f_m\tilde{\alpha}, \tag{4.53}
$$

where we introduce the abbreviation defined as

$$
\tilde{\alpha} = \frac{a^2\mu(a)(y_{1n}+3y_{3n}) - \int_0^a \frac{\partial\mu}{\partial r}(y_{1n}+3y_{3n})r^2dr}{\int_0^a (y_{1n}^2+6y_{3n}^2)\rho(r)r^2dr}. \tag{4.54}
$$

This can be compared with his solution [45]

$$
{}_n\boldsymbol{u}^{\mathrm{BM}}_{m2}(\boldsymbol{r},t) = (-1)^m\frac{2}{\sqrt{6}}h_0\bar{g}_n(t)\tilde{\alpha}\Re\{{}_n\boldsymbol{Q}_{m2}(\boldsymbol{r})\sin^{2-m}\left(\frac{e}{2}\right)\cos^{2+m}\left(\frac{e}{2}\right)\mathrm{e}^{im(\lambda+\nu)}\}, \tag{4.55}
$$

which can be recast as

$$ {}_n\boldsymbol{u}_{m2}^{\mathrm{BM}}(\boldsymbol{r},t) = \frac{2}{\sqrt{6}} h_0 \bar{g}_n(t) {}_n\boldsymbol{Q}_{m2}(\boldsymbol{r}) f_m^{\mathrm{BM}} \tilde{\alpha}, \tag{4.56} $$

with the function f_m^{BM} defined by

$$ \begin{aligned} f_m^{\mathrm{BM}} = = & \frac{1}{4}\sin^2(e)\mathrm{e}^{2i\nu}\delta_{m,0} \\ & + \cos^4\left(\frac{e}{2}\right)\mathrm{e}^{2i\lambda}\mathrm{e}^{2i\nu}\delta_{m,2} \\ & + \sin^4\left(\frac{e}{2}\right)\mathrm{e}^{-2i\lambda}\mathrm{e}^{2i\nu}\delta_{m,-2} \\ & - \sin\left(\frac{e}{2}\right)\cos^3\left(\frac{e}{2}\right)\mathrm{e}^{i\lambda}\mathrm{e}^{2i\nu}\delta_{m,1} \\ & - \sin^3\left(\frac{e}{2}\right)\cos\left(\frac{e}{2}\right)\mathrm{e}^{-i\lambda}\mathrm{e}^{2i\nu}\delta_{m,-1}. \end{aligned} \tag{4.57} $$

Just by simple comparison of the expressions (4.53) and (4.56) there are two differences: firstly, Ben-Menahem did not include the complex conjugate for the displacement eigenfunction ${}_n\boldsymbol{Q}_{m2}(\boldsymbol{r})$, even though it exists in the definition given by relation [26]; secondly, he misplaced the coefficients θ_m defined in his expression [36], since these are the values missing in expression (4.57) compared to (4.51).

If we try a different approach and recalculate the induced response [45] using expressions [42] and [43] obtained by contracting polarization tensor [15] and quadrupole moment tensor [44] we should obtain the same result [45]. Thus, we have

$$ \begin{aligned} F_{S_1} = & \frac{a^2\mu(a)y_{1n} - \int_0^a \frac{\partial\mu}{\partial r} y_{1n} r^2 dr}{3\int_0^a \rho_0 y_{3n} r^3 dr} (\varepsilon\varepsilon : \delta D_B) \\ = & \left(a^2\mu(a)y_{1n} - \int_0^a \frac{\partial\mu}{\partial r} y_{1n} r^2 dr\right) \frac{1}{3}\frac{24\pi}{5\sqrt{6}}\delta_{l,2}\frac{1}{2}4 \\ & \left[\frac{\sqrt{6}}{4}\sin^2 e\mathrm{e}^{2i\nu}\delta_{m,0}\right. \\ & + \cos^4\left(\frac{e}{2}\right)\mathrm{e}^{2i\lambda}\mathrm{e}^{2i\nu}\delta_{m,2} \\ & + \sin^4\left(\frac{e}{2}\right)\mathrm{e}^{-2i\lambda}\mathrm{e}^{2i\nu}\delta_{m,-2} \\ & + 2\sin^3\left(\frac{e}{2}\right)\cos\left(\frac{e}{2}\right)\mathrm{e}^{-i\lambda}\mathrm{e}^{2i\nu}\delta_{m,1} \\ & \left. - 2\sin\left(\frac{e}{2}\right)\cos^3\left(\frac{e}{2}\right)\mathrm{e}^{i\lambda}\mathrm{e}^{2i\nu}\delta_{m,-1}\right] \\ = & \frac{16\pi}{5\sqrt{6}}\delta_{l,2} f_m^{\mathrm{BM},2}(e,\lambda,\nu)\left(a^2\mu(a)y_{1n} - \int_0^a \frac{\partial\mu}{\partial r} y_{1n} r^2 dr\right) \end{aligned} \tag{4.58} $$

with function f_m^{BM2} defined as

$$\begin{aligned} f_m^{\mathrm{BM2}}(e,\lambda,\nu) = &\frac{\sqrt{6}}{4}\sin^2 e \mathrm{e}^{2i\nu}\delta_{m,0} \\ &+ \cos^4\left(\frac{e}{2}\right)\mathrm{e}^{2i\lambda}\mathrm{e}^{2i\nu}\delta_{m,2} \\ &+ \sin^4\left(\frac{e}{2}\right)\mathrm{e}^{-2i\lambda}\mathrm{e}^{2i\nu}\delta_{m,-2} \\ &+ 2\sin^3\left(\frac{e}{2}\right)\cos\left(\frac{e}{2}\right)\mathrm{e}^{-i\lambda}\mathrm{e}^{2i\nu}\delta_{m,1} \\ &- 2\sin\left(\frac{e}{2}\right)\cos^3\left(\frac{e}{2}\right)\mathrm{e}^{i\lambda}\mathrm{e}^{2i\nu}\delta_{m,-1}. \end{aligned} \tag{4.59}$$

Substituting this in [28] we have

$${}_n\boldsymbol{u}_{m2}^{\mathrm{BM2}}(\boldsymbol{r},t) = \frac{4}{\sqrt{6}}h_0\bar{g}_n(t){}_n\boldsymbol{Q}_{m2}(\boldsymbol{r})f_m^{\mathrm{BM},2}\tilde{\alpha}. \tag{4.60}$$

Eventually, we see that this approach also yields some differences. Function (4.59) is more similar to the relation (4.51) than (4.57). However, the values multiplying the Kronecker symbols $\delta_{m,1}$ and $\delta_{m,-1}$ are inverted compared to (4.51) and (4.57). We highly suspect that the reason for this comes from the definition of the quadrupole moment tensor [44], which we were not able to reproduce.

Let us now derive the solution of this study using fully normalized complex spherical harmonics defined as

$$Y_{lm}(\theta,\phi) = \sqrt{\frac{2l+1}{4\pi}}\sqrt{\frac{(l-m)!}{(l+m)!}}P_{lm}(\cos\theta)\mathrm{e}^{im\phi}, \tag{4.61}$$

with the associated Legendre function $P_{lm}(x)$ defined by (3.12). This assumption yields for the integrals I_1 and I_2 solutions that are different from our results (4.31) and (4.33). They are

$$\begin{aligned} I_1 = &\frac{2\sqrt{\pi}}{3}\delta_{l,0}\delta_{m,0}\begin{bmatrix}1&0&0\\0&1&0\\0&0&1\end{bmatrix} + \frac{2}{3}\sqrt{\frac{\pi}{5}}\delta_{l,2}\delta_{m,0}\begin{bmatrix}-1&0&0\\0&-1&0\\0&0&2\end{bmatrix} \\ &+ \sqrt{\frac{2\pi}{15}}\delta_{l,2}\begin{bmatrix}\delta_{m,2}+\delta_{m,-2} & i\delta_{m,2}-i\delta_{m,-2} & -\delta_{m,1}-\delta_{m,-1}\\ i\delta_{m,2}-i\delta_{m,-2} & -\delta_{m,2}-\delta_{m,-2} & -i\delta_{m,1}+-i\delta_{m,-1}\\ \delta_{m,1}-\delta_{m,-1} & -i\delta_{m,1}-i\delta_{m,-1} & 0\end{bmatrix}, \end{aligned} \tag{4.62}$$

and

$$
\begin{aligned}
I_2 = 2\sqrt{\frac{\pi}{5}}\delta_{l,2}\delta_{m,0}&\begin{bmatrix} -1 & 0 & 0 \\ 0 & -1 & 0 \\ 0 & 0 & 2 \end{bmatrix} \\
+ 3\sqrt{\frac{2\pi}{15}}\delta_{l,2}&\begin{bmatrix} \delta_{m,2}+\delta_{m,-2} & i\delta_{m,2}-i\delta_{m,-2} & -\delta_{m,1}-\delta_{m,-1} \\ i\delta_{m,2}-i\delta_{m,-2} & -\delta_{m,2}-\delta_{m,-2} & -i\delta_{m,1}+-i\delta_{m,-1} \\ \delta_{m,1}-\delta_{m,-1} & -i\delta_{m,1}-i\delta_{m,-1} & 0 \end{bmatrix}.
\end{aligned}
\tag{4.63}
$$

This, finally, gives us a new induced spheroidal response

$$
\mathbf{s}_k^{\mathrm{CSH}}(\mathbf{r},t) = 2\sqrt{\frac{2\pi}{15}}h_0\mathbf{s}_k(\mathbf{r})\bar{g}(t)\delta_{l,2}f_m^{\mathrm{CSH}}(e,\lambda,\nu)\alpha_k, \tag{4.64}
$$

with function $f_m^{\mathrm{CSH}}(e,\lambda,\nu)$ defined as

$$
\begin{aligned}
f_m^{\mathrm{CSH}}(e,\lambda,\nu) = \frac{\sqrt{6}}{4}&\sin^2 e\mathrm{e}^{2i\nu}\delta_{m,0} \\
&+ \cos^4\left(\frac{e}{2}\right)\mathrm{e}^{2i\lambda}\mathrm{e}^{2i\nu}\delta_{m,2} \\
&+ \sin^4\left(\frac{e}{2}\right)\mathrm{e}^{-2i\lambda}\mathrm{e}^{2i\nu}\delta_{m,-2} \\
&+ 2\sin\left(\frac{e}{2}\right)\cos^3\left(\frac{e}{2}\right)\mathrm{e}^{i\lambda}\mathrm{e}^{2i\nu}\delta_{m,1}. \\
&+ 2\sin^3\left(\frac{e}{2}\right)\cos\left(\frac{e}{2}\right)\mathrm{e}^{-i\lambda}\mathrm{e}^{2i\nu}\delta_{m,-1},
\end{aligned}
\tag{4.65}
$$

where CSH stand for complex spherical harmonic and α_k for the model dependent function (4.37). We repeat the same calculation just with the spherical harmonics defined as

$$
\tilde{Y}_{lm} = (-1)^m\sqrt{\frac{2l+1}{4\pi}}Y_{lm} \tag{4.66}
$$

which gives us

$$
\tilde{Y}_{lm} = \left(\frac{2l+1}{4\pi}\right)\sqrt{\frac{(l-m)!}{(l+m)!}}\tilde{P}_{lm}(\cos\theta)\mathrm{e}^{im\phi}, \tag{4.67}
$$

where for the associated Legendre function $\tilde{P}_{lm}(x)$ the valid relation is

$$
P_{lm}(x) = (-1)^m\tilde{P}_{lm}(x). \tag{4.68}
$$

This definition of spherical harmonics corresponds to the one in Ben-Menahem and Singh (1981) that is presumably used in Ben-Menahem (1983). The induced spheroidal response becomes

$$
\mathbf{s}_k^{\mathrm{CSH2}}(\mathbf{r},t) = \frac{2}{\sqrt{6}}h_0\mathbf{s}_k(\mathbf{r})\bar{g}(t)\delta_{l,2}\tilde{f}_m^{\mathrm{CSH2}}(e,\lambda,\nu)\alpha_k, \tag{4.69}
$$

with

$$\begin{aligned}\tilde{f}_m^{\mathrm{CSH2}}(e,\lambda,\nu) = &\frac{\sqrt{6}}{4}\sin^2 e \mathrm{e}^{2i\nu}\delta_{m,0}\\ &+\cos^4\left(\frac{e}{2}\right)\mathrm{e}^{2i\lambda}\mathrm{e}^{2i\nu}\delta_{m,2}\\ &+\sin^4\left(\frac{e}{2}\right)\mathrm{e}^{-2i\lambda}\mathrm{e}^{2i\nu}\delta_{m,-2}\\ &-2\sin\left(\frac{e}{2}\right)\cos^3\left(\frac{e}{2}\right)\mathrm{e}^{i\lambda}\mathrm{e}^{2i\nu}\delta_{m,1}.\\ &-2\sin^3\left(\frac{e}{2}\right)\cos\left(\frac{e}{2}\right)\mathrm{e}^{-i\lambda}\mathrm{e}^{2i\nu}\delta_{m,-1}.\end{aligned} \tag{4.70}$$

Therefore, one can use the transformation (4.66) between two definitions of spherical harmonics to obtain similar but not the same relations. With this transformation we arrive at the same expression for (4.51) and (4.70), while relation (4.69) still has some differences compared to relation (4.53). These dissimilarities concern how we define the displacement eigenfunctions and what normalization we use for the radial eigenfunctions. One of the differences concerns the definition of the Green tensor. We use a formalism where the definition of the Green tensor depends on the Earth model (see page 231 in Dahlen and Tromp (1998)). In Ben-Menahem and Singh (1981) those differences are not explicitly emphasized. In Ben-Menahem (1983) stated that he developed the displacement for radially heterogeneous, anelastic self-gravitating, rotating Earth models and thus he used the Green tensor defined by relation [25], depending on the real radial eigenfunctions and complex spherical harmonics. Additionally, his displacement eigenfunction at the receiver is complex conjugate. For the same Earth model we would use Green tensors containing complex radial eigenfunction and complex spherical harmonics (Dahlen and Tromp, 1998). Moreover, the displacement eigenfunction at the source would be dual. However, this could be simplified: anelasticity is ignored, therefore the radial eigenfunctions become real and the displacement eigenfunctions at the source become complex conjugate. At the end, we would have complex conjugate displacement eigenfunction at source unlike Ben-Menahem. Thus, if we follow our formalism for radially heterogeneous, anelastic self-gravitating, rotating Earth model we would derive integrals (4.62) and (4.63) for complex conjugate fully normalized spherical harmonic. In Tab. 4.2 we compare the functions that would be used in these two studies to derive displacement for radially heterogeneous, anelastic self-gravitating, rotating Earth model. The final solution highly depends on the spherical harmonic normalization, therefore on the normalization of radial eigenfunctions, on the definition of Green tensors and on the definition of the displacement eigenfunctions.

Tab 4.2: List of functions (spherical harmonics, associated Legendre functions, Green tensors, displacement eigenfunctions, normalization of displacement eigenfunctions, respectively) that are used to develop displacement for radially heterogeneous, anelastic self-gravitating, rotating Earth model for Ben-Menahem (1983) and Dahlen & Tromp (1998) formalism. Constants are $\Omega_{lm} = \frac{4\pi}{2l+1}\frac{(l-m)!}{(l+m)!}$ and $\kappa = \sqrt{(l(l+1))}$. Normalization of the displacement eigenfunction for Dahlen & Tromp (1998) is written for spherical non-rotating elastically isotropic Earth model, since the rotation is treated as a perturbation.

Ben-Menahem (1983)	This study
$Y_{lm}(\theta,\phi) = \sqrt{\frac{(l-m)!}{(l+m)!}} P_{lm}(\cos\theta)\mathrm{e}^{im\phi}$	$Y_{lm}(\theta,\phi) = \sqrt{\frac{2l+1}{4\pi}}\sqrt{\frac{(l-m)!}{(l+m)!}} P_{lm}(\cos\theta)\mathrm{e}^{im\phi}$
$P_{lm}(\cos\theta) = \frac{1}{2^l l!}(1-\cos^2\theta)^{m/2}\frac{d^{l+m}}{d\cos\theta^{[l+m]}}(\cos^2\theta-1)^l$	$P_{lm}(\cos\theta) = \frac{(-1)^m}{2^l l!}(1-\cos^2\theta)^{m/2}\frac{d^{l+m}}{d\cos\theta^{[l+m]}}(\cos^2\theta-1)^l$
$\mathbf{G}_k(\mathbf{r},\mathbf{r}';t) = \mathbf{Q}_k^*(\mathbf{r})\mathbf{Q}_k(\mathbf{r}')\bar{g}(t)\wedge_k$	$\mathbf{G}_k(\mathbf{r},\mathbf{r}';t) = (i\nu_k)^{-1}\mathbf{s}_k(\mathbf{r})\mathbf{s}_k^*(\mathbf{r}')\mathrm{e}^{i\nu_k t}$
$\mathbf{Q}_k(\mathbf{r}) = y_{1n}(r)\hat{\mathbf{e}}_r Y_{lm}(\theta,\phi) + y_{3n}(r)\nabla_1 Y_{lm}(\theta,\phi)$	$\mathbf{s}_k(\mathbf{r}) = U_k(r)\hat{\mathbf{e}}_r Y_{lm}(\theta,\phi) + \kappa^{-1}V_k(r)\nabla_1 Y_{lm}(\theta,\phi)$
$\int_V \mathbf{Q}_k(\mathbf{r})\mathbf{Q}_k^*(\mathbf{r})(\mathbf{r})\rho_0(r)dV = \Omega_{ml} I_n^S$	$\int_\otimes \rho^0 \mathbf{s}_k \cdot \mathbf{s}_k' dV = \delta_{kk'}$
$I_n^S = \int_0^a (y_{1n}^2 + l(l+1)y_{3n}^2)\rho(r)r^2 dr$	-

To further compare the solution revisited in this study with Ben-Menahem (1983), we will estimate the values of three components of the displacement from (4.39) to (4.41) with the function $f^m(e,\lambda,\nu)$ defined as (4.44). We focus on the ${}_0\mathrm{S}_2$ normal mode and the monochromatic source at the resonance frequency $\omega_g = \omega_k$ with the sensor position at the equator, i.e. at $\{\theta = \frac{\pi}{2}, \phi = \frac{\pi}{2}\}$, and source angles $\{e = \frac{\pi}{2}, \lambda = 0, \nu = 0\}$, which gives

$$f_b^m(e,\lambda,\nu) = \sqrt{\frac{\pi}{5}}\delta_{m,0} - i2\sqrt{\frac{\pi}{15}}\delta_{m,1} + \sqrt{\frac{\pi}{15}}\delta_{m,-2}. \tag{4.71}$$

The eigenfunctions and eigenfrequencies for a spherically symmetric, non-rotating Earth model are calculated for a transversely isotropic PREM model (Dziewonski and Anderson, 1981), modified for the oceanless case, using MINEOS software package (Woodhouse, 1988; Masters et al., 2011). These calculations are later used for obtaining the constant value $\hat{\zeta}_k$ given by (4.37). Further, we consider that an idealized accelerometer responds to the perturbation in gravitational potential and free-air change in the gravity in addition to the particle acceleration. These corrections are accounted for by replacing the PREM eigenfuntions U_k, V_k by $\bar{U}_k = U_k + \omega_k^{-2}2a^{-1}gU_k + (l+1)\omega_k^{-2}a^{-1}P_k$ and $\bar{V}_k = V_k - \kappa\omega_k^{-2}a^{-1}gU_k - \kappa\omega^{-2}a^{-1}P_k$, where P_k is the gravitational potential (Ashby and Dreitlein, 1975; Boughn and Kuhn, 1984; Dahlen and Tromp, 1998; Coughlin and Harms, 2014b) and g the gravity at the surface. Thus, we have

$${}_0\bar{U}_2 = {}_0U_2 + ({}_0\omega_2)^{-2}2a^{-1}g\ {}_0U_2 + 3({}_0\omega_2)^{-2}a^{-1}{}_0P_2 \tag{4.72}$$

$${}_0\bar{V}_2 = {}_0V_2 - \sqrt{6}({}_0\omega_2)^{-2}a^{-1}g\ {}_0U_2 - \sqrt{6}({}_0\omega_2)^{-2}a^{-1}{}_0P_2 \tag{4.73}$$

$$\begin{aligned} {}_0s_{2,r} = \sum_m {}_0s_{2,r}{}^m &= h_0\ {}_0\alpha_2\ {}_0\bar{U}_2 \sum_m \mathcal{Y}_{2m}(\theta,\phi)\ \Re\{f_b^m(e,\lambda,\nu)\bar{g}(t)\} \\ &= -\frac{1}{4\pi}h_0\ {}_0\alpha_2\ {}_0\bar{U}_2 \frac{{}_0\omega_2 \sin{}_0\omega_2 t - {}_0\gamma_2 \cos{}_0\omega_2 t}{{}_0\gamma_2({}_0\omega_2{}^2 + {}_0\gamma_2{}^2)}, \end{aligned} \tag{4.74}$$

$$ {}_0s_{2,\theta} = \sum_m {}_0s_{2,\theta}{}^m = -\frac{1}{\pi 2\sqrt{6}} h_0 \, {}_0\alpha_2 \, {}_0\bar{V}_2 \, \frac{{}_0\gamma_2 \sin {}_0\omega_2 t + {}_0\omega_2 \cos {}_0\omega_2 t}{{}_0\gamma_2({}_0\omega_2{}^2 + {}_0\gamma_2{}^2)}, \tag{4.75} $$

$$ {}_0s_{2,\phi} = \sum_m {}_0s_{2,\phi}{}^m = 0. \tag{4.76} $$

Using the values from Table 4.3 we calculate the radial and tangential displacements (4.74) and (4.75) depending on the GW source amplitude h_0 and for $t = 0$. The values are then multiplied by the radius of the Earth (a =6371 km) to account for the normalization and by 10^9 to convert from meters to nanometers, thus we have

$$ \begin{aligned} {}_0s_{2,r} &\approx 6.9 \cdot 10^{13} h_0 \text{ nm} \approx 6.9 \cdot 10^{-8} \text{ nm}, \\ {}_0s_{2,\theta} &\approx 2.5 \cdot 10^{16} h_0 \text{ nm} \approx 2.5 \cdot 10^{-5} \text{ nm}. \end{aligned} \tag{4.77} $$

Further, we can calculate the acceleration by multiplying by ${}_0\omega_2{}^2$

$$ \begin{aligned} {}_0a_{2,r} &\approx 2.6 \cdot 10^{8} h_0 \text{ nm/s}^2 \approx 2.6 \cdot 10^{-13} \text{ nm/s}^2, \\ {}_0a_{2,\theta} &\approx 9.6 \cdot 10^{10} h_0 \text{ nm/s}^2 \approx 9.6 \cdot 10^{-11} \text{ nm/s}^2. \end{aligned} \tag{4.78} $$

where we set $h_0 = 10^{-21}$ for the representation purpose only, since this was the strain value obtained at the recent first observation of GW (Abbott et al., 2016). However, in the mHz frequency band we expect to have different strain values for the binary black hole mergers.

Tab 4.3: MINEOS normalized values of the eigenfunctions U, V, P at the Earth surface $r = a$, frequency ω, quality factor Q for ${}_0\mathrm{S}_2$ and gravity value at the surface g. Used normalization for length is $R = 6371$ km, time $\frac{1}{\pi G \rho_a}$ and mass $\rho_a R^3$, where $G = 6.67408 \cdot 10^{-11}$ m^{3}kg^{-1}s^{-2} is the gravitational constant and $\rho_a = 5515.0$ kgm^{-3} is the average density.

$U(a)$	$V(a)$	$P(a)$	ζ	ω	Q	g	a
1.329	0.030	-0.847	0.273	1.807	509.648	1.333	1

For the same mode, Ben-Menahem's calculations in Ben-Menahem (1983) consisted of the same set of source angles, but with the sensor position at $\{\theta = 0, \phi = 0\}$. Further, for the resonance and $h_0 = 10^{-21}$ he found that the values for the horizontal displacement may reach the level of ${}_0s_{2,\theta,0}\, s_{2,\phi} \approx 10^{-8}$ cm $= 0.1$ nm, which gives ${}_0a_{2,\theta,0}\, a_{2,\phi} \approx 3.6 \cdot 10^{-7}$ nm/s^2, four orders of magnitude bigger than estimated in this study. However, this result should not be directly compared to our estimate because we do not use the same source type and therefore not the same source-time function. Ben-Menahem used a finite monochromatic wave source whereas we use an infinite monochromatic wave source. Only by considering a different source-time function there is already a difference of four orders of magnitude. Additionally, our source-time function definition for an infinite monochromatic source definition differs from the one in Ben-Menahem (1983), because our definition of the Green tensors differs. We also checked Ben-Menahem's calculations by using his equations

and approximations. For an infinite monochromatic source we obtain ${}_0u_\theta = 1.6 \cdot 10^{-6}$ nm and ${}_0a_\theta = 1.4 \cdot 10^{-13}$ nm/s^2, one order of magnitude smaller than our estimate. We believe that this order of magnitude difference still comes from a different definition of the source-time functions. Also, a significant difference is that in Ben-Menahem (1983) calculations are done for Jeffreys-Bullen and Gutenberg-Bullard Earth models (Ben-Menahem et al., 1971), whereas we use the PREM model.

When one talks about the signal detection at the Earth surface one should consider two factors, the first one is the instrument precision and stability and the other is the environmental noise level (Rosat and Hinderer, 2018). Only by combining all these information together with the possible detection threshold we can resolve the estimation of elusive signals, like GW signals. The minimal envelope of the environmental seismic noise may be represented by the widely used New Low Noise Model (NLNM) (Peterson, 1993). This model was developed empirically by taking the lowest noise levels recorded on the $\approx$ 10-day-long vertical components at 75 stations, after all earthquakes and transients were removed. The NLNM corresponds then to the lower envelope of power spectral densities (PSDs) calculated for all available seismometers. To answer a question how large the monochromatic signal needs to be to be detectable when embedded in the noise, we need to obtain a rough estimate of the noise standard deviation that represents the seismic background noise. This values is obtained from the PSD defined with NLNM. The PSD is frequency dependent and to define noise standard deviation from the PSD we can use the definition

$$\sigma^2 = \int_{f-\Delta f/2}^{f+\Delta f/2} P(f) df, \tag{4.79}$$

where σ^2 is variance of the signal in the frequency band Δf and $P(f)$ is frequency dependent PSD. Thus, if we integrate PSD over the frequency band of interest we can obtain the variance of the signal in that band. Therefore, if the PSD is constant near the frequency f we obtain

$$\sigma^2 = P(f)\Delta f. \tag{4.80}$$

Therefore, the variance of the signal in question depends on the frequency band-width. There is no exact answer what is the band-width of the target signal. In the case of the ${}_0S_2$ mode we can either take the splitting width which is $\Delta f = 20$ μHz or the width of the individual singlet broaden due to its Q-factor which would be $\Delta f = 5$ μHz. Since the NLNM is flat in the mHz band around ${}_0S_2$ frequency we set $P(f) = -151.88$ dB and this gives us

$$\sigma_{NLNM} = \sqrt{10^{-\frac{-151.88}{10}}}\sqrt{\Delta f}. \tag{4.81}$$

Considering (4.81) we can calculate the noise standard deviations when frequency band-width is define for entire multiplet or one singlet, presented in Tab. 4.4.

Tab 4.4: Estimate of the noise standard deviations for the frequency band-width of entire multiplet and one singlet for ${}_0S_2$ mode and the fixed PSD value of the NLNM.

	Δf	σ_{NLNM}
multiplet	20 μHz	$1.1390 \cdot 10^{-10}$
singlet	5 μHz	$5.6949 \cdot 10^{-11}$

With the PSD of the white noise defined as $\mathrm{PSD}_{\mathrm{noise}} = \sigma^2 T_0$ (where σ is noise standard deviation and T_0 is sampling interval) and the PSD of undamped harmonic signal defined as $\mathrm{PSD}_{\mathrm{signal}} = \frac{A^2 N T_0}{4}$ (where N is number of data points, A is amplitude of the signal), our signal amplitude needs to satisfy the relation $A > \frac{2\sigma}{\sqrt{N}}$ to be visible in the noisy data. Thus, to detect the radial component (4.78) buried in the noisy time series with standard deviations defined as in Tab. 4.4, one would need either $L = N\Delta t > \left(\frac{2\sigma_{NLNM}}{{}_0a_{2,r}}\right)^2 \Delta t > 1.46 \cdot 10^{18}$ years (multiplet band-width) or $3.65 \cdot 10^{17}$ (singlet band-width) years, if we set $\delta t = 60$ s. One can look at this differently and say that for this particular noise standard deviation and 10 years of recorded data and $\Delta t = 60$ s (thus $N = 5256000$), one would need the GW amplitude signal to be larger than either $h_0 > \frac{2\sigma_{NLNM}}{a_0\sqrt{N}} > 3.8 \cdot 10^{-13}$ (multiplet band-width) or $h_0 \approx 1.9 \cdot 10^{-13}$ (singlet band-width) to be detected on Earth, where ${}_0a_{2,r} = a_0 h_0 = 0.26 h_0$ m/s^2. These estimates are indicating how difficult is to measure the GW induced signal on Earth.

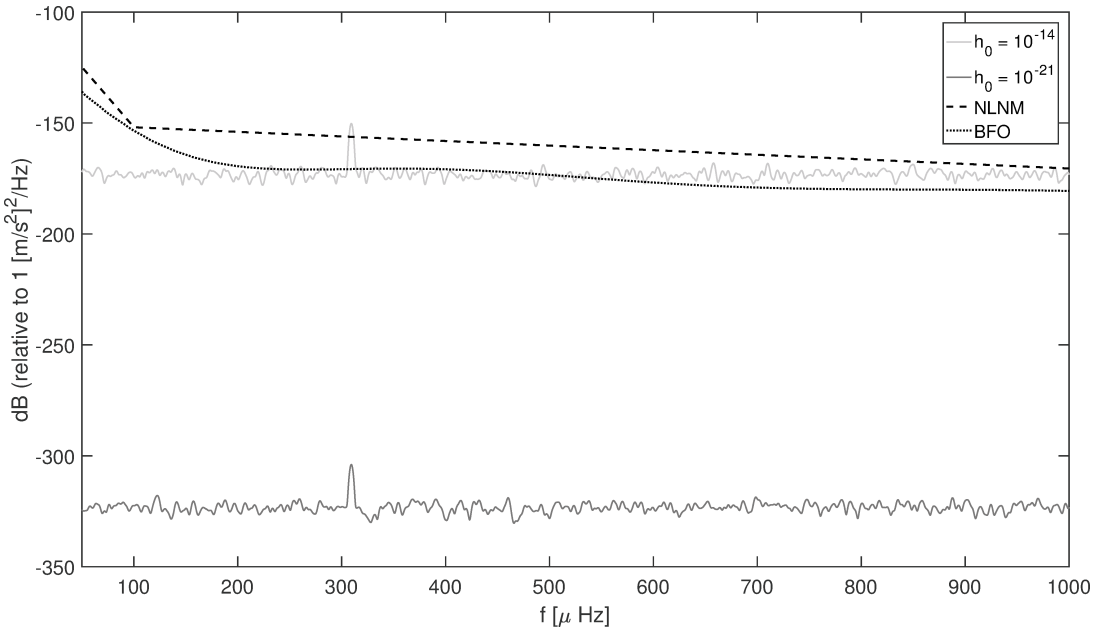

Fig 4.3: Comparison in terms of power spectral densities between NLNM model, observed acceleration signal at the BFO (Germany) station and synthetic noisy signals (4.74) obtained by stacking 209 stations for ${}_0S_2$ and m=-2. Dark grey signal is obtained for $h_0 = 10^{-21}$ and with the standard deviation of injected white noise adjusted to allow for the signal to emerge from the noise. It was achieved with the rms value of NLNM model for frequency bandwidth 20 μHz (see Tab. 4.4), but reduced by seven orders of magnitude. Light grey signal is obtained for the level of the noise set to match rms value of NLNM model. The value of h_0 is increased until the signal emerges from the noise. That is achieved for $h_0 = 10^{-14}$.

In Fig. 4.3 we show the PSD of the signal (4.74) obtained by stacking 209 synthetic resonances computed at stations from seismometer and superconducting gravimeter networks for ${}_0S_2$ and $m = -2$. Signal at each station depends on the station colatitude and longitude, GW amplitude which is set to $h_0 = 10^{-21}$ and is obtained for 19 days with $\Delta t = 60$ s. The noise level is primarily set to the value estimated above, $\sigma_{NLNM} = 1.1390 \cdot 10^{-10}\mathrm{m/s^2}$. Since, this high noise level completely prevails the signal, we start reducing the noise till our signal emerges from the noise. In the mentioned configuration the emerged signal is reached with $\sigma_{NLNM} = 3.6018 \cdot 10^{-18}\mathrm{m/s^2}$, seven orders of magnitude smaller than the first set. The stacking was performed with the optimal sequence estimation (Ding and Shen, 2013a), based on the assumption that displacement on the Earth's surface is decomposed in spherical harmonics. On the same figure we plot the PSD value for the NLNM model and PSD for the Black Forest Observatory station, the quietest station (Rosat and Hinderer, 2011). It is clear that the GW signal is far below the detection level, which is already stated in the paragraph above. In the next example, showed on the same figure, we calculate the stacked signal with the noise standard deviation $\sigma_{NLNM} = 1.1390 \cdot 10^{-10}\mathrm{m/s^2}$, and we

increase GW source amplitude h_0 until the signal emerges from the noise. This is finally reached with $h_0 = 10^{-14}$ for 19 day long signals. This estimate achieved by stacking a large number of time-series is one order of magnitude smaller than the one estimated in the previous paragraph. However this is still 4 orders of magnitude bigger than the expected GW source amplitudes in the mHz band ($\approx 10^{-18}$) for possible astrophysical sources (Moore et al., 2015). It should be noted that this estimates could be improved by considering longer time series. This is because the induced displacement is the forced solution, therefore by following the signal for longer than 19 days we would have better detection.

Besides NLNM, there is a more recent noise model proposed by Berger et al. (2004) (further BLNM), where 118 Global Seismograph Network stations were analyzed in the duration of one year. The analysis was performed on vertical and horizontal components and data were not scrutinized for earthquakes and transients or any other variation. As such, the envelope of the first percentile of the empirical distribution for all station and channels is lower than NLNM for frequencies < 2.5 Hz. The noise standard deviation for BLNM with sampling period of 10 s and vertical component is $\sigma_{BLNM} = 6.92 \cdot 10^{-10}\text{m/s}^2$ (-173.2 dB). The conclusion above is similar, since the improvement by one order of magnitude for σ_{NLNM}, is not significantly sufficient. For horizontal displacement the standard deviation for $T_0 = 10$ s is one order smaller, being $\sigma_{BLNM} = 6.10 \cdot 10^{-9}\text{m/s}^2$ (-154.3 dB). This means that for 10 years one would need GW amplitude to be larger than $h_0 > 10^{-13}$ to be detected on Earth. There are two more noise models, one proposed by McNamara and Buland (2004) and the other by Castellaro and Mulargia (2012), however they do not consider the lowest normal mode frequency band and therefore they could not be considered in this study.

From his flat-Earth model filled with a uniform isotropic elastic medium in the 1-Hz frequency band Dyson (1969) calculated the horizontal displacement for a horizontally incident GW to be $2 \cdot 10^{-17}$ cm $= 2 \cdot 10^{-10}$ nm, which was the same result derived by Weber (1968) and Dozmorov (1976b). This value is five orders of magnitude smaller than ours, which is not surprising since Dyson pointed out that his estimation might be pessimistic because this estimate involved several assumptions that could be wrong by several orders of magnitude, such as the type of source, the absence of the reflection or the resonance effects in the seismic response. Recalculating Dyson's values, De Sabbata et al. (1970) arrived at $1.4 \cdot 10^{-12}$ cm $= 1.4 \cdot 10^{-5}$ nm for the peak displacement, just by considering different values for the incoming GW flux and Q-factor, and these values are already comparable with (4.77). Several studies search for seismic signals at pulsar frequencies but without success (Wiggins and Press, 1969; Sadeh and Meidav, 1972; Mast et al., 1974). General conclusions were that the detection of such small signals is limited by Earth intrinsic noise and the short data series (Rundeko, 1994).

Many studies also provided the upper limits on the characteristic strain, the spectral energy density or dimensionless energy density of the GW stochastic backgrounds or GW burst (Forward et al., 1961; Weber, 1967; Zimmerman and Hellings, 1980; Boughn and Kuhn, 1984; Kravchuk et al., 1995). The level of the stochastic gravitational radiation is conventionally expressed as the energy density relative to the critical energy density, that is the energy density per logarithmic frequency interval, or as a characteristic rms strain (Maggiore, 2008). The most recent relevant estimation of the upper limit in the mHz band used an analytical solution of the Earth's normal modes for PREM model to calibrate normal mode amplitudes into GW strain data (Coughlin and Harms, 2014b). They estimated the upper limit of the GW energy density in the 0.035 - 0.15 Hz frequency band, normalized by the critical energy density of the Universe, to be between $\Omega_{\mathrm{GW}}({}_0\mathrm{S}_2) = 0.039$ to $\Omega_{\mathrm{GW}}({}_{13}\mathrm{S}_2) = 0.12$. These values translated into strain amplitude spectral density lie between $h_{GW}({}_0\mathrm{S}_2) = 2.2 \cdot 10^{-14}\mathrm{Hz}^{1/2}$ to $h_{GW}({}_{13}\mathrm{S}_2) = 6.2 \cdot 10^{-16}\mathrm{Hz}^{1/2}$. The authors stated this is still by a large amount above the predicted levels of the GW background from the cosmological models.

In our example above we focus on the resonance effect between GW and only one normal mode ${}_0\mathrm{S}_2$ by setting $\omega_g =_0 \omega_2$, however our results show that all the normal modes with the angular order $l = 2$ should be excited by the GW. To understand the relationship between the resonance effect between different modes we calculate the resonance response for hundred normal modes ($n = 0, ..., 99$) of angular order $l = 2$ (1 fundamental mode and 99 harmonics). The result, shown in Fig. 4.4, is calculated at the BFO station $(43.33°, 8.33°)$ for 30 day long time series with a constant h_0 set to 1 (for better visual clarity). We can see that some modes have higher resonance amplitudes than others, which makes them better candidates for the detection. To calculate the response of the Earth to the GW more precisely, one should consider the off-resonance modes as well. That is, the full excitation response should consider the sum of the resonance and the off-resonance normal modes (Boughn and Kuhn, 1984). It is expected that during the resonance between GW and a normal mode, the contribution of the mode in resonance is the largest contribution (due to the source-time function). However, this is true for the low frequencies modes, while the largest contribution for the high frequency modes is not necessarily coming from the mode in the resonance (Boughn and Kuhn, 1984). To demonstrate a relation between resonance and the off-resonance effect we plot in Fig. 4.5 the absolute amplitude values versus the radial order n. Each row on the y-axis represents the radial order for which the resonance was calculated, therefore $\omega_g =_n \omega_2$, and each column on the x-axis represents the absolute amplitude value of the radial order in the off-resonance regime. What we would expect is to have the largest value in the diagonal of this square, which would indicate that the largest

contribution comes form the mode in resonance. For example, from the figure, we can conclude that the first row on the y-axis stands for the values when $\omega_g =_0 \omega_2$ and in that case the largest contribution comes from ${}_0S_2$. Unlike the case before, for the row six on the y-axis, the largest contribution comes from column $n = 7$ on the x-axis and not $n = 6$, what is expected. This tells us that the prevailing factor in the amplitude is not the resonant frequency anymore, but other factors such as ${}_n\zeta_k$. For the reference we plot the values of ${}_nQ_2$-factors, ${}_nU_2$ eigenfunctions and ${}_n\zeta_2$ functions for all considered radial orders in Fig. 4.6. In the case considered above, since the factor defined by the resonance is order of 10^{-2} for ${}_6S_2$ and 10^{-3} for ${}_7S_2$ the prevailing factor becomes the product of two values ${}_n\zeta_{2n}U_2$ that are 0.008 and 2.295, respectively. Therefore when calculating the response of the Earth to the incoming GW it is more correct to include both the resonance and off-resonance effects. In reality it is hardly possible that the GW would have the exact frequency of the normal mode, consequently the full off-resonance effect should be considered. Thenceforth, the response should definitely consists of the sum of the normal modes closest to the GW frequency as well as other modes.

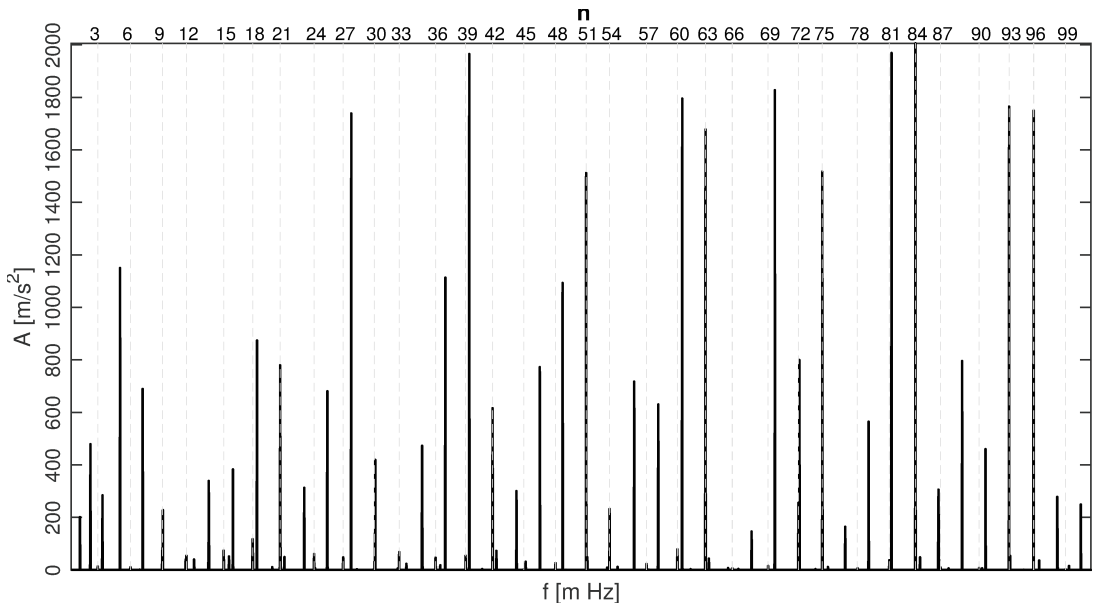

Fig 4.4: Resonance excitation of the Earth's normal modes due to monochromatic GW passing through Earth. Each frequency spike represent a resonance for a different radial order of a quadrupole mode. The light grey lines represent the normal mode frequency as a function of the radial order n indicated above the figure.

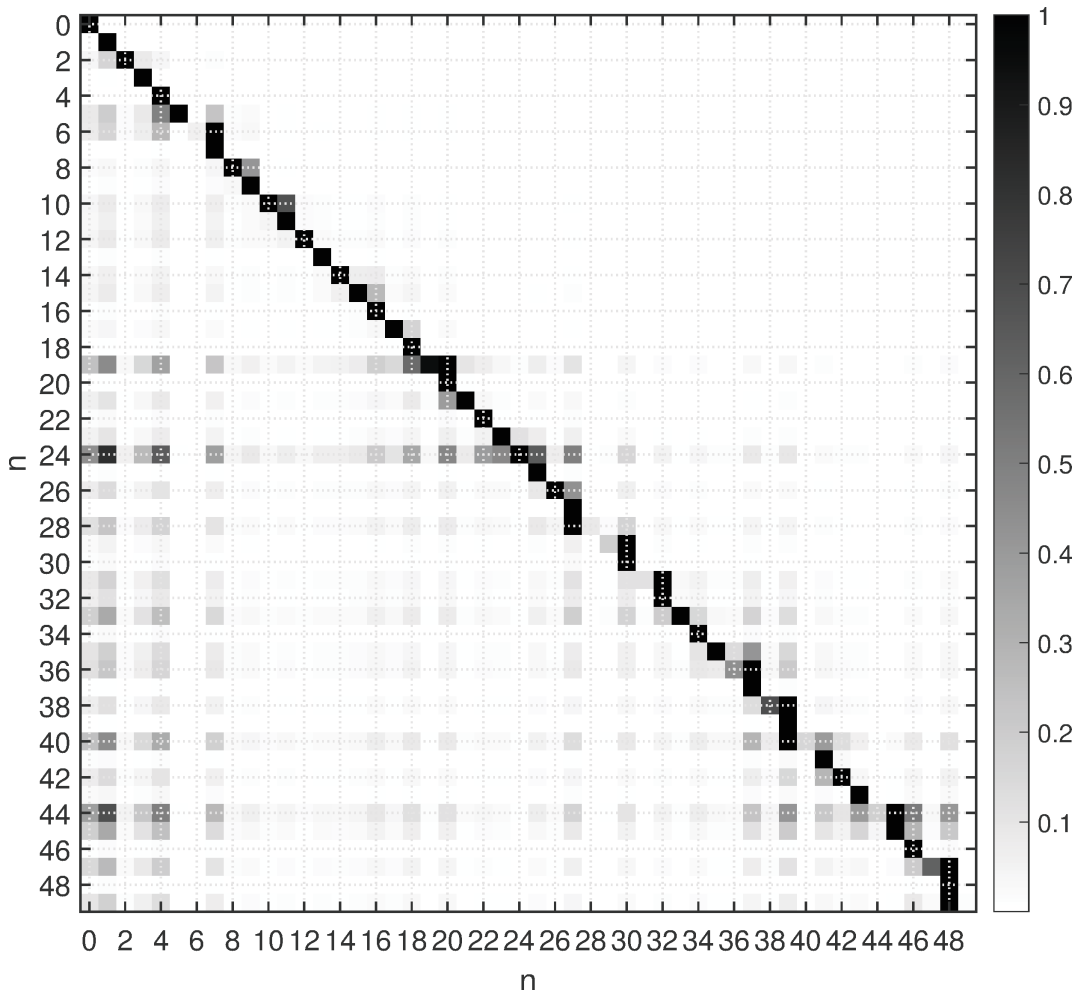

Fig 4.5: Absolute amplitude values for resonance and off-resonance modes. Each row on y-axis labelled by n represents the radial order of ${}_{\mathrm{n}}\mathrm{S}_2$ mode in resonance, for which $\omega_g =_0 \omega_2$, while each column on x-axis also labelled by n represents modes that are in the off-resonance regime. Each row is normalized with the largest value in that row. The black color represent the normal mode with the largest contribution.

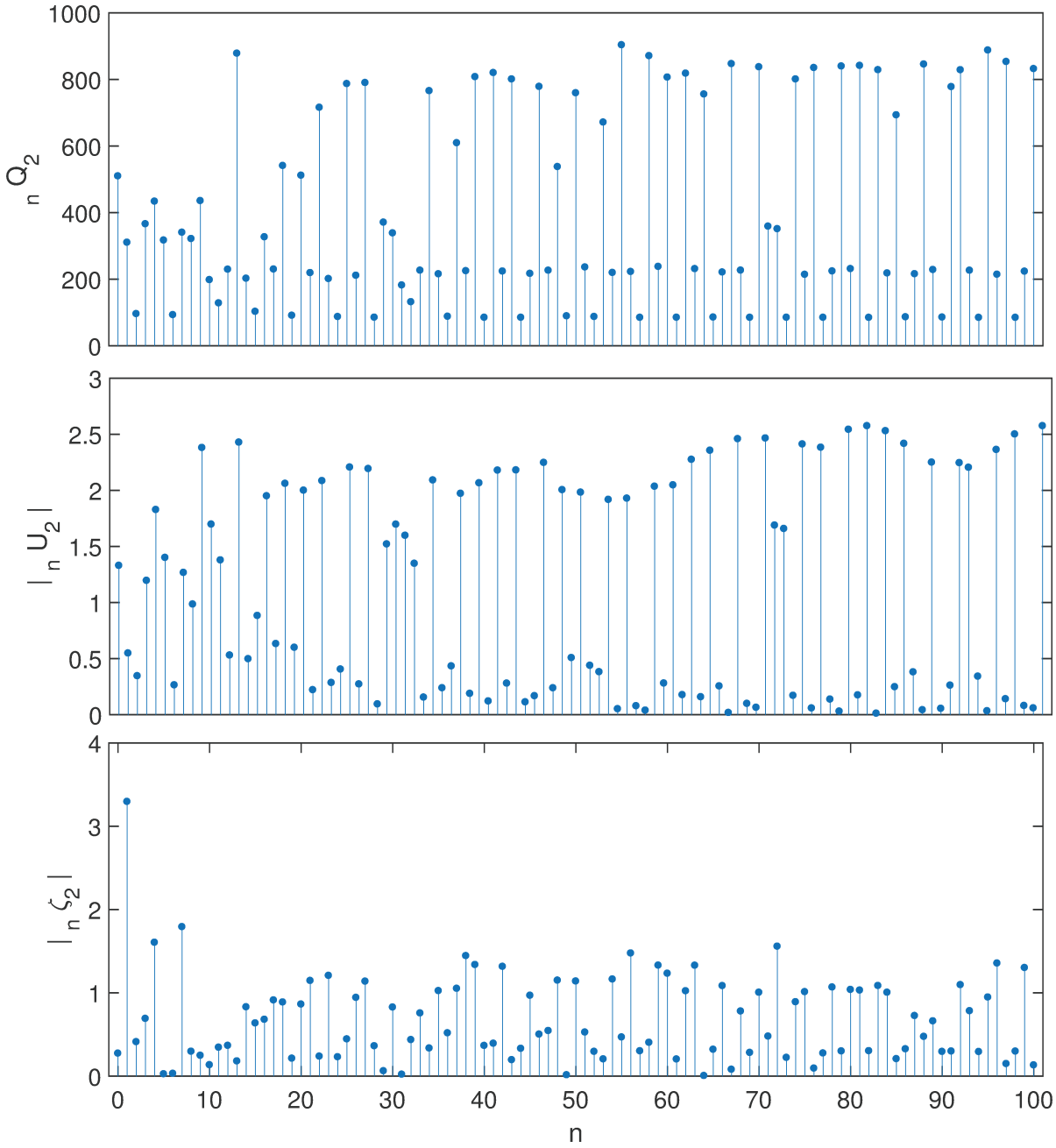

Fig 4.6: Values for ${}_nQ_2$-factors (up), ${}_nU_2(r=a)$ eigenfucntions at the free surface (middle) and ${}_n\zeta_2$ functions (bottom) for $n = 0, ..., 99$ radial orders and $l = 2$.

Theoretically, Earth resembles a spherical resonant-mass detector. It is argued that performances of the spherical resonant-mass detectors could improve the detection of GWs as compared to the resonant bars (Zhou and Michelson, 1995; Lobo, 1995; Maggiore, 2008). Firstly, due to their bigger mass they have a larger cross section for the absorption of GWs and hence a better sensitivity. Secondly, a sphere does not have a preferable orientation and offers a full sky coverage, unlike other detectors which have blind directions. Thirdly,

using the information about the excited quadrupolar modes it is possible to reconstruct the arrival direction and polarization of GW. Weber (1967) gave an estimate of the Earth cross section to be 10^4 m^2. Ruffini and Wheeler (1971) estimated the resonance integral of the absorption cross section for radiation incident from random directions and with random polarizations for a fluid globe model. This globe, held in a shape of a sphere by only gravitational forces, has a uniform density with an average value of 5.517 g/cm^3 and thus the quadrupole vibration period of 94 min. To roughly estimate the resonance integral for the Earth model with a quadrupolar vibration period of 54 min, they adjusted the moment tensor for the two models and arrived to an absorption cross section value of 4.7 cm^2 Hz. By comparison, the cross-section of the spherical resonant-mass detector, with the diameter of 3.2 m, mass of $4.6 \cdot 10^4$ kg and frequency of 840 Hz, has a resonance absorption cross section of $8.7 \cdot 10^{-20}$ cm^2 Hz (Zhou and Michelson, 1995), which is much smaller than the Earth's cross-section. Furthermore, all spherical resonant-mass detectors have relatively small sizes and thus are suitable for the exploration of high frequencies regions, unlike Earth where we could explore the mHz frequency band.

The detection of elusive signals, such as GW, is a problem consisting of several parts. It depends on the instrument precision, the ubiquitous environmental noise, the modeling of the signal we want to find and techniques performed for the search. Considering the specific problem in this study, that is detecting the GWs using the resonance effect between GWs and the normal modes of Earth in the gravimetric and seismic data, not all categories aforementioned have been fully scrutinized. What we know, from the geophysical perspective, is that the instruments with the best sensitivity in the 0.3 - 1 mHz band are superconducting gravimeters (Widmer-Schnidrig, 2003; Rosat and Hinderer, 2011), whose nominal sensitivity is generally referred to as 1 nGal= 10^{-11}m/s^2 (Hinderer et al., 2007). Also, it has been shown that instrumental self-noise is not the main issue in the detection threshold, but the environmental noise and many geophysical processes, such as seismic, atmospheric and tidal perturbations, that have not been reduced from gravimetric and seismic data (Rosat and Hinderer, 2018). This problem is substantial and complex, since it is more difficult to control and model unknown geophysical processes than to just compensate them, such as in the case of the laser interferometrical free mass antenna procedure. For this purpose it would be really interesting to use seismic noise compensation in the laser interferometry for the study of geophysical processes that produce it (Rundeko, 1994). Therefore, it is only reasonable to claim that to this day we are still only able to measure existing geophysical effects and estimate a new upper limit on the GW. One recent study (Mulargia and Kamenshchik, 2016) supported the idea of the whole Earth as a detector of the GW by utilizing the network of thousand of seismometers as a single gravitational antenna. They showed

that in the frequency range 0.1-10 Hz it is possible to resolve absolute strains $h \lessapprox 10^{-17}$ on burst gravitational pulses and $h \lessapprox 10^{-21}$ on periodic signals. However this does not comply with theoretical predictions for the cosmic gravitational radiations.

4.2.5 Conclusion

In this section we revisited the theoretical equations describing the interaction between Earth and GWs of astrophysical origin. This modeling is roughly based on several hypotheses. Firstly, GWs are monochromatic waves described by a source scalar value, a polarization tensor and a propagating vector. Secondly, the Earth is a non-rotating and anelastic body. Thirdly, the set-up is in the Earth's reference system. Fourthly, GWs are considered as a trigger of the Earth's normal modes, therefore they are represented as a force term in the Green tensor formalism. The derivation and analysis have shown that due to the fact that the GW tensor $h_{\mu\nu}$ is traceless and symmetric the only normal modes that couple with the GW are the ones with the degree $l = 2$. Also, the spheroidal induced displacement depends on the source scalar value h_0, the displacement eigenfunction $\mathbf{s}_k$ and a constant ζ_k, both depending on the Earth model, the source-time function $\bar{g}(t)$ and the three angles function $f^m(e, \lambda, \nu)$ defining the incoming GW in the Earth reference system. Specific configuration of the GW angles $f^m(e, \lambda, \nu)$ triggers specific singlets within the ${}_{\mathrm{n}}\mathrm{S}_2$ multiplet, and thus having information about individual singlets is giving us information about the position of the GW source in the sky. Considering the comparison between the resonant and off-resonant modes of low and high frequencies, it is shown that the low-frequency resonant modes have a larger response than the high-frequency modes and clearly the contributions of the low-frequency modes could be used exclusively in the computation of the induced displacement. However, it seems more reasonable to always consider the sum of all off-resonant modes near the frequency of the incoming GW to have a more representative solution.

Considering the measurements of the gravitationaly triggered normal modes, published values and the one in this study, show us that we are still obscured by the seismic noise of the geophysical origin. Even though instruments with appropriate sensitivity may exist, environmental noise will be a limiting factor. With the new era approaching new instruments of low-frequency sensitivity are developed, among others superconducting gravity gradiometers (SGG) (Griggs et al., 2017) and atom interferometers (Geiger et al., 2015; Canuel et al., 2018). These instruments have promising standpoint with improved sensitivities over their predecessors. However, the problem of the unknown geophysical processes present in data still remains.

The represented modeled interaction between Earth and GWs is restrained by some basic assumption and can be improved. Those upgrades concern the fact that if we want to scrutinize more realistic GW sources we should not be restrained by the Earth reference system. Therefore, in the next section we study the transformation from the celestial reference systems to the terrestrial reference system and how this is affecting our final induced spheroidal displacement. This introduces some effects that we have ignored, like Earth's rotation and its associated effects, which may become important.

4.3 Celestial Reference System and Anelastic, Rotating Earth Model

In this section we develop a new model of the interaction between GWs and Earth in terms of the normal modes. The analytical model is developed for a radially heterogeneous elliptical rotating model. For the GW sources we consider the double white-dwarf binary stars, therefore our source is now defined in the celestial reference system. Using The rotating Earth model implies considering the splitting of and coupling between multiplets that constitute the induced displacement. This section is organized as follows: firstly, we develop the rotating matrix that translates the source from the celestial reference system to the terrestrial reference system, secondly, we define the metric perturbation of the binary star system; thirdly, we define a Green tensor for a rotating, anelastic Earth that is going to use to develop the induced response; fourthly, we developed the induced spheroidal response due to incoming GWs from the double white-dwarf binary stars; fifth, we discuss the newly developed analytical model.

4.3.1 Rotation matrix from Celestial to Terrestrial Reference System

The equatorial coordinate system or the celestial coordinate system is a reference frame widely used to specify position of the celestial objects. The source location in the equatorial system is specified in terms of its right ascension α and declination δ angles. By specifying these two angles we define $\hat{\boldsymbol{k}}$. To assign a reference basis to each sky position, additionally we define vectors $\hat{\boldsymbol{i}}$ and $\hat{\boldsymbol{j}}$. We can require that $\hat{\boldsymbol{i}}$ is parallel to the celestial equator, i.e. perpendicular to the direction of the Earth's axis. We choose $\hat{\boldsymbol{i}}$ to point in the direction of decreasing right ascension, so that the third vector $\hat{\boldsymbol{j}} = \hat{\boldsymbol{k}} \times \hat{\boldsymbol{i}}$ points into the Northern Celestial Pole (Fig. 4.7).

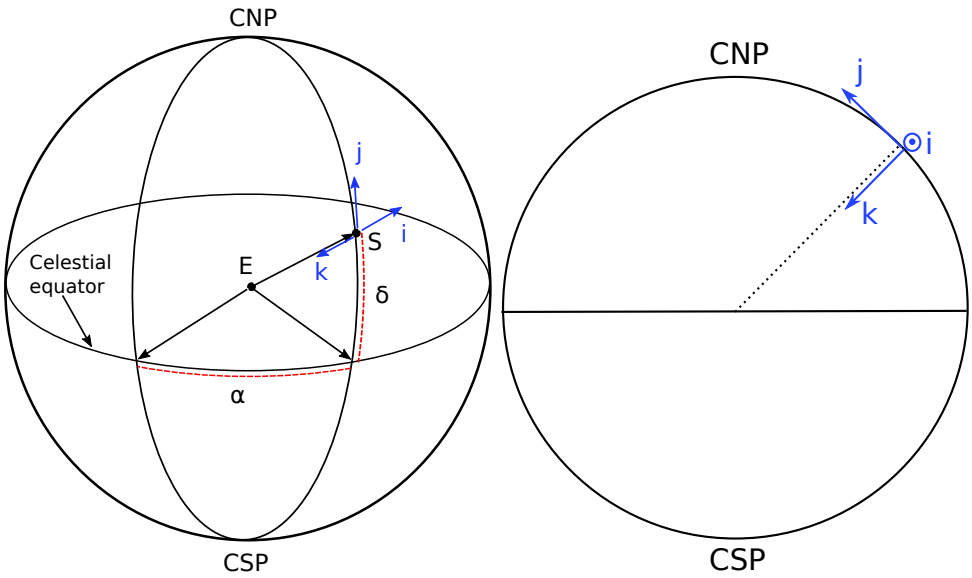

Fig 4.7: Celestial reference system where CNP stands for Celestial Northern Pole and CSP for Celestial Southern Pole. On left, E stands for Earth and S for star system. The right ascension α and declination δ angles are marked, together with three vectors $\hat{\boldsymbol{k}}$, $\hat{\boldsymbol{i}}$, $\hat{\boldsymbol{j}}$ that form the orthogonal basis in the celestial reference system. On right, the same orthogonal basis in side view. The vector $\hat{\boldsymbol{k}}$ points from a star system to the center of the celestial reference system, $\hat{\boldsymbol{i}}$ is parallel to the celestial equator and point in the direction of decreasing right ascension.

Using the unit vectors $\hat{\boldsymbol{i}}$ and $\hat{\boldsymbol{j}}$ we can construct a reference polarization basis for the traceless symmetric tensors that are transverse to $\hat{\boldsymbol{k}}$:

$$\begin{aligned} \boldsymbol{\varepsilon}_+ &= \hat{\boldsymbol{i}}\hat{\boldsymbol{i}}^{\mathrm{T}} - \hat{\boldsymbol{j}}\hat{\boldsymbol{j}}^{\mathrm{T}}, \\ \boldsymbol{\varepsilon}_\times &= \hat{\boldsymbol{i}}\hat{\boldsymbol{j}}^{\mathrm{T}} + \hat{\boldsymbol{i}}\hat{\boldsymbol{j}}^{\mathrm{T}}. \end{aligned} \tag{4.82}$$

Vectors $\hat{\boldsymbol{l}}$ and $\hat{\boldsymbol{m}}$ that we used to define polarization tensors in Section 4.1 lie in the same plane as $\hat{\boldsymbol{i}}$ and $\hat{\boldsymbol{j}}$ vectors. The reference basis is positioned relative to the natural basis using the angle between $\hat{\boldsymbol{i}}$ and $\hat{\boldsymbol{l}}$, measured counter-clockwise around $\hat{\boldsymbol{k}}$ (see Fig. 4.8), therefore we have

$$\begin{aligned} \hat{\boldsymbol{l}} &= \hat{\boldsymbol{i}}\cos\psi + \hat{\boldsymbol{j}}\sin\psi, \\ \hat{\boldsymbol{m}} &= -\hat{\boldsymbol{i}}\sin\psi + \hat{\boldsymbol{j}}\cos\psi. \end{aligned} \tag{4.83}$$

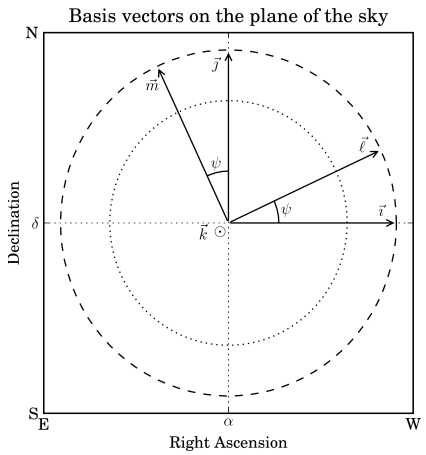

Fig 4.8: Rotation of the natural polarization unit vectors $\hat{\boldsymbol{l}}$ and $\hat{\boldsymbol{m}}$ respect to the reference polarization unit vectors $\hat{\boldsymbol{i}}$ and $\hat{\boldsymbol{j}}$ via (4.83). The polarization angle ψ is measured from $\hat{\boldsymbol{i}}$ to $\hat{\boldsymbol{l}}$, counter-clockwise around $\hat{\boldsymbol{k}}$. (From Whelan (2013)).

We can substitute (4.83) into (4.6) to get $\boldsymbol{e}_+$ and $\boldsymbol{e}_\times$ in terms of $\boldsymbol{\varepsilon}_+$ and $\boldsymbol{\varepsilon}_\times$

$$\begin{aligned} \boldsymbol{e}_+ &= \boldsymbol{\varepsilon}_+ \cos 2\psi + \boldsymbol{\varepsilon}_\times \sin 2\psi, \\ \boldsymbol{e}_\times &= -\boldsymbol{\varepsilon}_+ \sin 2\psi + \boldsymbol{\varepsilon}_\times \cos 2\psi. \end{aligned} \tag{4.84}$$

This shows that we need three angles to associate particular source to the polarization basis: the right ascension angle α and the declination angle δ, for the sky position and to define the propagation vector $\hat{\boldsymbol{k}}$, and an additional polarization angle ψ to define orientation of the basis $\{\boldsymbol{e}_+, \boldsymbol{e}_\times\}$ relative to some reference basis $\{\boldsymbol{\varepsilon}_+, \boldsymbol{\varepsilon}_\times\}$.

Since measurement in this study are performed on Earth, the reference basis needs to be expressed in the terrestrial reference system. A convenient basis for this is the one fixed to the Earth system: the unit vector $\hat{\boldsymbol{e}}^*_{\boldsymbol{3}}$ points parallel to the Earth's axis, from the center of the Earth to the North Pole; the unit vector $\hat{\boldsymbol{e}}^*_{\boldsymbol{1}}$ points from the center of the Earth to the point on the equator with 0° latitude and longitude. The remaining unit vector $\hat{\boldsymbol{e}}^*_{\boldsymbol{2}} = \hat{\boldsymbol{e}}^*_{\boldsymbol{3}} \times \hat{\boldsymbol{e}}^*_{\boldsymbol{1}}$ point from the center of the Earth to the point on the equator with latitude 0° and longitude 90°E. Next to this basis we need inertial basis with respect to the fixed stars: $\hat{\boldsymbol{e}}_{\boldsymbol{3}}$ points to the Celestial North Pole (which means $\hat{\boldsymbol{e}}^*_{\boldsymbol{3}} = \hat{\boldsymbol{e}}_{\boldsymbol{3}}$); the unit vector $\hat{\boldsymbol{e}}_{\boldsymbol{1}}$ points to the point with the declination $\delta = 0°$ and the right ascension $\alpha = 0$hr, i.e. the intersection of the ecliptic with the celestial equator known as the Vernal (March) Equinox; the third unit vector $\hat{\boldsymbol{e}}_{\boldsymbol{2}} = \hat{\boldsymbol{e}}_{\boldsymbol{3}} \times \hat{\boldsymbol{e}}_{\boldsymbol{1}}$ thus points to the point with $\delta = 0°$ and right ascension $\alpha = 6$hr (Whelan, 2013).

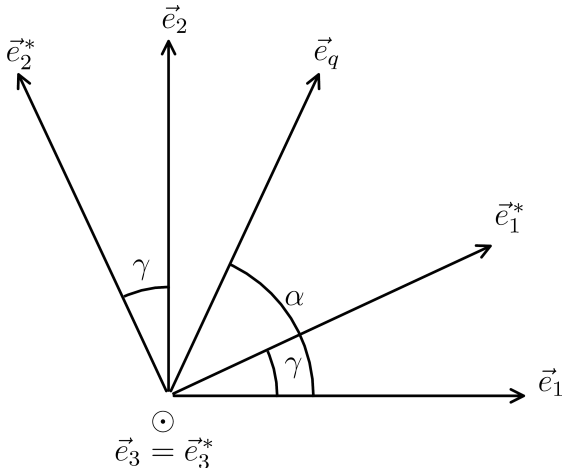

Fig 4.9: Relationship between the Earth-fixed system $\{\hat{\boldsymbol{e}}_1^*, \hat{\boldsymbol{e}}_2^*, \hat{\boldsymbol{e}}_3^*\}$ and the inertial system $\{\hat{\boldsymbol{e}}_1, \hat{\boldsymbol{e}}_2, \hat{\boldsymbol{e}}_3\}$ where $\hat{\boldsymbol{e}}_3^* = \hat{\boldsymbol{e}}_3$. Angle γ between these two systems is Greenwich Sidereal Time. Vector $\hat{\boldsymbol{e}}_q$ is the projection of the vector $\hat{\boldsymbol{k}}$ into the equatorial plane. (From Whelan (2013)).

The relationship between $\{\hat{\boldsymbol{e}}_1^*, \hat{\boldsymbol{e}}_2^*, \hat{\boldsymbol{e}}_3^*\}$ and $\{\hat{\boldsymbol{e}}_1, \hat{\boldsymbol{e}}_2, \hat{\boldsymbol{e}}_3\}$ is shown in Fig. 4.9. The relationship is defined by angle γ which corresponds to Sidereal Time. This angle increases by 24 hours, i.e. $360° = 2\pi$, every sidereal day of approximately 23 hours and 56 minutes. As the Earth rotates the starred unit vectors rotate in regards to the unstarred vectors. Vectors $\hat{\boldsymbol{e}}_1^*$ and $\hat{\boldsymbol{e}}_1$ coincide when the Sidereal Time at Greenwich is midnight. Therefore, we define angle γ to be the Greenwich Sidereal Time (GST) which is the angle from $\hat{\boldsymbol{e}}_1$ to $\hat{\boldsymbol{e}}_1^*$ measured counterclockwise around $\hat{\boldsymbol{e}}_3^*$. Therefore we have

$$\begin{aligned} \hat{\boldsymbol{e}}_1^* &= \hat{\boldsymbol{e}}_1 \cos\gamma + \hat{\boldsymbol{e}}_2 \sin\gamma, \\ \hat{\boldsymbol{e}}_2^* &= -\hat{\boldsymbol{e}}_1 \sin\gamma + \hat{\boldsymbol{e}}_2 \cos\gamma. \end{aligned} \tag{4.85}$$

To get the metric perturbation for an arbitrary sky point, we need to calculate components of $\hat{\boldsymbol{i}}$, $\hat{\boldsymbol{j}}$ and $\hat{\boldsymbol{k}}$ in a basis with given α and δ angles. We can then find $\hat{\boldsymbol{l}}$ and $\hat{\boldsymbol{m}}$ vectors for given ψ angle and using the reference matrices $\boldsymbol{\varepsilon}_{+,\times}$ obtain the natural polarization matrices $\boldsymbol{e}_{+,\times}$. The plane containing $\hat{\boldsymbol{e}}_3$ and $\hat{\boldsymbol{k}}$ is shown in Fig. 4.10. By projecting vector $\hat{\boldsymbol{k}}$ to the equatorial plane we can define unit vector $\hat{\boldsymbol{e}}_q$ from the observer to the source - pointing towards the point on the Celestial Equator with right ascension α, which also lies in the same plane. Since δ is the angle measured from the Celestial equator to the sky position of the source we can define

$$\hat{\boldsymbol{k}} = -\hat{\boldsymbol{e}}_q \cos\delta - \hat{\boldsymbol{e}}_3 \sin\delta. \tag{4.86}$$

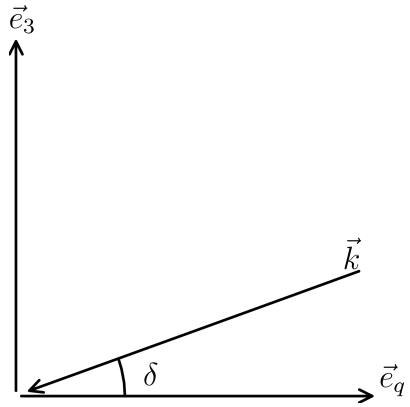

Fig 4.10: Projection of the unit vector $\hat{\boldsymbol{k}}$ into the equatorial plane represented by the vector $\hat{\boldsymbol{e}}_{\boldsymbol{q}}$. This vector point to the Celestial Equator with the right ascension α, while vector $\hat{\boldsymbol{e}}_{\mathbf{3}}$ points to Celestial North Pole. (From Whelan (2013)).

To get the components of $\hat{\boldsymbol{e}}_{\boldsymbol{q}}$ in the equatorial basis we look at the equatorial plane in Fig. 4.8. The right ascension α is the angle from the Vernal Equinox ($\hat{\boldsymbol{e}}_{\mathbf{1}}$) to the source point in the sky, therefore

$$\hat{\boldsymbol{e}}_{\boldsymbol{q}} = \hat{\boldsymbol{e}}_{\mathbf{1}} \cos\alpha + \hat{\boldsymbol{e}}_{\mathbf{2}} \sin\alpha, \tag{4.87}$$

and thus

$$\hat{\boldsymbol{k}} = -\hat{\boldsymbol{e}}_{\mathbf{1}} \cos\delta\cos\alpha - \hat{\boldsymbol{e}}_{\mathbf{2}} \cos\delta\sin\alpha - \hat{\boldsymbol{e}}_{\mathbf{3}} \sin\delta. \tag{4.88}$$

The components along $\hat{\boldsymbol{e}}_{\mathbf{1}}$, $\hat{\boldsymbol{e}}_{\mathbf{2}}$ and $\hat{\boldsymbol{e}}_{\mathbf{3}}$ will be constant for a given source. To get the components along the starred unit vectors, we just need to note that angle from $\hat{\boldsymbol{e}}^*_{\mathbf{1}}$ to $\hat{\boldsymbol{e}}_{\boldsymbol{q}}$ is $\alpha - \gamma$. In terms of the starred basis we have

$$\hat{\boldsymbol{e}}^*_{\boldsymbol{q}} = \hat{\boldsymbol{e}}^*_{\mathbf{1}} \cos(\alpha-\gamma) + \hat{\boldsymbol{e}}^*_{\mathbf{2}} \sin(\alpha-\gamma) \tag{4.89}$$

and thus

$$\hat{\boldsymbol{k}} = -\cos\delta\cos(\alpha-\gamma)\hat{\boldsymbol{e}}^*_{\mathbf{1}} - \cos\delta\sin(\alpha-\gamma)\hat{\boldsymbol{e}}^*_{\mathbf{2}} - \sin\delta\hat{\boldsymbol{e}}^*_{\mathbf{3}}. \tag{4.90}$$

To define the complementary and orthogonal vectors $\hat{\boldsymbol{i}}$ and $\hat{\boldsymbol{j}}$, as well as $\hat{\boldsymbol{l}}$ and $\hat{\boldsymbol{m}}$ vectors, we should consider the equatorial plane as shown in Fig. 4.11. The unit vector $\hat{\boldsymbol{i}}$ is parallel to the Celestial Equator and points in the direction of decreasing right ascension. Therefore, we have

$$\hat{\boldsymbol{i}} = \sin(\alpha-\gamma)\hat{\boldsymbol{e}}^*_{\mathbf{1}} - \cos(\alpha-\gamma)\hat{\boldsymbol{e}}^*_{\mathbf{2}}. \tag{4.91}$$

The last, the unit vector $\hat{\boldsymbol{j}}$ is

$$\hat{\boldsymbol{j}} = -\cos(\alpha-\gamma)\sin\delta\hat{\boldsymbol{e}}^*_{\mathbf{1}} - \sin(\alpha-\gamma)\sin\delta\hat{\boldsymbol{e}}^*_{\mathbf{2}} + \cos\delta\hat{\boldsymbol{e}}^*_{\mathbf{3}}. \tag{4.92}$$

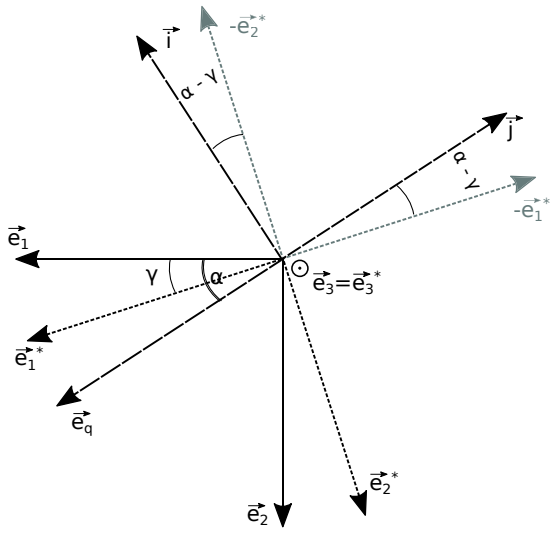

Fig 4.11: Equatorial plane viewed from the top where the unit vectors $\{\hat{\boldsymbol{e}}_1^*, \hat{\boldsymbol{e}}_2^*, \hat{\boldsymbol{e}}_3^*\}$ are associated with the Earth-fixed system and the unit vectors $\{\hat{\boldsymbol{e}}_1, \hat{\boldsymbol{e}}_2, \hat{\boldsymbol{e}}_3\}$ with the inertial star system. Vector $\hat{\boldsymbol{e}}_q$ is projection of the unit vector $\hat{\boldsymbol{k}}$ into the equatorial plane and it points to Celestial Equator. Vectors $\hat{\boldsymbol{i}}$ and $\hat{\boldsymbol{j}}$ together with $\hat{\boldsymbol{k}}$ define the orthogonal basis defined by the right ascension α and the declination δ angles. γ is Greenwich Sidereal Time.

From (4.91) and (4.92) using (4.83) we have

$$\begin{aligned}\hat{\boldsymbol{l}} &= (\sin(\alpha-\gamma)\cos\psi - \cos(\alpha-\gamma)\sin\delta\sin\psi)\hat{\boldsymbol{e}}_{\boldsymbol{1}}^* \\ &+ (-\cos(\alpha-\gamma)\cos\psi - \sin(\alpha-\gamma)\sin\delta\sin\psi)\hat{\boldsymbol{e}}_{\boldsymbol{2}}^* \\ &+ (\cos\delta\sin\psi)\hat{\boldsymbol{e}}_{\boldsymbol{3}}^*,\end{aligned} \tag{4.93}$$

$$\begin{aligned}\hat{\boldsymbol{m}} &= (-\sin(\alpha-\gamma)\sin\psi - \cos(\alpha-\gamma)\sin\delta\cos\psi)\hat{\boldsymbol{e}}_{\boldsymbol{1}}^* \\ &+ (\cos(\alpha-\gamma)\sin\psi - \sin(\alpha-\gamma)\sin\delta\cos\psi)\hat{\boldsymbol{e}}_{\boldsymbol{2}}^* \\ &+ (\cos\delta\cos\psi)\hat{\boldsymbol{e}}_{\boldsymbol{3}}^*.\end{aligned} \tag{4.94}$$

With the basis vectors $\hat{\boldsymbol{l}}$ and $\hat{\boldsymbol{m}}$ we can construct the natural polarization tensors $\boldsymbol{e}_{+,\times}$ in α, δ, ψ basis by applying the rotation

$$\boldsymbol{e}_+ = \mathbf{E}\cdot\begin{pmatrix}1 & 0 & 0\\ 0 & -1 & 0\\ 0 & 0 & 0\end{pmatrix}\cdot\mathbf{E}^{\mathrm{T}}, \qquad \boldsymbol{e}_\times = \mathbf{E}\cdot\begin{pmatrix}0 & 1 & 0\\ 1 & 0 & 0\\ 0 & 0 & 0\end{pmatrix}\cdot\mathbf{E}^{\mathrm{T}}, \tag{4.95}$$

where the rotation matrix $\mathbf{E}$ is

$$\mathbf{E} = \begin{pmatrix}\sin\alpha'\cos\psi - \cos\alpha'\sin\delta\sin\psi & -\sin\alpha'\sin\psi - \cos\alpha'\sin\delta\cos\psi & -\cos\alpha'\cos\delta\\ -\cos\alpha'\cos\psi - \sin\alpha'\sin\delta\sin\psi & \cos\alpha'\sin\psi - \sin\alpha'\sin\delta\cos\psi & -\sin\alpha'\cos\delta\\ \cos\delta\sin\psi & \cos\delta\cos\psi & -\sin\delta\end{pmatrix} \tag{4.96}$$

with $\alpha' = \alpha - \gamma$. For the calculation of Greenwich Sidereal Time we refer to Appendix A.

Next, we define the metric perturbation of the binary star system to be able to use the double white-dwarf binaries as the GW sources.

4.3.2 Metric perturbation for the binary star system

In general relativity, the quadrupole formula states that the GW amplitude h_{ij} is proportional to the second time derivative of the quadrupole moment of the source defined with expression

$$h_{ij}^{TT} = \frac{2}{r}\frac{G}{c^4}\ddot{Q}_{ij}^{TT}\left(t - \frac{r}{c}\right), \tag{4.97}$$

where

$$\begin{aligned}\ddot{Q}_{ij}^{TT}\left(t - \frac{r}{c}\right) &= \int \rho(x^i x^j - \frac{1}{3}\delta_{ij} r^2) d^3x \\ &= M^{ij} - \frac{1}{3}\delta^{ij} M_{kk},\end{aligned} \tag{4.98}$$

is the quadrupole moment in the transverse-traceless (TT) gauge evaluated at the retarded time $t - r/c$ and ρ is the matter density in a volume element d^3x at the position x^i, $G = 6.67408 \cdot 10^{-11}$ m^{3}kg^{-1}s^{-2} is gravitational constant and $c = 299792458$ m/s speed of light in the vacuum. If GW is propagating in $\hat{\boldsymbol{e}}_{\boldsymbol{z}}$ direction, relation (4.97) is modified into two polarization amplitude

$$\begin{aligned}h_+ &= \frac{1}{r}\frac{G}{c^4}(\ddot{M}_{11} - \ddot{M}_{22}), \\ h_+ &= \frac{2}{r}\frac{G}{c^4}\ddot{M}_{12}.\end{aligned} \tag{4.99}$$

To obtain waveform emitted in the arbitrary direction $\hat{\boldsymbol{e}}_{\boldsymbol{n}}$ one needs to compute the transformation from $(\hat{\boldsymbol{e}}_{\boldsymbol{x}}, \hat{\boldsymbol{e}}_{\boldsymbol{y}}, \hat{\boldsymbol{e}}_{\boldsymbol{z}})$ frame to $(\hat{\boldsymbol{e}}_{\boldsymbol{x'}}, \hat{\boldsymbol{e}}_{\boldsymbol{y'}}, \hat{\boldsymbol{e}}_{\boldsymbol{z'}})$ frame where $\hat{\boldsymbol{e}}_{\boldsymbol{n}} = \hat{\boldsymbol{e}}_{\boldsymbol{z'}}$ and $\hat{\boldsymbol{e}}_{\boldsymbol{n}}$ can be written in the first frame as

$$\hat{\boldsymbol{e}}_{\boldsymbol{n}} = (\sin\theta\sin\phi, \sin\theta\cos\phi, \cos\theta). \tag{4.100}$$

For the full derivation reader is referred to Maggiore (2008), here we write the final expressions for both polarization as

$$\begin{aligned}h_+ = \frac{1}{r}\frac{G}{c^4}\Big[&\ddot{M}_{11}(\cos^2\phi - \sin^2\phi\cos^2\theta) \\ &+\ddot{M}_{22}(\sin^2\phi - \cos^2\phi\cos^2\theta) \\ &-\ddot{M}_{33}\sin^2\theta \\ &-\ddot{M}_{12}\sin 2\phi(1 + \cos^2\theta) \\ &+\ddot{M}_{13}\sin\phi\sin 2\theta \\ &+\ddot{M}_{23}\cos\phi\sin 2\theta\Big],\end{aligned} \tag{4.101}$$

$$
\begin{aligned}
h_\times = \frac{1}{r}\frac{G}{c^4}\Big[&(\ddot{M}_{11} - \ddot{M}_{22})\sin 2\phi\cos\theta \\
&+2\ddot{M}_{12}\cos 2\phi\cos\theta \\
&-2\ddot{M}_{13}\cos\phi\sin\theta \\
&+\ddot{M}_{23}\sin\phi\sin\theta\Big].
\end{aligned}
\tag{4.102}
$$

Let's now consider a binary star system with masses m_1 and m_2 and their reduced mass defined as

$$
\mu = \frac{m_1 m_2}{m_1 + m_2}. \tag{4.103}
$$

For simplicity, we assume that the binary orbit is circular and we denote the separation between the centers of masses as a. Then Newtonian force balance dictates that the orbital angular velocity Ω is given by Kepler's law

$$
\Omega = \sqrt{\frac{G(m_1 + m_2)}{a^3}}. \tag{4.104}
$$

Next, we chose the binary orbit to lies in the $(\hat{\boldsymbol{e}}_{\boldsymbol{x}}, \hat{\boldsymbol{e}}_{\boldsymbol{y}})$ plane and is given by

$$
\begin{aligned}
x_0(t) &= a\cos(\Omega t), \\
y_0(t) &= a\sin(\Omega t), \\
z_0(t) &= 0.
\end{aligned}
\tag{4.105}
$$

In the center of mass frame with the mass coordinate $x_{CM} = \frac{m_1 x_1 + m_2 x_2}{m_1 + m_2} = 0$ the second mass moment is defined as $M^{ij} = \mu x_0^i(t) x_0^j(t)$, therefore we have

$$
M_{11} = \mu a^2 \frac{1 + \cos 2\Omega t}{2}, \tag{4.106}
$$

$$
M_{22} = \mu a^2 \frac{1 - \cos 2\Omega t}{2}, \tag{4.107}
$$

$$
M_{12} = \frac{1}{2}\mu a^2 \sin 2\Omega t, \tag{4.108}
$$

while other components are equal to zero. Further, we have

$$
\ddot{M}_{11} = -\ddot{M}_{22} = -2\mu a^2\Omega^2\cos 2\Omega t, \tag{4.109}
$$

$$
\ddot{M}_{12} = -2\mu a^2\Omega^2\sin 2\Omega t. \tag{4.110}
$$

Substituting above expressions into relations (4.101) and (4.102) we obtain

$$
h_+ = -2(1 + \cos^2\theta)\frac{G}{c^4}\frac{\mu a^2\Omega^2}{r}\cos[2(\Omega t + \phi)], \tag{4.111}
$$

$$
h_\times = -4\cos\theta\frac{G}{c^4}\frac{\mu a^2\Omega^2}{r}\sin[2(\Omega t + \phi)]. \tag{4.112}
$$

Therefore, according to above expression the quadrupole radiation is the twice the orbital angular velocity Ω of the source. The GW frequency is twice the orbital frequency

$$f = \frac{2\Omega}{2\pi} = \frac{\Omega}{\pi}. \tag{4.113}$$

Since GW field is calculated at the retarded time we additionally have $2\Omega t + \phi \to 2\Omega t - 2\Omega\frac{r}{c} + \phi$. Physically, ϕ describes the rotation around $\hat{\boldsymbol{e}}_{\boldsymbol{z}}$ axis and angle θ is equal to the inclination angle ι between the normal to the orbit and the line-of-sight. In this study we ignore the phase term $-2\Omega\frac{r}{c} + \phi$ and with $\theta = \iota$ we introduce two abbreviations

$$h_{+,c} = -2(1 + \cos^2\iota)\frac{G}{c^4}\frac{\mu a^2\Omega^2}{r}, \tag{4.114}$$

$$h_{\times,c} = -4\cos\iota\frac{G}{c^4}\frac{\mu a^2\Omega^2}{r}, \tag{4.115}$$

then (4.111) and (4.112) become

$$h_+ = h_{+,c}\cos(2\Omega t), \tag{4.116}$$

$$h_\times = h_{\times,c}\sin(2\Omega t). \tag{4.117}$$

The above expressions are used to define our binary sources.

Next, we define a Green tensor for a rotating, anelastic Earth that is used to calculate the induced spheroidal displacement.

4.3.3 Green tensor

The Green tensor for a rotating, anelastic Earth from Tab. 3.1 is

$$\mathbf{G}(\mathbf{r}, \mathbf{r}'; t) = \Re\sum_k (i\nu_k)^{-1}\mathbf{s}_k(\mathbf{r})\bar{\mathbf{s}}_k(\mathbf{r}')\mathrm{e}^{i\nu_k t}, \tag{4.118}$$

where $\mathbf{s}_k$ are the associated displacement eigenfunctions and $\bar{\mathbf{s}}_k$ their dual eigenfunctions. The eigenfunctions from Tab. 3.2 are

$$\mathbf{s}_k(\mathbf{r}) = \mathcal{U}_k(r)\mathbf{e}_r Y_{lm}(\theta,\phi) + \kappa^{-1}\mathcal{V}_k(r)\nabla_1 Y_{lm}(\theta,\phi) - \kappa^{-1}\mathcal{W}_k(r)(\mathbf{e}_r \times \nabla_1 Y_{lm}(\theta,\phi)). \tag{4.119}$$

Using the same reasoning as in Subsection 4.2.2 by keeping only the effect of anelasticity upon the eigenfrequencies the relation (4.119) becomes

$$\mathbf{s}_k(\mathbf{r}) = U_k(r)\mathbf{e}_r Y_{lm}(\theta,\phi) + \kappa^{-1}V_k(r)\nabla_1 Y_{lm}(\theta,\phi) - \kappa^{-1}W_k(r)(\mathbf{e}_r \times \nabla_1 Y_{lm}(\theta,\phi)), \tag{4.120}$$

where, naturally, $U_k(r), V_k(r), W_k(r)$ are real functions. In the absence of anelasticity the eigenfunction and their duals are complex conjugate: $\bar{\mathbf{s}}_k = \mathbf{s}_k^*$.

The effects of rotation and lateral heterogeneities introduce splitting of and coupling between the normal modes and to include those effects in Green tensor we need to calculate the quasi-degenerate super-multiplet splitting matrix (3.26). Next, using the similarity transformations one needs to calculate eigenvalues and eigenvectors of the splitting matrix to calculate the renormalized receiver and source displacement eigenfunctions in (4.118) by applying

$$\tilde{\mathbf{s}}_k(\mathbf{r}) = \mathbf{Z}^{\mathbf{T}} \left(\mathbf{I} - \frac{1}{2}\mathbf{T}^{\text{ell}} - \frac{1}{2}\mathbf{T}^{\text{lat}} - \frac{1}{2}\omega_0^{-1}\mathbf{W} \right) \mathbf{s}_k(\mathbf{r}) = \mathbf{Z}^{\mathbf{T}}\mathbf{M}\mathbf{s}_k(\mathbf{r}), \tag{4.121}$$

$$\tilde{\mathbf{s}}_k(\mathbf{r}') = \mathbf{Z}^{-1} \left(\mathbf{I} - \frac{1}{2}\mathbf{T}^{\text{ell}} - \frac{1}{2}\mathbf{T}^{\text{lat}} - \frac{1}{2}\omega_0^{-1}\mathbf{W} \right) \mathbf{s}_k(\mathbf{r}') = \mathbf{Z}^{-1}\mathbf{M}\mathbf{s}_k(\mathbf{r}'). \tag{4.122}$$

One needs to keep in mind that in the case of the group-coupling approximation $\mathbf{H}$ has a dimension $\sum_k(2l_k+1) \times \sum_k(2l_k+1)$ where k stands for the k multiplet within the group. The definition of a Green tensor is now altered to consider the effects of the splitting and the group-coupling

$$\mathbf{G}(\mathbf{r}, \mathbf{r}'; t) = \Re \sum_k (i\nu_k)^{-1} \tilde{\mathbf{s}}_k(\mathbf{r}) \tilde{\mathbf{s}}_k^*(\mathbf{r}') \mathrm{e}^{i(\nu_k + \delta\nu_k)t}. \tag{4.123}$$

Next we proceed with the calculation of the induced spheroidal response.

4.3.4 Induced spheroidal response

As for the induced spheroidal response in Section 4.2.3 to obtain solution one needs to insert a force term (4.8) into displacement (3.31) and take into account the boundary condition (3.3) on the surface. Therefore, the expressions below resemble the ones in Section 4.2.3, where differences come from the metric perturbation and newly defined Green tensor. The force term is now defined using the metric perturbation defined for a binary star system in terrestrial reference system. The relevant expressions that constitute the metric perturbation are

$$\boldsymbol{h} = h_+ \boldsymbol{e}_+ + h_\times \boldsymbol{e}_\times, \tag{4.124}$$

where amplitudes are

$$h_+ = h_{+,c} \cos(2\Omega t), \tag{4.125}$$

$$h_\times = h_{\times,c} \sin(2\Omega t), \tag{4.126}$$

and the polarization matrices defined by rotation matrix $\mathbf{E}$ are

$$\boldsymbol{e}_+ = \mathbf{E} \cdot \begin{pmatrix} 1 & 0 & 0 \\ 0 & -1 & 0 \\ 0 & 0 & 0 \end{pmatrix} \cdot \mathbf{E}^{\mathrm{T}}, \qquad \boldsymbol{e}_\times = \mathbf{E} \cdot \begin{pmatrix} 0 & 1 & 0 \\ 1 & 0 & 0 \\ 0 & 0 & 0 \end{pmatrix} \cdot \mathbf{E}^{\mathrm{T}}, \tag{4.127}$$

$$\mathbf{E} = \begin{pmatrix} \sin\alpha'\cos\psi - \cos\alpha'\sin\delta\sin\psi & -\sin\alpha'\sin\psi - \cos\alpha'\sin\delta\cos\psi & -\cos\alpha'\cos\delta \\ -\cos\alpha'\cos\psi - \sin\alpha'\sin\delta\sin\psi & \cos\alpha'\sin\psi - \sin\alpha'\sin\delta\cos\psi & -\sin\alpha'\cos\delta \\ \cos\delta\sin\psi & \cos\delta\cos\psi & -\sin\delta \end{pmatrix}, \tag{4.128}$$

with $\alpha' = \alpha - \gamma$. From this point we can already conclude that our solution will depend on the right ascension α angle, the declination δ angle, Greenwich Sidereal Time (GST) γ, the polarization angle ψ, the orbital inclination angle ι. Inserting force term into displacement we obtain

$$\begin{aligned} \mathbf{s}(\mathbf{r},t) =& -\int_{-\infty}^{t}\int_{V}\frac{\partial\mu}{\partial r}\mathbf{G}(\mathbf{r},\mathbf{r}';t-t')\cdot(\hat{\boldsymbol{e}}_r\cdot(h_+\boldsymbol{e}_+ + h_\times\boldsymbol{e}_\times))dV'dt' \\ &+\mu(a)\int_{-\infty}^{t}\int_{S}\mathbf{G}(\mathbf{r},\mathbf{r}';t-t')\cdot(\hat{\boldsymbol{e}}_r\cdot(h_+\boldsymbol{e}_+ + h_\times\boldsymbol{e}_\times))d\Sigma'dt' \\ =& -\int_{-\infty}^{t}\int_{V}\frac{\partial\mu}{\partial r}\mathbf{G}(\mathbf{r},\mathbf{r}';t-t')\cdot(\hat{\boldsymbol{e}}_r\cdot h_+\boldsymbol{e}_+)dV'dt' \\ &-\int_{-\infty}^{t}\int_{V}\frac{\partial\mu}{\partial r}\mathbf{G}(\mathbf{r},\mathbf{r}';t-t')\cdot(\hat{\boldsymbol{e}}_r\cdot h_\times\boldsymbol{e}_\times)dV'dt' \\ &+\mu(a)\int_{-\infty}^{t}\int_{S}\mathbf{G}(\mathbf{r},\mathbf{r}';t-t')\cdot(\hat{\boldsymbol{e}}_r\cdot h_+\boldsymbol{e}_+)d\Sigma'dt' \\ &+\mu(a)\int_{-\infty}^{t}\int_{S}\mathbf{G}(\mathbf{r},\mathbf{r}';t-t')\cdot(\hat{\boldsymbol{e}}_r\cdot h_\times\boldsymbol{e}_\times)d\Sigma'dt', \end{aligned} \tag{4.129}$$

where we separate + and × parts of the displacement. Further, we insert the definition of the modified Green tensor (4.123) and we obtain

$$\begin{aligned} \mathbf{s}_k(\mathbf{r},t) =& -h_{+,c}\tilde{\mathbf{s}}_k(\mathbf{r})\bar{g}_+(t,\Omega,\omega_k)\int_V\frac{\partial\mu}{\partial r}\tilde{\mathbf{s}}_k^*(\mathbf{r}')\cdot(\hat{\boldsymbol{e}}_r\cdot\boldsymbol{e}_+)dV' \\ &-h_{\times,c}\tilde{\mathbf{s}}_k(\mathbf{r})\bar{g}_\times(t,\Omega,\omega_k)\int_V\frac{\partial\mu}{\partial r}\tilde{\mathbf{s}}_k^*(\mathbf{r}')\cdot(\hat{\boldsymbol{e}}_r\cdot\boldsymbol{e}_\times)dV' \\ &+\mu(a)h_{+,c}\tilde{\mathbf{s}}_k(\mathbf{r})\bar{g}_+(t,\Omega,\omega_k)\int_S\tilde{\mathbf{s}}_k^*(\mathbf{r}')\cdot(\hat{\boldsymbol{e}}_r\cdot\boldsymbol{e}_+)d\Sigma' \\ &+\mu(a)h_{\times,c}\tilde{\mathbf{s}}_k(\mathbf{r})\bar{g}_\times(t,\Omega,\omega_k)\int_S\tilde{\mathbf{s}}_k^*(\mathbf{r}')\cdot(\hat{\boldsymbol{e}}_r\cdot\boldsymbol{e}_\times)d\Sigma', \end{aligned} \tag{4.130}$$

with the source-time functions as

$$\begin{aligned} \bar{g}_+(t,\Omega,\omega_k) &= \int_{-\infty}^{t}(i\nu_k)^{-1}\mathrm{e}^{i(\nu_k+\delta\nu_k)(t-t')}\cos(2\Omega t')dt' \\ &= \frac{1}{2}\int_{-\infty}^{t}(i\nu_k)^{-1}\mathrm{e}^{i(\nu_k+\delta\nu_k)(t-t')}(\mathrm{e}^{i2\Omega t'}+\mathrm{e}^{-i2\Omega t'})dt', \end{aligned} \tag{4.131}$$

$$\begin{aligned} \bar{g}_\times(t,\Omega,\omega_k) &= \int_{-\infty}^{t}(i\nu_k)^{-1}\mathrm{e}^{i(\nu_k+\delta\nu_k)(t-t')}\sin(2\Omega t')dt' \\ &= \frac{i}{2}\int_{-\infty}^{t}(i\nu_k)^{-1}\mathrm{e}^{i(\nu_k+\delta\nu_k)(t-t')}(-\mathrm{e}^{i2\Omega t'}+\mathrm{e}^{-i2\Omega t'})dt'. \end{aligned} \tag{4.132}$$

Using the convolution theorem, the same as for (4.23), we arrive at the expressions for the source-time functions

$$\begin{aligned}\bar{g}_+(t,\Omega,\omega_k) =&\frac{1}{4\pi}\int_{-\infty}^{+\infty}(i\nu_k)^{-1}\delta(\omega-2\Omega)\frac{1}{\gamma'_k+i(\omega-\omega'_k)}\mathrm{e}^{i\omega t}d\omega\\ &+\frac{1}{4\pi}\int_{-\infty}^{+\infty}(i\nu_k)^{-1}\delta(\omega+2\Omega)\frac{1}{\gamma'_k+i(\omega-\omega'_k)}\mathrm{e}^{i\omega t}d\omega\\ =&\frac{1}{4\pi}(i\nu_k)^{-1}\frac{1}{\gamma'_k+i(2\Omega-\omega'_k)}\mathrm{e}^{i2\Omega t}+\frac{1}{4\pi}(i\nu_k)^{-1}\frac{1}{\gamma'_k+i(-2\Omega-\omega'_k)}\mathrm{e}^{-i2\Omega t},\end{aligned} \tag{4.133}$$

$$\begin{aligned}\bar{g}_\times(t,\Omega,\omega_k) =&-\frac{i}{4\pi}\int_{-\infty}^{+\infty}(i\nu_k)^{-1}\delta(\omega-2\Omega)\frac{1}{\gamma'_k+i(\omega-\omega'_k)}\mathrm{e}^{i\omega t}d\omega\\ &+\frac{i}{4\pi}\int_{-\infty}^{+\infty}(i\nu_k)^{-1}\delta(\omega+2\Omega)\frac{1}{\gamma'_k+i(\omega-\omega'_k)}\mathrm{e}^{i\omega t}d\omega\\ =&-\frac{i}{4\pi}(i\nu_k)^{-1}\frac{1}{\gamma'_k+i(2\Omega-\omega'_k)}\mathrm{e}^{i2\Omega t}+\frac{i}{4\pi}(i\nu_k)^{-1}\frac{1}{\gamma'_k+i(-2\Omega-\omega'_k)}\mathrm{e}^{-i2\Omega t},\end{aligned} \tag{4.134}$$

where we used the abbreviation for the complex eigenfrequencies

$$\nu_k+\delta\nu_k=\omega_k+i\gamma_k+\delta\omega_k+i\delta\gamma_k=\omega'_k+\gamma'_k. \tag{4.135}$$

Combining + and × parts and extracting the polarization tensors we arrive at

$$\begin{aligned}\mathbf{s}_k(\mathbf{r},t)=&h_{+,c}\tilde{\mathbf{s}}_k(\mathbf{r})\bar{g}_+(t,\Omega,\omega_k)\left[-\int_V\frac{\partial\mu}{\partial r}\tilde{\mathbf{s}}_k^*(\mathbf{r}')\cdot(\hat{\boldsymbol{e}}_r\cdot\boldsymbol{e}_+)dV'+\mu(a)\int_S\tilde{\mathbf{s}}_k^*(\mathbf{r}')\cdot(\hat{\boldsymbol{e}}_r\cdot\boldsymbol{e}_+)d\Sigma'\right]\\ &+h_{\times,c}\tilde{\mathbf{s}}_k(\mathbf{r})\bar{g}_\times(t,\Omega,\omega_k)\left[-\int_V\frac{\partial\mu}{\partial r}\tilde{\mathbf{s}}_k^*(\mathbf{r}')\cdot(\hat{\boldsymbol{e}}_r\cdot\boldsymbol{e}_\times)dV'+\mu(a)\int_S\tilde{\mathbf{s}}_k^*(\mathbf{r}')\cdot(\hat{\boldsymbol{e}}_r\cdot\boldsymbol{e}_\times)d\Sigma'\right]\\ =&h_{+,c}\tilde{\mathbf{s}}_k(\mathbf{r})\bar{g}_+(t,\Omega,\omega_k)\boldsymbol{e}_+:\left[-\int_V\frac{\partial\mu}{\partial r}\tilde{\mathbf{s}}_k^*(\mathbf{r}')\hat{\boldsymbol{e}}_r dV'+\mu(a)\int_S\tilde{\mathbf{s}}_k^*(\mathbf{r}')\hat{\boldsymbol{e}}_r d\Sigma'\right]\\ &+h_{\times,c}\tilde{\mathbf{s}}_k(\mathbf{r})\bar{g}_\times(t,\Omega,\omega_k)\boldsymbol{e}_\times:\left[-\int_V\frac{\partial\mu}{\partial r}\tilde{\mathbf{s}}_k^*(\mathbf{r}')\hat{\boldsymbol{e}}_r dV'+\mu(a)\int_S\tilde{\mathbf{s}}_k^*(\mathbf{r}')\hat{\boldsymbol{e}}_r d\Sigma'\right].\end{aligned} \tag{4.136}$$

Considering only the spheroidal displacement, thus putting $W_k=0$ in (4.120), the displacement eigenfunction $\tilde{s}_k(\mathbf{r})=\mathbf{Z}^{-1}\mathbf{M}(U_k(r)\mathbf{e}_rY_{lm}^*(\theta,\phi)+\kappa^{-1}V_k(r)\nabla_1Y_{lm}^*(\theta,\phi))$ is substituted to (4.136), thus we have

$$\begin{aligned}\mathbf{s}_k(\mathbf{r},t)=&\tilde{\mathbf{s}}_k(\mathbf{r})\left(h_{+,c}\bar{g}_+(t,\Omega,\omega_k)\boldsymbol{e}_++h_{\times,c}\bar{g}_\times(t,\Omega,\omega_k)\boldsymbol{e}_\times\right):\\ &\left[\mathbf{Z}^{-1}\mathbf{M}\left(\mu(a)U_k(a)a^2-\int_r\frac{\partial\mu}{\partial r}U_k(r)r^2dr\right)\int_\Omega\hat{\boldsymbol{e}}_r\hat{\boldsymbol{e}}_rY_{lm}^*(\theta,\phi)d\Omega\right.\\ &\left.+\mathbf{Z}^{-1}\mathbf{M}\left(\mu(a)\kappa^{-1}V_k(a)a^2-\int_r\frac{\partial\mu}{\partial r}\kappa^{-1}V_k(r)r^2dr\right)\int_\Omega\hat{\boldsymbol{e}}_r\nabla_1Y_{lm}^*(\theta,\phi)d\Omega\right].\end{aligned} \tag{4.137}$$

We again arrive at the expressions that contain integrals of the dyadic products, however this time the spherical harmonics within the integral are complex conjugate. The first

integral from (4.137) is

$$I_1 = \int_\Omega \hat{\boldsymbol{e}}_r \hat{\boldsymbol{e}}_r Y^*_{lm}(\theta,\phi) d\Omega = \int_0^\pi \int_0^{2\pi} \hat{\boldsymbol{e}}_r \hat{\boldsymbol{e}}_r Y^*_{lm}(\theta,\phi) \sin\theta d\theta d\phi, \tag{4.138}$$

whose solution

$$\begin{aligned} I_1 = \frac{2\sqrt{\pi}}{3}\delta_{l,0}\delta_{m,0}\begin{bmatrix} 1 & 0 & 0 \\ 0 & 1 & 0 \\ 0 & 0 & 1 \end{bmatrix} + \frac{2}{3}\sqrt{\frac{\pi}{5}}\delta_{l,2}\delta_{m,0}\begin{bmatrix} -1 & 0 & 0 \\ 0 & -1 & 0 \\ 0 & 0 & 2 \end{bmatrix} \\ + \sqrt{\frac{2\pi}{15}}\delta_{l,2}\begin{bmatrix} \delta_{m,2}+\delta_{m,-2} & -i\delta_{m,2}+i\delta_{m,-2} & -\delta_{m,1}+\delta_{m,-1} \\ -i\delta_{m,2}+i\delta_{m,-2} & -\delta_{m,2}-\delta_{m,-2} & i\delta_{m,1}+i\delta_{m,-1} \\ -\delta_{m,1}+\delta_{m,-1} & i\delta_{m,1}+i\delta_{m,-1} & 0 \end{bmatrix}, \end{aligned} \tag{4.139}$$

differs from (4.31) in the third term. The same argument is aslo valid for the second integral

$$\begin{aligned} I_2 = \int_\Omega \hat{\boldsymbol{e}}_r \nabla_1 Y_{lm}(\theta,\phi) d\Omega = \int_0^\pi \int_0^{2\pi} \hat{\boldsymbol{e}}_r \hat{\boldsymbol{e}}_\theta \partial_\theta Y_{lm}(\theta,\phi) \sin\theta d\theta d\phi \\ + \int_0^\pi \int_0^{2\pi} \hat{\boldsymbol{e}}_r \hat{\boldsymbol{e}}_\phi (\sin\theta)^{-1} \partial_\phi Y_{lm}(\theta,\phi) \sin\theta d\theta d\phi, \end{aligned} \tag{4.140}$$

whose solution is

$$\begin{aligned} I_2 = 3\frac{2}{3}\sqrt{\frac{\pi}{5}}\delta_{l,2}\delta_{m,0}\begin{bmatrix} -1 & 0 & 0 \\ 0 & -1 & 0 \\ 0 & 0 & 2 \end{bmatrix} \\ + 3\sqrt{\frac{2\pi}{15}}\delta_{l,2}\begin{bmatrix} \delta_{m,2}+\delta_{m,-2} & -i\delta_{m,2}+i\delta_{m,-2} & -\delta_{m,1}+\delta_{m,-1} \\ -i\delta_{m,2}+i\delta_{m,-2} & -\delta_{m,2}-\delta_{m,-2} & i\delta_{m,1}+i\delta_{m,-1} \\ -\delta_{m,1}+\delta_{m,-1} & i\delta_{m,1}+i\delta_{m,-1} & 0 \end{bmatrix}. \end{aligned} \tag{4.141}$$

Again, only one term is different from the same integral in previous case (4.33), the second one. Since the polarization tensors are traceless and symmetric the contraction with the unitary matrix is zero, $\boldsymbol{e}_+ : \mathrm{I} = 0, \boldsymbol{e}_\times : \mathrm{I} = 0$. This leaves us with the complete expression

for the induced spheroidal displacement where only the contraction needs to be performed

$$\mathbf{s}_k(\mathbf{r},t)=\tilde{\mathbf{s}}_k(\mathbf{r})\left(h_{+,c}\bar{g}_+(t,\Omega,\omega_k)\boldsymbol{e}_+ + h_{\times,c}\bar{g}_\times(t,\Omega,\omega_k)\boldsymbol{e}_\times\right) : \left\{ \frac{2}{3}\sqrt{\frac{\pi}{5}}\delta_{m,0}\delta_{l,2}\begin{bmatrix}-1 & 0 & 0\\ 0 & -1 & 0\\ 0 & 0 & 2\end{bmatrix} + \right.$$
$$\left. +\sqrt{\frac{2\pi}{15}}\delta_{l,2}\begin{bmatrix}\delta_{m,2}+\delta_{m,-2} & -i\delta_{m,2}+i\delta_{m,-2} & -\delta_{m,1}+\delta_{m,-1}\\ -i\delta_{m,2}+i\delta_{m,-2} & -\delta_{m,2}-\delta_{m,-2} & i\delta_{m,1}+i\delta_{m,-1}\\ -\delta_{m,1}+\delta_{m,-1} & i\delta_{m,1}+i\delta_{m,-1} & 0\end{bmatrix}\right\}$$
$$\mathbf{Z}^{-1}\mathbf{M}\left(\mu(a)a^2\left(U_k(a)+\frac{3}{\sqrt{6}}V_k(a)\right)-\int_r\frac{\partial\mu}{\partial r}\left(U_k(r)+\frac{3}{\sqrt{6}}V_k(r)\right)r^2dr\right). \tag{4.142}$$

We introduce two abbreviations for + and × contractions in terms of the pattern functions $f_+^m(\gamma(t),\alpha,\delta,\psi)$, $f_\times^m(\gamma(t),\alpha,\delta,\psi)$. Therefore we have

$$\begin{aligned} f_+^m(\gamma(t),\alpha,\delta,\psi) = \boldsymbol{e}_+ : & \left\{ \frac{2}{3}\sqrt{\frac{\pi}{5}}\delta_{m,0}\begin{bmatrix}-1 & 0 & 0\\ 0 & -1 & 0\\ 0 & 0 & 2\end{bmatrix}\right.\\ & \left. +\sqrt{\frac{2\pi}{15}}\begin{bmatrix}\delta_{m,2}+\delta_{m,-2} & -i\delta_{m,2}+i\delta_{m,-2} & -\delta_{m,1}+\delta_{m,-1}\\ -i\delta_{m,2}+i\delta_{m,-2} & -\delta_{m,2}-\delta_{m,-2} & i\delta_{m,1}+i\delta_{m,-1}\\ -\delta_{m,1}+\delta_{m,-1} & i\delta_{m,1}+i\delta_{m,-1} & 0\end{bmatrix}\right\}\\ & = -2\sqrt{\frac{\pi}{5}}\delta_{m,0}\cos^2\delta\cos 2\psi\\ & + \frac{1}{2}\sqrt{\frac{2\pi}{15}}\mathrm{e}^{-2i\alpha'}\delta_{m,2}[-4i\sin 2\psi\sin\delta+(-3+\cos 2\delta)\cos 2\psi]\\ & + \frac{1}{2}\sqrt{\frac{2\pi}{15}}\mathrm{e}^{2i\alpha'}\delta_{m,-2}[4i\sin 2\psi\sin\delta+(-3+\cos 2\delta)\cos 2\psi]\\ & - \sqrt{\frac{2\pi}{15}}\mathrm{e}^{-i\alpha'}\delta_{m,1}[2i\sin 2\psi\cos\delta+\sin 2\delta\cos 2\psi]\\ & + \sqrt{\frac{2\pi}{15}}\mathrm{e}^{i\alpha'}\delta_{m,-1}[-2i\sin 2\psi\cos\delta+\sin 2\delta\cos 2\psi], \end{aligned} \tag{4.143}$$

$$
\begin{aligned}
f^m_\times(\gamma(t),\alpha,\delta,\psi) = \boldsymbol{e}_\times : \Bigg\{ & \frac{2}{3}\sqrt{\frac{\pi}{5}}\delta_{m,0}\begin{bmatrix} -1 & 0 & 0 \\ 0 & -1 & 0 \\ 0 & 0 & 2 \end{bmatrix} \\
& + \sqrt{\frac{2\pi}{15}}\begin{bmatrix} \delta_{m,2}+\delta_{m,-2} & -i\delta_{m,2}+i\delta_{m,-2} & -\delta_{m,1}+\delta_{m,-1} \\ -i\delta_{m,2}+i\delta_{m,-2} & -\delta_{m,2}-\delta_{m,-2} & i\delta_{m,1}+i\delta_{m,-1} \\ -\delta_{m,1}+\delta_{m,-1} & i\delta_{m,1}+i\delta_{m,-1} & 0 \end{bmatrix} \Bigg\} \\
& = 4\sqrt{\frac{\pi}{5}}\delta_{m,0}\cos^2\delta\cos\psi\sin\psi \\
& + \frac{1}{2}\sqrt{\frac{2\pi}{15}}\mathrm{e}^{-2i\alpha'}\delta_{m,2}[-4i\cos 2\psi\sin\delta-(-3+\cos 2\delta)\sin 2\psi] \\
& + \frac{1}{2}\sqrt{\frac{2\pi}{15}}\mathrm{e}^{2i\alpha'}\delta_{m,-2}[4i\cos 2\psi\sin\delta-(-3+\cos 2\delta)\sin 2\psi] \\
& + \sqrt{\frac{2\pi}{15}}\mathrm{e}^{-i\alpha'}\delta_{m,1}[-2i\cos 2\psi\cos\delta+\sin 2\delta\sin 2\psi] \\
& - 2\sqrt{\frac{2\pi}{15}}\mathrm{e}^{i\alpha'}\delta_{m,-1}\cos\delta[i\cos 2\psi+\sin\delta\sin 2\psi],
\end{aligned}
\tag{4.144}
$$

with $\alpha' = \alpha - \gamma(t)$. Introducing the abbreviation for the model dependent function

$$
\zeta_k = \left(\mu(a)a^2\left(U_k(a)+\frac{3}{\sqrt{6}}V_k(a)\right) - \int_r \frac{\partial\mu}{\partial r}\left(U_k(r)+\frac{3}{\sqrt{6}}V_k(r)\right)r^2dr\right) \tag{4.145}
$$

our displacement becomes

$$
\mathbf{s}_k(\mathbf{r},t) = \hat{\mathbf{s}}_k(\mathbf{r})\delta_{l,2}\left(h_{+,c}\bar{g}_+(t,\Omega,\omega_k)f^m_+(\gamma(t),\alpha,\delta,\psi) + h_{\times,c}\bar{g}_\times(t,\Omega,\omega_k)f^m_\times(\gamma(t),\alpha,\delta,\psi)\right)\hat{\zeta}_k. \tag{4.146}
$$

For relation (4.146) using the definition of displacement eigenfunction (4.120) for the spheroidal motions we can define three displacement components

$$
\begin{aligned}
\mathbf{s}_k(\mathbf{r}) = & \hat{\boldsymbol{e}}_r U_k(r)Y_{lm}(\theta,\phi) \\
& + \hat{\boldsymbol{e}}_\theta\left(\kappa^{-1}V_k(r)\partial_\theta P_{lm}(\cos\theta)\right) \\
& + \hat{\boldsymbol{e}}_\phi\left(\kappa^{-1}V_k(r)\frac{1}{\sin\theta}P_{lm}(\cos\theta)\partial_\phi \mathrm{e}^{im\phi}\right).
\end{aligned}
\tag{4.147}
$$

This, finally, defines the spheroidal induced displacement for k mode. The complete response is found by summing over all excited modes for the specific GW source. For better clarification we drop the subscript k and write the full response for the spheroidal radial displacement as

$$
\begin{aligned}
{}_n\mathbf{s}^m_2(\mathbf{r}) = & \sum_n\sum_m {}_nU_2(r)Y_{2m}(\theta,\phi)\left(h_{+,c}\bar{g}^m_+(t,\Omega,\omega_m)f^m_+(\gamma(t),\alpha,\delta,\psi)\right. \\
& \left. + h_{\times,c}\bar{g}^m_\times(t,\Omega,\omega_m)f^m_\times(\gamma(t),\alpha,\delta,\psi)\right){}_n\hat{\zeta}_2.
\end{aligned}
\tag{4.148}
$$

With no further explanation, here we also include corrections for an idealized accelerometer for the displacement eigenfunctions (see 4.72 and 4.73).

4.3.5 Discussion

Derived induced displacement (4.146) from the previous subsection can be compared to the one derived in Subsection 4.2.3 described with the relation (4.36). The individual members of the two displacements are comparable, however they are not identical due to the start conditions. For example, both expressions contain the displacement eigenfunctions at the receiver position, the scalar metric perturbations, the source-time functions, the pattern functions that depend on the angles of the incoming GW and the model dependent functions. Two important differences are the newly defined metric perturbation for a binary star system and the utilization of a rotating Earth model. The first alteration introduces the binary parameters into the induced displacement. The second alternation implies utilization of different Green tensors (compare (4.15) and (4.123)) and displacement eigenfunctions (compare (4.17) and (4.120)). Even so, from the integral solutions (4.139) and (4.141) we see that the only induced angular order is again quadrupole one. This means that displacement (4.146) only represents summation over all relevant quadrupole normal modes as demonstrated by equation (4.148). As emphasized in Subsection 4.3.3 the effects of the splitting of and coupling between the normal modes are introduced by calculating the similarity transformation matrices from the splitting matrices. We chose to calculate the splitting matrices in the group-coupling approximation, over the self- or full-coupling approximations for the reason that will be elaborated further in text. The selection of the multiplet chains, for which the splitting matrices are calculated, is tightly connected with the frequencies of the GWs sources.

The good candidates of the GW sources in mHz band are LISA verification binaries (Stroeer and Vecchio, 2006), a handful of known nearby galactic binary systems that are well known from electromagnetic observations. Binaries are divided in several classes, such as mass-transferring AM CVn binary systems, double white dwarf binary systems, (ultra-)compact x-ray binaries and cataclysmic variables. We chose to work with the detached double white dwarfs, since they vastly outnumber all other compact binary objects in the Galactic disk (Nelemans et al., 2001) and they are far away the simplest objects since there are no varying elements in these binaries. The list of detected double white dwarf binaries with their parameters is shown in Tab. 4.5. The location of the system in the sky using the ecliptic coordinates, the right ascension and the declination angles, together with the orbital period is considered to be exactly known (Stroeer and Vecchio, 2006). However, other parameters are considered to be unknown or poorly constrained. For example, it has been proven in astronomy that it is difficult to measure fundamental white dwarf binaries parameters, such as their masses and radii (Schmidt, 1996). Further, from the orbital periods one can calculate the GW frequencies and using relations (4.114) and (4.115) the

strength of the metric perturbation. Calculation of the metric perturbation strength requires information on the inclination and the polarization angles, among others. These angles are usually missing in the catalog or, in case of the polarization angle, are completely unknown, thus we set them to zero. Finally, the last source from Tab. 4.5 is ignored due to the missing information on the distance. The final values are shown in Tab. 4.6. Considering the range of the GW frequencies in Tab. 4.6 the normal modes that should be the most affected, when the GW passes the Earth, are the low frequency normal modes.

Tab 4.5: List of the double white dwarf binaries and their parameters: the orbital periods, the distances to the sources,the masses of the two stars, the inclination angle, the right ascension and the declination angle. Each parameter, except the right ascension and the declination, has associated uncertainties if they exist. The last column contains appropriate references. The table is based on link.

Name	Period	Δ	r	Δ	M_2	Δ	M_1	Δ	ι	Δ	α	δ	Refs.
	[s]	[s]	[pc]	[pc]	$M_\odot$	$M_\odot$	$M_\odot$	$M_\odot$	[°]	[°]	[h:m:s]	[h:m:s]	
SDSS J0651+2844	765.4	7.9	1000	-	0.50	-	0.25	-	86.9	1.6-1	06:51:33.338	28:44:23.37	Brown et al. (2011); Hermes et al. (2012)
SDSS J0935+4411	1188	44	660	-	>0.14	-	0.32	-	-	-	09:35:XX	44:11:YY	Brown et al. (2016); Kilic et al. (2014)
SDSS J0106-1000	2346	2	2400	-	0.43	-	0.17	-	67	13	01:06:57.39	-10:00:03.3	Kilic et al. (2011b)
SDSS J1630+4233	2390	4	830	-	>0.52	-	0.31	-	-	-	16:30:XX	42:33:YY	Brown et al. (2016); Kilic et al. (2011a)
SDSS J1053+5200	3680	10	1100	-	>0.26	-	0.20	-	-	-	10:53:53.89	52:00:31.0	Kilic et al. (2010)
SDSS J0923+3028	3884	-	270	-	>0.34	-	0.23	-	-	-	09:23:45.59	30:28:05.0	Brown et al. (2016, 2010)
SDSS J1436+5010	3957	10	800	-	>0.46	-	0.24	-	-	-	14:36:33.29	50:10:26.8	Kilic et al. (2010)
WD 0957-666	5269.81080	10^{-5}	135	20	0.32	0.03	0.37	0.02	50-86	-	09:58:54.96	-66:53:10.2	Moran et al. (1997); Bragaglia et al. (1995)
SDSS J0755+4906	5445	-	2620	-	> 0.81	-	0.17	-	-	-	07:55:52.40	49:06:27.9	Kilic et al. (2012)
SDSS J0849+0445	6800	-	930	-	> 0.64	-	0.17	-	-	-	08:49:10.13	04:45:28.7	Kilic et al. (2010)
SDSS J0022-1014	6902	-	790	-	> 0.19	-	0.33	-	-	-	00:22:07.65	-10:14:23.5	Kilic et al. (2012)
SDSS J2119-0018	7497	-	2500	-	> 0.75	-	0.17	-	-	-	21:19:21.96	-00:18:25.8	Kilic et al. (2012)
SDSS J1234-0228	7900	-	780	-	> 0.09	-	0.23	-	-	-	12:34:10.36	-02:28:02.8	Kilic et al. (2012)
WD 1101+364	12503	5	97	-15	0.36	-	0.31	-	25	-	11:04:32.61	36:10:49.5	Marsh (1995)
WD 1704+4807BC	12511	2	-	-	0.56	0.07	0.39	0.05	61	-	17:05:30.1	48:03:17	Maxted et al. (2000)

Tab 4.6: List of the double white dwarf binaries with their orbital frequencies and the associated relative errors and the metric perturbation strength for + and × terms.

Name	f_{gw} [mHz]	Δ [ppm]	$h_{+,c}$	$h_{\times,c}$
SDSS J0651+2844	2.613013	10321.4	-1.56e-22	-1.68e-23
SDSS J0935+4411	1.683502	37037.0	-1.48e-22	-1.48e-22
SDSS J0106-1000	0.852515	852.5	-2.23e-23	-1.51e-23
SDSS J1630+4233	0.836820	1673.6	-2.18e-22	-2.18e-22
SDSS J1053+5200	0.543478	2717.4	-4.85e-23	-4.85e-23
SDSS J0923+3028	0.514933	-	-2.67e-22	-2.67e-22
SDSS J1436+5010	0.505433	2527.2	-1.17e-22	-1.17e-22
WD 0957-666	0.379520	0	-4.37e-22	-3.98e-22
SDSS J0755+4906	0.367309	-	-3.23e-23	-3.23e-23
SDSS J0849+0445	0.294118	-	-6.60e-23	-6.60e-23
SDSS J0022-1014	0.289771	-	-5.14e-23	-5.14e-23
SDSS J2119-0018	0.266773	-	-2.58e-23	-2.58e-23
SDSS J1234-0228	0.253165	-	-1.85e-23	-1.85e-23
WD 1101+364	0.159962	399.9	-4.20e-22	-4.18e-22

The quadrupole normal modes in the frequency range from 0.10 to 3 mHz (fitting the frequency range in Tab. 4.6) are ${}_{n}S_2, n = 0, \ldots, 7$. From the splitting and coupling selection rules these modes form chains listed in Tab. 4.7. Although the first eight quadrupole modes are the focus in this study, we included modes ${}_{n}S_2, n = 8, \ldots, 23$ to test the far off-resonance regime effect on these modes. The choice to use group-coupling approximation in the calculation of the splitting matrix is based upon the needed frequency resolution. In the normal mode studies the frequency uncertainties are present due to the theoretical computations, utilization of the different 3D Earth models and the biased measurements (for further clarification on biased measurements see Section 6.1). However, all these errors are smaller than frequency uncertainties that we find in the double white dwarf binary catalog showed in third column in Tab. 4.6. To compare frequency uncertainties from binary catalog with the ones obtained using different 3D Earth models, we calculated eigenfrequencies for two multiplet chains, namely ${}_{0}S_2$ - ${}_{0}T_2$ - ${}_{2}S_1$ - ${}_{0}S_3$ and ${}_{2}S_0$ - ${}_{7}S_2$ for five 3D models of the shear-velocity variations in Earth's mantle, namely S40RTS (Ritsema et al., 2011), SP16b30 (Masters et al., 1996), S20RTS (Ritsema et al., 1999), SP12RTS (Koelemeijer et al., 2016), S362ANI (Kustowski et al., 2008). Listed 3D models differ between themselves due to the

dissimilar data types used for their building and due to dissimilar modeling approaches. For example, S20RTS and S40RTS use collections of Rayleigh wave phase velocities, the teleseismic body-wave traveltimes and the normal mode splitting function measurements, while SP12RTS uses additionally the P-waves traveltimes measurements and the new splitting measurements of 33 normal modes sensitive to the compressional-wave velocity and 9 Stoneley modes; S16b30 uses the differential body wave traveltimes, the surface-wave phase velocities and the normal mode structural coefficients; S362ANI uses the Love- and Rayleigh-wave phase velocities, the mantle- and body-wave waveforms and the teleseismic bodywave traveltimes. Calculated synthetic split and coupled eigenfrequencies are compared for different models by computing relative errors $\frac{|f-f_r|}{f_r} \cdot 1000000$ [ppm], where f_r is the referent frequency, the one calculated for S40RTS model. The results in Fig. 4.12 show that differences between models are systematic, reaching maximum values up to 700 ppm, but in average are 116 ppm. Next, we examine the errors introduced by using the group-coupling approximation instead of the full-coupling one when calculating the split and coupled frequencies. For this purpose we calculate the frequencies in full-coupling approximation up to 3 mHz (Al-Attar et al., 2012). The results are shown in Fig. 4.13 in terms of the relative error between frequencies calculated in group- and full-coupling approximation with frequencies from group-coupling approximation as the referent ones. Relative errors are in average three times larger than for the 3D Earth models, thus around 370 ppm, reaching maximum values up to 1126 ppm. Nevertheless, these relative errors are still smaller than the frequency errors found in the binary catalog. Consequently, for the current work it is sufficient to consider only the group-coupling approximation when calculating the split and coupled normal mode eigenfrequencies, since the frequency uncertainties within the binary measurements are larger. For all further calculation we only use S40RTS model. Also, we calculate all responses for the BFO station.

Tab 4.7: List of the multiplet chains and their frequency ranges used in the group-coupling approximation for the splitting matrix calculation. Multiplet chains for ${}_{n}S_2, n = 0, \ldots, 7$ modes are adopted from Deuss and Woodhouse (2001). Multiplets from $n = 8$ to $n = 23$ are used to check the far off-resonance regime.

Multiplets	f [mHz]	Multiplets	f [mHz]
${}_0S_2$ - ${}_0T_2$ - ${}_2S_1$ - ${}_0S_3$	0.309 - 0.469	${}_{12}S_2$	4.330
${}_0T_3$ - ${}_0S_4$ - ${}_1S_2$	0.586 - 0.680	${}_{13}S_2$	4.845
${}_0T_5$ - ${}_2S_2$ - ${}_1S_3$ - ${}_3S_1$	0.928 - 0.944	${}_{14}S_2$	5.374
${}_3S_2$	1.106	${}_{15}S_2$	5.557
${}_5S_1$ - ${}_4S_2$ - ${}_0S_{10}$ - ${}_0T_{11}$ - ${}_1T_5$	1.714 - 1.750	${}_{16}S_2$	5.697
${}_5S_2$ - ${}_0T_{14}$ - ${}_1T_7$ - ${}_0S_{13}$	2.091 - 2.113	${}_{17}S_2$	6.395
${}_5S_4$ - ${}_4S_5$ - ${}_2S_{10}$ - ${}_2T_4$ - ${}_6S_2$	2.380 - 2.411	${}_{18}S_2$	6.545
${}_2S_0$ - ${}_7S_2$	2.510 - 2.517	${}_{19}S_2$	7.078
${}_8S_2$	3.214	${}_{20}S_2$	7.357
${}_9S_2$	3.231	${}_{21}S_2$	7.514
${}_{10}S_2$	4.032	${}_{22}S_2$	8.207
${}_{11}S_2$	4.058	${}_{23}S_2$	8.561

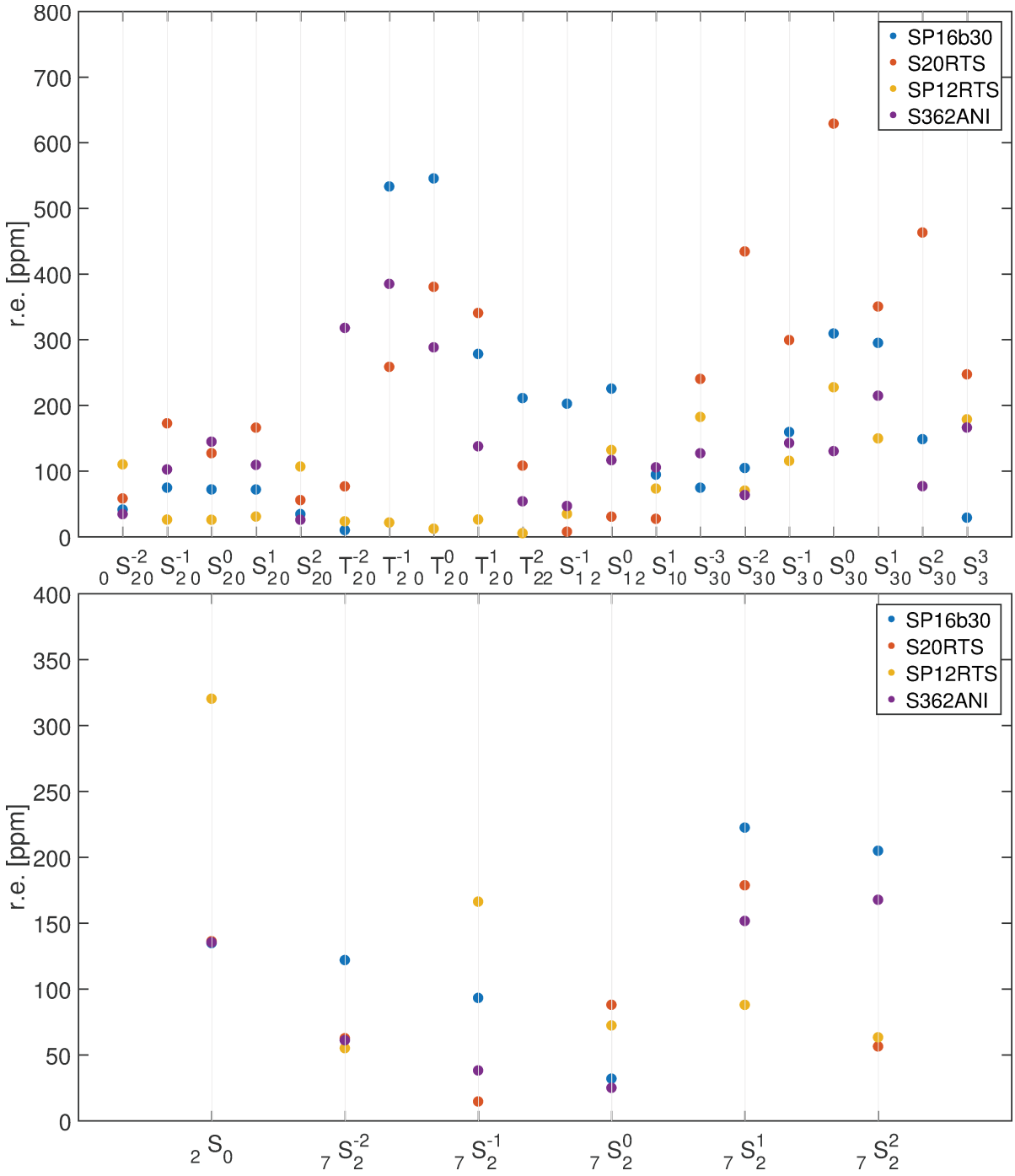

Fig 4.12: Split and coupled eigenfrequencies relative errors calculated for five models of the shear-velocity variations in Earth's mantle and two multiplet chains ${}_0S_2$ - ${}_0T_2$ - ${}_2S_1$ - ${}_0S_3$ (up) and ${}_2S_0$ - ${}_7S_2$ (bottom). Model S40RTS model is the referent one. y-axis stand for the relative error function.

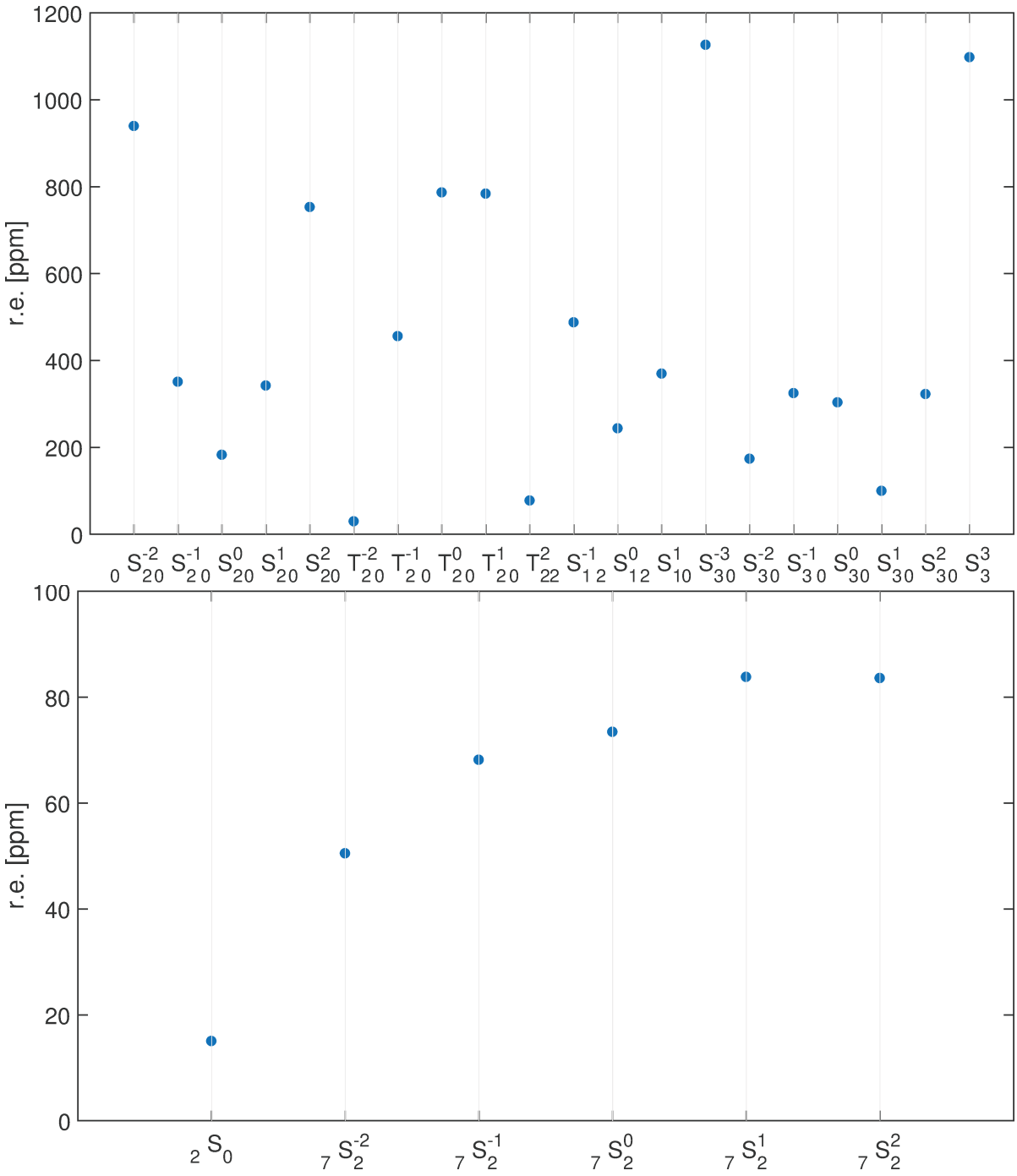

Fig 4.13: Split and coupled eigenfrequencies relative errors between full- and group-coupling approximations for two multiplet chains ${}_0S_2$ - ${}_0T_2$ - ${}_2S_1$ - ${}_0S_3$ (up) and ${}_2S_0$ - ${}_7S_2$ (bottom), with group coupling values as referent ones. Both set of frequencies (for full and group coupling) are calculated for S40RTS model. y-axis stand for the relative error function.

Comparing the exact GWs frequencies in Tab. 4.6 with the split and coupled quadrupole modes eigenfrequencies in Tab. 4.8 it is straightforward that we are not in a resonance regime and is it highly unlikely that we will ever be. Incorporating information from

the binary catalog in Tab. 4.6, the eigenfrequencies from Tab. 4.8 together with the displacement eigenfunctions, the model dependent functions ζ_k and the pattern functions $f^m_{+,\times}(\gamma(t), \alpha, \delta, \psi)$ we can calculate the complete induced spheroidal radial response for a rotating 3D Earth model to the incoming GWs. The results for each GW source are shown in Fig. 4.14 where all responses are summed in one total response, since on Earth we are receiving the summed response from all GW sources, and also on separate plot where they are plotted individually. The maximum spectral amplitudes for individual GW sources are listed in Tab. 4.10. We are primarily interested in the continuously forced motion, thus the frequencies of our responses are equal to GWs frequencies. If we scrutinize response for one catalog entry, let's say the first entry from the catalog (SDSS J0651+2844), a bit further by looking at its individual components for only one normal mode, for example ${}_0\mathrm{S}_2$, we can plot Fig. 4.15. We can see that the GW frequency of our response is split and this is consequence of the exponential functions within the pattern functions represented by expressions (4.143) and (4.144). These exponential functions depend on the right ascension angle and Greenwich Sidereal Time, in other words it means that the splitting of the GW frequencies is caused by rotation.

Tab 4.8: Split and coupled eigenfrequencies (in mHz) for 24 quadrupole modes calculated for S40RTS model.

Mode / m	-2	-1	0	1	2
${}_0S_2$	0.299874	0.304467	0.309087	0.313702	0.318335
${}_1S_2$	0.673504	0.677305	0.680566	0.683091	0.684999
${}_2S_2$	0.934869	0.936727	0.938229	0.939367	0.940150
${}_3S_2$	1.101922	1.105062	1.107022	1.108593	1.108834
${}_4S_2$	1.717967	1.721015	1.722665	1.723805	1.724158
${}_5S_2$	2.086851	2.090049	2.091603	2.093396	2.093913
${}_6S_2$	2.407423	2.409519	2.411163	2.412433	2.413250
${}_7S_2$	2.517429	2.516401	2.514741	2.519262	2.519715
${}_8S_2$	3.209084	3.212019	3.212971	3.215910	3.216284
${}_9S_2$	3.225804	3.230217	3.231335	3.234290	3.235501
${}_{10}S_2$	4.028591	4.031640	4.032067	4.034329	4.034675
${}_{11}S_2$	4.054522	4.057871	4.058929	4.060161	4.060605
${}_{12}S_2$	4.319723	4.326204	4.327935	4.332262	4.332948
${}_{13}S_2$	4.840962	4.841738	4.845084	4.848812	4.849457
${}_{14}S_2$	5.363416	5.372038	5.374407	5.379946	5.381128
${}_{15}S_2$	5.552475	5.556524	5.558518	5.559144	5.559708
${}_{16}S_2$	5.691855	5.693602	5.696764	5.700023	5.700832
${}_{17}S_2$	6.383572	6.392156	6.393636	6.400451	6.401756
${}_{18}S_2$	6.538620	6.540623	6.545051	6.549906	6.550698
${}_{19}S_2$	7.073365	7.077868	7.080399	7.080740	7.081474
${}_{20}S_2$	7.349424	7.351190	7.356375	7.361493	7.362804
${}_{21}S_2$	7.502535	7.513479	7.515454	7.523615	7.524762
${}_{22}S_2$	8.198689	8.200363	8.206567	8.211003	8.212599
${}_{23}S_2$	8.548147	8.560894	8.564423	8.572771	8.575040

Tab 4.9: Q-factors corresponding to the split and coupled eigenfrequencies for 24 quadrupole modes calculated for S40RTS model in Tab. 4.8.

Mode / m	-2	-1	0	1	2
${}_0S_2$	494.142110	501.707789	509.320483	516.925422	524.559878
${}_1S_2$	307.438499	309.151594	310.627192	311.775378	312.659810
${}_2S_2$	95.587854	95.820610	95.985271	96.062156	96.118498
${}_3S_2$	365.196019	366.236740	366.886285	367.407026	367.486779
${}_4S_2$	432.964520	433.728921	434.129037	434.410786	434.490357
${}_5S_2$	317.187615	317.673615	317.909833	318.182413	318.260972
${}_6S_2$	92.650176	92.722350	92.779936	92.834791	92.876552
${}_7S_2$	341.638798	341.991007	342.802680	342.952956	348.049296
${}_8S_2$	337.877156	338.186159	338.286414	338.595854	338.635213
${}_9S_2$	406.418421	406.974407	407.115289	407.487627	407.640126
${}_{10}S_2$	191.788285	191.933394	191.953731	192.061428	192.077912
${}_{11}S_2$	130.659712	130.767645	130.801712	130.841434	130.855726
${}_{12}S_2$	228.982397	229.325928	229.417716	229.647082	229.683414
${}_{13}S_2$	877.791921	877.932649	878.539316	879.215325	879.332293
${}_{14}S_2$	202.080223	202.405076	202.494342	202.703033	202.747577
${}_{15}S_2$	102.462099	102.536816	102.573610	102.585153	102.595569
${}_{16}S_2$	328.351345	328.452141	328.634546	328.822561	328.869214
${}_{17}S_2$	230.712993	231.023232	231.076696	231.323015	231.370179
${}_{18}S_2$	532.563443	532.726570	533.087255	533.482661	533.547178
${}_{19}S_2$	90.782761	90.840555	90.873048	90.877423	90.886844
${}_{20}S_2$	514.945983	515.069696	515.432982	515.791573	515.883464
${}_{21}S_2$	218.103160	218.421318	218.478731	218.715966	218.749334
${}_{22}S_2$	714.897810	715.043807	715.584783	715.971593	716.110714
${}_{23}S_2$	199.519432	199.816977	199.899331	200.094193	200.147139

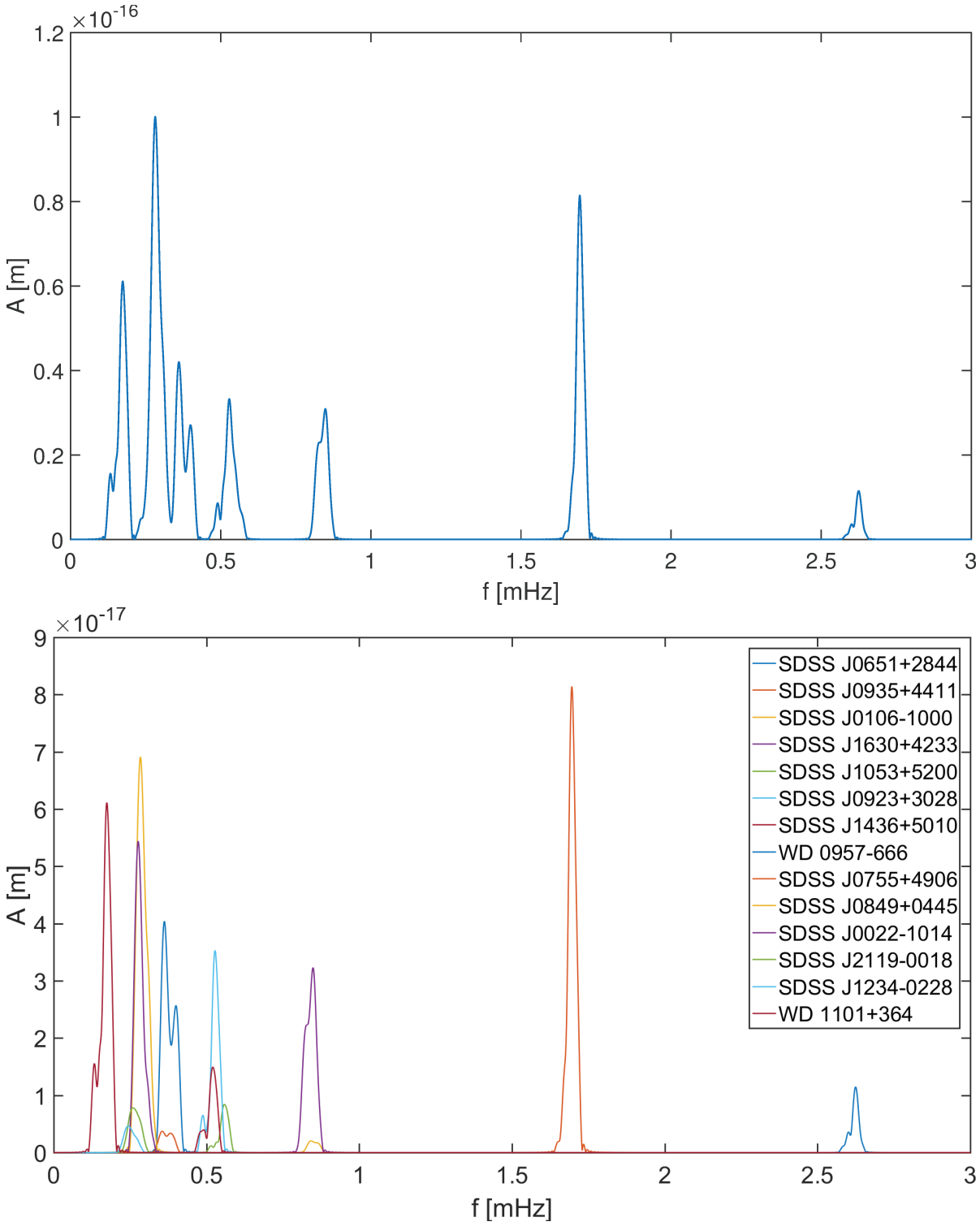

Fig 4.14: Induced spheroidal radial response for 14 GW sources from Tab. 4.5 when all responses are summed together (up) and when each response is plot individually (bottom) for one day long signals.

Tab 4.10: Maximum spectral amplitudes of the induced spheroidal radial responses shown in Fig. 4.14.

Name	A [$\cdot 10^{-18}$m]	A [$\cdot 10^{-22}$m/s^2]
SDSSJ0651+2844	11.47999	30.94457
SDSSJ0935+4411	81.43515	91.11686
SDSSJ0106-1000	2.04780	0.58756
SDSSJ1630+4233	32.30985	8.93221
SDSSJ1053+5200	8.42014	0.98185
SDSSJ0923+3028	35.31244	3.69649
SDSSJ1436+5010	14.95197	1.50795
WD0957-666	40.41132	2.29791
SDSSJ0755+4906	3.72761	0.19854
SDSSJ0849+0445	69.10639	2.36004
SDSSJ0022-1014	54.40300	1.80340
SDSSJ2119-0018	7.80692	0.21934
SDSSJ1234-0228	4.63214	0.11721
WD1101+364	61.13572	0.61757

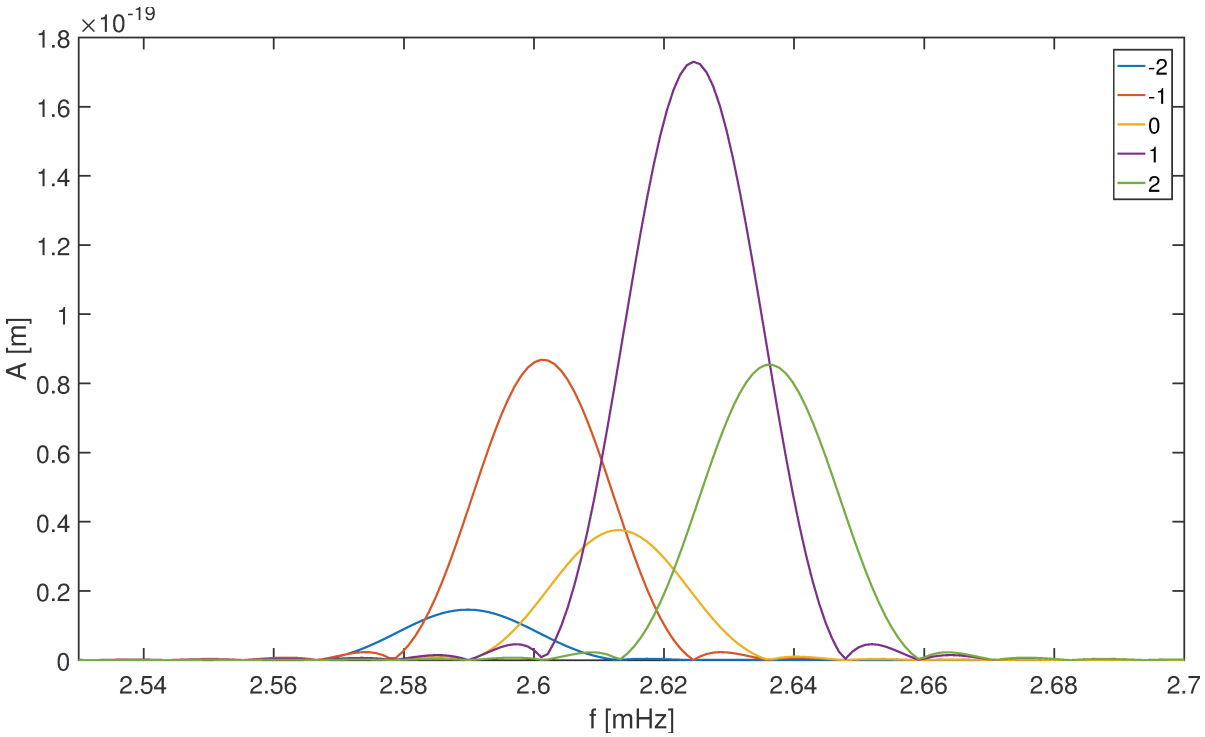

Fig 4.15: Induced spheroidal radial response of the GW source SDSS J0651+2844 split into five singlets.

Besides defining the splitting of the GW frequency, the pattern functions are also important since they define which singlets are going to be excited based on the declination δ and the polarization ψ angles of the binary system. For visualization we plot the dependency of the pattern functions on these two angles for different azimuthal orders for $f_+^m(\gamma(t), \alpha, \delta, \psi)$ in Fig. 4.16 and for $f_\times^m(\gamma(t), \alpha, \delta, \psi)$ in Fig. 4.17 where we set $\gamma(t), \alpha = 0$. From figures it is clear that there exist combinations of the declination andthe polarization angles when singlet defined by specific azimuthal order m is not going to be excited. The characteristics of the pattern functions are twofold. Firstly, if one has a possibility to measure only one or few of the excited singlets one can obtain a range of possible declination and polarization angles where this pattern would be possible. Secondly, if one can measure the frequency of the binary star with good precision then one can calculate the right ascension angle by observing how much the GW frequency is split. Our analytical response model confirms that the frequency uniquely depends on the GW frequency of the binary system, the right ascension angle and Greenwich Sidereal Time.

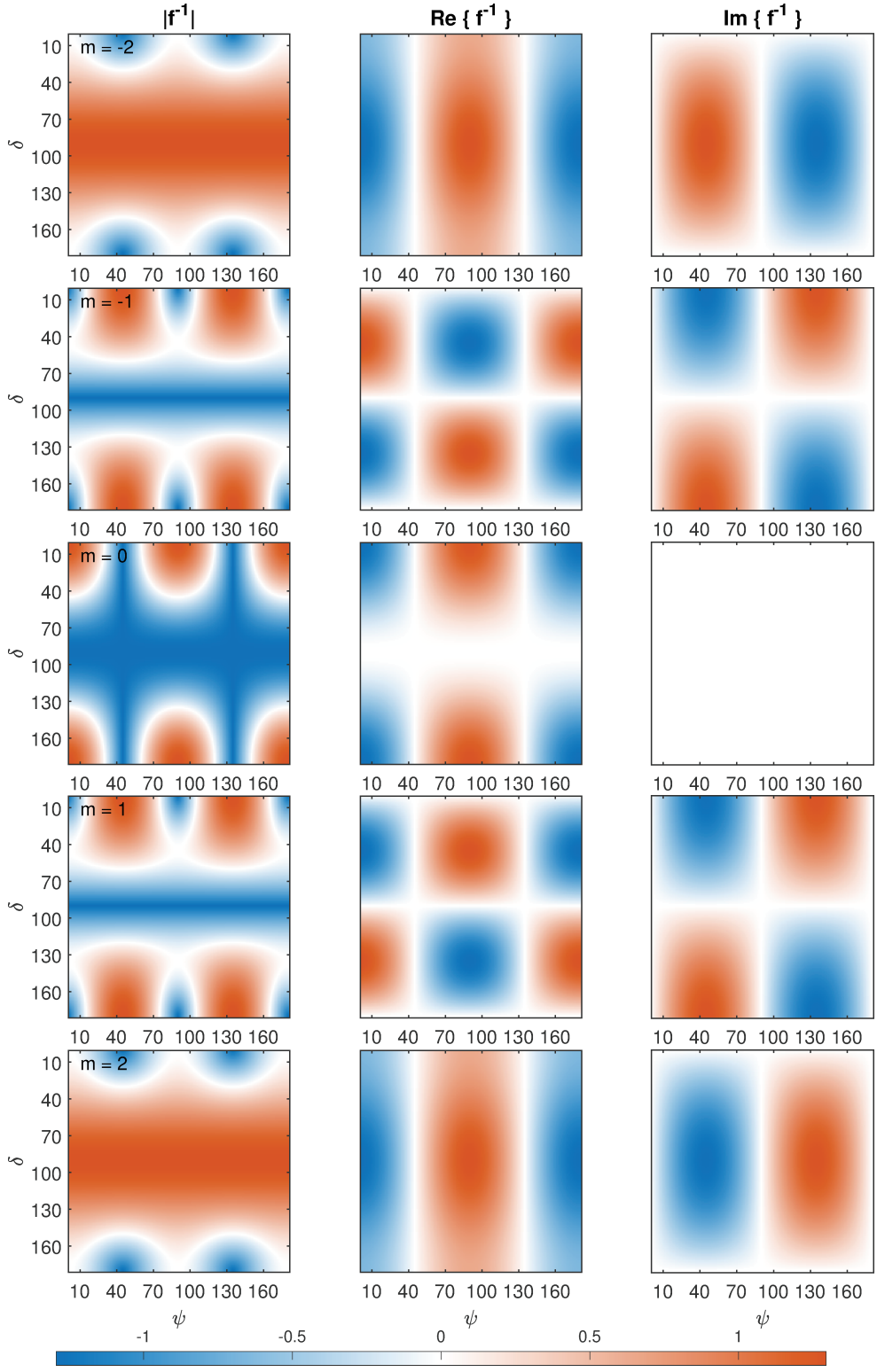

Fig 4.16: Pattern function $f_+^m(\gamma(t), \alpha, \delta, \psi)$ values for the declination δ versus the polarization ψ angles where Greenwich Sidereal Angle and the right ascension angle are set to zero ($\gamma(t) = 0, \alpha = 0$). From up to down each row stands for five azimuthal orders $m = -2, -1, 0, 1, 2$, respectively. From left to right each column stand for absolute, real and imaginary part of the function, respectively.

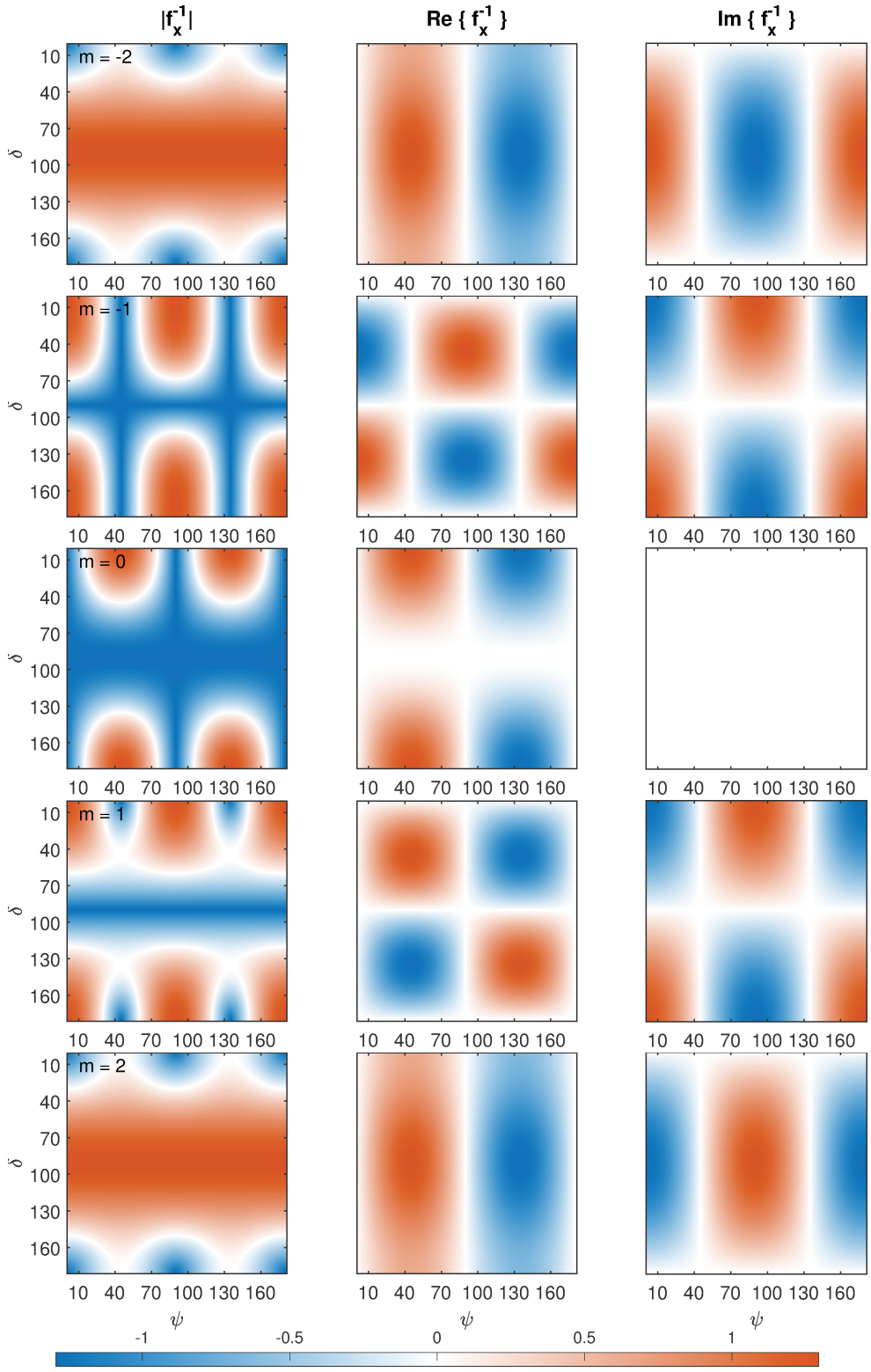

Fig 4.17: Same as Fig. 4.16 just for pattern function $f_{\times}^{m}(\gamma(t), \alpha, \delta, \psi)$.

If we go back to the full response shown in Fig. 4.14 we need to remind ourselves that

each of these displacements are defined as a collective contribution of 24 quadrupole modes. However, not all quadrupole modes contribute equally in the building of the response for a particular GW source. This statement is demonstrated in Fig. 4.18 for the first entry in the binary catalog, SDSS J0651+2844. The plot represents only response amplitude values for each mode and their singlets that are used to construct response for this particular GW source. Therefore, each row represents one quadrupole mode ${}_{\rm n}{\rm S}_2$ where $n = 0$ is the first row and $n = 23$ is the last row. Each column represents one azimuthal order, from left to right $m = -2, -1, 0, 1, 2$, respectively. Amplitudes are normalized by the maximum amplitude within all estimates. This particular source has a frequency that is closest to the frequency of ${}_7{\rm S}_2$ mode, whose singlets amplitudes are shown in the 8th row on the figure. It is no surprise that this mode contributes the most for this particular GW source, because in this case we are closest to the resonance regime based on the source-time functions (see (4.133) and (4.134)) shown in Fig. 4.19. Further, it is interesting that although ${}_6{\rm S}_2$ mode is close to this particular source frequency it does not have a sizeable effect. To understand this result it is useful to look individually at the values of functions that constitutes the response, such as the source-time functions amplitudes and the Q-factors, for these two modes. The values of source-time functions $\bar{g}_+(t, \Omega, \omega_k)$ and $\bar{g}_\times(t, \Omega, \omega_k)$ with $t = 0$ for the first entry in binary catalog are shown in Fig. 4.20. For both functions the most significant values are the ones for ${}_7{\rm S}_2$ mode, but we see that ${}_6{\rm S}_2$ mode is just behind ${}_7{\rm S}_2$ with twice smaller amplitudes. However, if we look at the amplitudes values, that consist of jointly contributions from the displacement eigenfunctions and the model dependent function ζ_k, for all modes and their singlets used in this study shown in Fig. 4.21, we see that ${}_6{\rm S}_2$ mode has significantly smaller amplitude than ${}_7{\rm S}_2$ mode. Therefore, both effects generate the final result that we see in Fig. 4.18. The complete response amplitudes for all other sources are shown in Fig. 4.22, 4.23, 4.24. Since GW sources in Fig. 4.23, 4.24 are closes to ${}_0{\rm S}_2$ mode (see Fig. 4.19) singlets of this mode contribute the most to the responses for these sources. The case of five sources (SDSS J0106-1000, SDSS J1630+4233, SDSS J1053+5200, SDSS J0923+3028, SDSS J1436+5010) in Fig. 4.22 is interesting one since all these modes have frequencies between and close to ${}_2{\rm S}_2$, ${}_1{\rm S}_2$ and eventually ${}_0{\rm S}_2$ mode. However, the largest contributions are mostly accomplished for ${}_3{\rm S}_2$, ${}_4{\rm S}_2$ modes. This is mostly predetermined by the amplitude values shown in Fig. 4.20. For same reason, we also observe ${}_7{\rm S}_2$ mode quite persistently. When approaching smaller frequencies the influence of ${}_0{\rm S}_2$ largely predominates. Next, the case of sources SDSS J0106-1000 and SDSS J1630+4233 is also an appealing one. These two sources have quite close frequencies and their response amplitudes have same pattern, however with different intensities compared to the maximum value. In conclusion, it seems that prevailing factor is not coming only from the closeness of the GW source frequencies to

the normal mode frequencies. The ${}_2S_2$ mode is rarely ever having large contribution since this mode has a very small amplitude values.

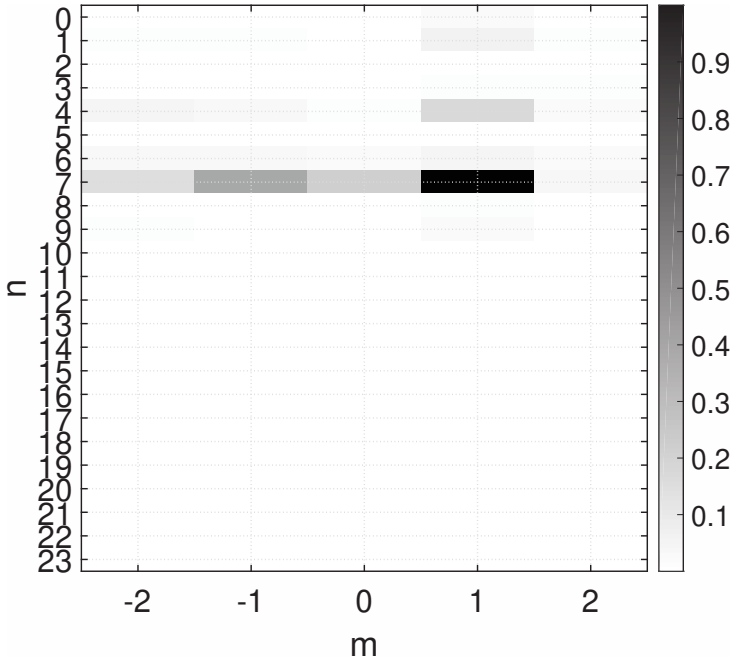

Fig 4.18: Normalized response amplitudes for SDSS J0651+2844 source frequency 2.61 mHz for all quadrupole modes and their singlets used for building the complete response for this particular source. The rows represent quadrupole modes ${}_nS_2$ where $n = 0$ is the first row and $n = 23$ is the last row. Each column represents one azimuthal order, from left to right $m = -2, -1, 0, 1, 2$, respectively.

Fig 4.19: Comparison of the quadrupole modes frequencies for ${}_n\mathrm{S}_2$, $n = 0, 1, 2, 3, 4, 5, 6, 7$ with the orbital frequencies of the binary systems listed in Tab. 4.5.

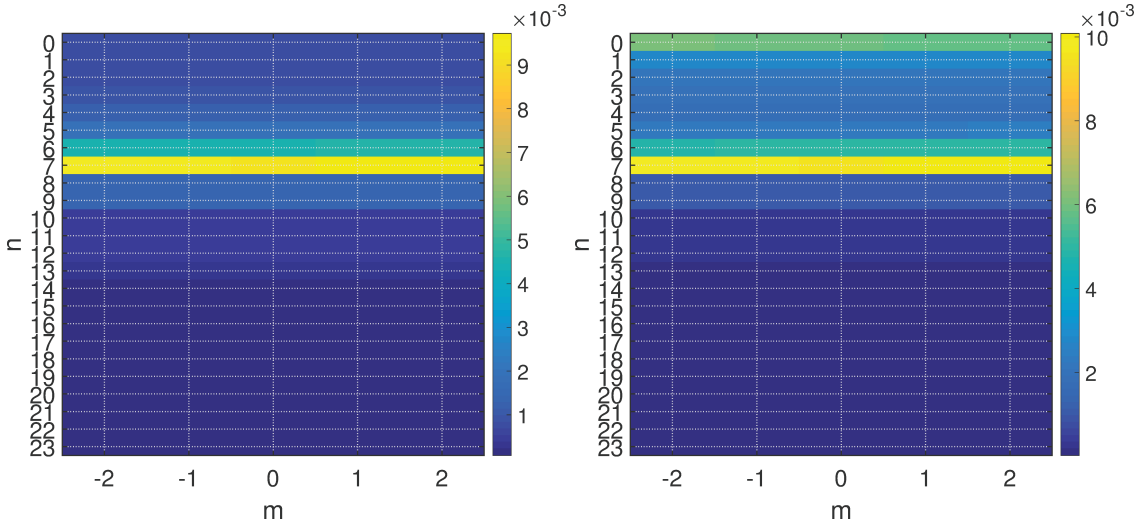

Fig 4.20: Amplitudes of the source-time functions $\bar{g}_+(t, \Omega, \omega_k)$ (left) and $\bar{g}_\times(t, \Omega, \omega_k)$ (right) with $t = 0$ and for SDSS J0651+2844 source. The rows represent quadrupole modes ${}_n\mathrm{S}_2$ where $n = 0$ is the first row and $n = 23$ is the last row. Each column represents one azimuthal order, from left to right $m = -2, -1, 0, 1, 2$, respectively.

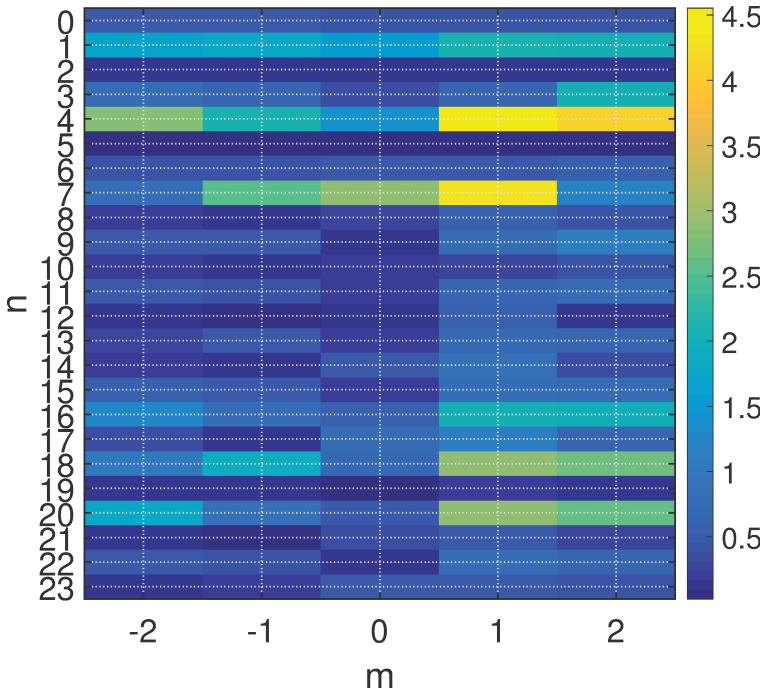

Fig 4.21: Amplitudes in terms of jointly contributions from displacement eigenfunction and model dependent functions ζ_k for all quadrupole modes ${}_{\mathrm{n}}\mathrm{S}_2$, where $n = 0$ is the first row and $n = 23$ is the last row. Each column represents one azimuthal order, from left to right $m = -2, -1, 0, 1, 2$, respectively.

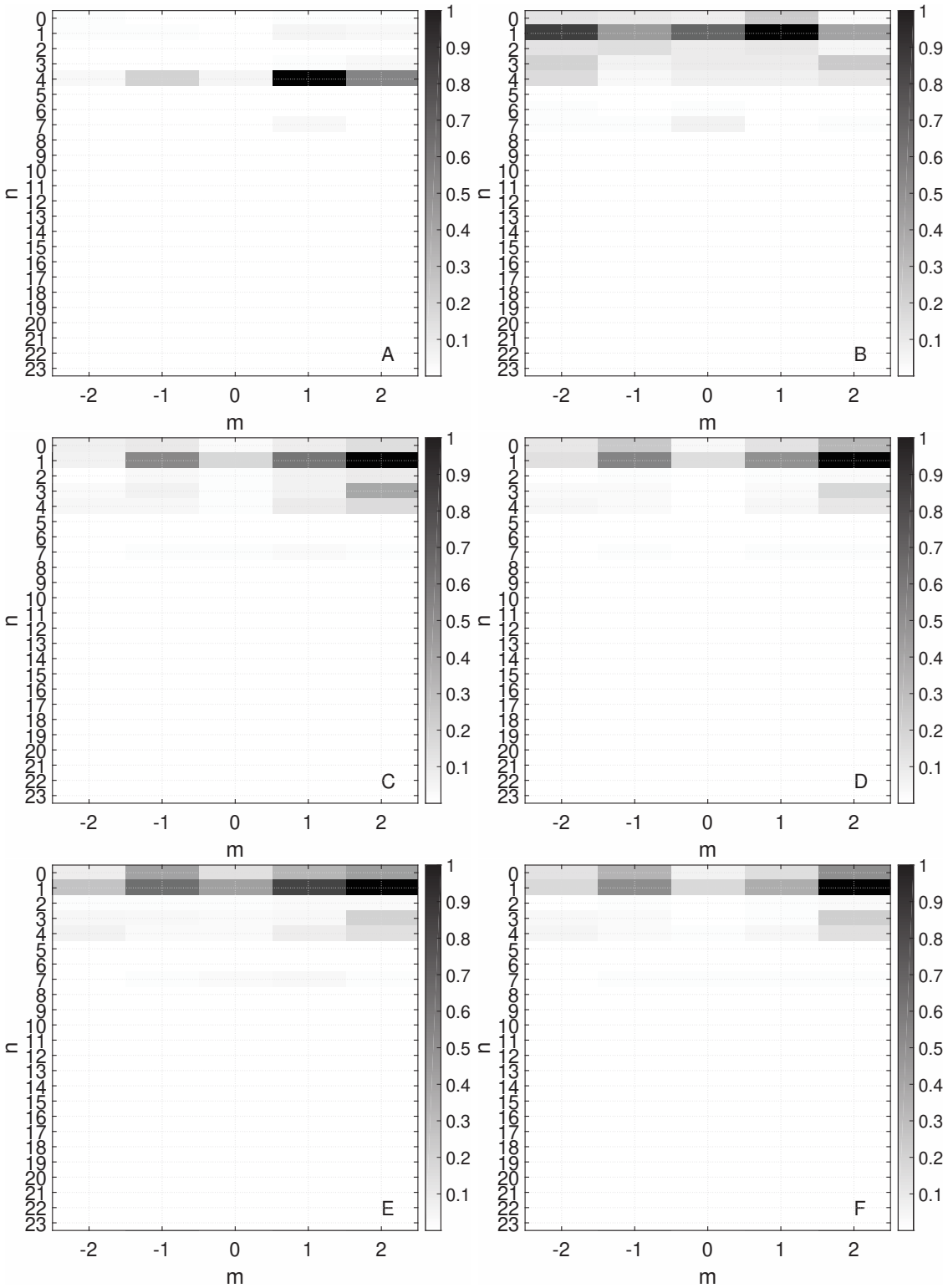

Fig 4.22: Same as Fig. 4.18 but for sources A) SDSS J0935+4411, B) SDSS J0106-1000, C) SDSS J1630+4233, D) SDSS J1053+5200, E) SDSS J0923+3028, F) SDSS J1436+5010 from left to right and up to bottom, respectively.

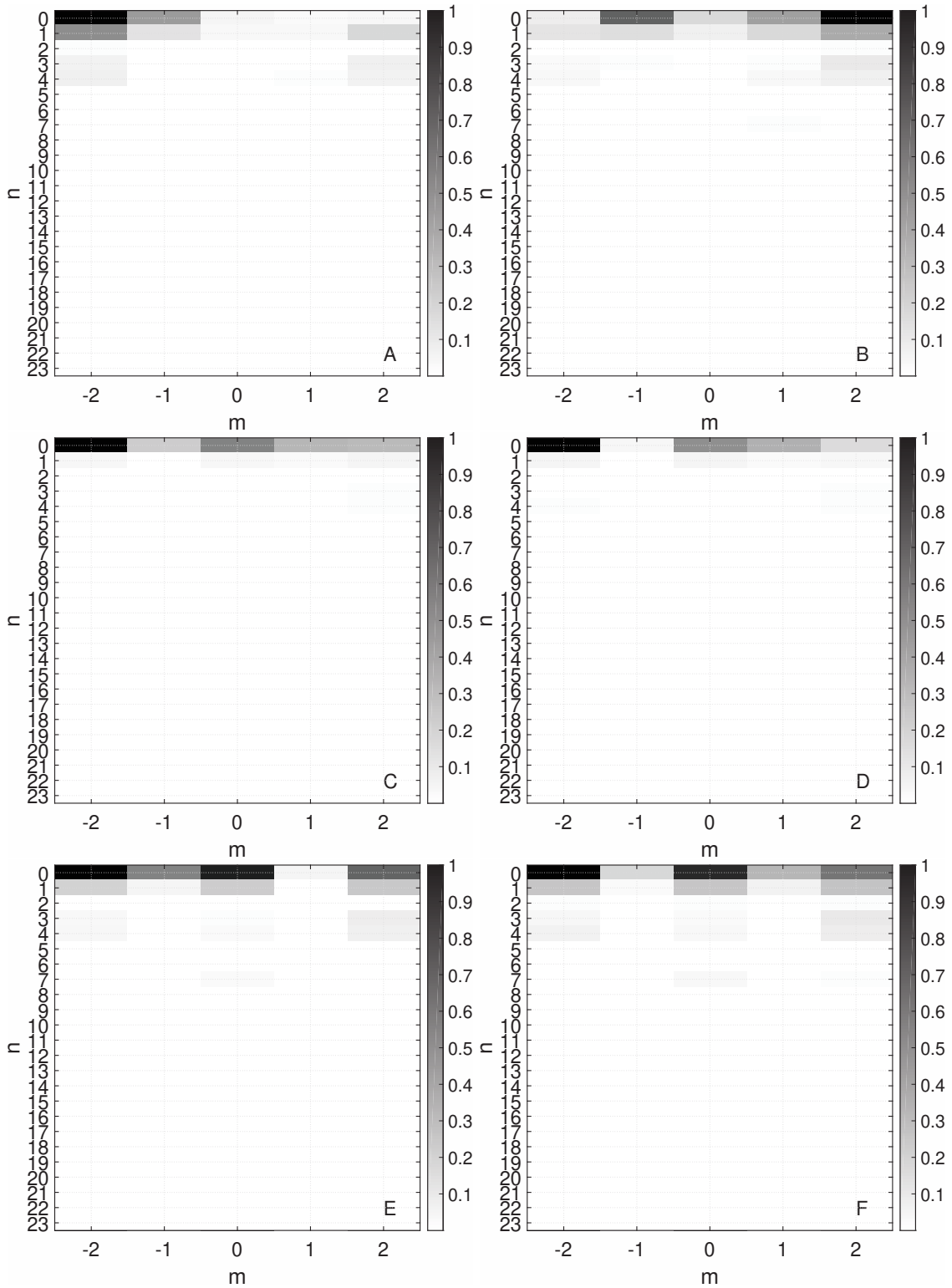

Fig 4.23: Same as Fig. 4.18 but for sources A) WD 0957-666, B) SDSS J0755+4906, C) SDSS J0849+0445, D) SDSS J0022-1014, E) SDSS J2119-0018, F) SDSS J1234-0228 from left to right and up to bottom, respectively.

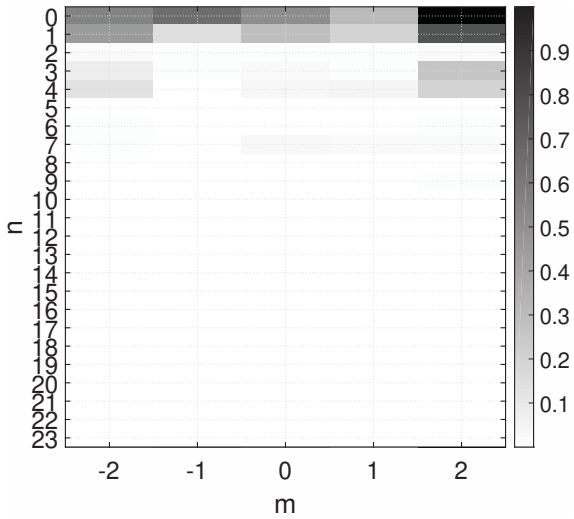

Fig 4.24: Same as Fig. 4.18 but for source WD 1101+364.

The response of the rotating Earth model to the GWs from a binary star system can be quantitatively compared to the response of the non-rotating Earth model to the GWs from the general source described by scalar value h_0 and angles $\{e, \lambda, \nu\}$ from Section 4.2.3. As emphasized earlier all responses for the rotating model are the off-resonance responses because the GW frequencies are not equal to normal mode frequencies. This implies that these responses could be larger in the resonance case. We focus on the second GW source from the binary catalog, SDSS J0935+4411, since this GW source has the largest response according to Tab. 4.10. Thus, for the S40RTS Earth model, J0935+4411 GW source, $t = 0$ at the BFO station the radial response amplitude for $l = 2, m = 1$ is

$$s_r = 6.0 \cdot 10^{-8} \text{ nm } (1.683502 \text{ mHz}). \tag{4.149}$$

Considering different frequency ranges the largest amplitude around the frequency of ${}_0\mathrm{S}_2$ mode comes from the GW source J0849+0445 and for this source the radial response amplitude using same parameters as above is

$$s_r = 1.0 \cdot 10^{-8} \text{ nm } (0.294118 \text{ mHz}). \tag{4.150}$$

If for the comparison we set that GW frequency for J0849+0445 source is equal to the frequency of ${}_0\mathrm{S}_2$ normal mode we obtain value for the radial response amplitude, just for ${}_0\mathrm{S}_2$ multiplet, to be

$${}_0s_2^2 = 2.2 \cdot 10^{-6} \text{ nm } (0.313702 \text{ mHz}) \tag{4.151}$$

which is two orders of magnitude larger than both responses (4.149) and (4.150). This value can be compared with the estimate of the induced radial displacement for the non-rotating model defined by relation (4.39). We also consider resonance response and ${}_0\mathrm{S}_2$

mode. Further, since this model requires three source angles $\{e, \lambda, \nu\}$ we set these to $\{e = \frac{\pi}{2}, \lambda = 0, \nu = 0\}$. Finally, the response for $t = 0$ and BFO station is

$$ {}_0s_2^2 = 9.4 \cdot 10^{-8} \text{ nm } (0.309262 \text{ mHz}). \tag{4.152}$$

Even though values at the resonance for the two models are not obtained in completely same conditions (e.g. the source angles for a non-rotating model versus the right ascension and the declination angles for a rotating model), still comparing them we notice that there is one to two orders of magnitude difference. One or two orders of magnitude difference comes from the source-time functions definition. For the non-rotating model the source-time function for $t = 0$ and at resonance, based on relation (4.39), is

$$ |\Re\{\bar{g}(t=0)\}| = \frac{1}{2\pi} \frac{4Q^2}{(4Q^2+1)\omega_k^2}, \tag{4.153}$$

and for the rotating model based on (4.133) and (4.134) we have

$$ |\Re\{\bar{g}_+(t=0)\}| = \frac{1}{2\pi} \frac{4Q^2}{(16Q^2+1)\omega_k^2}, \tag{4.154}$$

$$ |\Im\{\bar{g}_+(t=0)\}| = \frac{1}{\pi} \frac{8Q^3}{(16Q^2+1)\omega_k^2}, \tag{4.155}$$

$$ |\Re\{\bar{g}_\times(t=0)\}| = \frac{1}{\pi} \frac{4Q^3(8Q^2-1)}{(1+20Q^2+64Q^4)\omega_k^2}, \tag{4.156}$$

$$ |\Im\{\bar{g}_\times(t=0)\}| = \frac{1}{\pi} \frac{24Q^4}{(1+20Q^2+64Q^4).\omega_k^2}, \tag{4.157}$$

If we calculate the relative ratio between (4.154), (4.155), (4.156), (4.157) and (4.153) we get

$$ \frac{|\Re\{\bar{g}_+\}|}{|\Re\{\bar{g}\}|} \approx 0.25, \tag{4.158}$$

$$ \frac{|\Im\{\bar{g}_+\}|}{|\Re\{\bar{g}\}|} \approx Q, \tag{4.159}$$

$$ \frac{|\Re\{\bar{g}_\times\}|}{|\Re\{\bar{g}\}|} \approx \frac{8Q}{10+32Q^2}, \tag{4.160}$$

$$ \frac{|\Im\{\bar{g}_\times\}|}{|\Re\{\bar{g}\}|} \approx \frac{6}{10+32Q^2}, \tag{4.161}$$

where we have assumed that $Q \geq 100$. Therefore, the substantial contribution is coming from (4.155) due to (4.159), which also explains one to two orders of magnitude difference between the two models.

Furthermore, the induced spheroidal displacement that we developed for the elliptical and rotating Earth model in the Section 4.3.4 could be improved by considering the shear modulus perturbation. The Dyson force term (4.8) originally contain the shear modulus

gradient. Since in this work we only consider the radially dependent shear modulus the only term that contributes to the force term is the partial derivation along the radial component. However, we could improve this by adding the perturbation of the shear modulus defined as

$$\delta\mu = \frac{2}{3} r\epsilon \frac{\partial \mu}{\partial r} P_2(\cos\theta), \tag{4.162}$$

where ϵ is ellipticity (Dahlen and Tromp, 1998). This would add an additional term in our force term and then consecutively additional terms in our induced spheroidal solution. Likewise, observing the shear modulus profile (see PREM model profile on Fig. 4.25), as we argued before, we notice that this modulus has two discontinuities, precisely one at the free surface and one at the core mantle boundary. It should be emphasized that these two discontinuities have different contributions to the force term and consequently to the final solution.

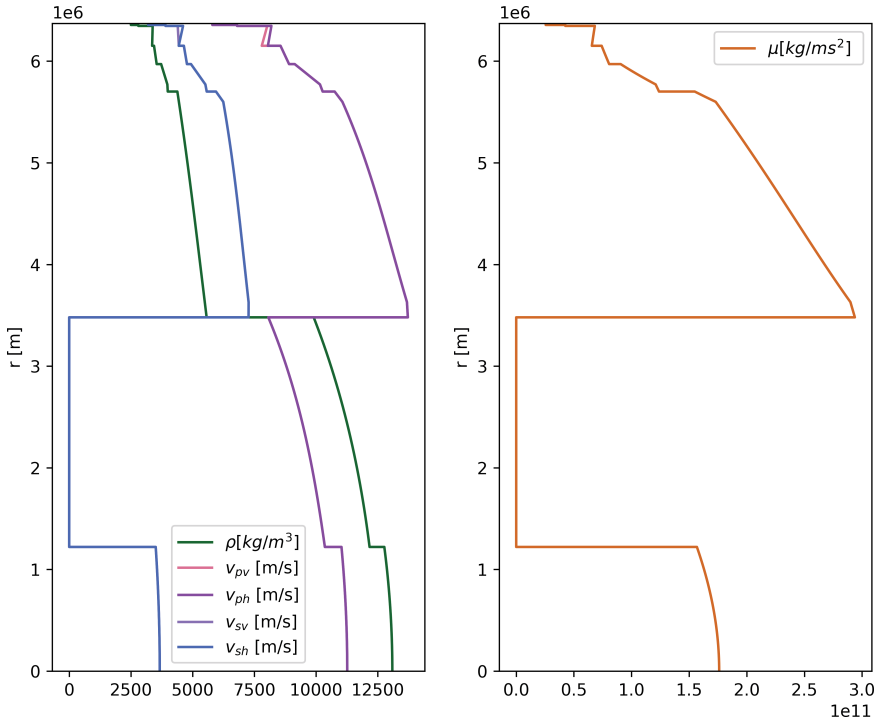

Fig 4.25: Density, horizontal and vertical P-velocity, horizontal and vertical S-velocity profiles (left) and shear modulus profile (right) of the PREM model.

4.3.6 Conclusion

In this section we have developed a new interaction model between a rotating anelastic Earth and GWs from the binary star sources. The interaction is expressed in terms of the response displacement. The model is based on several assumptions:

- the GW expressed in terms of the metric perturbation is defined for the binary star system in the celestial reference frame;
- the binary star system is defined by five parameters which are the masses of two stars, the GW frequency, the distance to the source and the inclination angle, all taken from the LISA verification binary catalog;
- the rotation from the celestial to terrestrial reference frame introduces four angles into the final response which are the right ascension, the declination, the polarization angle and Greenwich Sidereal Time angle;
- the considered Earth model is rotating and anelastic defined by Green tensor consisting of real radial eigenfunctions and complex spherical harmonics;
- the model also involves splitting of and coupling between normal modes calculated in the group-coupling approximation by defining the narrow band splitting matrix.

The final induced response depends on five functions: the radial displacement, the spherical harmonic depending on the location at the Earth surface, the scalars $h_+, h_\times$, the source-time functions $\hat{g}^m_{+,\times}(t, \Omega, \omega_m)$, the pattern functions $f^m_{+,\times}(\gamma(t), \alpha, \delta, \psi)$. The calculation once again confirmed that the only normal modes that couple with GWs are quadrupole ones. Therefore, the full response is defined as a summation over all radial n and azimutal m orders for $l = 2$. Fundamentally, in this model we are still interested in continuous forced motion. It has been also shown that due to the rotation the GW frequency is being split into five GW frequencies. Since the GW frequencies from binary star systems are not equal to the normal mode split and coupled eigenfrequencies we are also dealing with an off-resonance regime. During the modeling the split and coupled normal mode eigenfrequencies are calculated in a group-coupling approximation, because the errors introduced by this approximation are smaller than the uncertainties found in the catalog of binary star systems. It has been also shown that the each response obtained for one GW source is calculated by summing over 24 normal modes which do not contribute equally to the final displacement value. This effect is jointly determined by the source-time function (the closeness of the GW frequency to the split normal mode eigenfrequencies), then displacement eigenfunctions and the model dependent function ζ_k. The final estimates of the induced off-resonance displacement values are between $10^{-18} - 10^{-17}$ m.

Further, the detection possibilities of the induced spheroidal radial displacement developed in this section are studies in Chapter 5.

Chapter 5

Search for Gravitational Waves Using Matched Filtering

Detection of the small signals buried in the noise is very well covered topic in geophysical and physical studies, however it still presents a great challenge. The problem consists of understanding the characteristic of the target signal, its modeling and all possible included approximations; developing functional techniques that are not, preferably, time consuming for extracting the target signals from the noisy data; the acquisition of data in the preferred configuration and also using the instruments that have the required sensitivity level; the characterization of the noise existing in the measured data, that is identifying and removing everything that is not the target signal. In this chapter we are considering the second point in the context of the GW studies. In GW studies the usual target is the modeled signal and its detection is performed by utilizing the matched filtering technique (see Appendix B). Generally, one does not really know if the signal is present in the data and if it is present what is the starting time. The matched filter technique can answer to these two question simultaneously and therefore is more suitable in the GW studies over, for example, the Fourier transform.

In this chapter we consider the induced response developed in the Section 4.2.5 and we scrutinize how this signal could be found in the data measurements.

5.1 Introduction

In general, we consider that our instrument or detector as an output has a conventional form $d(t) = n(t)+w(t)$, where $d(t)$ is the data, $w(t)$ is the target signal and $n(t)$ is the noise. When dealing with the GW signals we are dealing with a case where $n(t) \gg h(t)$ and the question is how to detect the target signal when the signal itself is overwhelmed by the noise. In this situation we are compelled to know the signal at some level of accuracy. Each model is subjected to many approximations due to the difficulties in theoretical computations and

also due to the uncertainties introduced by the measurements of the parameters used in the model. In this section we acknowledge the standard deviations found in the catalog of the binary stars (see Tab. 4.5) and we study how these uncertainties influence the final response model from Section 4.3. Further, we utilize the matched filtering technique and perform several synthetic tests to scrutinize the performances of this technique.

5.2 Synthetic tests

Our analytical model from Section 4.3 depends on the binary star parameters which are obtained by measurements and naturally come with measurement uncertainties. The parameters modify either the amplitude or the amplitude and the frequency of our modeled waveform. For the purpose of understanding how the parameter's catalog uncertainties are affecting our waveform we perform sensitivity tests (Hamby, 1995). They consist of defining the range of possible values for each parameter determined by the standard deviations found in the catalog. For example, if p is the parameter and Δp is the parameter's standard deviation we can define range as

$$r_p = \{p - \Delta p, p + \Delta p\}, \tag{5.1}$$

with the step $\Delta r_p = \frac{2\Delta p}{n}$ defined to have n values in the range. There are seven parameters under consideration: the mass, the inclination angle, the declination angle, the right ascension angle, the distance, the polarization angle and the GW source frequency. For each parameter and for each value from its defined range of values we calculate waveform and by this generate a group of waveforms called a "bank of templates". We chose to work with one GW source from the binary catalog and that is SDSS J0935+4411, because this source has the largest amplitude based on Tab. 4.10. All waveforms within the bank of templates are calculated for the first eight multiplets and for all five singlets within the multiplet. We compute one day long signals with the sampling rate of 60 s and with the Greenwitch Sidereal Angle defined for 2012 year (see Appendix A). We also work with the acceleration response, because later on we combine this signal with the gravimetric data. The results for each parameter are shown in Fig. 5.1, 5.2 and 5.3. The bank of templates for the mass, the declination angle, the right ascension and the distance are showing the variability of the waveforms amplitudes, with the mass parameters having the largest variability. The bank of templates for the inclination angle, the polarization angle and the frequency are bit more complex. Since templates for the inclination angle are defined in range from 0 to π we see the influence of the $h_{+,c}$ and the $h_{\times,c}$ scalar values (see (4.114) and (4.115)), because for the defined range these scalar values change from one minimum to the other minimum and from the minimum to maximum values, respectively. The polarization angle is acting

through patter functions $f_+^m(\gamma(t),\alpha,\delta,\psi)$ and $f_\times^m(\gamma(t),\alpha,\delta,\psi)$ (see (4.143) and (4.144)). The values of these functions for the range of the polarization angle from 0 to π, when other angles are fixed (see Fig. 4.16 and 4.17), is showing us the difference between the two pattern functions. This is further expressed in the bank of templates where the singlets $m = \{-2,-1,0\}$ gradually merge. The bank of templates for the frequency parameter is the most specific one, since here the amplitude and the frequency of each wavefrom is affected. This is defined by the source-time function (see (4.133) and (4.134)).

Further, we define the sensitivity tests in the frequency domain by calculating expressions

$$\begin{aligned} s_1(f) &= |w(f;p-\Delta p+\Delta r_p)-w(f;p_d)| \\ &\vdots \\ s_n(f) &= |w(f;p-\Delta p+n\Delta r_p)-w(f;p_d)|, \end{aligned} \tag{5.2}$$

where w stands for the waveform from the bank of templates and p_d is the default parameter value for which the range was calculated at the first place. The results for the sensitivity tests for all seven parameters are shown in Fig. 5.4 and 5.5. On the horizontal axis we have a frequency and on the vertical axis we either write the parameter for which the signal was calculated (the inclination and the polarization angle) or we express differences between the parameter for which signal was calculated and default parameter by calculating relative error (the mass, the declination angle, the right ascension angle, distance, the GW source frequency). This was necessary since the inclination and the polarization angles are most of the time undefined, therefore the full range of all possible angles with non repeated values is taken as input for these two parameters. As expected all the parameters expect the frequency alter only the amplitude of the signals. Notice that scale for each parameter is different, where lowest to largest scale correspond to the declination, the distance, the right ascension, the mass, the inclination, the polarization angle and the GW source frequency, respectively. If for the purpose of further comparison we exclude results for the inclination and the polarization angle, we see that between the other five parameters the frequency is the best constrained, however it also has the largest sensitivity. Thus, even small change is producing a significant influence on the signal compared to other five parameters. For the frequency sensitivity plot in Fig. 5.5 we see that the largest deviations from the default signal generate even two frequency peaks, due to the fact that two subtracted signals have two different frequencies. In addition, changing the frequency between different templates also modify the amplitude of the templates, since amplitude depends on the relative difference between the GW source frequency and the normal mode eigenfrequencies. Also, for the frequency only one template within the bank of templates has the largest amplitude, but this doesn't need to be the template computed for the default

parameter, which is use as a referent template when calculating the sensitivity tests. This is apparent on the sensitivity results in Fig. 5.5, because the largest value (the most dissimilar value) is not associated for the edge of the range. Further, the right ascension and the declination angles seems to be defined with good accuracy in the catalog, but for the purpose of this test we artificially set standard deviations to be 5 degrees. The declination is better constrained, since it has smaller sensitivity.

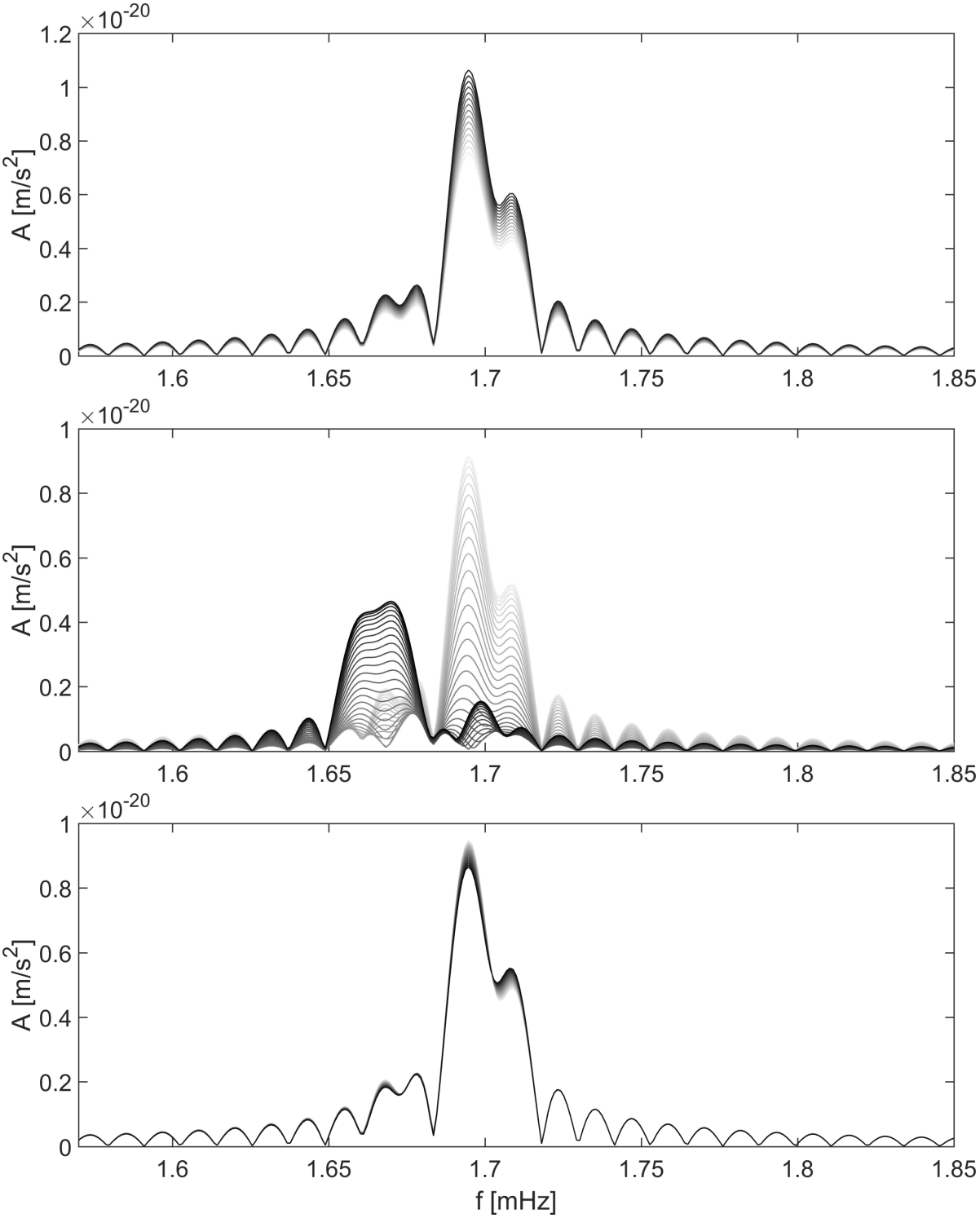

Fig 5.1: Bank of the acceleration templates for the mass (up), the inclination angle (middle) and the declination angle (bottom) parameter. The bank of templates for the mass parameter is defined by the standard deviations from the catalog of the binaries, for the inclination angle the full range of non-repeating angles is considered and for the declination angle we artificially set standard deviation to be 5°. The result is for SDSS J0935+4411 source.

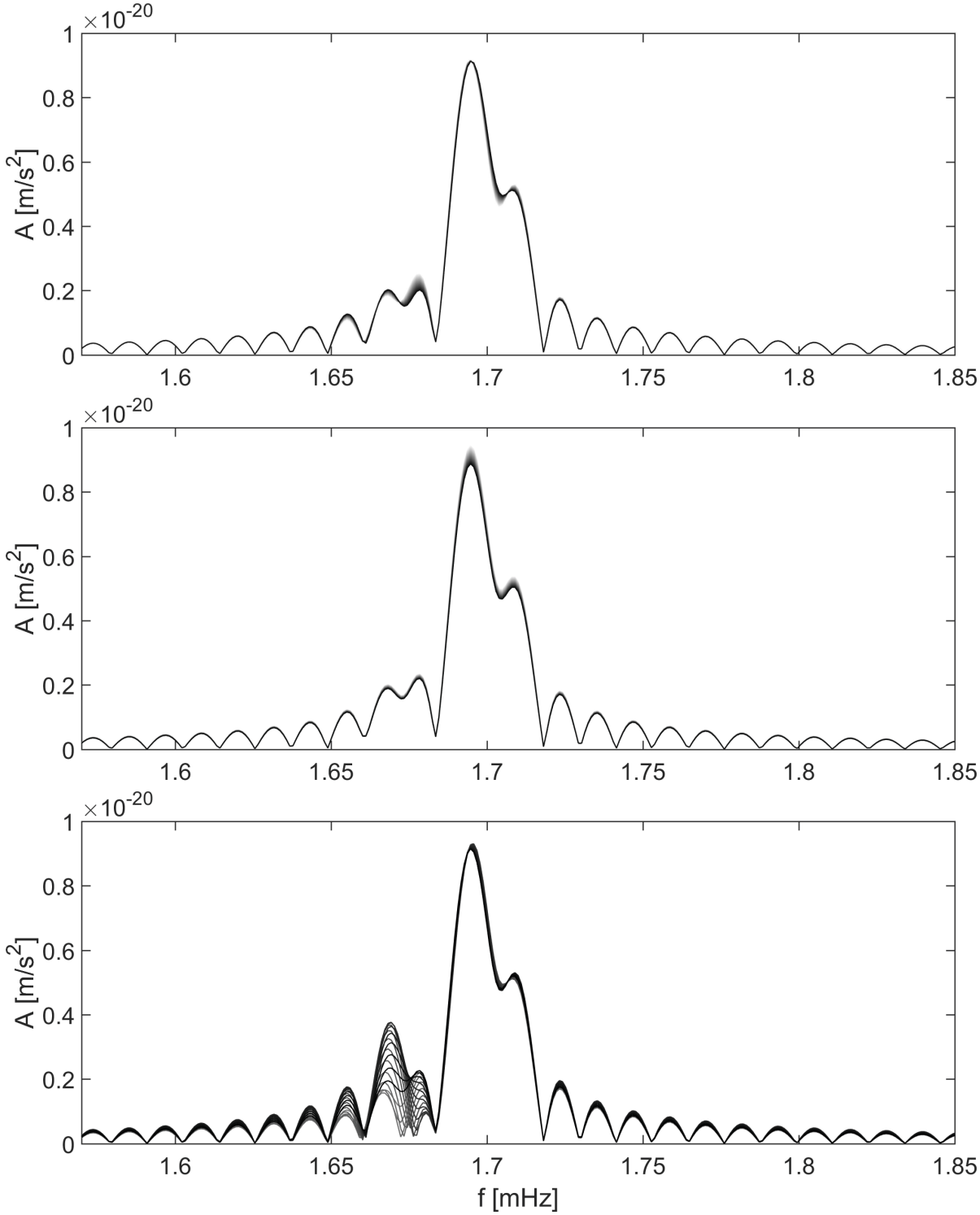

Fig 5.2: Bank of the acceleration templates for the right ascension angle (up), the distance (middle) and the polarization angle (bottom) parameter. The bank of templates for the right ascension parameter is defined by the standard deviations artificially set to be 5°. For the distance the standard deviations from the catalog of the binaries is used. For the polarization angle the full range of non-repeating angles is considered. The result is for SDSS J0935+4411 source.

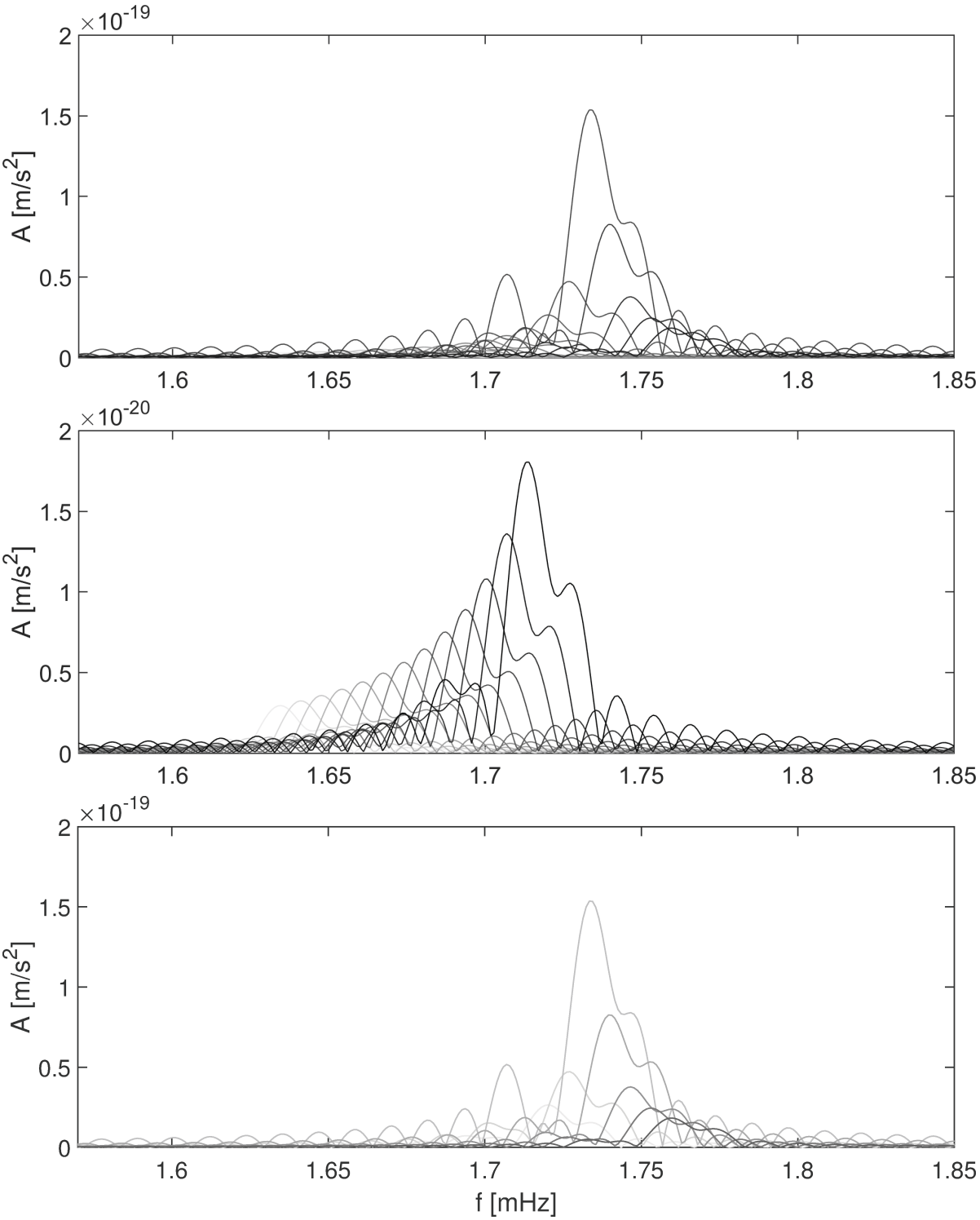

Fig 5.3: Bank of the acceleration templates for the GW source frequency parameter defined by the frequency standard deviations from the catalog of binaries. The result is for SDSS J0935+4411 source. We show all templates plot together (up) and the first 14 (middle) and last 6 templates (bottom) separately.

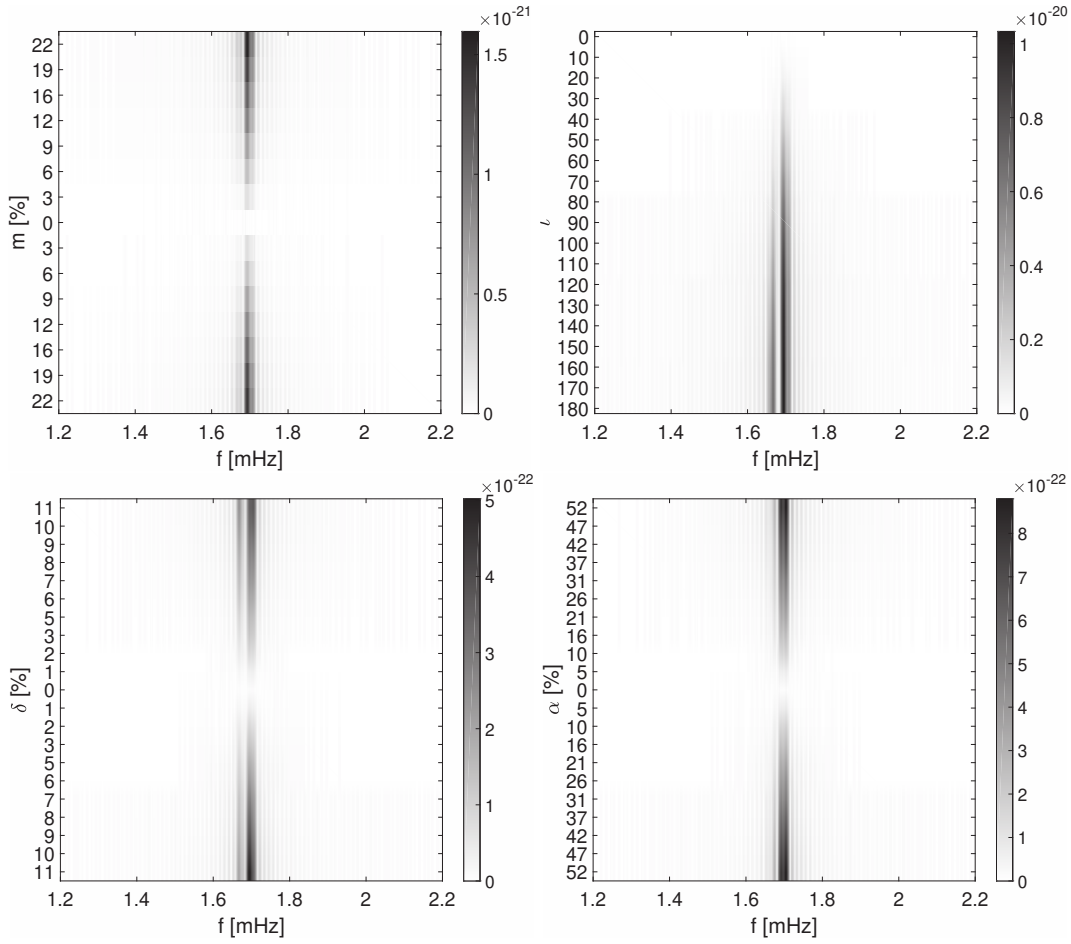

Fig 5.4: Sensitivities to the mass (up left), the inclination angle (up right), the declination (down left) and the right ascension angle (down right) parameters of the GW source. The default template is indicated with the zero relative error percentage, except for the inclination angle where zero indicates the value of the angle for which the template is calculated. The result is for SDSS J0935+4411 source.

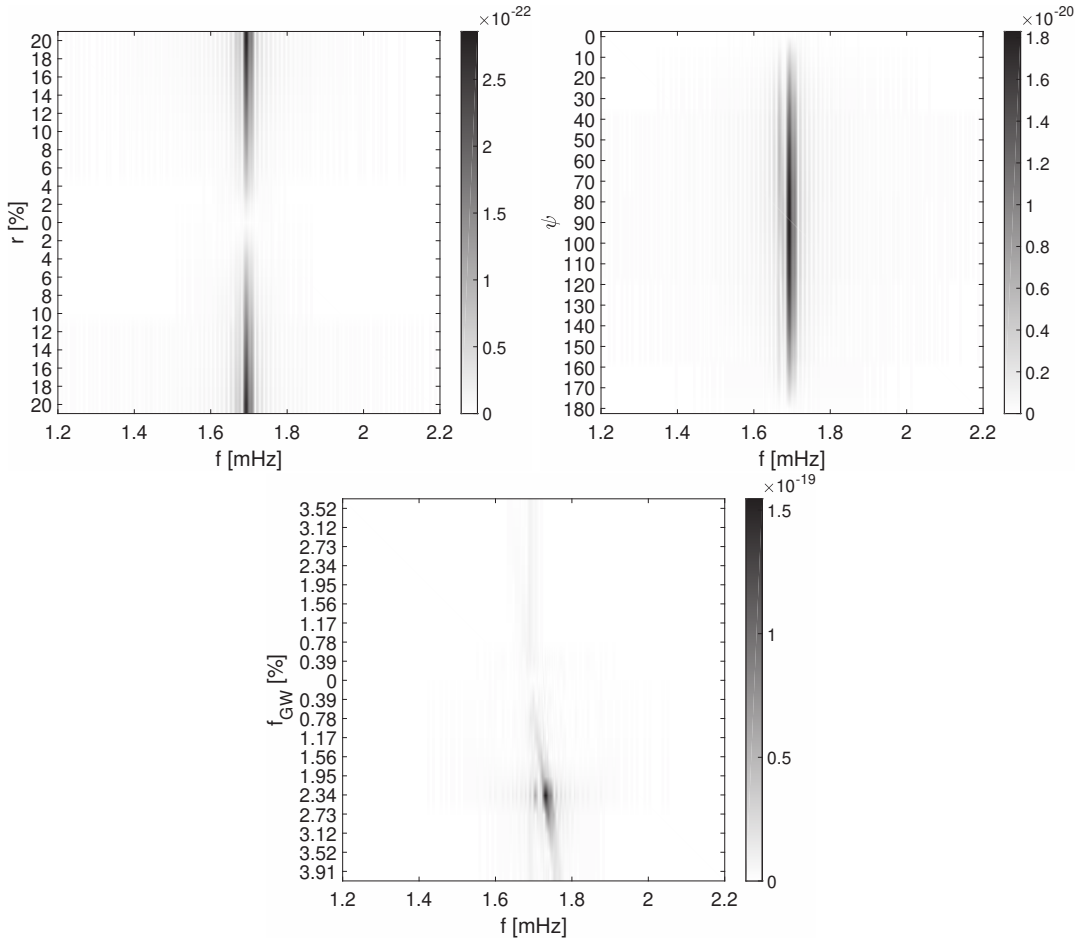

Fig 5.5: Same as Fig. 5.4 for the distance (up left), polarization angle (up right) and the GW source frequency (bottom) parameters. For polarization angle the same argument is valid as for the inclination angle. The result is for SDSS J0935+4411 source.

The results for the sensitivity tests above are indeed interesting in sense that one can better understand how the differences between templates are introduced due to the catalog standard deviations. However, further in the analysis it is even more important to understand how these uncertainties are affecting the main technique that is used for the search of these signals in data. As mentioned in the introduction this technique is the matched filtering. The introduction into the matched filter in Appendix B gives us a basic and complete overview. To further address the problem of the signal detection it is necessary to properly define and chose all parameters that determine the matched filtering performance. This is highly dependent on the type of signal we are searching for. In our case the signal we are working with is the simple periodic sinusoidal signal, which is different from the the first ever detected GW signal, the burst sweep signal. The burst signals are the transient phenomenon characteristic for the supernova explosions and final merging of the coalescing binaries that release large amount of the energy in less than 1 second or just few miliseconds.

In the case of the periodic signal it is important to track signal over a long period of time (Maggiore, 2008). Fortunately, this is possible using the matched filtering even if the data are not completely continuously recorded, since the matched filtering outputs are additive (see relation (B.3)). Lets now define the parameters used in the matched filter analysis. As an example we define a synthetic data $d(t)$ where the input GW signal $w(t)$ is the one for SDSS J0935+4411 source and the input noise $n(t)$ is the white Gaussian one. Next, within the synthetic data $d(t)$ of length M we define that signal of length N, which is not always present $M > N$. To perform matched filtering technique we also need to define a template $w_{template}(t)$ of length L. We set that length of the template $w_{template}(t)$ is smaller than length of the signal $w(t)$, thus $N > L$. Further, as stated earlier, since the recorded data where we perform the actual search are not continuous to simulate the realistic case we also need to define length of the window K where the matched filtering is performed. All these four lengths are shown in Fig. 5.6. Additionally, we also set the noise standard deviations relative to the GW signal amplitude, denoted as σ_N.

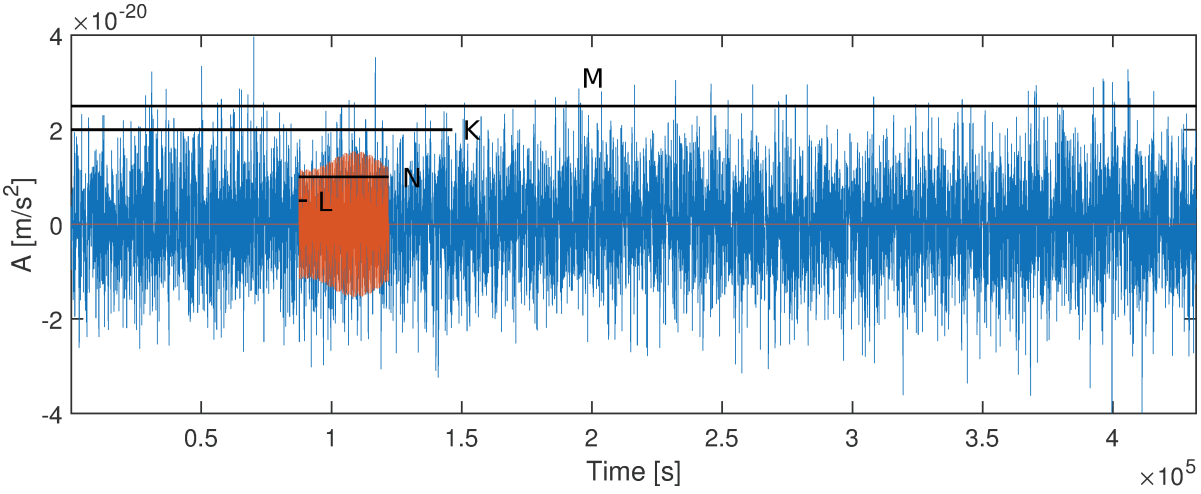

Fig 5.6: Synthetic data $d(t)$ of length $M = 5$ days consisting of white noise $n(t)$ of equal length and GW signal $w(t)$ for the SDSS J0935+4411 source of length $N \approx 9.5$ h. Indicated is also the template length of 5 periodic cycles $L < 1$ h and length of the window for which the matched filtering is performed of size $K = 2$ days.

It is of great interest to understand how length M, L, K affect the matched filter output when N is fixed. To perform these tests we need to set up an experiment defined in Appendix B. It involves obtaining the probability density functions (PDFs) for the two hypotheses: H_0 when the target signal is absent in the data and H_1 when the target signal is present in

the data. For obtaining these PDFs we follow a specific protocol expressed with relations

$$
\begin{gathered}
d(1,\ldots,M) = \sigma_N n(1,\ldots,M) + w(1,\ldots,N) \\
\Downarrow \\
d_1(1,\ldots,K), d_2(1,\ldots,K), \cdots, d_k(1,\ldots,K) \\
\Downarrow \\
\rho_{w,1}(1,\ldots,K), \rho_{w,2}(1,\ldots,K), \cdots, \rho_{w,k}(1,\ldots,K) \\
\Downarrow \\
\bar{\rho}_{w,1} = \sum_{i=1}^{K} \rho_{w,1,i}, \bar{\rho}_{w,2} = \sum_{i=1}^{K} \rho_{w,2,i}, \cdots, \bar{\rho}_{w,k} = \sum_{i=1}^{K} \rho_{w,k,i} \\
\Downarrow \\
p = \{\bar{\rho}_{w,1}, \bar{\rho}_{w,2}, \ldots \bar{\rho}_{w,k}\}
\end{gathered}
\tag{5.3}
$$

and illustrated in Fig. 5.7. Firstly, the synthetic signal $w(t)$ of length N is inserted into noisy time series of standard deviation σ_N and length M. The standard deviation of the noise is chosen so that the signal is not completely buried in the noise and it is actually a scaled value of the noise standard deviation from Peterson's NLNM model (Peterson, 1993) for Nyquist frequency 50 mHz $\sigma_{NLNM} = 8.0538 \cdot 10^{-9}$ m/s^2. Secondly, the data $d(t)$ of length M is divided into k windows of length K. Thirdly, for each window we calculate the matched filter output σ_w of length K defined by the expression (B.6) in Appendix B. Besides data of length K, the input into the matched filter technique is a size L template for which we perform the filtering. Following the definition of the matched filter (B.3) for each window we perform a Fourier transform of the data and template and since $L < K$ we zero pad the template to match the size of data. The power spectral density function $S_n(f)$ is calculated using the input noisy time series $\sigma_N n(t)$ and for each window k. The summed matched filter outputs $\bar{\rho}_w$ represents one statistically independent measurement used to build up a set of the measurements p, which is later used for the calculating of the PDFs for the two hypotheses, H_0 and H_1. The relative position of the two PDFs is telling us how sensitive our matched filter technique is or, in other words, what is the probability that our background noise is oscillating to the most expected value of our signal. Since the PDFs are represented as histogram PDFs, the area of each bin represent the relative number of observations and the sum of all bar areas is less than or equal to 1. Therefore, the PDFs plots are also showing us what is the most expected value of our noise or signal and what is the probability of the most expected values and also any value presented on the histogram. The calculation of the PDFs requires large set of the measurements. This is obtained by repeating the protocol 2500 times, for which we are still within the acceptable time frame, by fixing all the parameters and by only changing the input white Gaussian

noise time series. Complementary to the PDF plots we also calculate Receiver Operating Characteristic (ROC) curves. All further results are commented in terms of the relative position of the two PDF functions and the ROC curves.

In Fig. 5.7 the ROC curve show us that there is 99.79 % chance that the matched filter analysis will be able to distinguish between two hypotheses for this specific set up. Naturally, if we increase the noise standard deviation σ_N the matched filter performance is deteriorating and this is shown in Fig. 5.8. We chose to work with the template that is not the same length as the input signal N, because this is a situation one is dealing when working with the observations. We expect that the nearly periodic signal from the inspiral phase of the two binary stars lasts very long time (longer that the existing network of sensor on the Earth) and it is impossible to have the template of the same length. For the example in Fig. 5.7 we chose a template to be one periodic cycle of the signal and in Fig. 5.9 we show results when the template length is equal to ten periodic cycles. We see that the results are better for later example, because the two PDFs distributions are more separated. However, the general probabilities of the two hypotheses are smaller and our expected values are more spread, specially for the H_1 hypothesis. Next, we consider length of the window K. The size of this window determine the size of the smaller data set on which we perform the Fourier and inverse Fourier transform within the matched filter technique (see relation (B.7)). If length of the window is smaller than length of the signal, $K < N$, or if signal is not completely captured within the size of this default window, then the signal is physically divided in ≥ 2 windows. Since our statistical measurement is defined as the sum over all signal-to-noise ratios within one window of length K, dividing the signal in more than one window, generally decreases the sum value $\bar{\rho}_w$ and shifts the PDF of the H_1 hypothesis left on the plot. Even so, this is also the case because we have less data in the matched filter output and by summing this output the expected value is smaller. Therefore, the PDF for the H_0 hypothesis is also shifted on left. We also observe that the general probability is better in later case, however the detection is still the same in both cases (the relative position of the two PDFs are the same). This is demonstrated in Fig. 5.10. In conclusion, the choice of the template length L has a more important effect on the general outcome of the matched filter technique than the choice of the window length K. Further, we decided to work with $M = 145$ days, $N =1$ day, $K = 1$ day, $L = 1$ cycle and $\sigma_N = 5.1 \cdot 10^{-21}$ m/s^2.

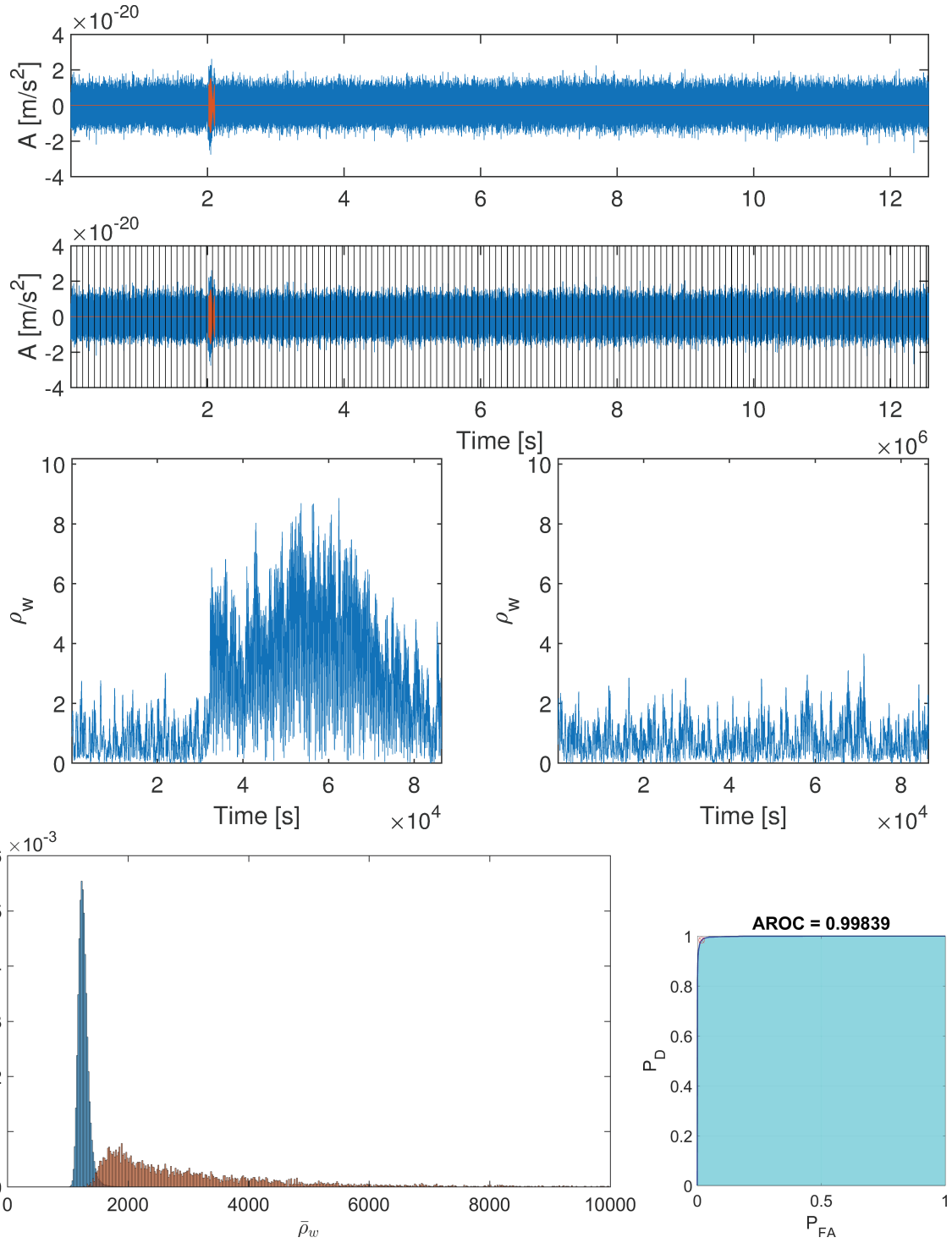

Fig 5.7: Protocol expressed by the relations (5.3). From up to down: the first row, the synthetic signal $w(t)$ of length $N = 1$ day inserted into the noisy time series $\sigma_N n(t)$ of the standard deviation $\sigma_N = 5.1 \cdot 10^{-21}$ m/s^2 and length $M \approx 145$ days constitute data $d(t)$ of length M; the second row, data $d(t)$ is separated in $k = 145$ smaller data sets of length $K = 1$ day; the third row, represent the two matched filter outputs ρ_w of length K for window when there is a signal and when there is no signal present; the fourth row, the PDFs for the two hypotheses H_0 (blue) and H_1 (orange) for 2500 randomly generated signals (left) and the ROC curve for these two probabilities (right).

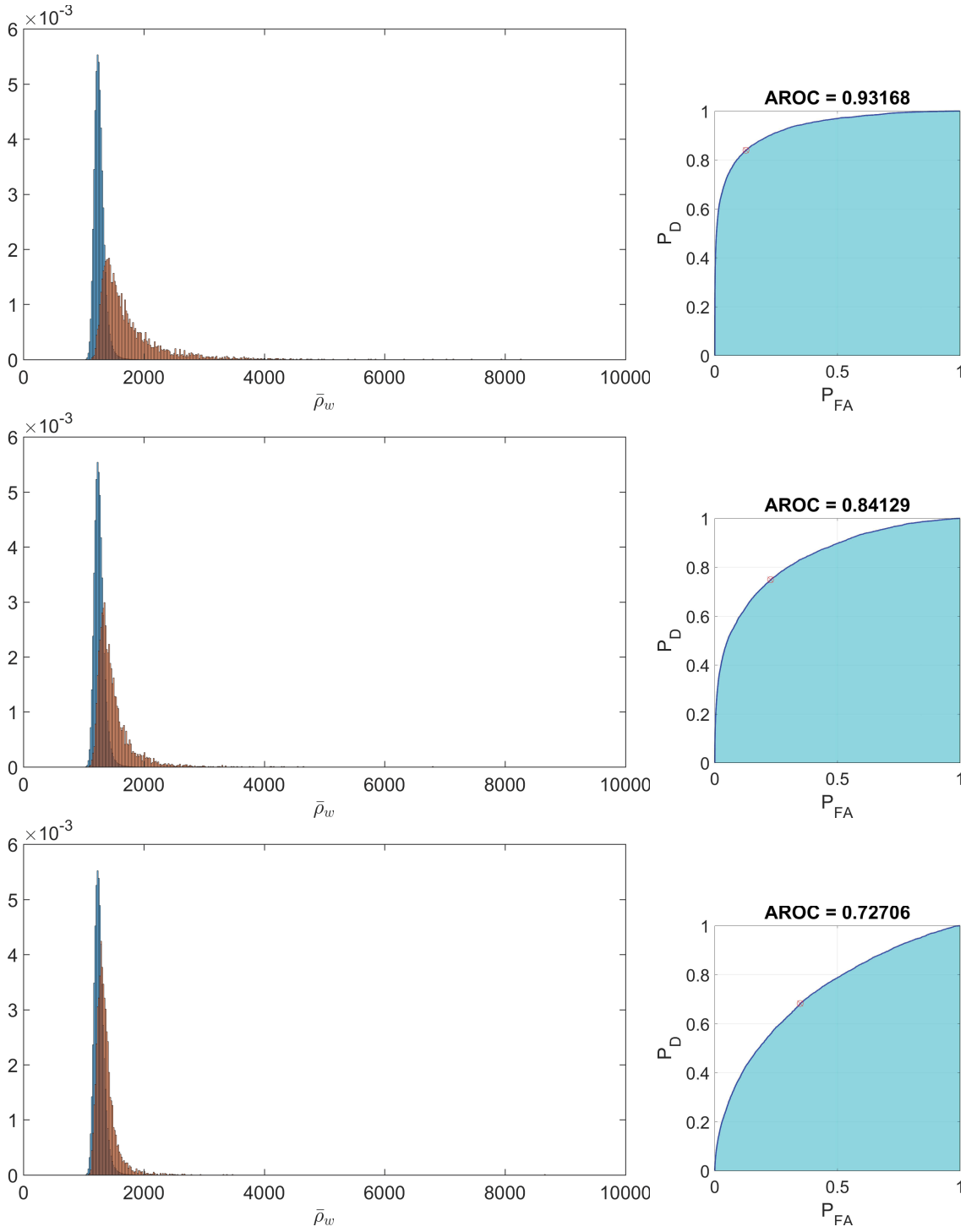

Fig 5.8: PDFs for the two hypotheses H_0 (blue) and H_1 (orange) (left) and the ROC curves (right) for the three different noise standard deviations σ_N: $1.3 \cdot 10^{-20}$ m/s^2 (up), $2.0 \cdot 10^{-20}$ m/s^2 (middle), $3.2 \cdot 10^{-20}$ m/s^2 (bottom). All the other parameters are the same as in Fig. 6.1.

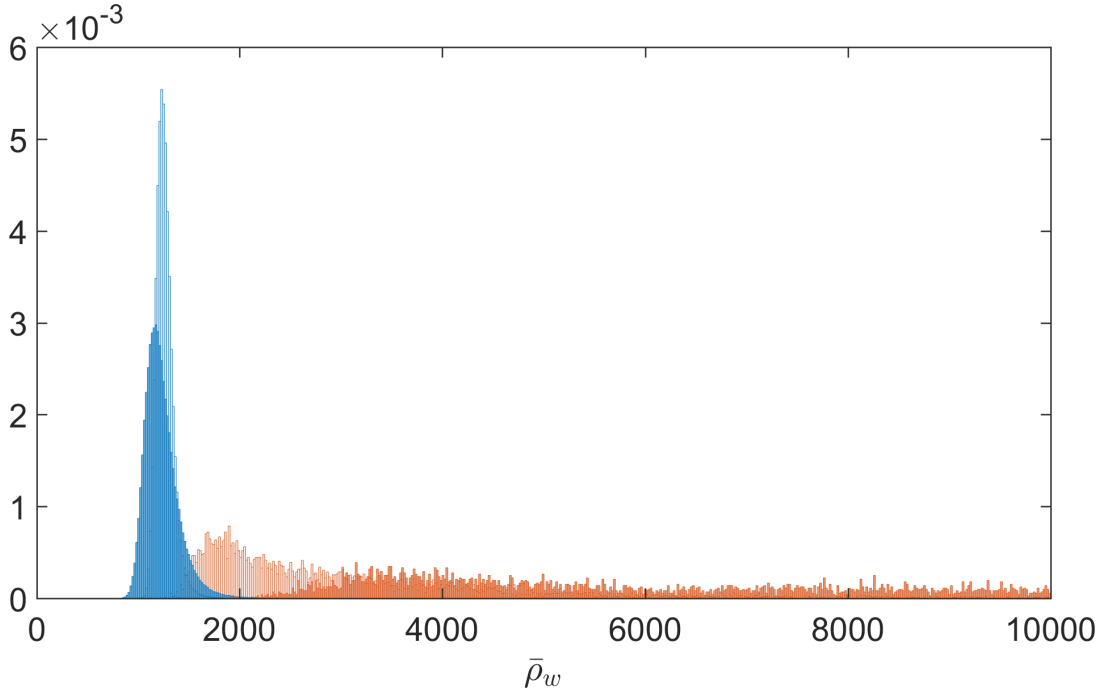

Fig 5.9: PDFs for the two hypotheses H_0 (blue) and H_1 (orange) when template is one cycle long (background) and ten cycles long (foreground) with all the other parameters same as in Fig. 6.1.

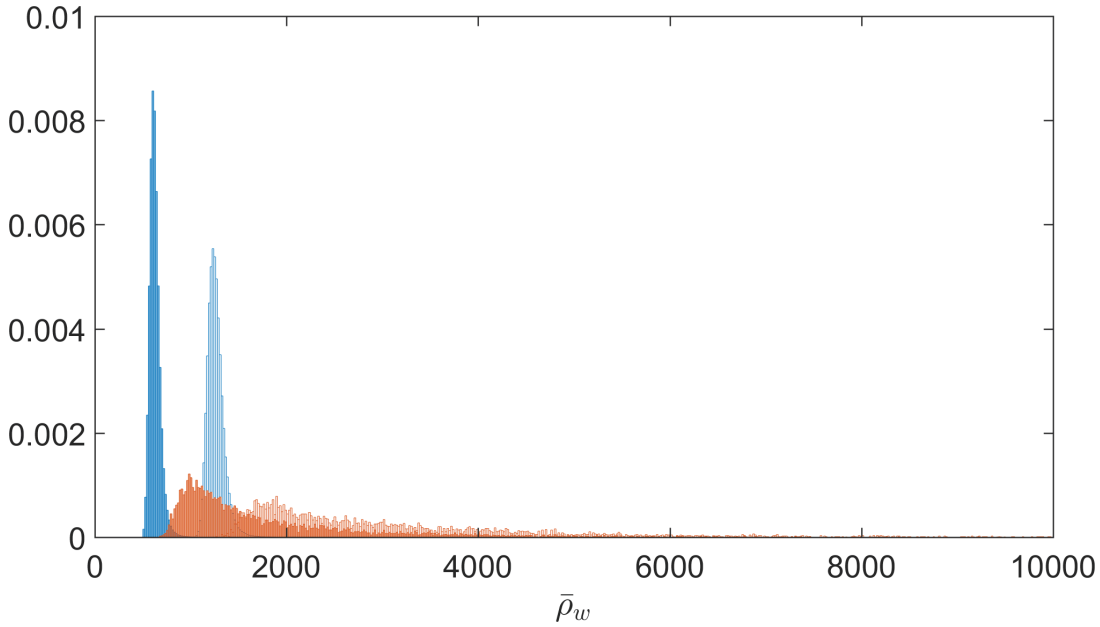

Fig 5.10: PDFs for the two hypotheses H_0 (blue) and H_1 (orange) for $K = 1$ (background) and $K = 0.5$ day (foreground) and with all the other parameters same as in Fig. 6.1.

Next, we test how the PDFs of the hypothesis H_1 depend on the uncertainties found in the binary star catalog by calculating the PDF for each waveform from the bank of

templates of each parameter. In all further test the noise standard deviations is always the same, therefore the position of the PDF of the hypothesis H_0 is always the same. Meaning, that further we can only study the relative position of the PDFs of the hypothesis H_1. Naturally, we would expect that any parameter that is changing the amplitude of our signal is eventually affect the signal-to-noise ratio of the matched filter technique and therefore also the relative position of the two PDFs. The results, for the two edge waveforms from the bank of templates and for all seven parameters are shown in Fig. 5.11, 5.12 and 5.13. From the figures we see that only three parameters out of seven (the mass, the inclination and the frequency) have waveforms that notably effect the PDFs. Other parameters, even though they do affect the amplitude they do not have large enough diversity within their bank of templates to generate the PDFs that would differ from each others. The results for the mass parameter are not surprising, since a larger mass binaries have larger signals amplitudes which was already apparent on the bank of templates figure. The range of values for the inclination angle set between 0 and π generate the minimum and the minimum and maximum of the metric perturbation scalars defined by (4.114) and (4.115), respectively. Therefore the outcome of the PDFs is also not surprising, however this result is not giving us answer that we need and without the standard deviation associated with the inclination measurement we cannot conclude anything further. The complexity of the frequency parameter expressed by the bank of templates is also transferred to the PDFs results. We can notice that the most important factor for the PDFs calculating is the amplitude of the template. The beginning of the bank of templates for the frequency parameter is characterized by the smallest amplitude within this bank and this corresponds to the PDF function that is the leftmost on the plot. The larger the amplitude the more PDF of the hypothesis H_1 is right on the plot and thus we expect better detection.

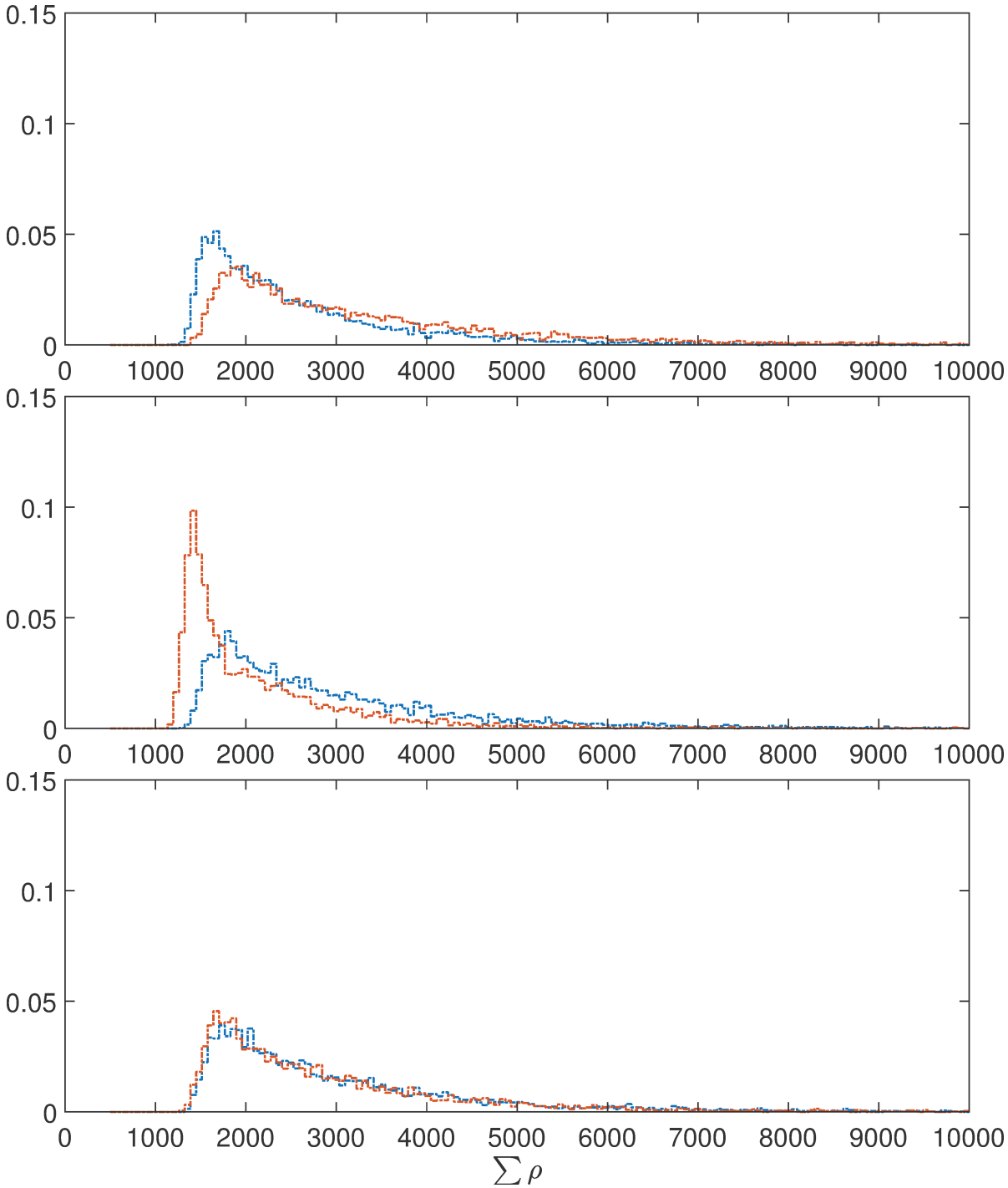

Fig 5.11: Two PDFs for the H_1 hypothesis calculated for the edge templates (the left edge, when parameter value is smaller than the default parameter is denoted by blue; the right edge, when parameter value is bigger than the default parameter is denoted by orange) in the bank of templates for the mass (up), the inclination angle (middle) and the declination angle (bottom) parameter.

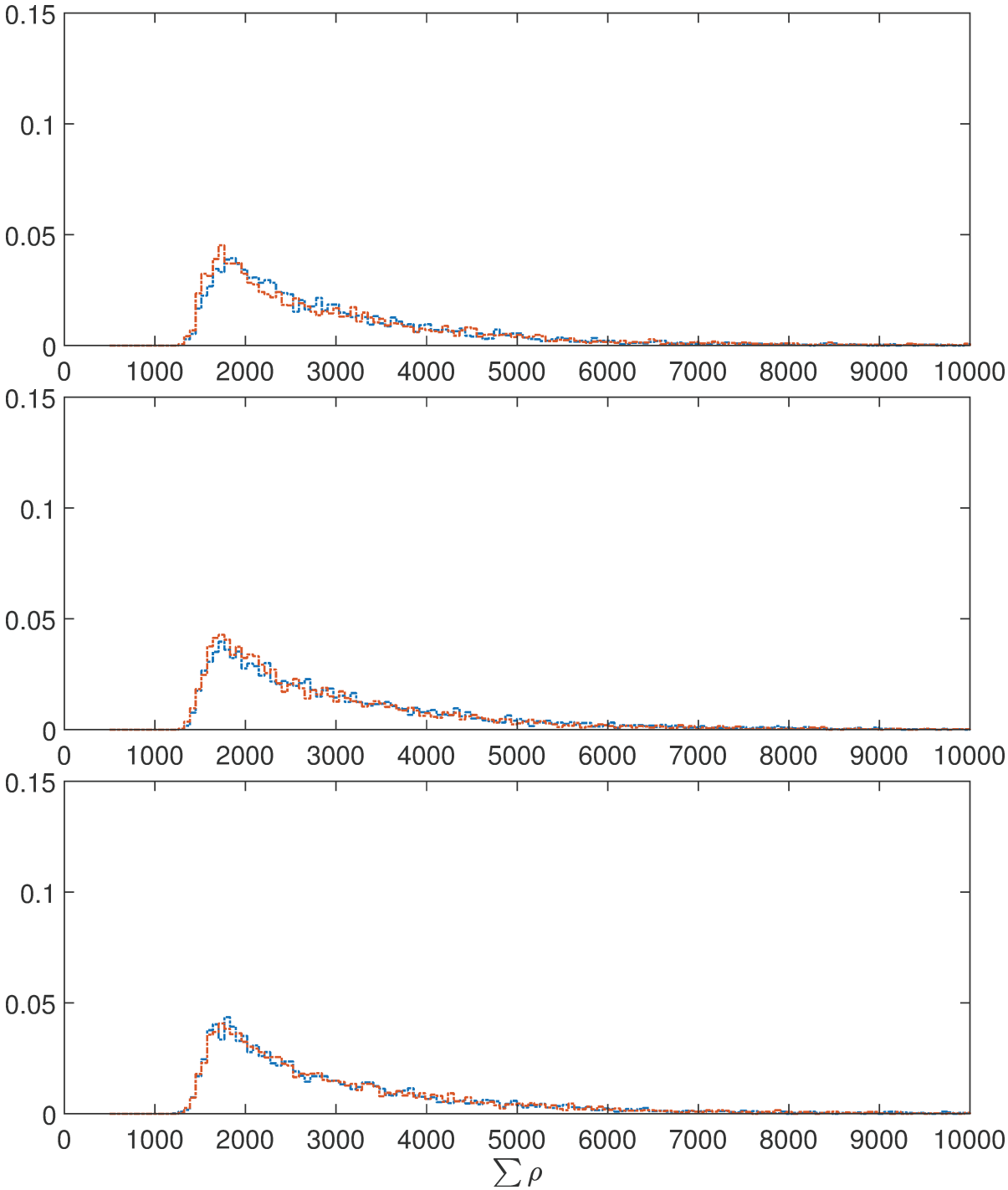

Fig 5.12: Same as Fig. 5.11 just for the right ascension angle (up), the distance (middle) and the polarization angle (bottom) parameter.

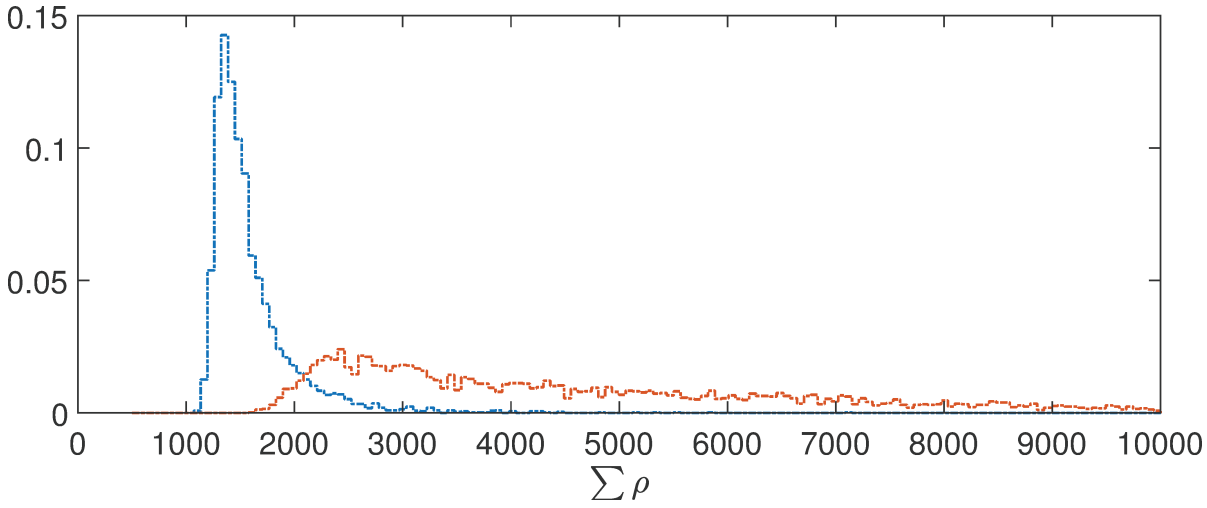

Fig 5.13: Same as Fig. 5.11 just for the frequency parameter.

Final test performed involve testing how the PDFs are behaving when the signal $w(t)$ we are searching for and template $w_{template}(t)$ we perform search with do not match. We again work with the banks of templates of the seven parameters. We set that the default template we perform the matched filtering with is always the first template within the bank of templates for each parameter. The results are shown in Fig. 5.14 and 5.15. They are very similar for all seven parameters, lacking any shift to the right or left in the plot. We only notice that the height of the PDFs change. Overall, the results signify that the matched filtering technique is nonsensitive to the uncertainties associated with the parameters from the binary catalog. This is encouraging, since it means that we can still perform search for the signals in data even if we are not sure that the parameters characterizing the template are same as the parameters of the signal. This is valid within the range of the standard deviations found in the catalog.

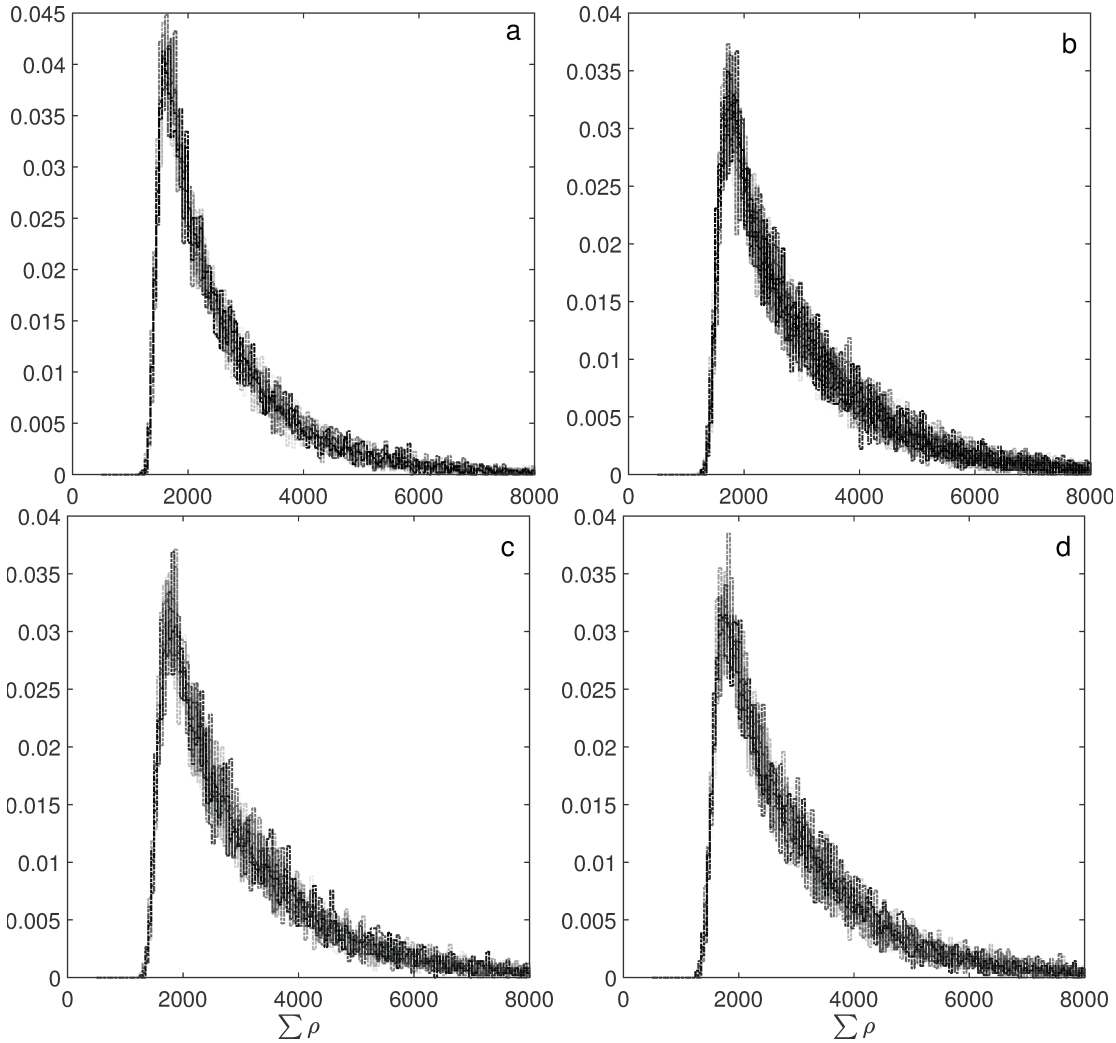

Fig 5.14: PDFs calculated for each template from the bank of templates for the case when the waveform $w(t)$ and the template $w_{template}(t)$ do not match for a) the mass, b) the inclination angle, c) the declination angle, d) the right ascension angle.

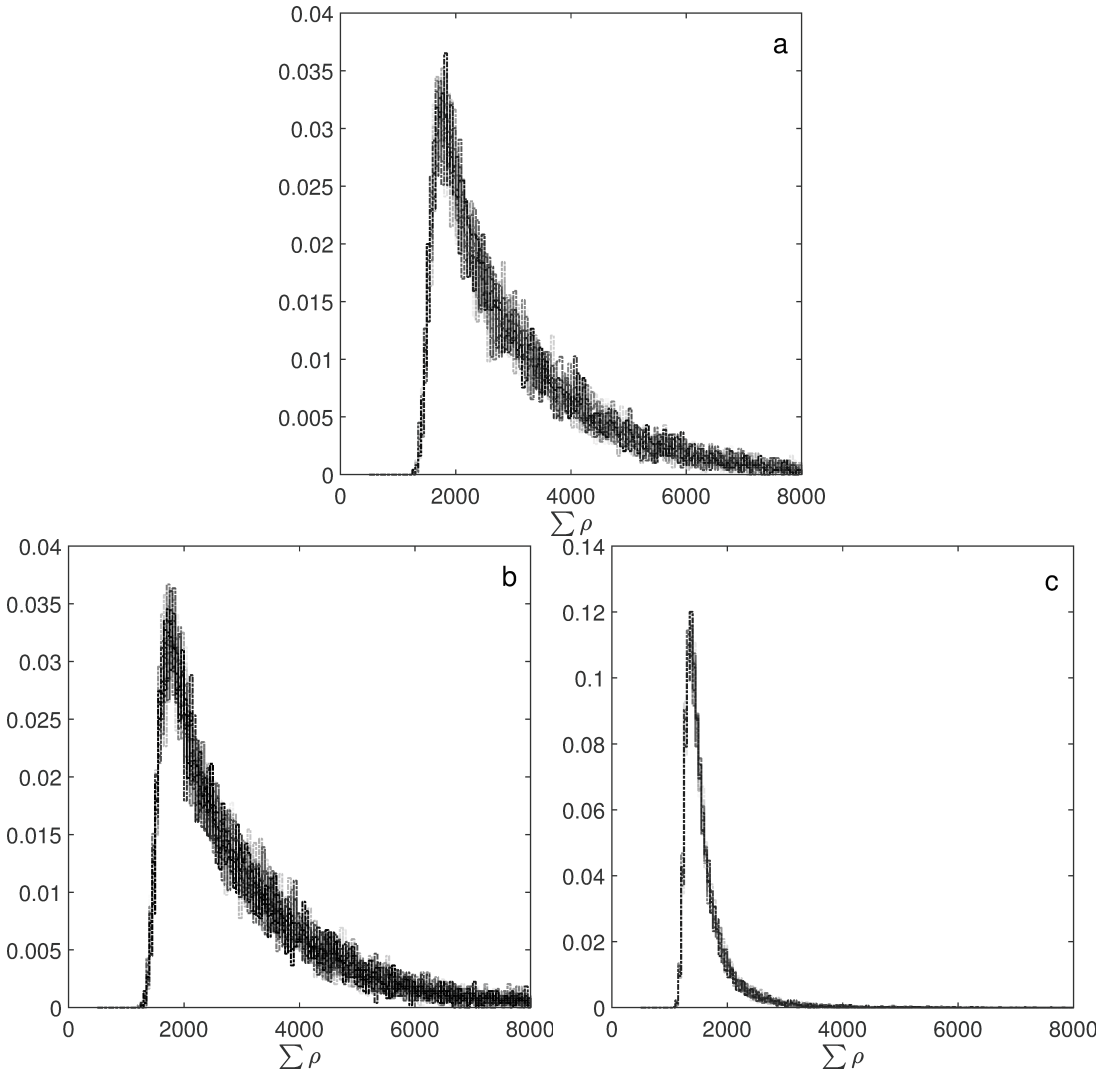

Fig 5.15: Same as Fig. 5.14 just for a) the distance, b) the polarization angle, c) the GW source frequency.

Further, we perform the search for the signal using the matched filtering technique in real observations.

5.3 Observations

The matched filtering technique is also applied using the observations by inserting the synthetic signal in the observations. We chose to work with the gravimeter data from the superconductive gravimeter placed at the most quiet station which is the Black Forest Observatory (BFO), positioned in Schiltach in Germany $(43.33°, 8.33°)$. To find the most quite data set at the BFO we first look up for the year, within the time range from 1998 to 2017, that has the least number of earthquakes. The finally chosen year is 2012 and the

plot of the earthquake distribution through out the year is shown in Fig. 5.16.

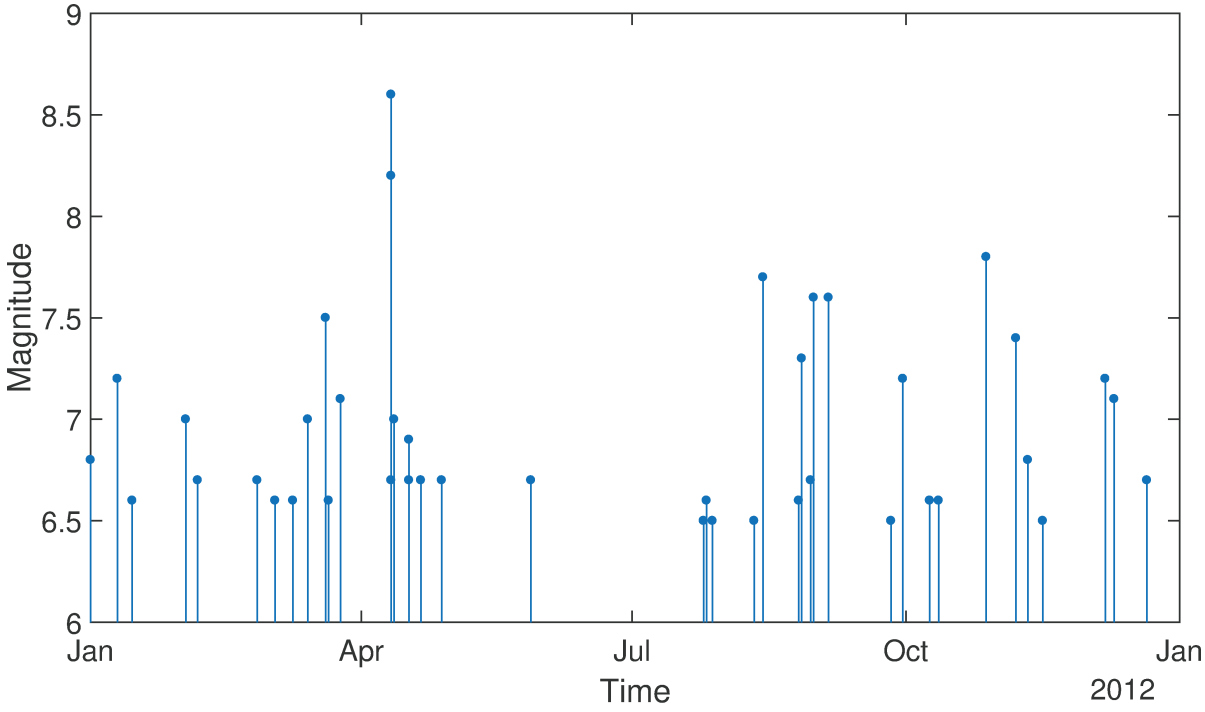

Fig 5.16: Distribution of the earthquakes of magnitude larger than 6.5 for year 2012 at the Black Forest Obsrvatory station, Germany $(43.33°, 8.33°)$.

Next step is to select days without the earthquakes and that have, in general, very low power spectral density (PSD). To obtain this we first remove the earthquakes by removing the direct P and S phases; second, we divide our one year long time signal into one day long time signals; third, we calculate the PSD for each one day long time signals using the Welch average periodogram method Welch (1967); fourth, we compute the 1st, 25th, 50th and 75th percentile of all previously calculated PSDs by considering only the frequency band from 1 to 3 mHz. The final percentiles together with New Low Noise Model (NLNM) Peterson (1993) are shown in Fig. 5.17. We finally chose to work with the 25th percentile, therefore the remaining data set, shown in Fig. 5.18, consists of 58 days. The data are are also high-pass filtered with a cut-off frequency at 0.1 mHz to remove tides and other long-period effects. We also correct the atmospheric pressure effects by using a nominal admittance of -3 $nm/s^2/hPa$. It is important to emphasis that after the data processing the normal modes and other periodic signals are still present in the data and we can see their presence in Fig. 5.17. Afterwards, some days are removed by subjective reasoning and finally we are left with 47 days.

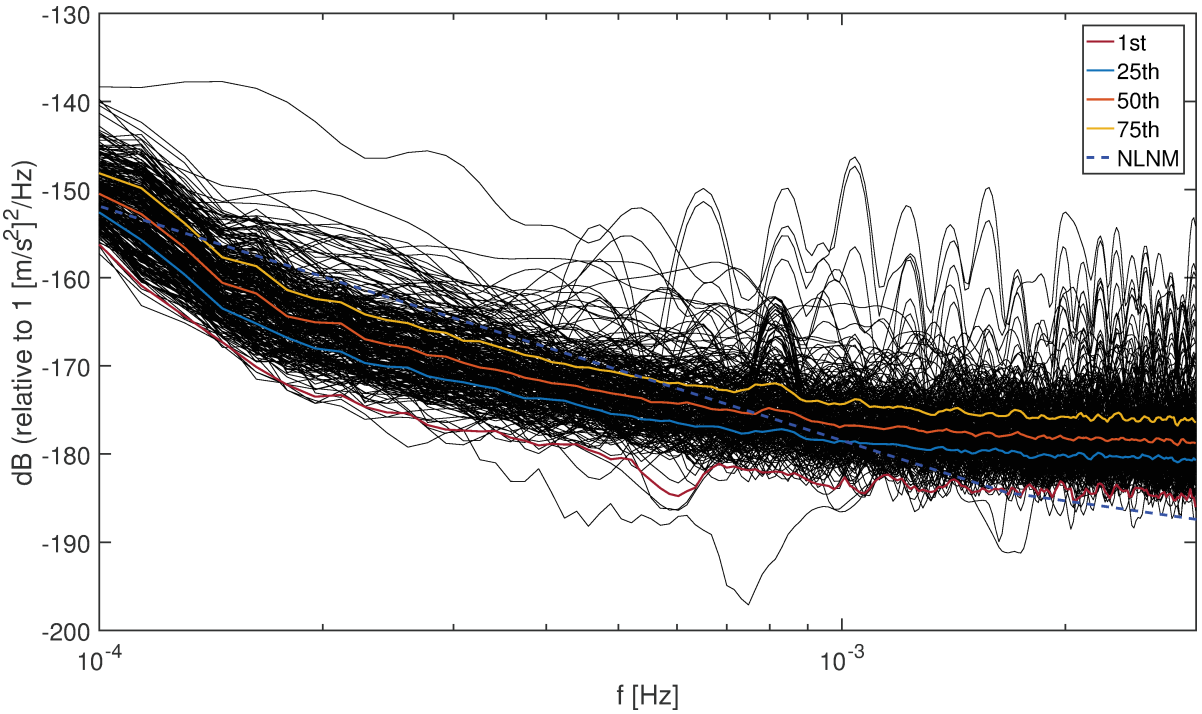

Fig 5.17: PSDs of the one day long signals for year 2012 at BFO station with 1st, 25th, 50th and 75th percentile marked together with the NLNM.

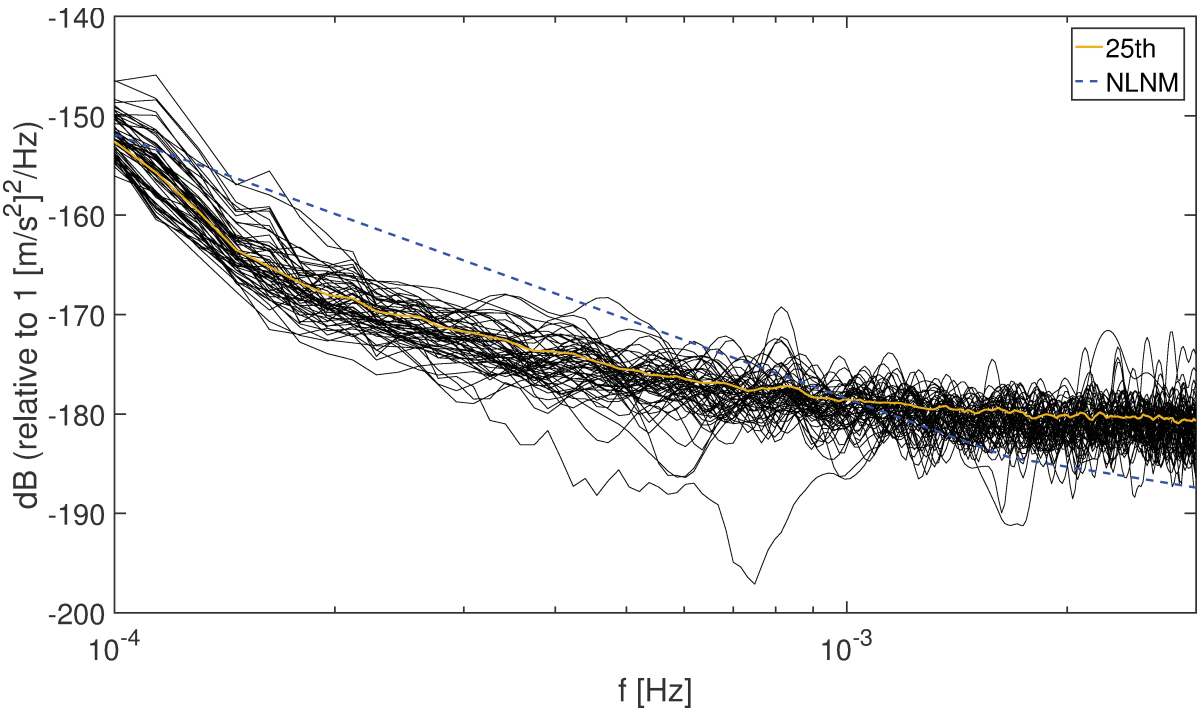

Fig 5.18: Same as Fig. 5.17 just for 25th percentile only.

It is clear from the start that inserting a original synthetic signal from the section above

into the observations means that the synthetic signal will be completely buried with noise, since there is around eleven orders of magnitude difference. Therefore, it is expected that the matched filtering is not going to work with the proposed set up. However, we are still interested in using the observational data because the noise is not completely white Gaussian anymore. Considering this fact, the question is, whether the usual detection using the matched filtering is more complicated with non-white noise. To test this, we firstly adopt the matched filter parameter from the synthetic test, that is we keep $N = 1$ day, $K = 1$ day, $L = 1$ cycle and now $M = 47$ days. Secondly, we scale the noise standard deviations of the observational data to match the standard deviation of the synthetic signal, so that their ratio is one. Thirdly, we scale the white noise time series so that its standard deviation is equal to the one of observational time series, thus their ratio of standard deviations is also one. Fourthly, we simultaneously apply the matched filtering on the data where we inserted synthetic signal into white Gaussian noise and on the data where our signal is inserted into non-white observational noise. To be able to use the matched filtering technique with non-white noise we need to modify the one-sided PSD function $S(f)$ in relation (B.3). For this purpose we redefine $S(f)$ to be a constant value and calculate it using a definition of the PSD for the white noise defined as $\mathrm{PSD}_{\mathrm{noise}} = \sigma^2 T_0$, where σ is the noise standard deviation and T_0 is the sampling rate. The results of this test are shown in Fig. 5.19 for white noise and in 5.20 for observational noise for the smaller window where we inserted the synthetic signal. The matched filter output for the observational noise produces satisfactory output, however one needs to remember that we use different definition of function $S(f)$.

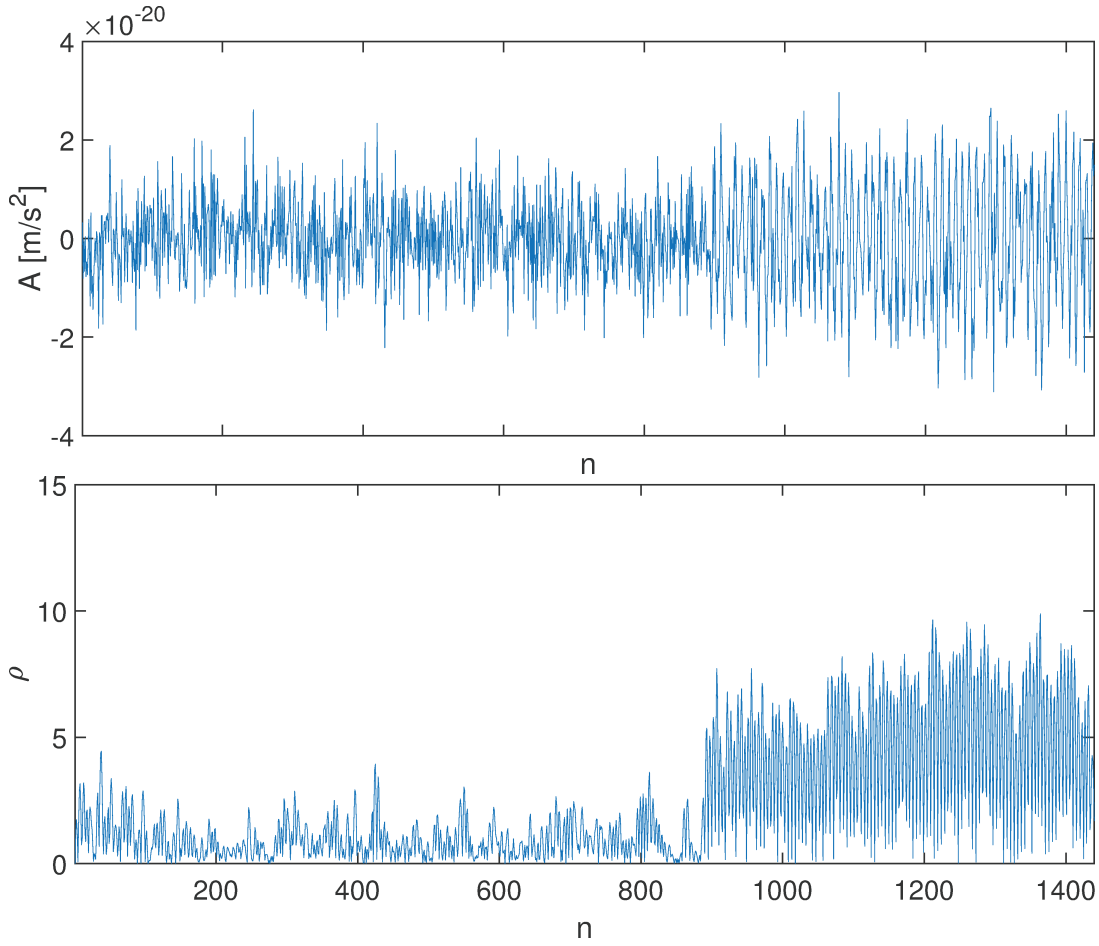

Fig 5.19: Synthetic signal inserted into white noisy time series with $\sigma_N = 7.5 \cdot 10^{-21}$ m/s^2 (above) and the matched filter output (below) for window where the signal is inserted.

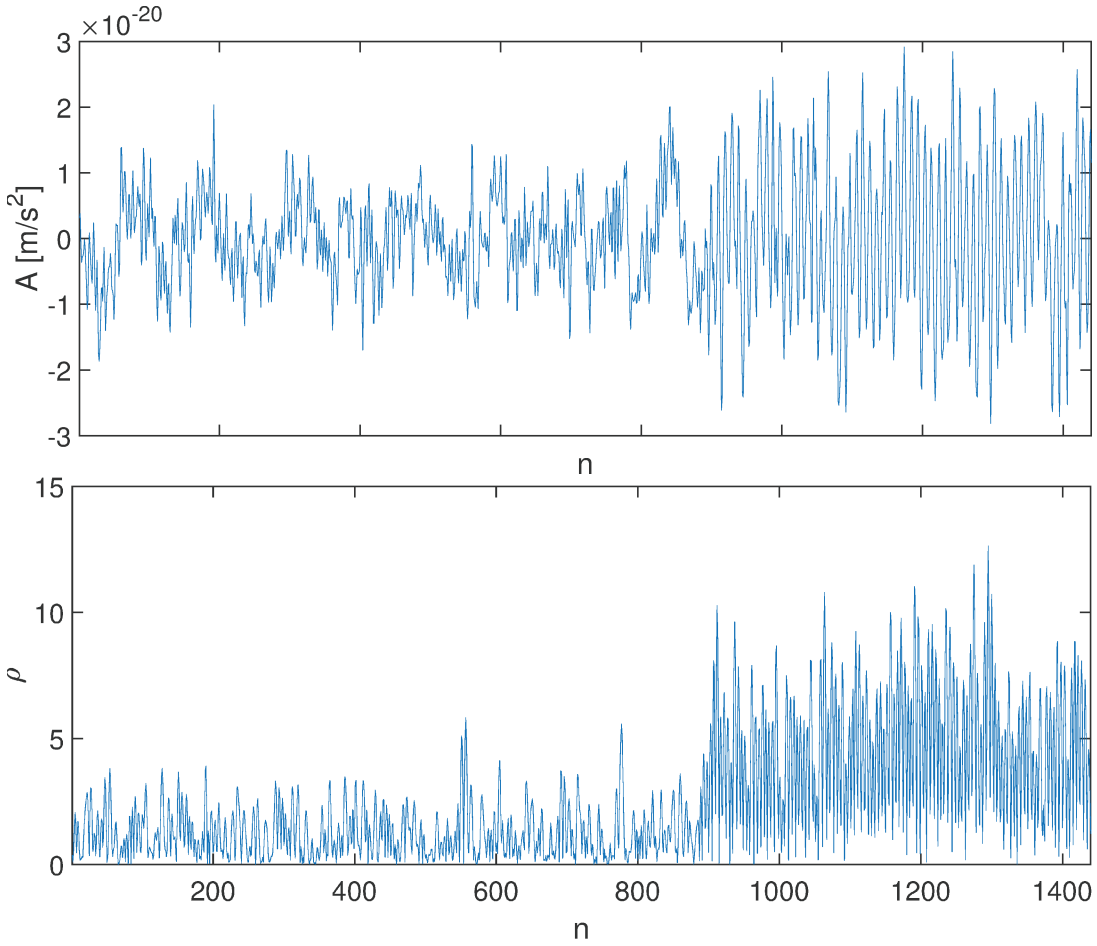

Fig 5.20: Synthetic signal inserted into observational noisy time series scaled with scalar $1.2 \cdot 10^{10}$ (above) and the matched filter output (below) for window where the signal is inserted.

The performed analysis on one station in general would not be enough to detect an event. To be able to recognize false events from the true ones, it would be preferable to perform search on several stations, to look for the coincident events. Since we can use the synthetic response from the Section 4.2.5 to generate templates for different station in different time of the year, the later idea is manageable, however the appropriate data sets in the mHz regime on Earth do not exit. This represent the biggest downside of this research on the Earth.

5.4 Conclusion

The above analysis showed us that when performing the search for the GW from the binary stars, in the mHz frequency band, some of the parameters defining the GW response model influence the general rate of the detection. For example, the larger mass means the better

detection. However, more importantly, this study showed us that even if the parameters of our model are not completely the same as the parameters of the signal in data, we still have a good chance of detecting it. And this works only if the differences are within the the standard deviations found in the catalog of the binary stars. Meaning that the model generated using the parameters found in the catalog are satisfying, at least for the first stage of the search when one only needs to identify the possible GW events. Moreover, we also showed that the GW response model is crucial to understand the probability of the detection rate. Because having a realistic model and also the expected noise level in the data one can inquiry the threshold for which one would expect the detection. The further steps in this search, not covered in this study, would be to statistically test the obtained events above the predetermined threshold and then also to study the exact or the true parameters of the binary stars Abbott et al. (2016). The search could be improved by defining the optimal matched filtering parameters, for example using the longer template that is also consistent with the data length. The model could be also improved by considering the spindown of the inspiral phase of the binaries Maggiore (2008). However, this might be more important for the final stage of the search, when one requires the exact binary star parameters.

Considering the detection of the binary GW signal on Earth the conclusions are contradictory. There are many advantages, but only one drawback. The existing network of gravimeters and seismometers, that has been operating for over a two decades now, offers a possibility to look for many coincident detections around the globe and to follow the signal over a long period of time. This is also possible because our model is dependent on the specific position on the surface and it contains the rotation of the Earth. However, in practice this is not feasible since the noise in the data is substantial. Therefore, this study might have better opportunity in the space, but more about the perspective is discussed in the chapter Conclusion and Perspectives 7.

Chapter 6

Uncertainties in Normal Mode Studies

In the context of the normal mode studies the usual targets are normal mode eigenfrequencies, Q-factors or the splitting function coefficients. There is no standardized technique used for obtaining those values. We measure the normal mode parameters after an earthquake and usually Fourier transform is sufficient, since it enables us to see which modes are being excited.

In this chapter we discuss how one can obtain information about the Earth structure within the normal mode studies and what are the difficulties and uncertainties one encounters when measuring the frequencies and Q-factors of the normal modes.

Results of this Chapter are published in Majstorović et al. (2019a) (link).

6.1 Introduction

Until the present day, the interior of the Earth represents a great challenge in geophysics. The normal modes studies have long provided some of the essential discoveries. For example, they contributed to building spherically symmetric Earth models (Dziewonski and Anderson, 1981) as well as 3D models of lateral heterogeneities (Ritsema et al., 2011; Moulik and Ekström, 2014; Koelemeijer et al., 2016). However, even though normal mode studies contributed in the estimation of the lateral density variations (Ishii and Tromp, 1999, 2001; Trampert et al., 2004), the resolution of density is still controversial (Resovsky and Ritzwoller, 1999; Romanowicz, 2001; Kuo and Romanowicz, 2002; Al-Attar et al., 2012; Akbarashrafi et al., 2017). During the years many methods were developed, from the well-established techniques to retrieve eigenmodes frequencies and quality factors, such as stripping (Gilbert, 1971; Ritzwoller et al., 1986) and stacking methods (Courtier et al., 2000). Further, techniques like the autoregressive and non-linear fit of a resonance function have also been widely used (e.g. Chao and Gilbert, 1980; Rosat et al., 2005; Ding and

Shen, 2013a), while splitting function coefficients are usually determined through iterative non-linear spectral fitting (Woodhouse and Giardini, 1985; Ritzwoller et al., 1986, 1988; Giardini et al., 1987, 1988; Resovsky and Ritzwoller, 1998; Deuss et al., 2011, 2013). For more complete insight into existing techniques the reader is referred to the papers by Masters and Gilbert (1983), Ding and Shen (2013a), Ding and Chao (2015a). Despite these various studies and methods substantial uncertainties and inconsistency in the singlets eigenfrequencies and splitting function coefficients measurements still exist (Pachhai et al., 2016; Akbarashrafi et al., 2017).

A reason for this is the inherent problem of spectral leakage and mode-mode interference, which introduce a systematic bias in spectral peak measurements in frequency domain and consequently also in the split singlet frequencies measurements (Guoming et al., 1983). This issue has been more or less solved by introducing data tapering, however this solution is more efficient for well isolated low-frequency modes (Dahlen, 1982a). The next essential problem is the presence of noise in recorded displacements. Substantial studies have been done on the estimation of station noise levels (e.g. Rosat et al., 2003; Rosat and Hinderer, 2011) and noise sources (Widmer-Schnidrig, 2003, and references therein). Nevertheless, the question of how the noise deteriorates estimates, how it introduces bias in methods and what is the level of sensitivity of the methods are still important to understand.

The calculation of realistic normal mode displacements is another problem in normal mode studies. The problem is twofold, since one needs to truncate the infinite normal mode set to a finite one and also accurately implement the mode coupling theory (Dahlen, 1968, 1969; Woodhouse and Dahlen, 1978; Woodhouse, 1980, 1983; Woodhouse and Giardini, 1985). It is known that self- and group-coupling approximations introduce biases over the full-coupling approximation (SC, GC, FC, respectively) (Deuss and Woodhouse, 2001, 2004; Irving et al., 2008, 2009; Al-Attar et al., 2012; Yang and Tromp, 2015; Akbarashrafi et al., 2017). These theoretical errors cannot be ignored for the frequencies higher than 1 mHz, where FC calculations are necessary to obtain sufficiently accurate spectra (Yang and Tromp, 2015). They also have for sure affected earlier studies where the measurements substantially depend on the comparison of the synthetically calculated normal mode displacements with the observations. However, since in this study we do not implement those measurements, we just acknowledge these theoretical errors as being significant.

There are still important issues in normal mode studies, that have been acknowledged, but not properly scrutinized. In this study the focus is set on the inevitable presence of noise in the records and the number of stations used during the measurement process. For example, for the signal to noise ratio (SNR) ≤ 50 the aforementioned effects have higher errors than theoretical errors introduced by the SC, GC and FC approximations. Therefore,

the objective of this paper is to measure sensitivity and to test performance of the commonly used methods under the influence of noise and number of stations. The tested methods are, the stacking method, called the optimal sequence estimation (OSE) introduced by Ding and Shen (2013a), and the autoregressive method for the estimation of normal mode's parameters introduced by Chao and Gilbert (1980)(ARFD80).

Motivated by the previous findings, we decide first to test these methods on synthetic seismograms. Experiments contain two main parts, one is the gradually addition of noise in my records and the other part is the usage of different networks in OSE. The purpose of both parts is the quantification of noise and network effect on the estimates of eigenfrequencies, quality factors and amplitudes. The importance of noise effect is implicit, on the other hand the network effect is linked with the OSE feature. Theoretically, the measured frequency of a normal mode should be the same anywhere on the Earth and the usage of different station network should have the same results. Consequently, if one wants to measure the split frequencies of specific modes one only needs to consider those stations which are not located on the nodal lines of the eigendisplacements (Masters et al., 2000; Häfner and Widmer-Schnidrig, 2013). Thus, the second part of this work aims at testing whether any systematic bias is introduced by the network effect. We also validate the accuracy of my complex eigenfrequency estimate graphically using the phasor walkout method (Zürn and Rydelek, 1994). Furthermore, once measured, the split eigenfrequencies are used to retrieve the splitting function coefficients using a perturbation theory of the first-order (Dahlen, 1974; Ritzwoller et al., 1988; Widmer et al., 1992; Häfner and Widmer-Schnidrig, 2013).

Since we are interested in the method's performances my tests include only one source mechanism, also only one multiplet chain is used at the time and we focus on the low-frequency modes, where one can use the SC approximation. The interest in the highly precise measurement of the low-frequency split eigenfrequencies is valuable, since it is known that any existing density model should fit split frequencies perfectly (Widmer-Schnidrig, 2003). For suitable candidates, we chose to work with the lowest frequency multiplet chain ${}_0S_2 - {}_0T_2 - {}_2S_1 - {}_0S_3$, spanning from 0.309 mHz to 0.468 mHz, and the lowest frequency multiplet chain where there is a significant interference between adjacent multiplets, ${}_0T_5 - {}_2S_2 - {}_1S_3 - {}_3S_1$, spanning from 0.928 mHz to 0.943 mHz. For the purpose of analyzing complex eigenfrequencies and splitting function coefficients the specific protocol is established (Fig. 6.1): firstly, we stack records using OSE stacking method (Appendix D); secondly, we calculate complex eigenfrequencies, quality factors (further on Q-factors), and amplitudes of target singlets using ARFD80 method (Appendix C); thirdly, we check the validity of eigenfrequency estimates using the phasor walkout method (Appendix E); and

finally from the eigenfrequencies we estimate splitting function coefficients. The real observations results are also presented, based on long period seismometer and superconducting gravimeter (SG) data after six earthquakes of magnitude larger than 8.3, for multiplets ${}_0S_2, {}_2S_1, {}_0S_3$ and ${}_3S_1$.

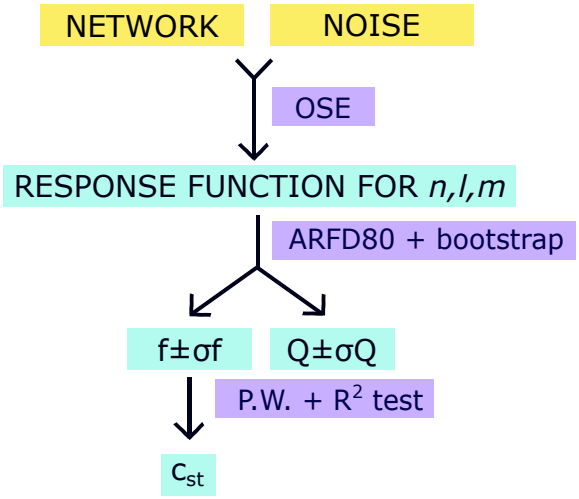

Fig 6.1: Diagram of the used protocol, where the input data are in yellow color, output data in blue and used methods in purple. The input data, the network of stations and noise level, are used to obtain response functions for specific normal mode described by radial n, angular l and azimuthal m order in the stacking process by OSE method. Further, from each function the complex frequency and Q-factor are estimated using ARFD80 method and phasor walkout is used to validate the estimated values. Finally, from the obtained singlets complex frequencies the splitting function coefficients are estimated.

6.2 Synthetic Experiments

To test how the methods are influenced by different noise levels and station distributions, experiments are conducted by simulating records using real earthquakes parameters. Synthetic seismograms are calculated for a 3D Earth model by means of normal mode summation and perturbation theory. Reference basis functions, eigenfrequencies and the associated eigenfunctions, for a spherically symmetric, non-rotating Earth model are obtained for PREM model using MINEOS software package (Woodhouse, 1988) with a cut-off frequency of 80 mHz. Perturbations due to rotation, ellipticity and lateral heterogeneities are introduced by computing the splitting matrix H_k for the GC approximation (Dahlen and Tromp, 1998, p. 643) using S40RTS 3D Earth model (Ritsema et al., 2011). Therefore, shear wave velocity perturbation $\delta \ln V_s$ is calculated from S40RTS model, where compressional wave velocity perturbation are scaled by $\delta \ln V_p = 0.5 \delta \ln V_s$ and density perturbation by $\delta \ln \rho = 0.3 \delta \ln V_s$. Source vector is calculated using the Global CMT Catalog solutions (Dziewonski et al., 1981; Ekström et al., 2012).

The analyses are done for the spheroidal modes of two multiplet chains, namely ${}_0S_2 - {}_0T_2 - {}_2S_1 - {}_0S_3$ and ${}_0T_5 - {}_2S_2 - {}_1S_3 - {}_3S_1$, that have frequencies < 1.5 mHz. Target modes are considered in the GC approximation, that is the multiplets within the chain were coupled and isolated from all the other modes (Deuss and Woodhouse, 2001).

For the ${}_0S_2 - {}_0T_2 - {}_2S_1 - {}_0S_3$ chain we generate seismograms for the magnitude 9.0 Tohoku earthquake that occurred on March 11, 2011 at 05:46 UTC with the epicenter approximately 70 kilometers east of the Oshika Peninsula of Tohoku. Station database is built from the Global Seismograph Network (GSN - IRIS/USGS) consisting of 81 stations. From this general network we define 4 groups of stations, namely "full" network which contains all stations (81 stations), "northern" network with stations in northern hemisphere (53 stations), "southern" network with stations in southern hemisphere (28 stations) and "selected" network which contains only 10 stations chosen for specific reasons (see Fig. 6.2), explained further in the text.

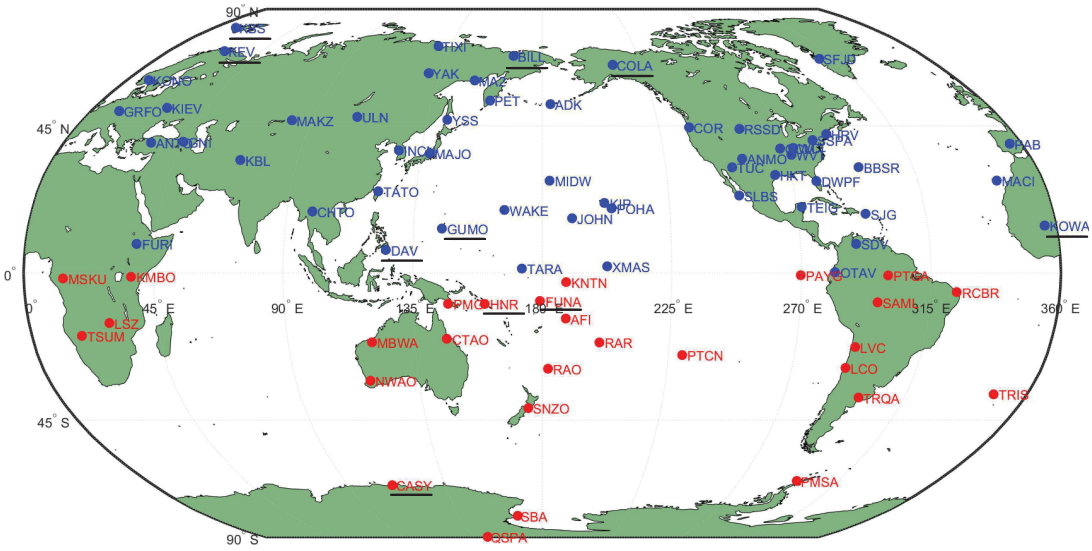

Fig 6.2: Station database build from Global Seismograph Network, where 4 group of stations are: "full" network of 81 stations (circle mark), "northern" network with 53 stations in northern hemisphere (blue color), "southern" network with 23 stations in southern hemisphere (red color) and "selected" network which 10 stations (underlined).

Noise is generated using a random function that draws scalars from the standard normal distribution with zero mean and variance one and is added to the synthetic time series. If the station displacement is denoted by x_s and if the noise function is denoted by x_n the simple relation between the two is established by

$$x_{s+n} = x_s + \sigma_n x_n, \tag{6.1}$$

σ_n being the noise standard deviation with the acceleration unit nm/s^2, which we gradually increase in the analysis from 1 to 10. For every experiment of specific station network and noise level the results are estimated frequency, Q-factor, amplitude, OSE resonance function and the phasor walkouts with associated R^2-tests of the target singlet.

From the three spheroidal modes in the ${}_0S_2-{}_0T_2-{}_2S_1-{}_0S_3$ chain, we show results for ${}_0S_2$ and ${}_2S_1$, while the results for ${}_0S_3$ are more or less similar to the ones for ${}_0S_2$. To successfully analyze ${}_0S_2$ one needs to use at least 4 hours of data to separate this multiplet from the next multiplet in frequency domain, 2.5 days to separate singlets within the multiplet, while the 1.1 Q cycle is 19 days for having the optimal SNR (Dahlen, 1982a). We choose 15 day-long records which are zero-padded till 90 days to obtain a frequency resolution of order 10^{-8} Hz with a sampling rate of 10 s. After the 2011 event, amplitudes of $m = \pm 1$ singlets are better excited than amplitudes of $m = \pm 2$ singlets and specially compared to $m = 0$ (Ding and Shen, 2013b). For this reason, the selected network contains only 10 stations for which the $m = 0$ singlet is visibly excited.

Since ${}_0S_2$ mode has 5 singlets, the full experiment for 4 different network of stations and 10 noise levels consists of 200 frequency estimates, 200 Q-factor estimates, 200 OSE resonant functions, 1000 phasor walkout estimates (since we test for 5 frequencies) and 1000 associated R^2-tests. Considering that all results and conclusions can be drawn from the results of only one singlet, we choose to do so. The results for the best excited singlet $m = 1$ of ${}_0S_2$, noted ${}_0S_2^1$, are in Fig. 6.3. The results, quite straightforward, confirm that when noise is gradually added the SNR decreases and standard deviations increase. Furthermore, the results for the full network are overall foremost while the estimates have the smallest standard deviations and relative errors. Besides, estimates become more scattered around the true synthetic value (dashed line) with noise increment. However, not all frequency estimates contain the true synthetic values within their standard deviations. Conclusions drawn for the frequency estimates are also applicable to the estimates of Q-factors (see Fig. 6.4). In the case of Q-factors, relative error for full network is not more than 6.2 % ($\sigma_n = 9$ nm/s^2) while it increases to 50 % ($\sigma_n = 9$ nm/s^2) for selected network. The variability of the OSE resonance functions due to different networks and noise levels is shown in Fig. 6.5 where we plot the maximum and the minimum of the resonance function assemblage. The four out of five singlets are in all experiments nicely excited and not buried in the noise, however this is not the case for the ${}_0S_2^0$ singlet.

Further, to better understand our results we examine the phasor walkout for five test frequencies $f_s = \{f_e - 2\sigma_f, f_e - \sigma_f, f_e, f_e + \sigma_f, f_e + 2\sigma_f\}$ and three cases: 1) full network with noise level $\sigma_n = 1$ nm/s^2 and relative error 1.4 ppm 2) full network with $\sigma_n = 9$ nm/s^2 and 66.6 ppm (the largest for this network, frequency with its standard deviation

does not include the synthetic value), 3) selected network with $\sigma_n = 8$ nm/s^2 and 251.1 ppm (the largest for the whole data set). The results shown in Fig. 6.6 demonstrate that the phasor walkout method successfully distinguishes between five different test frequencies and additionally indicates that the centre one is the true frequency of the stacked signal when the noise level is only $\sigma_n = 1$ nm/s^2. This encourages us to further use this method, when the noise levels are higher. Moreover, mutual comparison of these three cases demonstrates how noise deteriorates our estimates: with more noise our phase is consistently abrupt causing twisting of the walkout pattern, which nevertheless has the propensity to straightness. However, we can expect that in some cases, where this twisting is more prominent, the R^2-test will be difficult to accomplish. For the second case we can ask ourselves: why do the estimated frequencies not include the true synthetic value within their standard deviations? Our goal is to understand where the bias is coming from, OSE or ARFD80 method. From the theoretical background, if the ARFD80 method failed in estimating frequency, which means that the bias is not coming from the stacking, by plotting the phasor walkout one should obtain a curved line for $f_s = f_e$. However if the estimated frequency is the true frequency of this harmonic signal one should have a straight line. In the latter case, it means that the OSE method introduced a bias by producing a slight peak shift of the singlet due to noise input. The results in Fig. 6.6 confirm that the bias is introduced with OSE method because the R^2-test is the highest for the central frequencies indicating that ARFD80 method estimated true frequency of stacked signal. Additionally, we can confirm that the bias introduced with OSE method is generated by the noise input, since the estimates of eigenfrequencies without added noise are not biased. Furthermore, observing the phasor walkout graphs and R^2-tests of the three cases it is evident that the first case has the highest R^2-test, while the third case, the lowest R^2-test, meaning that the first case holds the highest linearity and the third one the lowest.

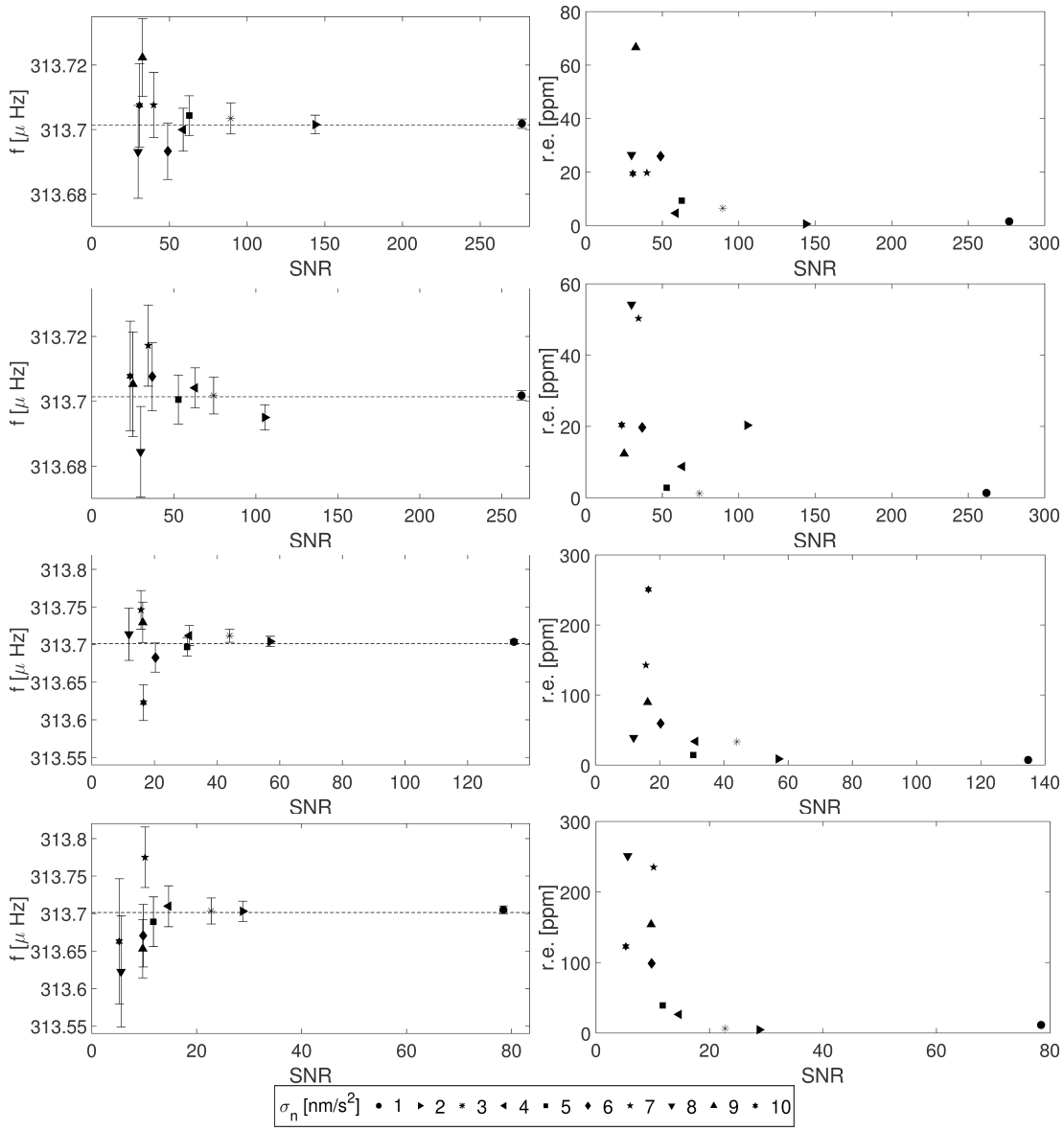

Fig 6.3: Synthetic experiments for ${}_0S_2^1$ singlet conducted for four station distributions: 1) full (the first row), 2) northern (the second row), 3) southern (the third row), 4) selected (the fourth row) networks. Figures on the left represent the estimated frequencies versus SNR for ten different noise levels. Figures on the right represent the relative errors of frequencies with regard to synthetic value (dashed line) versus SNR for ten noise levels. Be careful, the vertical scales of the left-side figures are optimized, thus the full and the northern networks have the same scale and the southern and the selected networks too.

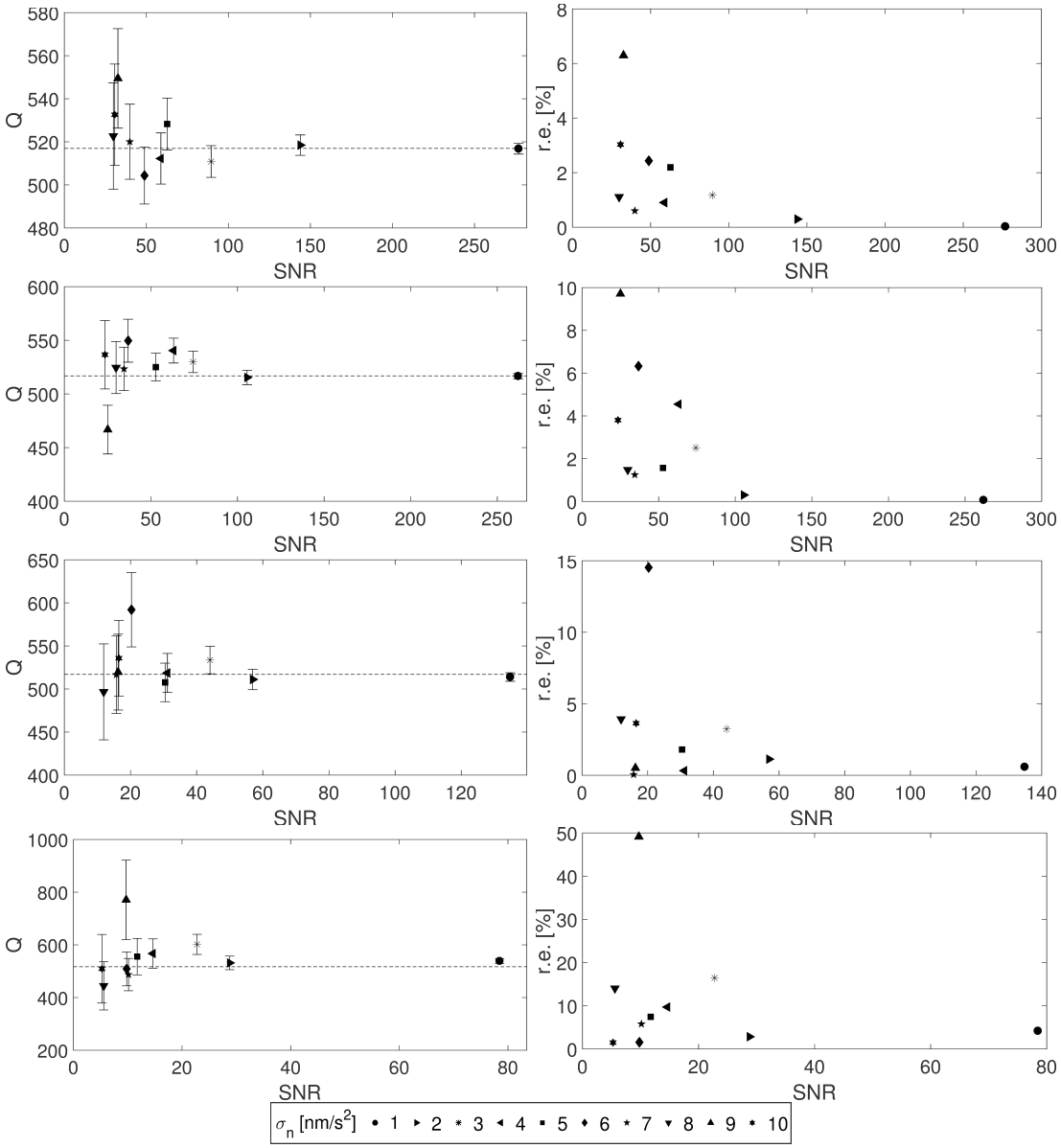

Fig 6.4: Synthetic experiments for ${}_0S_2^1$ singlet conducted for four station distributions: 1) full (the first row), 2) northern (the second row), 3) southern (the third row), 4) selected (the fourth row) networks. Figures on the left represent the estimated Q-factors versus SNR for ten different noise levels. Figures on the right represent the relative errors of Q-factors with regard to synthetic value (dashed line) versus SNR for ten noise levels.

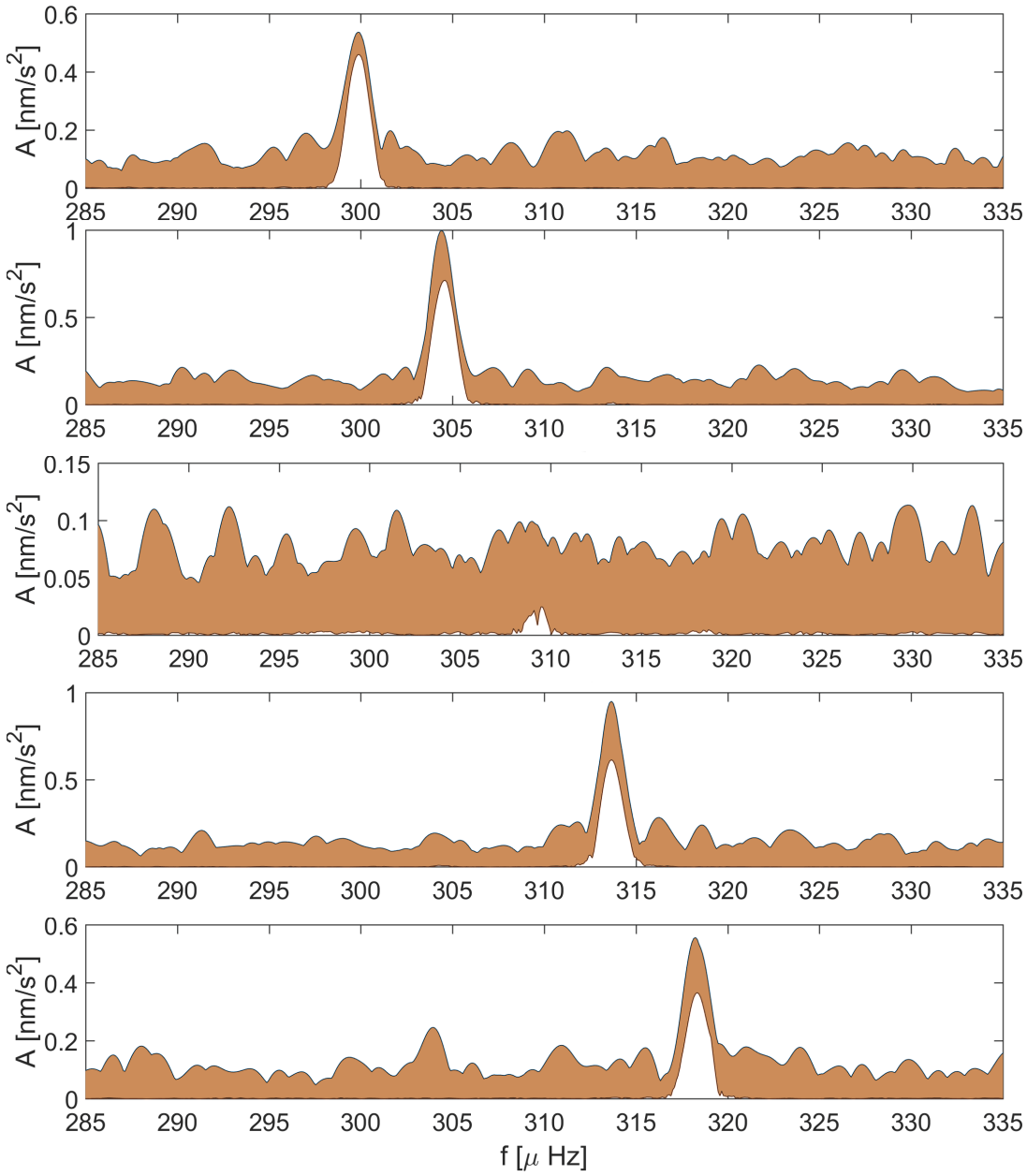

Fig 6.5: Variability of the OSE resonance functions due to four different networks and ten noise levels for the ${}_0S_2$ mode.

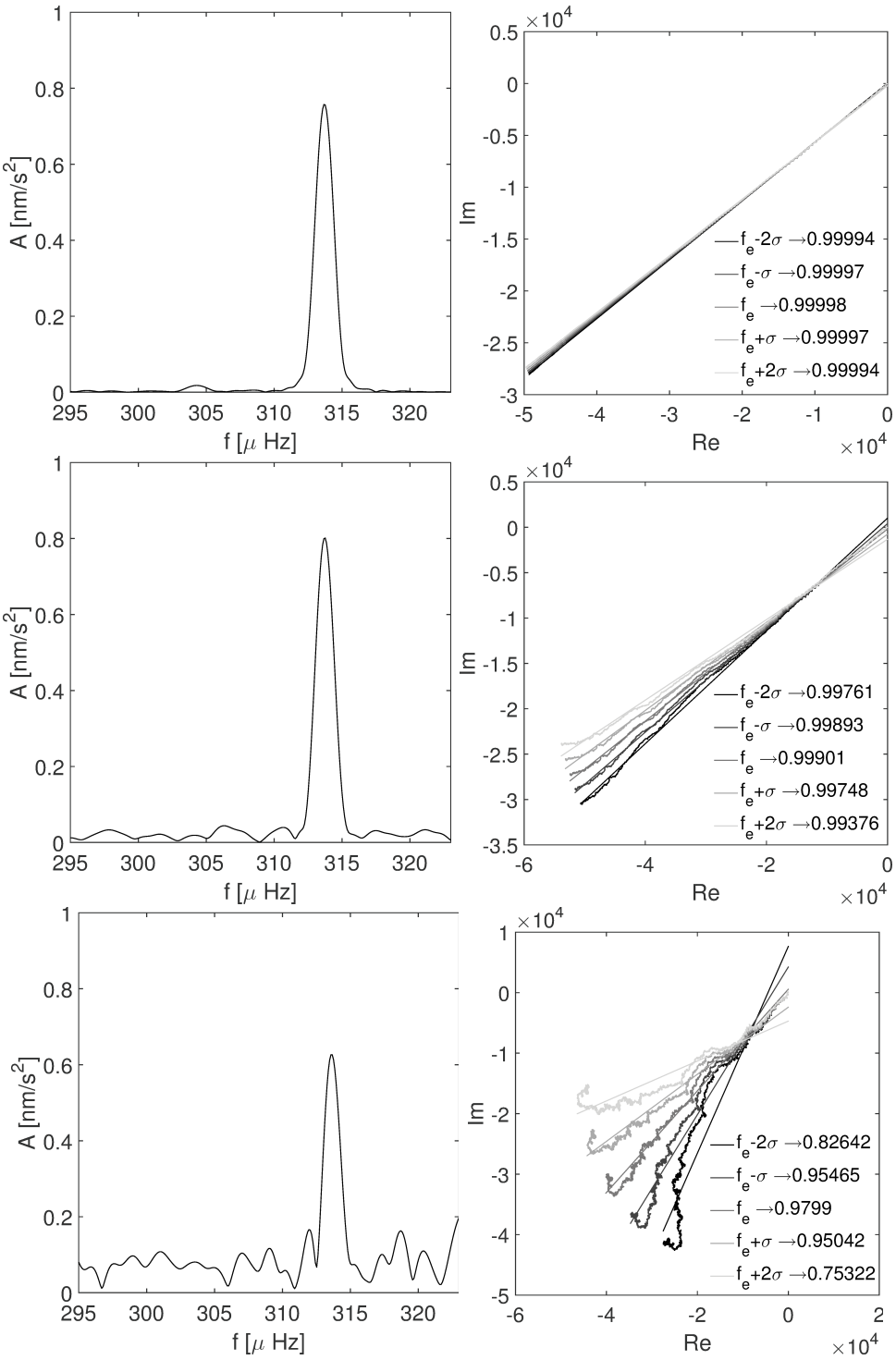

Fig 6.6: Fourier Transform of OSE stacked signals (left) with associated phasor walkouts and applied R^2-test values (right) for five test frequencies with f_e being the estimated frequency of stacked signal on left and σ the standard deviation. Three cases are shown: full network with noise level $\sigma_n = 1$ nm/s^2(top), full network with $\sigma_n = 9$ nm/s^2 (middle) and selected network with $\sigma_n = 8$ nm/s^2 (bottom). Results are for ${}_0S_2^1$ singlet.

Studying the relationship between relative errors and SNRs within all experiments conducted for the ${}_0S_2$ multiplet, thus considering all singlets, one can notice that for each SNR one can associate a range of possible relative errors. Meaning that, it does not necessarily means that solution with larger SNR has smaller relative error and thus better estimate. Considering this fact, we decide to compare relationship between standard deviations estimated with the bootstrap method and the one estimated from the maximum relative error from all our experiments (i.e. 200 experiments for 5 singlets, 10 noise levels and 4 networks) for a specific SNR. In Fig. 6.7 we plot the aforementioned standard deviations versus SNR in log scale. Standard deviations estimated from maximum relative errors are obtained using the formula

$$\sigma_{r.e.}(\text{SNR}) = \max \text{r.e.}(\text{SNR}) f_{syn}, \tag{6.2}$$

where max r.e.(SNR) is, as stated before, a maximum relative error for the specific SNR. Surprisingly, both estimates of standard deviations are exponentially dependent on SNR. However, standard deviations, recalculated from the relative errors, are for most cases higher than the bootstrap standard deviations. This implies that for most SNRs, especially for the lower values, we can have bootstrap standard deviations which are smaller than the actual differences between synthetic values and estimated values. We can conclude that even though we have good precision on our estimates we have poor accuracy due to the biases introduced by all used methods.

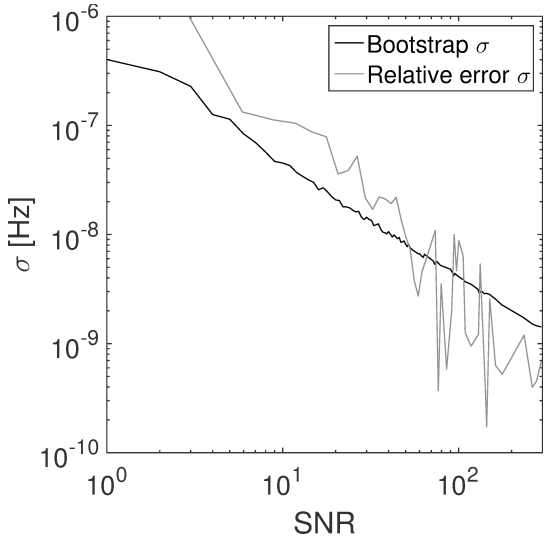

Fig 6.7: Estimated frequency bootstrap standard deviations (black line) and standard deviations estimated from frequency relative errors (gray line) versus SNRs for all experiments of ${}_0S_2$ multiplet.

From the built catalog consisting of frequencies and their associated standard deviations for each singlet within the ${}_0S_2$ multiplet using Eq. (3.30) we can calculate the splitting

function coefficients associated for each network and noise level. For that we need the values of a, b and c parameters and of the degenerate frequency $\bar{\omega}_k$. The parameters a, b, and c are estimated by fitting a parabola to the synthetic singlets frequencies for a rotating hydrostatic ellipsoidal Earth model derived from PREM. Please note that these parameters could also be computed directly using explicit formulas form Dahlen and Sailor (1979). $\bar{\omega}_k$ is a degenerate eigenfrequency of the spherical non-rotating PREM model. In the next step we subtract the first term in (3.29) from singlet frequencies to arrive at

$$\omega_m^{residual} = \gamma_{20}^{mm} c_{20} + \gamma_{40}^{mm} c_{40}, \tag{6.3}$$

because for ${}_0S_2$ azimuthal order is 2, thus $s = 2, 4$. Since it was found from some studies of aspherical structures that the degree 2 structure is much larger in amplitude than the degree 4 (Ritzwoller et al., 1986; Widmer et al., 1992) we decide to fit only for degree 2 structure in (6.3) (for example, for the S40RTS model c_{20} is 6 times larger than c_{40}). The real coefficient γ_{20}^{mm} is calculated using the SC approximation theory (Dahlen and Tromp, 1998). The results for c_{20} splitting function coefficients are shown in Fig. 6.8. They are calculated using non-weighted and weighted ordinary least squares method where weights are obtained from frequency standard deviations. To be consistent with observed values, we estimate the referent value (dashed line in Fig. 6.8) in the same manner. That is, from the synthetic singlet frequencies, calculated for a rotating Earth model with lateral heterogeneities (S40RTS model), we first remove the effects of rotation and ellipticity using previously estimated a, b, and c parameters and next we fit just for c_{20} using relation (6.3). We are aware that this procedure may introduce a small bias in our referent value, however this is necessary for the value to be comparable with the measured ones (due to the diagonalization of the splitting matrix (Dahlen and Tromp, 1998, p. 650)).

It is usually expected that the weighted solutions have overall better results than the non-weighted solutions, however Fig. 6.8 shows that the non-weighted solutions have similar results as weighted solutions specially when SNR is large and there are enough stations. As analysis progresses the non-weighted solutions become expectedly more deteriorated and off balanced. It is important to emphasize that each splitting function coefficients is obtained considering five biased frequencies and their associated standard deviations, however it seems that this effect is the most relevant for all non-weighted solutions and for weighted solutions in case of 10 stations, impacting both the structure coefficients and their associated standard deviations. The latter one is evident due to the fact that the standard deviations are in some occasions uncorrelated with the number of stations used or noise level amplitude (Fig. 6.8). Besides, it is encouraging that weighted c_{20} coefficients are close

to and contain synthetic values within the estimated standard deviations for most of the experiments.

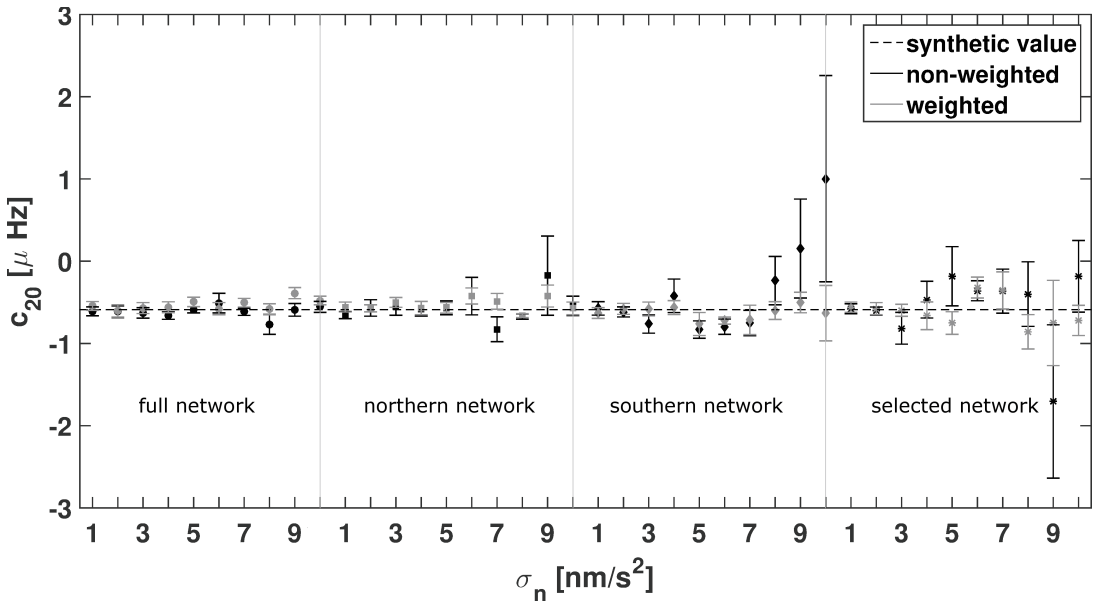

Fig 6.8: Splitting function coefficient c_{20} inverted from eigenfrequencies estimated in synthetic experiments for ${}_0S_2$ multiplet considering four different station distributions and ten noise levels.

For comparison, let us consider now the case of the $m = -1$ singlet of ${}_2S_1$ multiplet. In this case the selected network contains stations where all three singlets of this multiplet are excited. For the analysis we use around 12 day time-series, which are zero padded to 72 days. The conclusions made for the ${}_0S_2$ multiplet are valid for this multiplet too. However, since this mode is poorly excited, the number of stations used in the stacking method becomes more critical than for ${}_0S_2$. During the experiments, not for all combinations of noise levels and station distributions singlets emerge during the stacking. The relative errors become quite large compared to ${}_0S_2$, ranging from 56 ppm (full network) to 323 ppm (selected network) for $\sigma_n = 1$ nm/s^2 and phasor walkouts become much more complex with more loops indicating the higher noise influence (Fig. 6.9). During the analysis the number of used stations and associated records' SNR become more relevant. If we have two stacked signals with the same SNR, one of them could be built for the singlet with less excited amplitude, more stations and lower noise level, and the other stacked signal could be built for the singlet with better excited amplitude, less stations and higher noise level. Even though we end up with the same SNR, the ARFD80 method frequently fails in estimating the true frequency of stacked signal for the first case according to the R^2-test. Instead, the estimated frequencies are within the estimated standard deviations. Hence, it seems that

ARFD80 is sensitive to the singlet starting amplitude to be stacked, that is the method is becoming unreliable when starting signals of singlets are buried in noise.

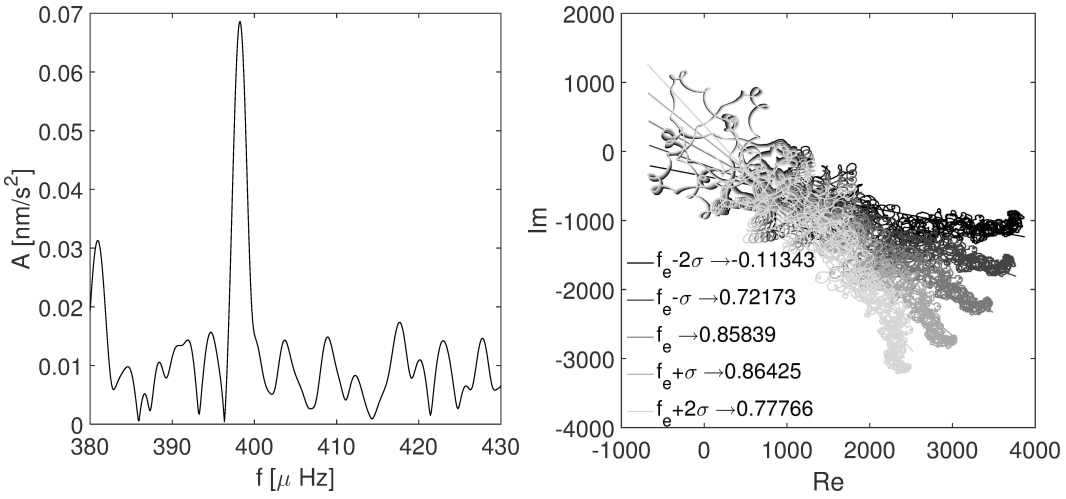

Fig 6.9: Fourier Transform of OSE signal (left) with associated phasor walkout and R^2-test values (right) for five test frequencies with f_e being the estimates frequency of stacked signal on left and σ the standard deviation. Results correspond to selected network with $\sigma_n = 1$ nm/s^2 for ${}_2S_1^{-1}$ singlet with SNR of 5.8.

The performances of the used methods are tested on the higher frequency multiplet chain ${}_0T_5 - {}_2S_2 - {}_1S_3 - {}_3S_1$, characterized by more prominent mode-mode interferences. It is known from the PREM model prediction that three modes ${}_2S_2$, ${}_1S_3$, ${}_3S_1$ have very different Q-factors, but similar frequencies. Their Q-factors are approximately 96, 283, 827 and frequencies 937.85 μHz, 939.83 μHz, 943.95 μHz, respectively. The frequency difference between ${}_2S_2$ and ${}_3S_1$ is 6.1 μHz, which means that one needs 2.8 days to separate them in frequency domain, but the ${}_2S_2$ has the Q-cycle duration of 1.18 days, thus it is impossible to observe this mode without interference of ${}_3S_1$ and ${}_1S_3$. The quickly decaying ${}_2S_2$ mode is always predominate by slower decaying ${}_3S_1$ and ${}_1S_3$ modes. The observation of the ${}_1S_3$ mode has the similar issues due to the presence of ${}_3S_1$ mode. The measurement of ${}_3S_1$ is easier than the other two, however the existing overlapping with ${}_1S_3$ mode introduces the contamination in the measurement of the ${}_3S_1$ splitting frequencies (Rogister, 2003; Roult et al., 2010; Shen and Wu, 2012; Ding and Shen, 2013a,b; Chao and Ding, 2014). Although there are several studies which measured the ${}_3S_1$ frequencies (Roult et al., 2010; Shen and Wu, 2012; Ding and Shen, 2013a,b; Chao and Ding, 2014) only in the work by Chao and Ding (2014) the frequencies of all three modes ${}_2S_2$, ${}_1S_3$, ${}_3S_1$ are recovered using spherical harmonics stacking (Buland et al., 1979) in the SC approximation.

In the present study, the aforementioned characteristics of this chain prevent us from conducting the station distribution analysis, while it is already difficult to find combination

of stations where some singlets are excited above noise level. Once the best combination of stations has been found we perform noise analysis. The OSE method turns out to be less successful in generating isolated singlets than in the case of the ${}_0S_2$ multiplet chain and the phasor walkouts consistently generate beating patterns indicating the existence of neighboring singlets. The example for the relatively successful OSE resonance functions for ${}_1S_3$ multiplet is showed in Fig. 6.10. The figure is showing the comparison between the synthetic resonance functions obtained for the cases of the GC approximation considering ${}_0T_5 - {}_2S_2 - {}_1S_3 - {}_3S_1$ and the SC approximation considering only ${}_1S_3$.

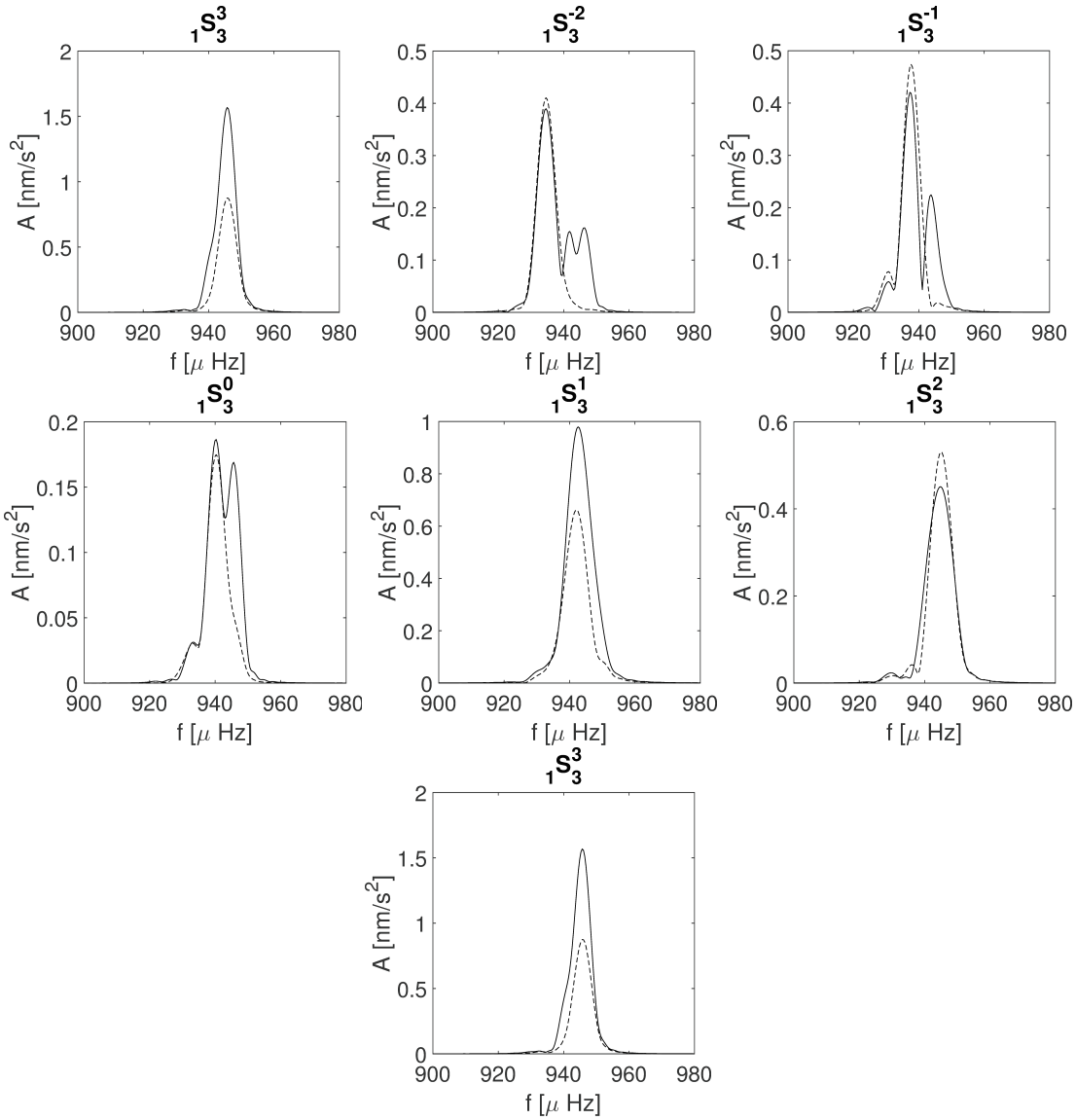

Fig 6.10: Comparison between the synthetic resonance functions obtained for group coupling (solid line) and self coupling (dashed line) approximations for the singlets of ${}_1S_3$ multiplet.

In our knowledge there is only one study that claims that ${}_2S_2$, ${}_1S_3$, ${}_3S_1$ multiplets can

be successfully recovered in the SC approximation. According to the recent work OSE is successfully performing for the higher frequency modes in the SC approximation (Zeng and Shen, 2017) and in the GC approximation (Zeng and Shen, 2018), however Fig. 6.10 seems to suggest us that OSE is not working sufficiently good for the coupled multiplets in the SC approximation. For the ${}_3S_1$ multiplet there are more studies which claim that this multiplet could be recovered in the SC approximation (Roult et al., 2010; Shen and Wu, 2012; Ding and Shen, 2013a,b).

6.3 Observations

The methods and procedure conducted on synthetic data are now applied to the long-period seismometer and superconducting gravimeter data recorded after the six latest earthquakes of magnitude greater than 8.3. Seismogram database is built considering earthquakes with epicenters off the west coast of Sumatra island, Indonesia in 2004, off the coast of central Chile in 2010, off the Pacific coast of Tohoku, Japan in 2011, near the Indonesian province of Aceh in 2012, in the Sea of Okhotsk in western Pacific Ocean in 2013 and offshore from Illapel, Chile in 2015. The long-period STS-1 and STS-2 seismometer data are requested from IRIS service for LHZ channel with 125 stations in total. The RDseed software is used to read SEED volumes and to retrieve SAC files. Next the Python package Obspy (Beyreuther et al., 2010; Megies et al., 2011; Krischer et al., 2015) is used to perform instrument deconvolution and finally the TSoft software (Van Camp and Vauterin, 2005) is used to clear time series of glitches, small gaps etc. The accepted records are decimated to 60 s after low-pass filtering and cut 5 hours after the earthquake. 12 day-long time records (rarely 10 days due to deteriorated time series) are then used. Seismometer data are not corrected for the atmospheric pressure effect because most of the barometric data is missing. Thus to be consistent during the analysis we skip this part. Gravimeter database is built considering the same earthquakes and downloaded from the IGETS website (http://igets.u-strasbg.fr/). The downloaded files are first merged, then the instrumental and pressure scale factors are applied. Further, the gaps and spikes are fixed and finally we apply a high pass least-squares filter with a cut-off frequency of 0.1 mHz to remove tides and other long-period effects. Atmospheric pressure effects are finally corrected using a nominal admittance of -3 nm/s^2/hPa (Zürn and Widmer-Schnidrig, 1995).

In view of the synthetic experimental results we base our analysis of observed data on the SNRs. That is, after choosing the target singlet we estimate SNR from each seismogram and gravimetric record and organize them by decreasing SNR and eventually choose the first half of the records, with the highest SNRs. Chosen records are stacked and the SNR of this newly stacked signal is calculated, which we call $\mathrm{SNR}_{\mathrm{base}}$. In the next steps, we

either add or remove one signal from the chosen first half, perform again the stacking and calculation of the SNR of newly stacked signal, which we call $\mathrm{SNR}_{\mathrm{base}+1}$ if we add signal and $\mathrm{SNR}_{\mathrm{base}-1}$ if we remove signal. If either $\mathrm{SNR}_{\mathrm{base}+1} > \mathrm{SNR}_{\mathrm{base}}$ or $\mathrm{SNR}_{\mathrm{base}-1} > \mathrm{SNR}_{\mathrm{base}}$ we continue adding or removing n signals until either $\mathrm{SNR}_{\mathrm{base}+\mathrm{n}} < \mathrm{SNR}_{\mathrm{base}+(\mathrm{n}-1)}$ or $\mathrm{SNR}_{\mathrm{base}-\mathrm{n}} < \mathrm{SNR}_{\mathrm{base}-(\mathrm{n}-1)}$. Once we find the combination of records which produces the highest SNR for target singlet, we perform the calculation of complex frequencies with ARFD80 method and additionally validate our eigenfrequencies with the phasor walkout representation.

For the purpose of comparing observed results with synthetic results, we decide to analyze the same multiplets as in synthetic experiments, namely ${}_0\mathrm{S}_2$, ${}_0\mathrm{S}_3$, ${}_2\mathrm{S}_1$ and ${}_3\mathrm{S}_1$. There have been numerous studies dedicated to the estimates of the frequencies of the aforementioned multiplets, however the first study of all singlets of ${}_0\mathrm{S}_2$ and ${}_0\mathrm{S}_3$ multiplets was done by Buland et al. (1979), for the triplet ${}_2\mathrm{S}_1$ by Rosat et al. (2003) and for ${}_3\mathrm{S}_1$ by Chao and Gilbert (1980). Our process of searching for the stacked signal with the highest SNR resulted in obtaining different station distributions, different numbers of stations and different percentages of used earthquakes for each singlet. The estimated split frequencies, Q-factors and associated standard deviations along with the SNR of stacked signals and number of stations used are shown in Tab. 6.1, 6.2, 6.3 together with published values. During the analysis the OSE method successfully isolates singlets and the phasor walkout graphs with the associated R^2-test indicate that the true eigenfrequencies of stacked signals are within the estimated standard deviations. The example of stacked signals for ${}_2\mathrm{S}_1$ and ${}_3\mathrm{S}_1$ is shown in Fig. 6.11. It is important to notice that the phasor walkout patterns for observed data and synthetic experiments are quite different. The walkout pattern for real data is characterized with repeated loops and twists, where the first characteristics indicate the presence of a harmonic function of close frequency with the dominant amplitude compared with the amplitude of tested signal and the second characteristics indicate the noise presence and the phase abruptness, which is expected due to the imperfections of the observed data, such as remaining glitches.

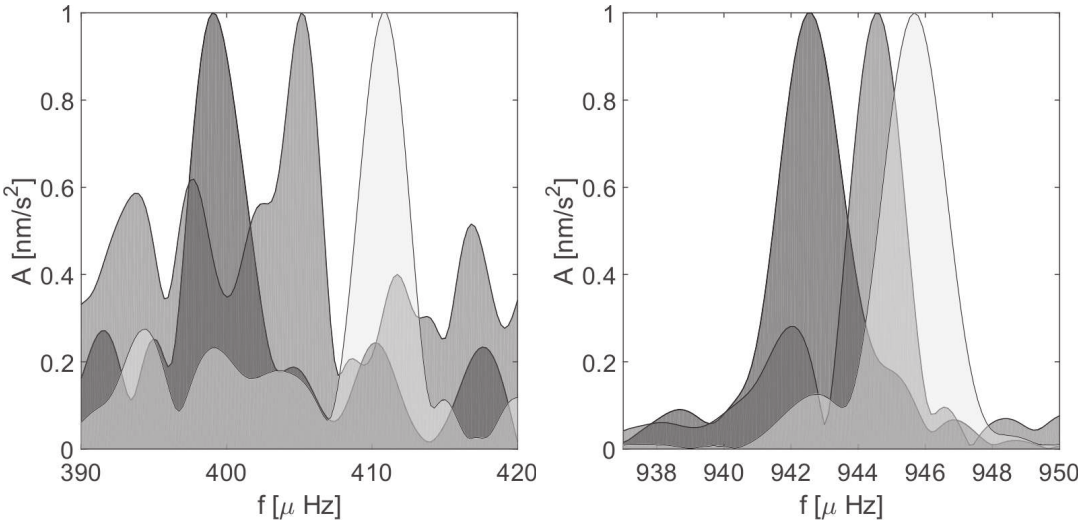

Fig 6.11: ${}_2S_1$ and ${}_3S_1$ singlets obtained using the OSE stacking method applied on 7 and 12 days long time series, respectively. The amplitude values are 0.08, 0.05, 0.20 nm/s^2 for ${}_2S_1$ and 0.51, 0.25, 0.81 nm/s^2 for ${}_3S_1$.

The new set of estimated eigenfrequencies with associated standard deviations is used to calculate a new axisymmetric splitting function coefficient of second order. As for the synthetic case, to be able to use Eq. (6.3), we subtracte the a, b, c parameters from the split eigenfrequencies. In this case a, b, c parameters are estimated by fitting the frequencies for the PREM model, calculated for a rotating ellipsoidal oceanless Earth model (Rogister, 2003). The results for non-weighted and weighted (where weights are frequency standard deviations) solution are shown in Tab. 6.4 and compared with published values. The splitting function coefficients from Häfner and Widmer-Schnidrig (2013) are estimated by subtracting a, b, c parameters as in this work.

At this stage it is difficult to thoroughly compare results of this study with previously published values, considering that all other studies used different methods and data to obtain the estimates. Thus, it is difficult to conclude which study is less biased and more relevant. Summarizing the information from the ten published studies used in Tab. 6.1 and 6.2, we notice that most studies used no more than three earthquakes in their analysis, where all of them used Sumatra earthquake from 2004. Next, the majority used around 11 stations, with the exception of Deuss et al. (2011) where they even used 300 spectra for some modes, Chao and Ding (2014) 96 records, Ding and Chao (2015b) 46 records and Roult et al. (2010) 247 records. However, it is not always clear whether all the records are used in the analysis of all target modes in their studies. Most of the studies used SG records, except (Deuss et al., 2011), Chao and Ding (2014) and Roult et al. (2010) who used only seismograms. Further, the methods for obtaining the modal parameters are different (see Tab. 6.1 and

Tab 6.1: Estimated eigenfrequencies (in μHz) and Q-factors with associated standard deviations, SNRs and number of stations N used in the stacking for ${}_0S_2$ and ${}_0S_3$ multiplets compared with published values. Methods applied: * Lorentzian fitting, $^\diamond$ nonlinear iterative least squares inversion, $^\circ$ multitapers, $^\triangledown$ ARFD80, $^\triangleleft$ ensemble empirical mode decomposition, $^\triangleright$ AR-spectrum and ARFD80.

${}_0S_2$	m	-3	-2	-1	0	1	2	3
This work	f	-	299.939	304.619	309.226	313.830	318.431	-
		-	± 0.013	± 0.009	± 0.018	± 0.012	± 0.013	-
	Q	-	412.8	477.3	481.7	484.8	469.6	-
		-	± 14.6	± 13.7	± 26.2	± 17.8	± 17.2	-
	SNR	-	39	53	27	39	40	-
	N	-	33	35	60	68	50	-
Roult et al. (2010)*	f	-	299.98	304.47	309.22	313.74	318.35	-
Deuss et al. (2011)$^\diamond$	f	-	299.93	304.63	309.28	313.86	318.40	-
Rosat et al. (2012)*	f	-	299.96	304.58	309.25	313.83	318.44	-
		-	± 0.022	± 0.051	± 0.033	± 0.046	± 0.021	-
Häfner and Widmer-Schnidrig (2013)$^\circ$	f	-	299.948	304.612	309.269	313.840	318.429	-
		-	± 0.009	± 0.006	± 0.016	± 0.005	± 0.009	-
	Q	-	486	473	512	488	498	-
		-	± 16	± 9	± 29	± 8	± 15	-
Ding and Shen (2013b)$^\triangledown$	f	-	299.958	304.588	309.263	313.835	318.422	-
		-	± 0.0081	± 0.0046	± 0.011	± 0.0014	± 0.0074	-
	Q	-	509.4	484.7	394.4	520.2	532.7	-
		-	± 12.1	± 9.3	± 14.3	± 8.1	± 10.1	-
Shen and Ding (2014)$^\triangleleft$	f	-	299.994	304.618	309.278	313.865	318.424	-
		-	± 0.011	± 0.0078	± 0.0091	± 0.0077	± 0.0096	-
Ding and Chao (2015b)$^\triangleright$	f	-	299.967	304.587	309.372	313.850	318.396	-
		-	± 0.014	± 0.0078	± 0.050	± 0.0069	± 0.013	-
${}_0S_3$								
This work	f	461.705	464.132	466.459	468.724	470.781	472.838	474.724
		±0.023	±0.012	±0.020	±0.040	±0.020	±0.012	±0.015
	Q	418.2	410.1	439.9	298.5	433.9	438.0	408.6
		18.3	9.8	17.0	15.1	16.8	9.5	10.5
	SNR	25.14	46.10	27.95	17	27.37	49.38	40.66
	N	50	55	51	39	51	55	50
Roult et al. (2010)*	f	461.60	464.17	466.40	468.60	470.76	472.75	474.70
Rosat et al. (2012)*	f	461.67	464.24	466.39	-	470.84	472.66	474.74
		±0.054	± 0.078	± 0.036	-	± 0.030	± 0.078	± 0.068
Ding and Shen (2013b)$^\triangledown$	f	461.623	464.219	466.535	468.549	470.657	472.843	474.831
		± 0.0049	± 0.0018	± 0.0026	± 0.0052	± 0.0024	± 0.0017	± 0.0035
	Q	351.5	418.5	348.4	424.4	356.9	397.7	417.2
		± 19.1	± 9.2	± 15.8	± 22.5	± 14.5	± 10.0	± 16.3
Shen and Ding (2014)$^\triangleleft$	f	461.618	464.161	466.397	468.650	470.734	472.816	474.727
		± 0.018	± 0.011	± 0.026	± 0.030	± 0.022	± 0.011	± 0.019

Tab 6.2: Estimated eigenfrequencies (in μHz) and Q-factors with associated standard deviations, SNRs and number of stations N used in the stacking for $_2S_1$ triplet compared with published values. Methods applied: * Lorentzian fitting, $^\diamond$ nonlinear iterative least squares inversion, $^\times$ OSE and ARFD80, $^\triangledown$ ARFD80, $^\triangleleft$ ensemble empirical mode decomposition, $^\triangleright$ AR-spectrum and ARFD80, $^\otimes$ multi-station experiment technique, † spherical harmonic stacking and ARFD80.

$_2S_1$	m	-1	0	1
This work	f	398.854	405.290	410.880
		± 0.347	± 0.316	± 0.108
	Q	250.5	391.0	404.8
		98.9	237.6	91.0
	SNR	3.3	2.6	8.2
	N	34	23	34
Roult et al. (2010)*	f	397.70	403.94	410.63
Deuss et al. (2011)$^\diamond$	f	397.92	405.18	410.45
Rosat et al. (2012)*	f	398.10	-	410.82
		± 0.98	-	± 0.18
Ding and Shen (2013a)$^\times$	f	397.982	-	411.051
		± 0.12	-	± 0.055
Ding and Shen (2013b)$^\triangledown$	f	398.662	405.014	410.768
		± 0.0085	± 0.0027	± 0.0012
	Q	365.9	448.3	385.6
		± 20.3	± 15.7	± 11.8
Shen and Ding (2014)$^\triangleleft$	f	398.363	404.757	410.810
		± 0.043	± 0.039	± 0.019
Ding and Chao (2015b)$^\triangleright$	f	398.174	404.955	410.806
		± 0.2	± 0.079	± 0.064

Tab 6.3: Estimated eigenfrequencies (in μHz) and Q-factors with associated standard deviations, SNRs and number of stations N used in the stacking for ${}_3S_1$ triplet compared with published values. Methods applied: * Lorentzian fitting, $^\diamond$ nonlinear iterative least squares inversion, $^\times$ OSE and ARFD80, $^\triangledown$ ARFD80, $^\triangleleft$ ensemble empirical mode decomposition, $^\triangleright$ AR-spectrum and ARFD80, $^\otimes$ multi-station experiment technique, † spherical harmonic stacking and ARFD80.

${}_3S_1$				
This work	f	942.565	944.570	945.661
		± 0.019	± 0.032	± 0.005
	Q	873.2	649.5	903.9
		± 31.3	± 28.1	± 9.5
	SNR	30.42	20.91	103
	N	82	12	82
Roult et al. (2010)*	f	942.56	944.19	945.79
Shen and Wu (2012)$^\otimes$	f	942.598	944.113	945.864
		± 0.42	± 0.27	± 0.21
Ding and Shen (2013a)$^\times$	f	942.267	944.765	945.763
		± 0.022	± 0.051	± 0.018
Ding and Shen (2013b)$^\triangledown$	f	942.426	944.713	945.612
		± 0.0025	± 0.0017	± 0.0046
	Q	943.8	773.6	629.5
		± 12.5	± 10.1	± 18.4
Chao and Ding (2014)†	f	942.57	944.20	945.76
		± 0.028	± 0.092	± 0.034
	Q	801	625	650
		± 20	± 31	± 22

Tab 6.4: Second order axisymmetric structure coefficients for ${}_0S_2$ compared with published values. The structure coefficients are computed from the singlet frequencies (*) or the nonlinear iterative least squares inversion ($^\diamond$).

References	c_{20} [μHz]
This work (weighted)*	-0.7233 ± 0.0623
This work (non-weighted)*	-0.7428 ± 0.0633
Ritzwoller et al. (1986)*	-0.30 ± 0.65
Deuss et al. (2011)$^\diamond$	-0.66 ± 0.32
Häfner and Widmer-Schnidrig (2013) (weighted)*	-0.7404 ± 0.0466
Häfner and Widmer-Schnidrig (2013) (non-weighted)*	-0.6902 ± 0.0398

6.2). The estimation of standard errors is performed either by using the bootstrap method along with the weighted mean (Häfner and Widmer-Schnidrig, 2013; Ding and Shen, 2013b; Shen and Ding, 2014), or just the bootstrap method (Ding and Chao, 2015b), or using the error analysis from Dahlen (1982b) (Rosat et al., 2012) or the error analysis from Chao and Gilbert (1980) (Ding and Shen, 2013a; Chao and Ding, 2014) and the least-square fitting (Shen and Wu, 2012). Methodologically, only Ding and Shen (2013a) used the same process analysis as in this paper, however they used only 8 and 11 SG records for obtaining the estimates for ${}_2S_1$ and ${}_3S_1$, respectively, and thus their results may be more biased. Further, directly comparing the measured eigenfrequencies and their standard deviations we can conclude that not all measurements agree within their standard errors. Whether it is a problem in the small data sets within some studies or biases introduced with the methods, it is difficult to comment. We would have the complete information by comparing the SNR values and used number of stations for each estimate, unfortunately, this information is usually missing. Considering the error analysis, the error estimated by the bootstrap method is the statistical error, while the error analysis from Dahlen (1982b) and Chao and Gilbert (1980) give the formal errors. In the view of our synthetic tests, we show that for the most relevant SNRs the estimated error by the bootstrap method is understimated. However, one needs to remember that this error reflects the bias from the used OSE and ARFD80 methods. For our tests it is shown that using around and more than 50 stations in the analysis is generating satisfying estimates. Compared to the frequency estimates, the Q-factor estimates are more scattered, but this has been already known since it is more difficult to measure amplitude than frequency of a mode. The structure coefficient estimates are satisfying since they agree well with published values, bearing in mind that they are estimated using frequencies and their standard deviations obtained for different station distributions. It is true that we can always argue that our estimates are close to published values, however the question of accuracy remains. Only a truthfully comparison of all relevant methods in the same condition can tell which study is the most precise.

6.4 Conclusions

We have quantified the effects of different station distributions and noise levels on the estimation of eigenfrequencies, Q-factors and splitting function coefficients of the gravest seismic modes. A specific protocol was used: the OSE method for stacking signals, the ARFD80 method for obtaining the estimates of harmonic parameters and finally the phasor walkout together with R^2-test for validating the estimated eigenfrequencies. The methods were tested on synthetically generated data and on observations. Synthetic experiments have shown that when noise is gradually added, the SNR of the stacked signals decreases

and standard deviations of estimated frequencies and Q-factors increase, being overall more scattered around the true synthetic value. Results are foremost when more records are included in the stacking. More importantly it has been shown that OSE method is sensitive to different station distributions under the noise influence. Furthermore, the performances of ARFD80 method become deteriorated when the stacking signal is obtained with the less excited signals, that is when the input signals have SNR ≤ 2. However, even for those cases the estimates are within the standard deviations. Moreover, it turns out that the standard deviations calculated with the bootstrap method are not sufficient to include all biases introduced with the methods, that is to say our standard deviations are for most cases underestimated. Thus, even though we have a good precision on our estimates, the accuracy can be poor. This analysis showed that we do not need a priori model to estimate structure coefficients, but results may be biased. Finally, we have proposed new eigenfrequency and Q-factor estimates for ${}_0S_2$, ${}_0S_3$, ${}_2S_1$ and ${}_3S_1$ and also new estimates for the axisymmetric degree-2 structure coefficient from ${}_0S_2$ eigenfrequencies measurements. The results are in good agreement with previously published values, even though the methods are different and thus presumably introduce different biases into the estimates. With the synthetic test performed, we are confident in our new estimates, specially for the ones obtained with more than 50 stations. Finally, future tomographic models that use the splitting function measurements should take into account the existing biases mentioned in this work.

Chapter 7

Conclusion and Perspectives

The main subject of this thesis is modeling the interaction between the GWs from astrophysical sources and the Earth. Two models are considered: the revisited one for a radially heterogeneous non-rotating Earth model (1D Earth model) and a newly developed one for a radially heterogeneous elliptical rotating Earth model (3D Earth model). The solutions of both models are expressed in terms of the normal modes. The GWs are represented by plane waves in the flat space-time approximation. They consist of two main polarizations, the plus and cross one. The induced displacement at the Earth's is developed by defining the displacement as the convolution between the Green tensor and the force term. The Green tensor is defined for a specific Earth model, while the force term is determined for a given GW source. The revisited model is based on the study done by Ben-Menahem (1983) and it involves an infinite monochromatic source expressed by a scalar value, a polarization tensor and a propagation vector. The calculation is performed such as if the source of the GW is within the Earth reference system. The new model is derived for a system of binary stars. It depends on seven parameters of the binary source (the masses, the inclination angle, the polarization angle, the right ascension, the declination and the GW source frequency) and the transformation matrix from the celestial to the terrestrial reference system. Additionally, since the model is rotating the splitting of and coupling between modes are also introduced. Both derivation show that the only normal modes that couple with the GWs are quadrupole ones. Their responses are expressed in terms of five functions: the displacement eigenfunction at the surface; the source-time function that depends on the GW source frequency and the normal mode frequency; the scalar metric perturbation which is for the 1D model just a value and for the 3D model depends on the binary parameters; the pattern functions that depend on the angles of the incoming GW. These pattern functions define which singlet is going to be excited and additionally for the 3D model the functions also determine the splitting of the response due to the Earth's rotation; the model dependent function that is actually the same for both models. The induced response for the 1D model

is calculated in a resonance regime, while the one for the 3D model is in a off-resonance regime. By comparing their estimates, the later one has two orders of magnitude larger response due to different definition of the source-time functions.

The newly developed model for a 3D Earth, naturally, includes some approximations. For example, one of them concerns the calculation of the splitting of and coupling between normal modes that is based on the group-coupling approximation, instead of the full-coupling one. However, the frequency uncertainties due to the coupling approximations or due to the different shear velocity models or due to the uncertainties introduced by general measurements in the normal modes studies, are in general smaller than the frequency uncertainties found in the catalog of the binary stars. Next, another approximation concerns the circular binary orbit or not including the spindown of binaries as well. Nevertheless, for the first stage of the GW search these refinements are unnecessary. During the search for the GW signals performed by the matched filter technique the basic response model, defined by the parameters from the catalog of the binary stars, is indeed sufficient at least to generate events over a predetermined threshold.

In the GW studies we do not know if the signal is present in the data and even if we believe that it is there we do not know when it started and how long we can follow it in time. The matched filtering technique is suitable for this type of search since it answers these two questions, whether the GW signal is present in the data and when it started. In the normal modes studies we know that after an earthquake the Earth is set to vibrations, the normal modes. The Fourier transform is sufficient to observe these modes and to measure them as well. Measuring the normal mode parameters such as frequencies, Q-factors and the splitting function coefficients, we further define constraints on the 3D Earth models. During the past years many techniques have been proposed to extract those parameters from the measurements. However some biases are unavoidable. In this thesis we have quantified some of these biases. By applying three methods (OSE, ARFD80 and the phasor walkout) we test how the frequency estimates are affected by the number and distribution of stations used and different noise levels applied. The results are not straightforward when noise is involved in the measurements and generally more stations means better estimates. This study also provides new eigenfrequency and Q-factor estimates for ${}_0S_2$, ${}_0S_3$, ${}_2S_1$ and ${}_3S_1$ and also new estimates for the axisymmetric degree-2 structure coefficient from ${}_0S_2$ eigenfrequencies measurements. Ideally, all measurements within the normal mode studies should be interpreted in the context of the used methods and data.

The very first measurement of a GW, and all other successors, was accomplished in the high frequency band using an apparatus that is kept in an exceptionally controlled environment to reach required sensitivities. The low frequency band is much more complicated

than high frequency band due to the seismic, environmental and other 'non-stationary' noise sources. This produces the ten orders of magnitude difference between the GW response model developed in this thesis and the most sensitive instrument in the mHz band, the superconducting gravimeters. However, the work might not be ending here since chances for some improvement exist. Firstly, the developed induced spheroidal displacement model showed us that if we know more GW sources we should be able to obtain a response model of larger amplitude. Secondly, if we have more stations to perform the stacking method we would again increase the amplitude of our target signal. Thirdly, since the developed response model is the model of a forced oscillator the signal is not attenuating and thus it is always present in the data and it should be there for a long time. Therefore, using the matched filtering technique we should be able to follow this signal for an extensive amount of time, thus improving the chances of its detection.

The future of the GW detection on Earth in the mHz band is very challenging, however it could be supplemented with the measurement in space. For example, Coughlin and Harms (2014c) were the first ones to consider Apollo seismic data to calculate the upper limit of the isotropic stochastic background. Their work consisted in calculating the correlation of data from pairs of seismometers on Earth and Moon. Since the Moon has the lowest ambient seismic noise currently measured, their results offer probably the best upper limits that can currently be achieved with seismometers in the frequency range 0.1–1 Hz. They also emphasized the advantage of the data correlation between seismometers from Moon and Earth, since in this case there is no seismic correlation due to seismic activity present at both seismometers locations. It would be very interesting to conduct the same study just by using the data from Mars. On November 26, 2018, the InSight spacecraft successfully landed on Mars surface, thus deploying the SEIS (Seismic Experiment for Internal Structure) instrument (Lognonné et al., 2019). Mars differs from Earth in the sense that we expect to observe seismic events with magnitudes lower than on Earth and also since there is no ocean or human activity, we also expect lower seismic noise compared to Earth. The largest contribution to the noise is expected to come from environmental effects such as large thermal changes, magnetic field impact, large pressure signal and winds (Mimoun et al., 2017). Thus, one idea would be to perform a correlation search between SEIS instrument on Mars and seismometers on Earth. This could offer us with a new upper limit of the isotropic stochastic background. Furthermore, with the new interaction model between the GWs and the Earth, we now know how to model the same interaction model between the GWs and the normal modes of Mars. This would gives us, just as in the case of Earth, a sensitivity level in terms of the induced displacement level.

The story about the GW interaction with elastic bodies might not be finishing here. In this study we did not focus on the toroidal modes and this could represent one extension of this work. Studying the interaction between toroidal modes and GWs could offer us new standpoints on the GW detection and maybe even better estimates of the response model amplitudes.

In conclusions, this thesis gives us new perspectives and a theoretical framework for the detection and search of GWs. It emphasizes the use of planets, such as Earth, Moon or Mars, as GW detector and thus presents the advantages and disadvantages associated with that subject. Since the study is concerned about the Earth the associated frequency range of the search is the milliherz band and thus is complementary to the high frequency searches where successful detections have been already accomplished. Considering the fact that future will bring new technologies combined with optimized data algorithms, this method could potentially lead to the new detection of GWs.

Appendix A

Greenwich Sidereal Time

Calculation of Greenwich Sidereal Time (GST) is obtained by conversion from the UTC time. Following Petit and Luzum (2010) (and references inside) the GST refers to the equinox and is related to the Earth Rotation Angle (ERA), that refers to the Celestial Intermediate Origin, by the following relationship

$$\mathrm{GST} = d\mathrm{T}_0 + \mathrm{ERA} + \int_{t_0}^{t} \widehat{(\phi_A + \Delta\psi_1)} \cos(\omega_A + \Delta\epsilon_1) dt - \chi_A + \Delta\psi \cos\epsilon_A + \Delta\psi_1 \cos\omega_A, \quad \text{(A.1)}$$

where $\Delta\psi_1$ and $\Delta\epsilon_1$ are nutation angles in longitude and obliquity referred to the ecliptic of epoch and χ_A is the precession of the ecliptic along the equator (i.e. the right ascension component of the precession of the ecliptic). We can also write above relation as

$$\mathrm{GST} = \mathrm{ERA(UT1)} - \mathrm{EO}, \quad \text{(A.2)}$$

therefore to calculate GST we need to define two parameters, ERA(UT1) ans EO. The second parameter, EO, is the equation of the origins defined by

$$\mathrm{EO} = -d\mathrm{T}_0 - \int_{t_0}^{t} \widehat{(\phi_A + \Delta\psi_1)} \cos(\omega_A + \Delta\epsilon_1) dt - \chi_A + \Delta\psi \cos\epsilon_A + \Delta\psi_1 \cos\omega_A \quad \text{(A.3)}$$

which is the Celestial Intermediate Origin (CIO) based right ascension of the equinox along the moving equator. The EO accounts for the accumulated precession and nutation in right ascension from J2000.0 to the date t. Constant term $d\mathrm{T}_0$ was chosen to ensure continuity in UT1 at the date of change. A numerical expression for EO consistent with the IAU 2006/2000A precession-nutation model, that is ensuring consistency at the microarcsecond level and the continuity in UT1 at the date of change, is

$$\mathrm{EO} = -0.014509'' - 4612.156534''t - 1.3915817''t^2 + 0.00000044''t^3 - \Delta\psi \cos\epsilon_A - \sum_k C'_k \sin\alpha_k, \quad \text{(A.4)}$$

where the polynomial part provide the accuracy in arcseconds and last two terms in microarcseconds. For the current models we will disregard the non-polynomial part. The

nutation in longitude $\Delta\psi$ and obliquity $\Delta\epsilon$ are given by series within the IAU 2000 nutation model. They are referred to the ecliptic of date with t measured in Julian centuries from epoch J2000.0 and defined as

$$\Delta\psi = \sum_{i=1}^{N}(A_i + A_i' t)\sin(\mathrm{ARG}) + (A_i'' + A_i''' t)\cos(\mathrm{ARG}), \tag{A.5}$$

where the lunisolar terms in the nutation series is characterized by a set of five integers N_j ans five Fundamental Arguments F_j, namely the Delaunay variables (l,l',F,D,Ω), which defines $\mathrm{ARG} = \sum_{j=1}^{5} N_j F_j$. The expression for the fundamental arguments of nutation are given by the following expressions

$$F_1 \equiv l = 134.96340251^\circ + 1717915923.2178'' t + 31.8792'' t^2 + 0.051635'' t^3 - 0.00024470'' t^4, \tag{A.6}$$

$$F_2 \equiv l' = 357.52910918^\circ + 129596581.0481'' t - 0.5532'' t^2 + 0.000136'' t^3 - 0.00001149'' t^4, \tag{A.7}$$

$$F_3 \equiv F = 93.27209062^\circ + 1739527262.8478'' t - 12.7512'' t^2 - 0.001037'' t^3 + 0.00000417'' t^4, \tag{A.8}$$

$$F_4 \equiv D = 297.85019547^\circ + 1602961601.2090'' t - 6.3706'' t^2 + 0.006596'' t^3 - 0.00003169'' t^4, \tag{A.9}$$

$$F_5 \equiv \Omega = 125.04455501^\circ - 6962890.5431'' t + 7.4722'' t^2 + 0.007702'' t^3 - 0.00005939'' t^4. \tag{A.10}$$

where l stands for mean anomaly of the Moon, l' for mean anomaly of the Sun, $F = L - \Omega$ with L for mean longitude of the Moon and Ω for mean longitude of the ascending node of the Moon and, finally, D for mean elongation of the Moon from the Sun. In the above equations t is usually measured in Julian centuries in Barycentric Dynamical Time (TSB), however Terrestrial Time (TT) can be used instead, since this is introducing difference at the 0.01 μas level. Next, the cosine argument ϵ_A is the mean obliquity of date t is defined as

$$\epsilon_A = \epsilon_0 - 46.836769'' t - 0.0001832'' t^2 + 0.00200340'' t^3 - 0.000000576'' t^4 + 0.0000000434'' t^5, \tag{A.11}$$

where $\epsilon_0 = 84381.406''$ is the mean obliquity at J2000.0 of the ecliptic. The date t we define as

$$t = (\mathrm{TT} - 2000\ \mathrm{January\ 1d\ 12h\ TT})\ \mathrm{in\ days}/36525. \tag{A.12}$$

This definition is consistent with IAU 1994 Resolution C7 which recommends that the epoch J2000.0 is defined at the geocenter and at the date 2000 January 1.5 TT = Julian Date

2451545.0 TT. The second term in (A.2), defining UT1 from the ERA, is conventionally defined as

$$\mathrm{ERA}(\mathrm{T_u}) = 2\pi(0.7790572732640 + 1.00273781191135448\mathrm{T_u}), \tag{A.13}$$

where T_u = (Julian UT1 date - 2451545.0), and UT1 = UTC + (UT1- UTC), or equivalently

$$\mathrm{ERA}(\mathrm{T_u}) = 2\pi(\text{UT1 Julian day fraction} + 0.7790572732640 + 0.00273781191135448\mathrm{T_u}). \tag{A.14}$$

With relation (A.14) we completely defined GST and its calculation.

Appendix B

Matched Filter And Detection Statistics

The standard way of extracting signal of known waveform from the noisy data is by utilizing the matched filter technique, also know as Wiener Filter (Wiener, 1949) or optimal filter. Here we present a short introduction and for more details the reader is referred to Feller (1950); Allen and Romano (1999); Allen (2004); Allen et al. (2012).

First, we introduce convention for the Fourier transform of the continuous quantities as

$$\tilde{x}(f) = \int_{-\infty}^{\infty} x(t) \mathrm{e}^{-2\pi i f t} dt \tag{B.1}$$

and

$$x(t) = \int_{-\infty}^{\infty} \tilde{x}(f) \mathrm{e}^{2\pi i f t} df \tag{B.2}$$

where $\tilde{x}(f)$ is the Fourier transform of $x(t)$.

Now, let's assume that we have a data time series $d(t)$ that either consists of stationary Gaussian white noise $d(t) = n(t)$ alone or a signal $w(t)$ in addition to the noise $d(t) = n(t)+w(t)$. Since we assume that $n(t)$ is stationary Gaussian white noise we can also assume that it has a zero mean and we can define the one-sided power spectral density $S_n(f)$ as $\langle \tilde{n}(f)\tilde{n}^*(f')\rangle = \frac{1}{2} S_n(|f|)\delta(f - f')$. The matched filter is a linear filter that maximizes the signal-to-noise (further in text SNR) ratio in the presence of additive stochastic noise. The filter function is define to "match" the signal we are looking for. In the case of our data stream $d(t)$ and signal $w(t)$ it is defined as

$$m(t) = 4\Re \int_0^{\infty} \frac{\tilde{d}(f)\tilde{w}^*(f)}{S_n(f)} \mathrm{e}^{2\pi i f t} df, \tag{B.3}$$

where the filter itself is

$$K(f) = \frac{\tilde{w}(f)}{S_n(f)}. \tag{B.4}$$

The optimal value of SNR ratio is given as

$$\sigma_w^2 = 4\int_0^\infty \frac{|\tilde{w}(f)\tilde{w}^*(f)|}{S_n(f)}df, \tag{B.5}$$

therefore the amplitude SNR ratio of the matched filter is defined as

$$\rho_w(t) = \frac{|m(t)|}{\sigma_w}. \tag{B.6}$$

Of course, if we are searching for specific signal, obviously, we do not know the exact waveform $w(t)$, but we have a template $w_{template}(t)$ that resembles our signal in some degree. Therefore, our matched filter is more accurately written as

$$m(t) = 4\Re\int_0^\infty \frac{\tilde{d}(f)\tilde{w}^*_{template}(f)}{S_n(f)}\mathrm{e}^{2\pi i f t}df, \tag{B.7}$$

and consequently (B.5) as

$$\sigma_w^2 = 4\int_0^\infty \frac{|\tilde{w}_{template}(f)\tilde{w}^*_{template}(f)|}{S_n(f)}df. \tag{B.8}$$

The more our template resembles the signal we are searching we have higher SNR ratio, consequently SNR ratio, in some sense, characterize the quality of the filter performance. However, it is difficult to quantitatively say how much one value of SNR ratio is better than the other one. This quantification is defined within the detection statistics. More specifically, the value ρ_w is quantitatively related to the basic characteristic of the receiver performing the optimum detection. This theory involves defining the probability of the "false alarm" (probability of detecting signal when one is not present) and "false dismissal" (probability of not detecting signal when one is present).

In order to decide whether or not we have detected a signal in statistical manner, we first need to define two hypotheses:

$$\begin{aligned} &H_0 : d(t) = n(t), \\ &H_1 : d(t) = n(t) + w(t), \mu > 0 \end{aligned} \tag{B.9}$$

that is, the signal is either absent or present and characterized by some fixed, unknown, mean value $\mu > 0$ in our data, thus two hypotheses are mutually exclusive. Further, let's define set of n measurements over statistically independent time intervals each of length T (for measurement to be statistically independent this time intervals should be non-overlapping) as $p := \{\rho_1, \rho_2, \cdots, \rho_n\}$. The n measurements are independent samples drawn from a normal distribution having mean $\mu := \langle\rho\rangle$ and variance $\sigma^2 = \langle\rho^2\rangle - \langle\rho\rangle^2$. Since set p represent one experiment we can construct a sample mean defined as

$$\hat{\mu} := \frac{1}{n_i}\sum_{i=1}^{n}\rho_i, \tag{B.10}$$

and sample variance

$$\hat{\sigma}^2 := \frac{1}{n-1}\sum_{i=1}^{n}(\rho_i - \hat{\mu})^2. \tag{B.11}$$

The existence of noise is intrinsic in all experiments involving signal detection, therefore an experiment p is a random variable, which can be statistically described by probability density functions (further as PDF) as

- $P(p|0)$ is PDF for an experiment p that does not contain signal,
- $P(p|\mu)$ is PDF for an experiment p that does contain signal of the unknown mean μ,

and are defined as

$$P(p|0) = \frac{1}{(2\pi\hat{\sigma})^{-n/2}}\exp\left[-\sum_{i=1}^{n}\frac{\rho_i^2}{2\hat{\sigma}^2}\right], \tag{B.12}$$

$$P(p|\mu) = \frac{1}{(2\pi\hat{\sigma})^{-n/2}}\exp\left[-\sum_{i=1}^{n}\frac{(\rho_i-\mu)^2}{2\hat{\sigma}^2}\right]. \tag{B.13}$$

The decision rule that, based on the outcome of the experiment, chooses between two hypotheses (B.9) can be visually represented by two disjoint regions R_0 and R_1: if $p \in R_0$, then H_0 is chosen; if $p \in R_1$, then H_1 is chosen. The existence of an experiment in either of these two regions is characterized by two, already mentioned errors

- *false alarm* - when H_1 is chosen and H_0 is really true;
- *false dismissal* - when H_0 is chosen and H_1 is really true.

Error are defined in terms of conditional probabilities as

$$\text{false alarm rate (FAR)} := P_{FA} := \int_{R_1} dpP(p|0), \tag{B.14}$$

$$\text{false dismissal rate (FDR)} := P_M := \int_{R_0} dpP(p|\mu), \tag{B.15}$$

$$\text{detection rate (DR)} := P_D := 1 - \text{FDR}. \tag{B.16}$$

In order for the decision rule to work in some optimal way one possibility is to minimize the probability of the error, written in terms of P_{FA} and P_{M}, as

$$P_{\text{e}} = \mathsf{p}_0 P_{FA} + \mathsf{p}_1 P_M. \tag{B.17}$$

where p_0 and p_1 are *a priori* or prior probabilities for H_0 and H_1, respectively. However, since one usually does not know *a priori* probabilities, one can chose decision rule that minimizes the false dismissal rate by fixing the false alarm rate. The most utilized decision rule in the literature is known as the Neyman-Pearson criterion (Neyman et al., 1933). Without going into details how and why the Neyman-Pearson criterion is generally used, for our purpose we simply state: the Neyman-Pearson criterion is satisfied if, given the outcome of the experiment p, we form the estimators $\hat{\mu}$ and $\hat{\sigma}^2$ an choose

- H_0 if $\hat{\mu} < \frac{z_\alpha \hat{\sigma}}{\sqrt{n}}$,
- H_1 if $\hat{\mu} \geq \frac{z_\alpha \hat{\sigma}}{\sqrt{n}}$,

where z_α is a Gaussian random variable having zero mean and unit variance for which the area under the standard normal distribution to its right is equal to α.

The Neyman-Pearson bound and the two disjoint regions R_0 and R_1 can be graphically represented first by plotting the PDFs for H_0 and H_1 hypotheses and second by plotting P_{FA} versus P_D rate. The latter one is referred to as the Receiver Operating Characteristic (ROC). Normally, the ROC can be defined for any decision rule that causes P_D to be uniquely fixed, once P_{FA} is specified. In Fig. (B.1) we show three cases of PDFs for H_0 and H_1 hypotheses and their associated ROC curves. The more the PDFs are separated the larger the area under the ROC curve (AROC) is.

Finally, based on the theory above one should be able to set a threshold for $\rho_w(t)$ in order to identify an event candidates for tested templates. Once that the event candidates are identified further tests are required to select those events that truly belong to the signals. For detailed explanation on this topic reader is referred to Allen et al. (2012).

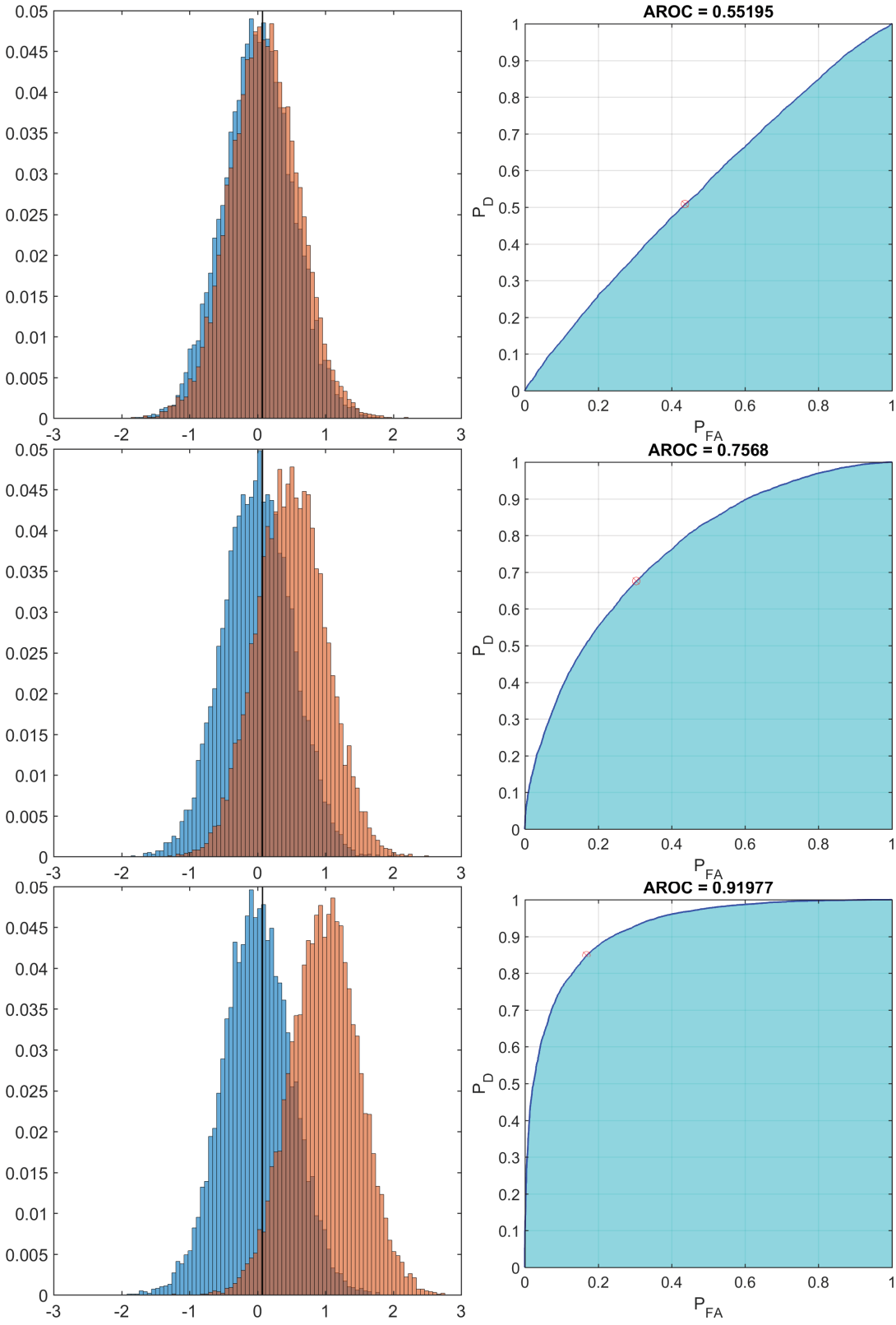

Fig B.1: Probability density functions for H_0 (blue) and H_1(orange) hypothesis (left column) and associated ROC curves (right column). AROC stand for the area under the ROC curves.

Appendix C

Autoregressive Method in Frequency Domain

The recorded ground displacement after an earthquake at any point at the surface of the Earth is a discrete time series. It represents the supersposition of discrete modes of oscillation that can be represented in the complex domain with exponential functions. The measurement of exponential parameters, e.g. amplitudes and exponential arguments, is performed using the ARFD80 method, which is based on the Prony technique for extracting exponential signals from time series. Only the basic outline will be presented, and for further discussion the reader is referred to the papers by Chao and Gilbert (1980) and Chao (1990).

For the estimation of the harmonic function parameters we chose the ARFD80 method because it has been proven to be very successful. This method is fast, highly accurate, multi-mode estimation suitable and easy to implement (Chao and Gilbert, 1980; Masters and Gilbert, 1983; Ding and Shen, 2013b; Ding and Chao, 2015a,c,b; Zeng and Shen, 2017, 2018).

A displacement represented as discrete time series of superimposed decaying, complex exponential functions can be written as

$$x(t) = \sum_{j=1}^{M} [A_j \mathrm{e}^{\mathrm{i}\sigma_j t} + A_j^* \mathrm{e}^{-\mathrm{i}\sigma_j^* t}], \quad t = \Delta t, 2\Delta t, \ldots, N\Delta t, \tag{C.1}$$

where M is the number of recorded modes, Δt is sampling rate, N is the number of data samples, A_j are the complex amplitudes, σ_j are the complex frequencies that can be written in terms of eigenfrequencies and decay rates as $\sigma_j = \omega_j + i\alpha_j$, and $*$ denotes the complex conjugate. Complex amplitudes A_j and complex frequencies σ_j are unknowns to be determined. For this purpose (C.1) can be represented by a recursive system of linear difference

equations of order $2M$

$$x(t) = \sum_{i=1}^{2M} S_i x(t - i\Delta t), \quad t = 2M\Delta t + \Delta t, \ldots, N\Delta t, \tag{C.2}$$

where S_i are real constant coefficients. If for the demonstration we put $M = 1$ the relation (C.1) and (C.2) become

$$x(t) = A_1 \mathrm{e}^{\mathrm{i}\sigma_1 t} + A_1^* \mathrm{e}^{-\mathrm{i}\sigma_1^* t}, \quad t = \Delta t, 2\Delta t, \ldots, N\Delta t, \tag{C.3}$$

$$\begin{bmatrix} x(3\Delta t) \\ \vdots \\ x(N\Delta t) \end{bmatrix} = \begin{bmatrix} x(2\Delta t) & x(\Delta t) \\ \vdots & \vdots \\ x(N\Delta t - \Delta t) & x(N\Delta - 2\Delta t) \end{bmatrix} \begin{bmatrix} S_1 \\ S_2 \end{bmatrix}, \tag{C.4}$$

Substituting (C.3) into the first equation of (C.4) (Masters, G. lectures' notes) with a little bit algebra it is easy to see that

$$\begin{aligned} S_2 &= -\mathrm{e}^{-2\alpha_1 \Delta t}, \\ S_1 &= 2\cos(\omega_1 \Delta t)\mathrm{e}^{-\alpha_1 \Delta t}, \end{aligned} \tag{C.5}$$

thus, by solving for coefficients S_1 and S_2 we can found frequency ω_1 and decay rate α_1 and Q-factor $Q_1 = \omega_1 / 2\alpha_1$.

The calculation of the real coefficients S_i using (C.2) is heavy in the time domain, while the number of excited modes after the earthquake is large and unknown. The problem is resolved by considering that the basis functions $\mathrm{e}^{i\sigma_j}$ are separated into individual peaks in frequency domain. Basically, the main idea behind the ARFD80 method is to Fourier transform Eq. (C.4) in order to solve a system of linear equations for narrow frequency band containing the small number of modes. The advantage of this procedure is to focus on the narrow frequency range where the mode is expected to occur. This enables re-sizing the linear system (C.4). As shown earlier, if $M = 1$ the system to solve consists of two unknowns and $K > 2M$ linear equations, where usually $3 \leq K \leq 5$ and it represents 3 or 5 frequencies that describe the position of the spectral peak in the frequency domain we study. The described analysis plainly depends on the Fourier transform and hence bears all technical advantages and disadvantages of the Fourier transform. To reduce the side-band levels of the spectral peaks due to spectral leakage we perform tapering with a Hann window and to refine the waveform frequency resolution we perform zero padding to each column in (C.4).

Even though ARFD80 is capable of analyzing small group of modes, we focus on analyzing one mode at once, hence it was important to observe a spectral peak in frequency domain that belongs to the target singlet. When the singlet is visible we choose at least five

frequencies that describe the position of the spectral peak in frequency domain, one which defines the main peak and two on each side of the main peak. After solving linear system (C.4) in frequency domain and obtaining coefficients S_i, calculating frequencies, decay rates and Q-factors we also estimate complex amplitudes (Chao and Gilbert, 1980) used in bootstrap experiments for the calculation of parameter's standard deviations following Häfner and Widmer-Schnidrig (2013). Simultaneously, for every estimate we also measure the SNR as the ratio of peak amplitude of the singlet over the root mean square amplitude of two narrow frequency bands targeting the singlet.

Appendix D

Optimal Sequence Estimation

Successful estimation of harmonic function parameters such as complex frequency, Q-factor and amplitude, substantially depends on the representation of the spectral peak in frequency domain. One can improve spectral peak representation by increasing the time series length, however bearing in mind the trade off between frequency resolution and noise level. An alternative option is to use stacking methods to enhance the SNR of the target signal. Here we will give a short introduction to the optimal sequence estimation (Ding and Shen, 2013a). The OSE was first applied in the search for the Slichter modes (Slichter, 1961), which are the three translational modes of the inner core, (Ding and Shen, 2013a; Ding and Chao, 2015c), but its application extended to the retrieval of other normal modes (Ding and Chao, 2015a; Zeng and Shen, 2017, 2018) as well as to the pole tide signals (Ding and Chao, 2016). It has been proven that OSE has better performance than other stacking methods, such as the spherical harmonic stacking (SHS) (Buland et al., 1979) and the multistation experiment (MSE) (Courtier et al., 2000), since it was developed on the basis of these two methods using the principle of the noise-term elimination (Zeng and Shen, 2017). The OSE has been successfully extended to transverse components (Ding and Chao, 2015a) and applied in the GC approximation, where nearby modes were grouped as an isolated cluster (Zeng and Shen, 2017). In terms of frequency range it has been successfully applied in the SC approximation from 0.309 mHz ($_0S_2$) to 9.865 mHz ($_{27}S_2$) (Ding and Shen, 2013a; Ding and Chao, 2015b; Zeng and Shen, 2017) and in the spheroidal-spheroidal GC approximation from 1.413 mHz ($_4S_1$) to 2.822 mHz ($_6S_3$) (Zeng and Shen, 2018). Most studies claim that OSE in the SC approximation is performing accurately and as a consequence it can be applied to the modes with f $\leq$ 1.5 mHz (Zeng and Shen, 2017, 2018). Furthermore, even though the OSE method proved to be the foremost among the stacking methods, some limitations have been identified. For example, the dependence on records SNRs and the number of stations used in stacking (Ding and Shen, 2013a; Zeng and Shen, 2017).

The radial component of the displacement at the surface of the anelastic Earth model with the singlet complex eigenfrequency σ_m is defined as

$$u_R(\Omega, t) = \sum_m {}_nU_l Y_l^m(\Omega) s_m(\boldsymbol{r_0}) \mathrm{e}^{\mathrm{i}\sigma_m t} \tag{D.1}$$

where ${}_nU_l$ is the value taken by the radial eigenfunction at the surface, $Y_l^m(\Omega)$ is the spherical harmonic function of degree l and order m and $\Omega = (\theta, \phi)$ are the colatitude and longitude of the receiver. For brevity we will introduce $\epsilon_m = {}_nU_l s_m(\boldsymbol{r_0})$ and $A_m = \epsilon_m \mathrm{e}^{\mathrm{i}\sigma_m t}$ therefore (D.1) becomes

$$u_R(\Omega, t) = \sum_m A_m Y_l^m(\Omega), \tag{D.2}$$

and for $j = 1, \ldots, N$ stations from relation (D.2) one can form a multistack

$$\mathbf{U} = \mathbf{Y}\mathbf{A}, \tag{D.3}$$

where

$$\mathbf{U} = \begin{bmatrix} u_R(\Omega_1, t) \\ u_R(\Omega_2, t) \\ \vdots \\ u_R(\Omega_N, t) \end{bmatrix}, \tag{D.4}$$

$$\mathbf{Y} = \begin{bmatrix} Y_L^{-L}(\Omega_1) & Y_L^{-L+1}(\Omega_1) & \ldots & Y_L^{L}(\Omega_1) \\ Y_L^{-L}(\Omega_2) & Y_L^{-L+1}(\Omega_2) & \ldots & Y_L^{L}(\Omega_2) \\ \vdots & & & \vdots \\ Y_L^{-L}(\Omega_N) & Y_L^{-L+1}(\Omega_N) & \ldots & Y_L^{L}(\Omega_N) \end{bmatrix}, \tag{D.5}$$

$$\mathbf{A} = \begin{bmatrix} \varepsilon_{-L} \exp^{\mathrm{i}\sigma_{-L}t} \\ \varepsilon_{-L+1} \exp^{\mathrm{i}\sigma_{-L+1}t} \\ \vdots \\ \varepsilon_{L} \exp^{\mathrm{i}\sigma_{L}t} \end{bmatrix}, \tag{D.6}$$

for $t = 1, \ldots, n$ time samples. In (D.3) $\mathbf{U}$ is a $[N \times n]$ matrix of radial-component observations, $\mathbf{Y}$ is a $[N \times (2L+1)]$ matrix of spherical harmonics and $\mathbf{A}$ is a $[(2L+1) \times n]$ matrix to be inverted for which each row consists of only one singlet for the target (N, L) multiplet. If $N > (2L+1)$ system (D.3) can be solved by the general least-squares procedure

$$\mathbf{A} = (\mathbf{Y}^T \mathbf{p} \mathbf{Y})^{-1} \mathbf{Y}^T \mathbf{p} \mathbf{U} \tag{D.7}$$

where $\mathbf{p}$ is a weight whose values can be chosen to be inversely proportional to the SNR of the target mode. Equation (D.7) defines the OSE method.

Separating each singlet resonance function within a multiplet in matrix **A** by yielding only one spectral peak in spectral domain corresponding to the target singlet, gives OSE advantage over e.g. the least squares spectral analysis (Vanícek, 1969), the product spectral analysis (Smylie, 1992) and the cross-spectrum anaysis (Hinderer et al., 1995), where all singlets within the multiplet would appear together in only one spectrum. Furthermore, the OSE method does not require the information about the source mechanism, which gives it advantage over e.g. the singlet stripping method (Gilbert, 1971; Ritzwoller et al., 1986). For more comparison we recommend paper by Ding and Shen (2013a).

Appendix E

Phasor Walkout

In signal processing one usually face the problem whether the spectral peak observed in the frequency domain corresponds to a harmonic signal or noise. One way to address this problem is to use the phasor walkout method revisited by Zürn and Rydelek (1994). Essentially, it is a graphical representation of Fourier transform for a test frequency where one estimates the complex contribution of the Fourier transforms for each sample and sums the corresponding vectors in the complex plane. The shape and behavior of the resulting vector pattern, the walkout, gives us information about the signal properties.

The derivation process is quite straightforward. If we consider a time series x_j, for $j = 1, \ldots, N$ equidistantly sampled with sampling rate Δt, that may consist of a signal with the frequency f_0, the phasor walkout contributions obtained for the test frequency f_s are

$$p_j(f_s) = x_j \mathrm{e}^{-\mathrm{i}2\pi f_s (j-1)\Delta t}, \quad j = 1, \ldots, N. \tag{E.1}$$

Noticeably, these contributions are complex and they are recognized as vectors in a two-dimensional space. Deriving the full phasor walkout pattern is achieved by adding these vectors graphically and successively in the complex plane. For a better understanding it is useful to look at the function (E.1) where x_j defines the scaling of walkout and the exponential factor defines the walkout rotation by angle $2\pi f_s \Delta t$. Firstly, the walkout has a loop-like circular shape if the scaling factor is constant. This loop shape is completely defined by the rotation angle, that is the full loop of 2π is closed in K steps, where $K = 2\frac{f_n}{f_s}$, with f_n being Nyquist frequency ($f_n = \frac{1}{2\Delta t}$). Consequently, the loop-like circular shapes are K polygons. If K is an integer the polygons are aligned and if K is not an integer the polygons are rotated with respect to each other. If we now consider that x_j is noise, one would no longer have polygons with the constant phase change in successive samples, but randomly changing phases which would result in a random walk.

One important case to consider is a simple harmonic function $x_j = A_0 \cos(2\pi f_0 (j-1)\Delta t)$ in which case the phasor walkout for tested frequency f_s is

$$p_j(f_s) = \frac{A_0}{2}\left(\mathrm{e}^{\mathrm{i}2\pi(f_0-f_s)(j-1)\Delta t} + \mathrm{e}^{-\mathrm{i}2\pi(f_0+f_s)(j-1)\Delta t}\right). \tag{E.2}$$

Assuming that $f_0 \neq f_s$ the shape of (E.2) is still a polygon even though a more complicated one, because each axis, the real and complex ones, now contains the sum of two trigonometric functions instead of one trigonometric function. The rotation angle is now changed and it is $2\pi(f_0 - f_s)\Delta t$, hence the full circle is now reached with K steps, where $K = \frac{2f_n}{|f_0 - f_s|}$. An interesting feature is obtained when $f_0 = f_s$, so (E.2) becomes

$$p_j(f_s) = \frac{A_0}{2}\left(1 + \mathrm{e}^{-\mathrm{i}4\pi f_0 (j-1)\Delta t}\right). \tag{E.3}$$

Examining (E.3) one can notice that the complex part is bounded by a sine function, while the real part is progressively advancing because of the constant term, number one, in its definition. Strikingly, this means that the phasor walkout of a harmonic signal, when $f_0 = f_s$, is going to gradually progress without curving, hence showing linearity. This is the most useful feature of the phasor walkout: by examining the phasor walkout pattern, one can conclude that the tested signal is really a harmonic signal with frequency f_0.

Furthermore, it is important to consider the case of signals consisting of two harmonic functions with very close frequencies, because this is often the case in normal mode studies. Work on this topic has been also done by Zürn and Rydelek (1994). Due to the very similar harmonic function frequencies in frequency domain the phasor walkout of each harmonic function now depends on the relative amplitude between the two functions. The phasor walkout at the frequency of the signal with larger amplitude has rapid phase changes, while the phasor walkout of the signal with smaller amplitude has slower phase changes and additional loops. However, the most important is that both walkouts show linear progress, which is not the case if the tested frequencies are different from the true harmonic frequencies. Different cases are studied in the Appendix of the paper.

The situation is becoming even more complicated when the signals are contaminated by noise. The regularity of the phasor walkout in the presence of noise is more or less deteriorated. In such circumstances it is useful to use a range of tested frequencies to calculate the phasor walkouts. Theoretically, if the estimated frequency f_e is the true frequency of the harmonic function only the phasor walkout with $f_s = f_e$ should be a straight line and for all other tested frequencies the phasor walkouts should be softly curved. As stated before differences between slightly different tested frequencies are sometimes difficult to observe due to the presence of noise. To overcome this problem, we propose to compute the coefficient of determination R^2 (Draper and Smith, 1998) on our phasor walkouts.

Basically, this includes fitting a linear model on our phasor walkout and then estimating R^2 coefficient, which is a statistical feature determining how well the fitted model describes the data. This would be an additional statistical test to show how much our phasors are actually straight or curved. Hence, having a basic linear model $Y = aX + b$ one should estimate the a and b coefficients, Y being the complex part of phasor walkout and X, the real part of the walkout. The next step is to build a linear model Y_m using estimated a and b coefficients and X data: $Y_m = aX + b$. Ending up with observed data Y and modeled data Y_m one can calculate the coefficient of determination R^2 defined by

$$R^2 = 1 - \frac{\sum_i (Y_i - Y_{m,i})^2}{\sum_i (Y_i - \bar{Y})^2}, \tag{E.4}$$

where $\bar{Y}$ is the mean of the Y_i. Values of R^2 fall between 0 and 1, with a value 1 indicating that all variance is accounted for by the model, that is all of the data points fall perfectly on the regression line. Therefore, the coefficient of the determination for our five tested frequencies should be the largest for $f_s = f_e$ if f_e is the true frequency of the harmonic function. Finally, the R^2-test does not provide us with the frequency estimates, but with the statistical values for our estimated frequencies. An example of the method performance for the cosine signal is shown on figure (E.1) with three tested frequencies $\{f_e - \sigma, f_e, f_e + \sigma\}$, where in this case f_e is truth frequency of tested signal and for this frequency the R^2-test is the closest to 1.

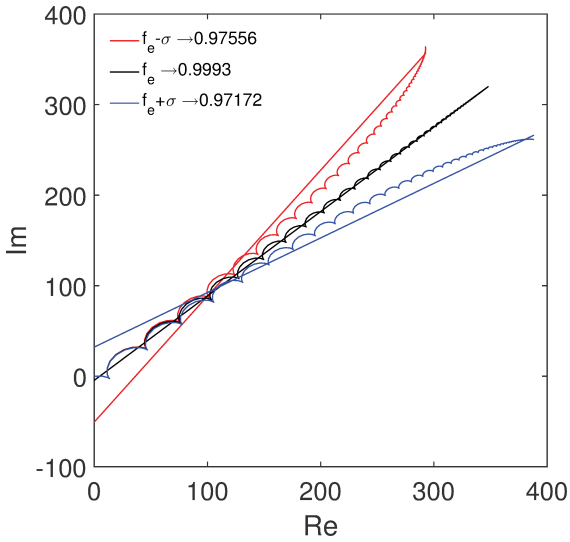

Fig E.1: The result of the R^2-test for three different tested frequencies $\{f_e - \sigma, f_e, f_e + \sigma\}$, where f_e is truth frequency of tested signal, thus the R^2-test is the closest to 1.

For the signal defined as

$$x_j = A_k \cos(2\pi f_k (j-1)\Delta t + \theta_k) \mathrm{e}^{-\alpha_k (j-1)\Delta t}, \quad j = 1, \ldots, N, \tag{E.5}$$

the phasor walkout is defined as

$$p_j(f_s = f_k) = \frac{1}{2} A_k \mathrm{e}^{-\alpha_k (j-1)\Delta t} \{[\cos(\theta_k) + \cos(4\pi f_k (j-1)\Delta t + \theta_k)] + \mathrm{i}[\sin(\theta_k) - \sin(4\pi f_k (j-1)\Delta t + \theta_k)]\} \tag{E.6}$$

and for constants $A_k > 0$, $\theta_k > 0$ and condition $|\sin(\theta_k)| > |\sin(4\pi f_k (j-1)\Delta t + \theta_k)|$, the phasor walkout is placed in the first quadrant of Cartesian two-dimensional system, where x-axis is real axis and y-axis is imaginary axis. In other case, $|\sin(\theta_k)| < |\sin(4\pi f_k (j-1)\Delta t + \theta_k)|$, the phasor would be placed in the fourth quadrant of the Cartesian system. This is also true if $\theta_k < 0$. Both axes have constant value in terms of phase angle θ_k, which implies that the phasor walkout is progressing in the straight inclined line. If for some reason the amplitude is negative, which can be the case due to stacking, the combined effect of amplitude and phase angle defines the quadrant of the Cartesian system in witch the phasor walkout is placed. That is, besides the first and fourth quadrant the phasor walkout could be also placed in the second and the third quadrant. The mentioned effects are demonstrated using the signal containing two harmonic functions of close frequencies, called "beats". In this case the signal is defined as

$$x_j = A_1 \cos(2\pi f_1 j \Delta t + \theta_1) + A_2 \cos(2\pi f_2 j \Delta t + \theta_2), \tag{E.7}$$

where $f_1 \approx f_2$. The study is carried out by calculating the phasor walkout for tested frequencies $f_s = f_1$ and $f_s = f_2$ for several different cases:

1. setting $\theta_1 > 0, \theta_2 < 0$, $|\theta_1| = |\theta_2|$, $|A_1| = |A_2| > 0$;
2. setting $|\theta_1| = |\theta_2| > 0$, $|A_1| > |A_2| > 0$;
3. setting $|\theta_1| = |\theta_2| > 0$, $|A_1| > |A_2| > 0$ and decay rate $\mathrm{e}^{\left(-\frac{\pi f_1}{Q} i \Delta t\right)}$ to both harmonic functions.

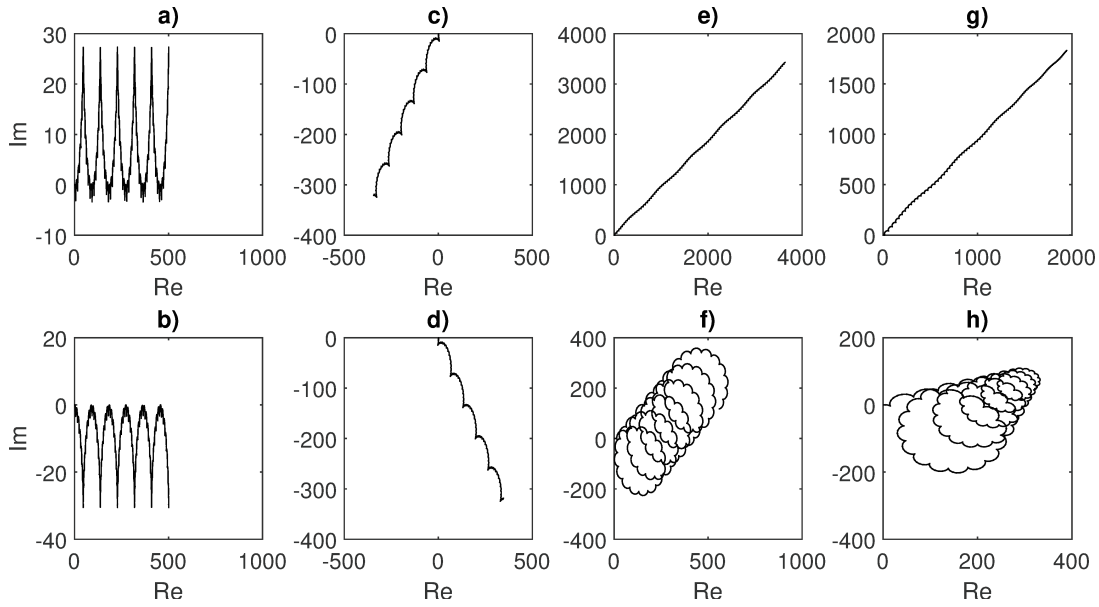

Fig E.2: The phasor walkout for a signal with two harmonic functions of frequencies $f_1 = 9$ mHz and $f_2 = 10.1$ mHz for several different cases. From a) to g) the tested frequency is $f_s = f_1$, while for b) to h) $f_s = f_2$. Cases a) and b) the starting signal is defined by (E.7) with $A_1 = A_2 = 1$ [nm/s^2], $\theta_1 = \theta_2 = 0$. In c) and d) phases are added $\theta_1 = 0.75$ and $\theta_2 = -0.75$ are added. In e) and f) phases are the same $\theta_1 = \theta_2 = 0.75$ and amplitudes are added with $A_1 = 10$ [nm/s^2] and $A_2 = 1$ [nm/s^2]. In g) and h) phases and amplitudes stay the same but a decay rate defined with $\exp\left(-\frac{\pi f_1}{100} \mathrm{i} \Delta t\right)$ is added.

The results are shown in Fig. E.2. The phasor walkout for the basic signal defined in (E.7) with $A_1 = A_2 = 1$ [nm/s^2], $\theta_1 = \theta_2 = 0$ and tested for the frequencies of both harmonic functions is shown on a) for $f_s = f_1$ and on b) for $f_s = f_2$. It is important to notice the regularity of this walkout, that is progressive advantage due to the fact that the tested frequencies is the same as the frequencies of one of the harmonic functions within the signal. In the next example, on c) and d) figures, study case (i) is shown. Added phases cause the inclination of the walkout to have either positive imaginary axis for $\theta > 0$ (case c) or negative imaginary axis for $\theta < 0$ (case d). On figures e) and f), study case (ii) is shown. Now, even though both cases show linearity, the phasor walkout of the harmonic function with smaller amplitude (f) has slower phase change and additional loops, while the harmonic function with larger amplitude has rapid phase changes (e). The final study case (iii) is shown on figures g) and h). Adding decay rate is affecting the phasor walkouts amplitude causing the final walkout to have cone shape. In conclusion, the phasor walkout of the two harmonic functions of similar frequencies heavily depends on the amplitude ratio of the harmonic functions within the signal. Having more similar amplitudes will cause walkouts to have straight lines and thus enabling easier conclusion about the existence of particular harmonic function in the signal.

Next, we simulate signal containing the five ${}_0S_2$ singlets, where each singlet is defined as (E.5) with $\theta_k = 0$. Therefore, in case of ${}_0S_2$ mode k is 5. The signal is 15 days long with a sampling rate of 60 s. We simulated ten cases which parameters are summarized in Table E.1. Results are shown in Fig. E.3 and E.4. The frequency used for calculating the walkout in each case is marked with the asterisk, for example, in the j case we tested for the ${}_0S_2^{-1}$ singlet. Compared to the previous case the differences between singlets frequencies are about 100 times smaller introducing a considerable effect of the coupling between the singlets - the walkouts become more complex. In the experiments from a to e, we fix the same amplitude for all singlets and gradually increase the number of singlets in the signal from case a having one singlet, ${}_0S_2^{-2}$, to case e having all five singlets. Adding more singlets is affecting the phasor walkout of the first singlet obviously. While in the first case the walkout is simple cone-like in other cases the number and complexity of loops are more prominent. In the experiments from f to j we change the amplitudes of singlets and test for different singlets. In the case f we calculate the walkout for the ${}_0S_2^0$ singlet and even though the signal is the same as in case e the walkout output is much different. At the same time it is also more difficult to argue about the straightness even though a regularity exists. Similar conclusions are valid for the cases h and i. We can claim that regularity exists, however the straightness of the walkout is completely deteriorated. Therefore, it is reasonable to conclude that small singlets in close vicinity of singlets with higher amplitude are completely under-dominated resulting in phasor walkouts which are not straight but adopt loop-like shapes.

Tab E.1: Singlets parameters used to calculate signals, where f [μHz] is the frequency of the signal, Q the quality-factor and A [nm/s^2] amplitude. Amplitude marked with the asterisk points to the singlet which frequency is used as test frequency for obtaining the phasor walkout patters in Fig. E.3 and E.4.

	Mode	${}_0S_2^{-2}$	${}_0S_2^{-1}$	${}_0S_2^0$	${}_0S_2^1$	${}_0S_2^2$
	f	300.001	304.493	309.064	313.716	318.452
	Q	494.6	501.8	509.3	517.0	525.0
a	A	50*	0	0	0	0
b	A	50*	50	0	0	0
c	A	50*	50	50	0	0
d	A	50*	50	50	50	0
e	A	50*	50	50	50	50
f	A	50	50	50*	50	50
g	A	20*	50	10	50	20
h	A	20	50	10*	50	20
i	A	2*	50	5	50	10
j	A	2	2*	5	50	10

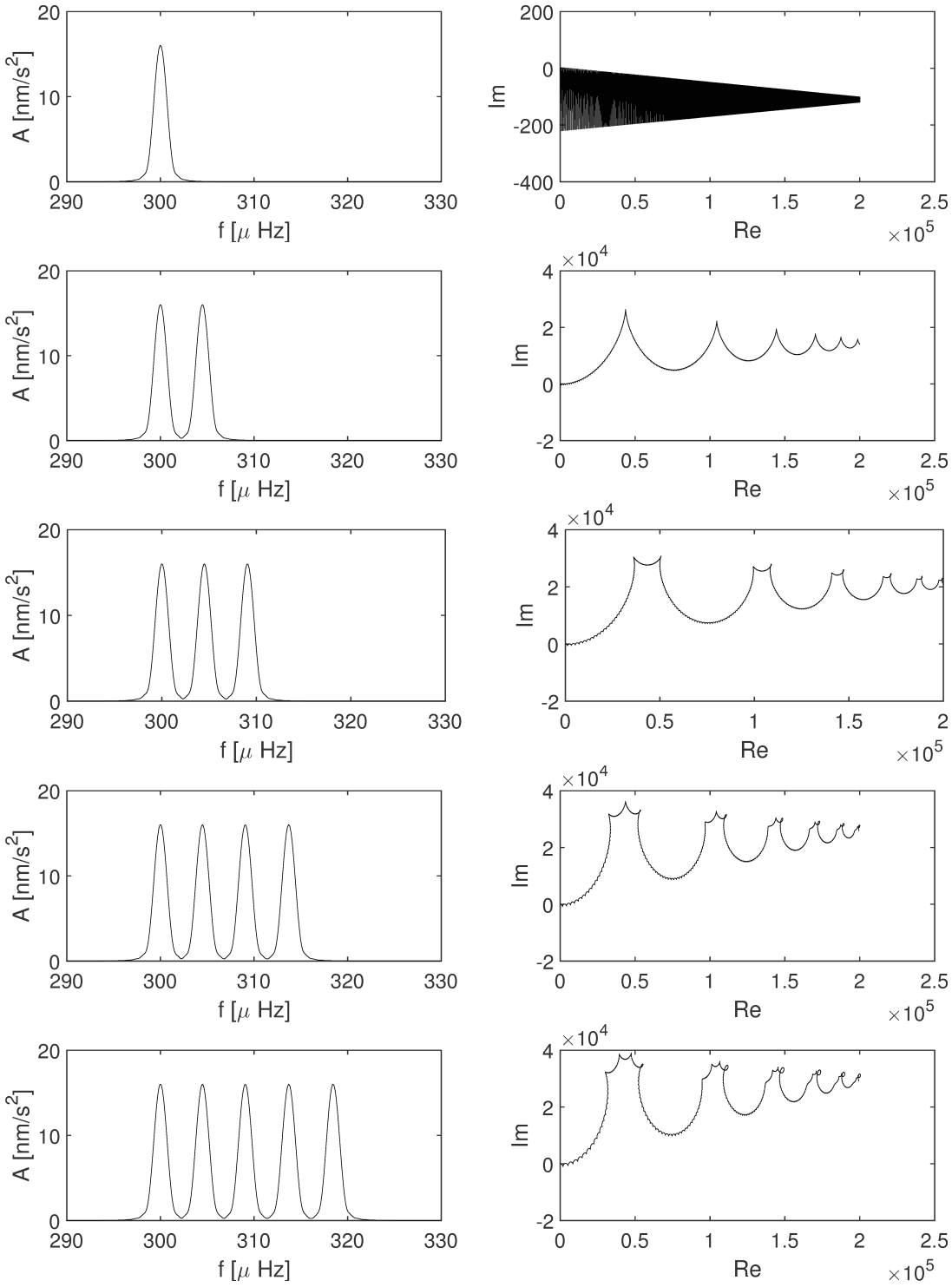

Fig E.3: Synthetic signals (left) and appropriate phasor walkouts (right) for the experiment setups a, b, c, d, e from Table E.1. In all setups the phasor walkout is calculated for the ${}_0\mathrm{S}_2^{-2}$ singlet.

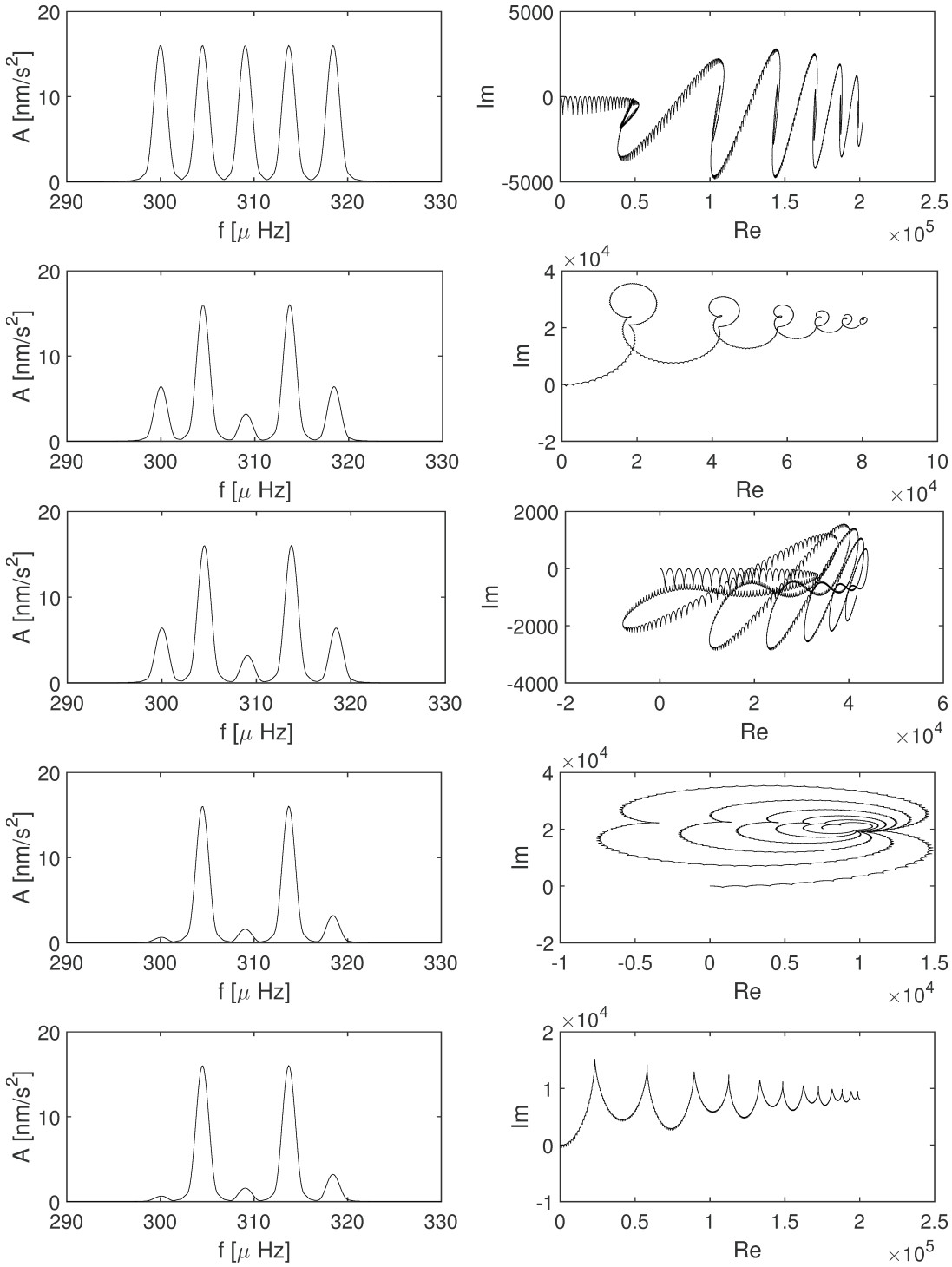

Fig E.4: Synthetic signals (left) and appropriate phasor walkouts (right) for the experiment setups f, g, h, i, j from Table E.1. In setups f and h the phasor walkout is calculated for the ${}_0\mathrm{S}_2^0$ singlet, in g and i for ${}_0\mathrm{S}_2^{-2}$ singlet and in j for ${}_0\mathrm{S}_2^{-1}$ singlet.

Bibliography

J. Aasi et al. Advanced ligo. *Classical and Quantum Gravity*, 32, 2015.

J. Abadie et al. All-sky search for gravitational-wave bursts in the second joint LIGO-Virgo run. *Physical Review D*, 85, 2012.

B. P. Abbott et al. LIGO: the Laser Interferometer Gravitational-Wave Observatory. *Reports on Progress in Physics*, 72(7), 2009.

B. P. Abbott et al. Observation of gravitational waves from a binary black hole merger. *Phys. Rev. Lett.*, 116:061102, Feb 2016.

B. P. Abbott et al. Gwtc-1: A gravitational-wave transient catalog of compact binary mergers observed by ligo and virgo during the first and second observing runs. 2018.

T. Accadia et al. Virgo: a laser interferometer to detect gravitational waves. *Journal of Instrumentation*, 7, 2012.

F. Acernese et al. Advanced Virgo: a second-generation interferometric gravitational wave detector. *Classical and Quantum Gravity*, 32(2), 2014a.

F. Acernese et al. Advanced virgo: a second-generation interferometric gravitational wave detector. *Classical and Quantum Gravity*, 32, 2014b.

O. D. Aguiar. Past, present and future of the Resonant-Mass gravitational wave detectors. *Research in Astronomy and Astrophysics*, 11, 2011.

O. D. Aguiar et al. The status of the Brazilian spherical detector. *Classical and Quantum Gravity*, 19, 2002.

F Akbarashrafi, D Al-Attar, A Deuss, J Trampert, and A P Valentine. Exact free oscillation spectra, splitting functions and the resolvability of Earth's density structure. *Geophysical Journal International*, 213(1):58–76, 2017.

D. Al-Attar, J. H. Woodhouse, and A. Deuss. Calculation of normal mode spectra in laterally heterogeneous earth models using an iterative direct solution method. *Geophysical Journal International*, 189(2):1038–1046, 2012.

Anderson W. G. Allen, B., P. R. Brady, D. A. Brown, and J. D. E. Creighton. FINDCHIRP: An algorithm for detection of gravitational waves from inspiraling compact binaries. *Physical Review D*, 85(122006), 2012.

B. Allen. A χ^2 time-frequency discriminator for gravitational wave detection. *Physical Review D*, 71(062001), 2004.

B. Allen and J. D. Romano. Detecting a stochastic background of gravitational radiation: Signal processing strategies and sensitivities. *Physical Review D*, 59(102001), 1999.

P. Amaro-Seoane, S. Aoudia, S. Babak, P. Binétruy, E. Berti, A. Bohé, C. Caprini, M. Colpi, N. J. Cornish, K. Danzmann, J.-F. Dufaux, J. Gair, O. Jennrich, P. Jetzer, A. Klein, R. N. Lang, A. Lobo, T. Littenberg, S. T. McWilliams, G. Nelemans, A. Petiteau, E. K. Porter, B. F. Schutz, A. Sesana, R. Stebbins, T. Sumner, M. Vallisneri, S. Vitale, M. Volonteri, and H. Ward. Low-frequency gravitational-wave science with eLISA/NGO. *Classical and Quantum Gravity*, 29(12), 2012.

M. Ando. Current status of TAMA. *Classical and Quantum Gravity*, 19(7), 2002.

J. W. Armstrong. Low-Frequency Gravitational Wave Searches Using Spacecraft Doppler Tracking. *Living Reviews in Relativity*, 9(1), 2006.

N. Ashby and J. Dreitlein. Gravitational wave reception by a sphere. *Physical Review D*, 12(2):336–349, 1975.

P. Astone et al. Long-term operation of the Rome "Explorer" cryogenic gravitational wave detector. *Physical Review D*, 47, 1993.

P. Astone et al. The gravitational wave detector NAUTILUS operating at T = 0.1 K. *Astroparticle Physics*, 7, 1997.

A. Babak, S.and Petiteau, A. Sesana, P. Brem, P. A. Rosado, S. R. Taylor, A. Lassus, J. W. T. Hessels, C. G. Bassa, M. Burgay, R. N. Caballero, D. J. Champion, I. Cognard, G. Desvignes, J. R. Gair, L. Guillemot, G. H. Janssen, R. Karuppusamy, M. Kramer, P. Lazarus, K. J. Lee, L. Lentati, K. Liu, C. M. F. Mingarelli, S. Osłowski, D. Perrodin, A. Possenti, M. B. Purver, S. Sanidas, R. Smits, B. Stappers, G. Theureau, C. Tiburzi, R. van Haasteren, A. Vecchio, and J. P. W. Verbiest. European Pulsar Timing Array

limits on continuous gravitational waves from individual supermassive black hole binaries. *Monthly Notices of the Royal Astronomical Society*, 455(2):1665–1679, 2016.

A. Ben-Menahem. Excitation of the Earth's Eigenvibrations by Gravitational Radiation from Astrophysical Sources. *II Nuovo Cimento C*, 6(1):49–71, 1983.

A. Ben-Menahem and J. Singh, S. *Seismic waves and sources*. Mineola, Dover Publications, Inc., 1981.

A. Ben-Menahem, M. Israel, and U. Levite. Theory and Computation of Amplitudes of Terrestrial Line Spectra. *Geophysical Journal of the Royal Astronomical Society*, 25: 307–406, 1971.

P.L. Bender, I. Ciufolini, K. Danzmann, W.M. Folkner, J. Hough, D. Robertson, A. Rüdiger, M. Sandford, R. Schilling, B.F. Schutz, R. Stebbins, T. Sumner, P. Touboul, S. Vitale, H. Ward, W. Winkler, J. Cornelisse, F. Hechler, Y. Jafry, and R. Reinhard. LISA. Laser Interferometer Space Antenna for the detection and observation of gravitational waves. A Cornerstone Project in ESA's Long Term Space Science Programme "Horizon 2000 Plus". *Pre-Phase A Report*, 1995.

J. Berger, P. Davis, and Ekström. Ambient Earth noise: A survey of the Global Seismographic Network. *Journal of Geophysical Research*, 109:1–10, 2004.

M. Beyreuther, R. Barsch, L. Krischer, T. Megies, Y. Behr, and J. Wassermann. ObsPy: A Python Toolbox for Seismology. *Seismological Research Letters*, 81(3):530–533, 2010.

S. P. Boughn and J. R. Kuhn. Limits on a stochastic GW background from observations of terrestrial and solar oscillations. *The Astrophysical Journal*, 286:387–391, 1984.

A. Bragaglia, A. Renzini, and P. Bergeron. Temperatures, gravities, and masses for a sample of bright DA white dwarfs and the initial-to-final mass relation. *The Astrophysical Journal*, 443(2):735–752, 1995.

W. R. Brown, M. Kilic, C. Allende Prieto, and S. J. Kenyon. The ELM Survey. I. A Complete Sample of Extremely Low-mass White Dwarfs. *The Astrophysical Journal*, 723 (2):1072–1081, 2010.

W. R. Brown, M. Kilic, J. J. Hermes, C. Allende Prieto, S. J. Kenyon, and D. E. Winget. A 12 Minute Orbital Period Detached White Dwarf Eclipsing Binary. *The Astrophysical Journal Letters*, 737(1), 2011.

W. R. Brown, M. Kilic, S. J. Kenyon, and A. Gianninas. Most Double Degenerate Low-mass White Dwarf Binaries Merge. *The Astrophysical Journal Letters*, 824(1), 2016.

R. Buland, J. Berger, and F. Gilbert. Observations from the IDA network of attenuation and splitting during a recent earthquake. *Nature*, 277:358–362, 1979.

T. L. Campante, I. Lopes, D. Bossini, A. Miglio1, and W. J. Chaplin. Asteroseismology of Red-Giant Stars as a Novel Approach in the Search for Gravitational Waves. *Astronomy in Focus*, pages 363–364, 2015.

B. Canuel et al. Exploring gravity with the miga large scale atom interferometer. *Scientific Reports*, 8(14064):064024, 2018.

B. Carter and H. Quintana. Foundations of general relativistic high-pressure elasticity theory. *Proceedings of the Royal Society of London A*, 331:57–83, 1972.

S. Castellaro and F. Mulargia. A Statistical Low Noise Model of the Earth. *Seismological Research Letters*, 83(1):39–48, 2012.

Benjamin F. Chao. On the use of maximum entropy/autoregressive spectrum in harmonic analysis of time series. *Pure and Applied Geophysics*, 134(2):303–311, 1990.

Benjamin F. Chao and H. Ding. Spherical harmonic stacking for the singlets of Earth's normal modes of free oscillation. *Geophysical Research Letters*, 41(15):5428–5435, 2014.

Benjamin F. Chao and Freeman Gilbert. Autoregressive estimation of complex eigenfrequencies in low frequency seismic spectra. *Geophysical Journal International*, 63(3):641–657, 1980.

L. Conti, F. Marin, M. D. R. Rosa, G. A. Prodi, L. Taffarello, J. P. Zendri, M. Cerdonio, and S. Vitale. An optical transduction chain for the AURIGA detector. *AIP Conference Proceedings*, 523, 2001.

M. Coughlin and J. Harms. Upper Limit on a Stochastic Background of Gravitational Waves from Seismic Measurements in the Range 0.05 Hz to 1 Hz. *Physical review letters*, 112:101102, 2014a.

M. Coughlin and J. Harms. Constraining the gravitational wave energy density of the Universe using Earth's ring. *Physical review*, D 90:042005, 2014b.

M. Coughlin and J. Harms. Constraining the gravitational wave energy density of the Universe in the Range 0.1 Hz to 1 Hz using the Apollo Seismic Array. *Physical review*, D 90:102001, 2014c.

N. Courtier, B. Ducarme, J. Goodkind, J. Hinderer, Y. Imanishi, N. Seama, H. Sun, J. Merriam, B. Bengert, and E. Smylie, D. Global superconducting gravimeter observations and the search for the translational modes of the inner core. *Physics of the Earth and Planetary Interiors*, 117:3–20, 2000.

J. Crowder and N. J. Cornish. Beyond LISA: Exploring Future Gravitational Wave Missions. *Physical Review D*, 72(8), 2005.

F. A. Dahlen. The normal modes of a rotating, elliptical earth. *Geophysical Journal of the Royal Astronomical Society*, 16(4):329–367, 1968.

F. A. Dahlen. The Normal Modes of a Rotating, Elliptical Earth—II Near-Resonance Multiplet Coupling. *Geophysical Journal of the Royal Astronomical Society*, 18(4):397–436, 1969.

F. A. Dahlen. Inference of the Lateral Heterogeneity of the Earth from the Eigenfrequency Spectrum: a Linear Inverse Problem. *Geophysical Journal International*, 38(1):143–167, 1974.

F. A. Dahlen. Attenuation in the earth at low frequencies. *Geophysical Journal International*, 69(2):537–549, 1982a.

F. A. Dahlen. The effect of data windows on the estimation of free oscillations parameters. *Geophysical Journal of the Royal Astronomical Society*, 69:537–549, 1982b.

F. A. Dahlen and R. V. Sailor. Rotational and elliptical splitting of the free oscillations of the Earth. *Geophysical Journal International*, 58(3):609–623, 1979.

F. A. Dahlen and J. Tromp. *Theoretical global seismology*. Princeton University Press, 1998.

V. De Sabbata, P. Fortini, C. Gualdi, and S. Petralia. A Proposal for Combined Efforts Regarding Geophysical Research and Detection of Gravitation Waves. 1970.

A. Deuss and J. H. Woodhouse. Theoretical free-oscillation spectra: the importance of wide band coupling. *Geophysical Journal International*, 146(3):833–842, 2001.

A. Deuss and J. H. Woodhouse. Iteration method to determine the eigenvalues and eigenvectors of a target multiplet including full mode coupling. *Geophysical Journal International*, 159(1):326–332, 2004.

Arwen Deuss, Jeroen Ritsema, and Hendrik Van Heijst. Splitting function measurements for Earth's longest period normal modes using recent large earthquakes. *Geophysical Research Letters*, 38(4):1–5, 2011.

Arwen Deuss, Jeroen Ritsema, and Hendrik van Heijst. A new catalogue of normal-mode splitting function measurements up to 10 mHz. *Geophysical Journal International*, 193 (2):920–937, 2013.

P. E. Dewdney, P. J. Hall, R. T. Schilizzi, and T. J. L. W. Lazio. The Square Kilometre Array. *Proceedings of the IEEE*, 97(8), 2009.

Hao Ding and Benjamin F Chao. Data stacking methods for isolation of normal-mode singlets of Earth's free oscillation: Extensions, comparisons, and applications. *Journal of Geophysical Research : Solid Earth*, 120(7):5034–5050, 2015a.

Hao Ding and Benjamin F. Chao. Detecting harmonic signals in a noisy time-series: The z-domain autoregressive (AR-z) spectrum. *Geophysical Journal International*, 201(3): 1287–1296, 2015b.

Hao Ding and Benjamin F. Chao. The Slichter mode of the Earth: Revisit with optimal stacking and autoregressive methods on full superconducting gravimeter data set. *Journal of Geophysical Research B: Solid Earth*, 120(10):7261–7272, 2015c.

Hao Ding and Benjamin F. Chao. Solid pole tide in global GPS and superconducting gravimeter observations: Signal retrieval and inference for mantle anelasticity. *Earth and Planetary Science Letters*, 459:244–251, 2016.

Hao Ding and Wen-Bin Shen. Search for the Slichter modes based on a new method: Optimal sequence estimation. *Journal of Geophysical Research: Solid Earth*, 118(9): 5018–5029, 2013a.

Hao Ding and Wen-Bin Shen. Determination of the complex frequencies for the normal modes below 1mHz after the 2010 Maule and 2011 Tohoku earthquakes. *Annals of Geophysics*, 56(5), 2013b.

I. M. Dozmorov. Theory of elastic solids in the gravitational internal system of reference (GISR). *Soviet Physics Journal*, 19(6):741–745, 1976a.

I. M. Dozmorov. Interaction of a gravitational wave with an elastic body. *Soviet Physics Journal*, 19(7):883–888, 1976b.

R. Draper, N. and H. Smith. *Applied Regression Analysis 3rd Edition*. Wiley-Interscience, 1998.

J. Dyson, F. Seismic response of the Earth to a gravitational wave in the 1-Hz band. *The Astrophysical Journal*, 156:529–540, 1969.

A. M. Dziewonski, T.A. Chou, and J. H. Woodhouse. Determination of earthquake source parameters from waveform data for studies of global and regional seismicity. *Journal of Geophysical Research*, 86:2825–2852, 1981.

Adam M. Dziewonski and Don L. Anderson. Preliminary reference Earth model. *Physics of the Earth and Planetary Interiors*, 25(4):297–356, 1981.

A. Einstein. Näherungsweise Integration der Feldgleichungen der Gravitation. *Preussische Akademie der Wissenschaften, Sitzungsberichte*, 1:688–696, 1916.

A. Einstein. Gravitationswellen. *Preussische Akademie der Wissenschaften, Sitzungsberichte*, 1:154–167, 1918.

G. Ekström, M. Nettles, and A. M. Dziewonski. The global CMT project 2004-2010: Centroid-moment tensors for 13,017 earthquakes. *Physics of the Earth and Planetary Interiors*, 200–201:1–9, 2012.

W. Feller. *An Introduction to Probability Theory and Its Applications*. John Wiley & Sons, Inc., 1950.

E. A. Flinn. Free Oscillations of the Earth - a Critique. *Nature*, 232:112, 1971.

R. L. Forward, D. Zipoy, J. Weber, S. Smith, and H. Benioff. Upper Limit for Interstellar Millicycle Gravitational Radiation. *Nature*, 2(4763):573, 1961.

R. Geiger, L. Amand, A. Bertoldi, B. Canuel, W. Chaibi, C. Danquigny, I. Dutta, B. Fang, S. Gaffet, J. Gillot, D. Holleville, A. Landragin, M. Merzougui, I. Riou, D. Savoie, and P. Bouyer. Matter-wave laser Interferometric Gravitation Antenna (MIGA): New perspectives for fundamental physics and geosciences. 2015.

Domenico Giardini, Xiang-Dong Li, and John H Woodhouse. Three-dimensional structure of the Earth from splitting in free-oscillation spectra, 1987.

Domenico Giardini, Xiang-Dong Li, and John H. Woodhouse. Splitting Functions of Long-Period Normal Modes of the Earth. *Journal of Geophysical Research*, 93(B11):13716, 1988.

F. Gilbert. The Diagonal Sum Rule and Averaged Eigenfrequencies. *Geophysical Journal International*, 23(1):119–123, 1971.

E. N. Glass and J. Winicourt. Elastic general relativistic systems. *Journal of Mathematical Physics*, 13:1934–1940, 1972.

C. E. Griggs, M. V. Moody, R. S. Norton, H. J. Paik, and K. Venkateswara. Sensitive Superconducting Gravity Gradiometer Constructed with Levitated Test Masses. *Physical Review Applied*, 8:064024, 2017.

H. Grote. The GEO 600 status. *Classical and Quantum Gravity*, 27(8), 2010.

X. Guoming, L. Knopoff, and W. Zürn. Variations of period and Q of free oscillations due to mode overlap. *Geophysical Journal International*, 72(3):709–719, 1983.

R. Häfner and R. Widmer-Schnidrig. Signature of 3-D density structure in spectra of the spheroidal free oscillation 0S2. *Geophysical Journal International*, 192:285–294, 2013.

D. M. Hamby. A comparison of sensitivity analysis techniques. *Health Physics*, 68:195–204, 1995.

G. M. Harry et al. Advanced LIGO: the next generation of gravitational wave detectors. *Classical and Quantum Gravity*, 27(8), 2010.

I. S. Heng, D. Blair, E. Ivanov, and M. E. Tobar. Long term operation of a niobium resonant bar gravitational wave antenna. *Physics Letters A*, 218, 1996.

J. J. Hermes, M. Kilic, W. R. Brown, D. E. Winget, C. Allende Prieto, A. Gianninas, A. S. Mukadam, A. Cabrera-Lavers, and S. J. Kenyon. Rapid Orbital Decay in the 12.75-minute Binary White Dwarf J0651+2844. *The Astrophysical Journal Letters*, 757 (2), 2012.

J. Hinderer, D. Crossley, and O. Jensen. A search for the Slichter triplet in superconducting gravimeter data. *Physics of the Earth and Planetary Interiors*, 90(3–4):183–195, 1995.

J. Hinderer, D. Crossley, and R. J. Warburton. Gravimetric Methods – Superconducting Gravity Meters. *Treatise Geophys.*, 3:65–122, 2007.

G. Hobbs. The Parkes Pulsar Timing Array. *Classical and Quantum Gravity*, 30(22), 2013.

J. C. E. Irving, A. Deuss, and J. Andrews. Wide-band coupling of Earth's normal modes due to anisotropic inner core structure. *Geophysical Journal International*, 174(3):919–929, 2008.

J. C. E. Irving, A. Deuss, and J. Andrews. Normal mode coupling due to hemispherical anisotropic structure in Earth's inner core. *Geophysical Journal International*, 178(2): 962–975, 2009.

M. Ishii and J. Tromp. Normal-mode and free-air gravity constraints on lateral variations in velocity and density of the Earth's mantle. *Science*, 285:1231–1236, 1999.

M. Ishii and J. Tromp. Even-degree lateral variations in the Earth's mantle constrained by free oscillations and the free-air gravity anomaly. *Geophysical Journal International*, 145 (1):77–96, 2001.

O. G. Jensen. Seismic Detection of Gravitational Radiation. *Reviews of geophysics and space physics*, 17(8):2057–2069, 1979.

L. Ju, D. G. Blair, and C. Zhao. Detection of gravitational waves. *Reports on Progress in Physics*, 63:1317–1427, 2000.

H. G. Khosroshahi and Y. Sobouti. Response of a star to gravitational waves. *Astronomy & Astrophysics*, 321:1024–1026, 1997.

M. Kilic, W. R. Brown, C. Allende Prieto, S. J. Kenyon, and J. A. Panei. The Discovery of Binary White Dwarfs that will Merge Within 500 Myr. *The Astrophysical Journal*, 716 (1):122–130, 2010.

M. Kilic, W. R. Brown, J. J. Hermes, C. Allende Prieto, S. J. Kenyon, D. E. Winget, and K. I. Winget. SDSS J163030.58+423305.8: a 40-min orbital period detached white dwarf binary. *Monthly Notices of the Royal Astronomical Society: Letters*, 418(1), 2011a.

M. Kilic, W. R. Brown, S. J. Kenyon, C. Allende Prieto, J. Andrews, S. J. Kleinman, K. I. Winget, D. E. Winget, and J. J. Hermes. The shortest period detached binary white dwarf system. *Monthly Notices of the Royal Astronomical Society*, 413, 2011b.

M. Kilic, W. R. Brown, C. Allende Prieto, S. J. Kenyon, C. O. Heinke, M. A. Agueros, and S. J. Kleinman. The ELM Survey. IV. 24 White Dwarf Merger Systems. *The Astrophysical Journal*, 751(2), 2012.

M. Kilic, W. R. Brown, A. Gianninas, J. J. Hermes, C. Allende Prieto, and S. J. Kenyon. A new gravitational wave verification source. *Monthly Notices of the Royal Astronomical Society: Letters*, 444(1), 2014.

P. Koelemeijer, A. Deuss, and J. Ritsema. Observations of core-mantle boundary Stoneley modes. *Geophysical Research Letters*, 40(11):2557–2561, 2013.

P. Koelemeijer, J. Ritsema, A. Deuss, and H.-J. Van Heijst. SP12RTS: a degree-12 model of shear- and compressional-wave velocity for Earth's mantle. *Geophysical Journal International*, 204(2):1024–1039, 2016.

M. Kramer and D. J. Champion. The European Pulsar Timing Array and the Large European Array for Pulsars. *Classical and Quantum Gravity*, 30(22):993–1002, 2013.

V. K. Kravchuk, A. V. Gusev, and V. N. Rudenko. Preliminary test of new algorithm for searching gravitational-wave perturbation in Earth crust noises. *international Journal of Modern Physics D*, 4(1):63–67, 1995.

L. Krischer, T. Megies, R. Barsch, M. Beyreuther, T. Lecocq, C. Caudron, and J. Wassermann. ObsPy: a bridge for seismology into the scientific Python ecosystem. *Computational Science & Discovery*, 8(1), 2015.

Chaincy Kuo and Barbara Romanowicz. On the resolution of density anomalies in the Earth's mantle using spectral fitting of normal-mode data. *Geophysical Journal International*, 150(1):162–179, 2002.

B. Kustowski, G. Ekström, and A. M. Dziewoński. The shear-wave velocity structure in the upper mantle beneath Eurasia. *Geophysical Journal International*, 174(3):978–992, 2008.

G. Laske and R. Widmer-Schindrig. *Treatise on geophysics. 1, Seismology and structure of the earth*, chapter Normal Mode & Surface Wave Observations, pages 67–125. Amsterdam u.a.: Elsevier.

Xiang-Dong Li, Domenico Giardini, and J. H. Woodhouse. Large-scale three-dimensional even-degree structure of the Earth from splitting of long-period normal modes. *Journal of Geophysical Research*, 96(B1):551, 1991.

B. Linet. Equations Governing the Oscillations of a Self-Gravitating Elastic Sphere under the Influence of Gravitational Waves. *General Relativity and Gravitation*, 16(1):89–98, 1984.

J. A. Lobo. What can we learn about gravitational wave physics with an elastic spherical antenna? *Physical Review D*, 52(2):591–604, 1995.

P. Lognonné et al. SEIS: Insight's Seismic Experiment for Internal Structure of Mars. *Space Science Reviews*, 215(12), 2019.

I. Lopes. Quadrupole stellar oscillations: The impact of gravitational waves from the Galactic Center. *Physical Review D*, 95:123015, 2017.

I. Lopes and J. Silk. Helioseismology and asteroseismology: looking for gravitational waves in acoustic oscillations. *The Astrophysical Journal*, 794:1–7, 2014.

I. Lopes and J. Silk. Nearby stars as gravitational wave detectors. *The Astrophysical Journal*, 807:1–9, 2015.

I. Lopes and J. Silk. Gravitational Waves from Stellar Black Hole Binaries and the Impact on Nearby Sun-like Stars. *The Astrophysical Journal*, 844:1–7, 2017.

Michele Maggiore. *Gravitational Waves, Volume 1, Theory and Experiments*. Oxford University Press, 2008.

J. Majstorović, S. Rosat, S. Lombotte, and Y. Rogister. Testing performances of the optimal sequence estimation and autoregressive method in the frequency domain for estimating eigenfrequencies and zonal structure coefficients of low-frequency normal modes. *Geophysical Journal International*, 216(2):1157–1176, 2019a.

J. Majstorović, S. Rosat, and Y. Rogister. Earth's spheroidal motion induced by a gravitational wave in flat spacetime. *Physical Review D*, 100(4):044048, 2019b.

R. N. Manchester. The International Pulsar Timing Array. *Classical and Quantum Gravity*, 30(22), 2013.

T. R. Marsh. The discovery of a short-period double-degenerate binary star. *Monthly Notices of the Royal Astronomical Society*, 275(1), 1995.

T. S. Mast, J. E. Nelson, and J.A. Saarloos. Search for Gravitational radiation from pulsars. *The Astrophysical Journal*, 187:L49–L51, 1974.

G. Masters, S. Johnson, G. Laske, and H. Bolton. A shear-velocity model of the mantle. *Philosophical Transactions of the Royal Society London A*, 354:1385–1411, 1996.

Guy Masters and Freeman Gilbert. Attenuation in the earth at low frequencies. *Royal Society of London Series A-Mathematical Physical and Engineering Sciences*, 308(1504): 479–522, 1983.

Guy Masters, Gabi Laske, and Freeman Gilbert. Autoregressive estimation of the splitting matrix of free-oscillation multiplets. *Geophysical Journal International*, 141(1):25–42, 2000.

Guy Masters, J. H. Woodhouse, and Freeman Gilbert. Mineos v1.0.2 [software], Computational Infrastructure for Geodynamics. *Available from: geodynamics.org, doi: NoDOI, url: https://geodynamics.org/cig/software/mineos/*, 2011.

E. Mauceli, Z. K. Geng, W. O. Hamilton, W. W. Johnson, S. Merkowitz, A. Morse, B. Price, and N. Solomonson. The Allegro gravitational wave detector: Data acquisition and analysis. *Physical Review D*, 54, 1996.

P. F. L. Maxted, T. R. Marsh, C. K. J. Moran, and Z. Han. The triple degenerate star WD 1704+481. *Monthly Notices of the Royal Astronomical Society*, 314(2):334–337, 2000.

B. McKernan, K. E. S. Ford, B. Kocsis, and Z. Haiman. 2014.

M. McLaughlin. The North American Nanohertz Observatory for Gravitational Waves. *Classical and Quantum Gravity*, 30(22), 2013.

D. E. McNamara and R. P. Buland. Ambient Noise Levels in the Continental United States. *Bulletin of the Seismological Society of America*, 94(4):1517–1527, 2004.

T. Megies, M. Beyreuther, R. Barsch, L. Krischer, and J. Wassermann. ObsPy - What can it do for data centers and observatories? *Annals of geophysics*, 54(1):47–58, 2011.

D. Mimoun et al. The Noise Model of the SEIS Seismometer of the InSight Mission to Mars. *Space Science Reviews*, 211(1-4):383–428, 2017.

C. J. Moore, R. H. Cole, and C. P. L. Berry. Gravitational-wave sensitivity curves. *Classical and Quantum Gravity*, 32(1):015014, 2015.

C. Moran, T. R. Marsh, and A. Bragaglia. A detached double degenerate with a 1.4-h orbital period. *Monthly Notices of the Royal Astronomical Society*, 288(2):538–544, 1997.

P. Moulik and G. Ekström. An anisotropic shear velocity model of the Earth's mantle using normal modes, body waves, surface waves and long-period waveforms. *Geophysical Journal International*, 199(3):1713–1738, 2014.

F. Mulargia and A. Kamenshchik. The gravitational resolving power of global seismic networks in the 0.1–10 Hz band. *Physics Letters A*, 380:1503–1507, 2016.

G. Nelemans, L. R. Yungelson, and S. F. Portegies Zwart. The gravitational wave signal from the Galactic disk population of binaries containing two compact objects. *Astronomy & Astrophysics*, 375:890–898, 2001.

J. Neyman, E. S. Pearson, and K. Pearson. IX. On the problem of the most efficient tests of statistical hypotheses. *Philosophical Transactions of the Royal Society of London*, 231, 1933.

W.-T. Ni. Gravitational wave detection in space. *International Journal of Modern Physics D*, 25(14), 2016.

Surya Pachhai, Hrvoje Tkalčić, and Guy Masters. Estimation of splitting functions from Earth's normal mode spectra using the neighbourhood algorithm. *Geophysical Journal International*, 204(1):111–126, 2016.

J. Peterson. Observations and Modelling of Seismic Background Noise. *Open-File Report 93–332. U.S. Department of Interior, Geological Survey, Albuquerque, New Mexico*, 1993.

G. Petit and B. Luzum. *IERS Conventions (2010)*. Frankfurt am Main: Verlag des Bundesamts für Kartographie und Geodäsie, 2010.

F. A. E. Pirani. Republication of: On the physical significance of the riemann tensor. *General Relativity and Gravitation*, 41:1215–1232, 2009.

M. Punturo et al. The Einstein Telescope: a third-generation gravitational wave observatory. *Classical and Quantum Gravity*, 27(19), 2010.

J. S. Resovsky and M. H. Ritzwoller. New and refined constraints on three-dimensional Earth structure from normal modes below 3 mHz. *Journal of Geophysical Research*, 103 (B1):783–810, 1998.

J. S. Resovsky and M. H. Ritzwoller. Regularization uncertainty in density models estimated from normal mode data. *Geophysical Research Letters*, 26(15):2319–2322, 1999.

J. Ritsema, H. J. van Heijst, and J. H. Woodhouse. Complex Shear Wave Velocity Structure Imaged Beneath Africa and Iceland. *Science*, 286(5446):1925–1928, 1999.

J. Ritsema, A. Deuss, H. J. Van Heijst, and J. H. Woodhouse. S40RTS: A degree-40 shear-velocity model for the mantle from new Rayleigh wave dispersion, teleseismic traveltime and normal-mode splitting function measurements. *Geophysical Journal International*, 184(3):1223–1236, 2011.

Michael Ritzwoller, Guy Masters, and Freeman Gilbert. Observations of anomalous splitting and their interpretation in terms of aspherical structure. *Journal of Geophysical Research*, 91(B10):10203–10228, 1986.

Michael Ritzwoller, Guy Masters, and Freeman Gilbert. Constraining aspherical structure with low-degree interaction coefficients: Application to uncoupled multiplets. *Journal of Geophysical Research*, 93(B6):6369–6396, 1988.

Y. Rogister. Splitting of seismic-free oscillations and of the Slichter triplet using the normal mode theory of a rotating, ellipsoidal earth. *Physics of the Earth and Planetary Interiors*, 140(1–3):169–182, 2003.

B. Romanowicz. Can we resolve 3D density heterogeneity in the lower mantle? *Geophysical Research Letters*, 28(6):1107–1110, 2001.

S. Rosat and J. Hinderer. Noise levels of superconducting gravimeters: Updated comparison and time stability. *Bulletin of the Seismological Society of America*, 101(3):1233–1241, 2011.

S. Rosat and J. Hinderer. Limits of Detection of Gravimetric Signals on Earth. *Scientific Reports*, 8:15324, 2018.

S. Rosat, J. Hinderer, D. Crossley, and L. Rivera. The search for the Slichter mode: comparison of noise levels of superconducting gravimeters and investigation of a stacking method. *Physics of the Earth and Planetary Interiors*, 140:183–202, 2003.

S. Rosat, T. Sato, Y. Imanishi, J. Hinderer, Y. Tamura, H. McQueen, and M. Ohashi. High-resolution analysis of the gravest seismic normal modes after the 2004 Mw = 9 Sumatra earthquake using superconducting gravimeter data. *Geophysical Research Letters*, 32(13): L13304, 2005.

S. Rosat, T. Sato, Y. Imanishi, J. Hinderer, Y. Tamura, H. McQueen, and M. Ohashi. Correction to "High-resolution analysis of the gravest seismic normal modes after the 2004 Mw = 9 Sumatra earthquake using superconducting gravimeter data". *Geophysical Research Letters*, 39(22):L22601, 2012.

G. Roult, J. Roch, and E. Clévédé. Observation of split modes from the 26th December 2004 Sumatra-Andaman mega-event. *Physics of the Earth and Planetary Interiors*, 179: 45–59, 2010.

R. Ruffini and J. A. Wheeler. Relativistic cosmology and space platforms. *European Space Research Organization*, 1971.

V. N. Rundeko. Application of gravitational antennae for fundamental geophysical problems. In E. Coccia, G. Pizzella, and F.Ronga, editors, *Gravitational wave experiments*, pages 277–281. World Scientific Publishing Co. Pte. Ud., P 0 Box 128, Farrer Road, Singapore 9128, 1994.

D. Sadeh and M. Meidav. Periodicities in seismic reponse caused by Pulsars CP1133. *Nature*, 240:136–138, 1972.

B. S. Sathyaprakash and B. F. Schutz. Physics, Astrophysics and Cosmology with Gravitational Waves. *Living Rev. Relativity*, 2, 2009.

H. Schmidt. The triple degenerate star WD 1704+481. *Astronomy and Astrophysics*, 311: 852–857, 1996.

B. Schutz. *A First Course in General Relativity*. Cambridge University Press, 2009.

Wen-Bin Shen and H. Ding. Observation of spheroidal normal mode multiplets below 1 mHz using ensemble empirical mode decomposition. *Geophysical Journal International*, 196(3):1631–1642, 2014.

Wen-Bin Shen and B. Wu. A case study of detecting the triplet of 3S1 using superconducting gravimeter records with an alternative data preprocessing technique. *Annals of Geophysics*, 55(2):293–300, 2012.

D. M. Siegel and M. Roth. Excitation of non-radial stellar oscillations by gravitational waves: a first model. *Monthly Notices of the Royal Astronomical Society*, 408:1742–1748, 2010.

D. M. Siegel and M. Roth. Excitation of stellar oscillations by gravitational waves: hydrodynamic model and numerical results from the Sun. *The Astrophysical Journal*, 729:1–17, 2011.

D. M. Siegel and M. Roth. On the feasibility of employing solar-like oscillators as detectors for stochastic background of gravitational waves. *Astronomische Nachrichten*, 333(10): 978–982, 2012.

D. M. Siegel and M. Roth. An upper bound from helioseismology on the stochastic background of gravitational waves. *The Astrophysical Journal*, 784:1–6, 2014.

B. Slichter, L. The Fundamental Free Mode of the Earth's Inner Core. *Proceedings of the National Academy of Sciences of the United States of America*, 47(2):186–190, 1961.

D. E. Smylie. The Inner Core Translational Triplet and the Density Near Earth's Center. *Science*, 255(1):1678–1682, 1992.

K. Somiya. Detector configuration of KAGRA–the Japanese cryogenic gravitational-wave detector. *Classical and Quantum Gravity*, 29(12), 2012.

A. Stroeer and A. Vecchio. The LISA verification binaries. *Classical and Quantum Gravity*, 23(19), 2006.

R. Takahashi and T. Nakamura. The Decihertz Laser Interferometer Can Determine the Position of the Coalescing Binary Neutron Stars within an Arcminute a Week before the Final Merging Event to the Black Hole. *The Astrophysical Journal Letters*, 596(2), 2003.

K. S. Thorne and R. D. Blandford. *Modern Classical Physics Optics, Fluids, Plasmas, Elasticity, Relativity, and Statistical Physics*. Princeton University Press, 2017.

J. Trampert, F. Deschamps, J. Resovsky, and D. Yuen. Probabilistic tomography maps chemical heterogeneities throughout the lower mantle. *Science*, 306:853–856, 2004.

V. S. Tuman. Observation of Earth Eigen Vibrations Possibly Excite by Gravity Waves. *Nature*, 230:101–106, 1971.

V. S. Tuman. A search for gravity waves by means of the earth eigen vibrations. *General Relativity and Gravitation*, 4(4):279–287, 1973.

M. Van Camp and P. Vauterin. Tsoft: graphical and interactive software for the analysis of time series and Earth tides. *Computers & Geosciences*, 31(5):631–640, 2005.

P. Vanícek. Approximate spectral analysis by least-squares fit. *Astrophysics and Space Science*, 4(4):387–391, 1969.

A. D. Waard, L. Gottardi, J. V. Houwelingen, , A. Shumack, and G. Frossati. MiniGRAIL, the first spherical detector. *Classical and Quantum Gravity*, 20, 2003.

R. Walgate. Gravitational waves on the Sun? *Nature*, 305:665, 1983.

J. Weber. Detection and generation of gravitational waves. *Phys. Rev.*, 117:306–313, 1959.

J. Weber. Gravitational radiation. *Physical Review Letter*, 18(13):498–501, 1967.

J. Weber. Gravitational radiation from the pulsars. *Physical Review Letters*, 21(6):395–396, 1968.

P. Welch. The use of fast Fourier transform for the estimation of power spectra: A method based on time averaging over short, modified periodograms. *IEEE*, 15, 1967.

J. T. Whelan. Lectures on gravitational wave data analysis. https://dcc.ligo.org/public/0106/T1300666/003/Whelan_notes.pdf, 2013. Accessed: 2019-07-08.

Rudolf Widmer, Guy Masters, and Freeman Gilbert. Observably split multiplets data analysis and interpretation in terms of large scale aspherical structure. *Geophysical Journal International*, 111(3):559–576, 1992.

R. Widmer-Schnidrig. What can Superconducting Gravimeters contribute to normal mode seismology. *Bulletin of the Seismological Society of America*, 93(3):1370–1380, 2003.

N. Wiener. *Extrapolation, Interpolation, and Smoothing of Stationary Time Series*. MIT Press, 1949.

R. A. Wiggins and F. Press. Search for Seismic Signals at Pulsar Frequencies. *Journal of Geophysical Research*, 74(22):5351–5352, 1969.

J. H. Woodhouse. The coupling and attenuation of nearly resonant multiplets in the Earth's free oscillation spectrum. *Geophysical Journal of the Royal Astronomical Society*, 61(2): 261–283, 1980.

J. H. Woodhouse. The joint inversion of seismic waveforms for lateral variations in earth structure and earthquake source parameters. *Geophysical Journal of the Royal Astronomical Society*, LXXXV:366–397, 1983.

J. H. Woodhouse. *In:Doornbos DJ. (ed) Seismological Algorithms, Computational Methods and Computer Programs*, chapter The calculation of Eigenfrequencies and Eigenfunctions of the free oscillations of the Earth and the Sun, pages 321–370. London: Academic Press, 1988.

J. H. Woodhouse and F. A. Dahlen. The effect of a general aspherical perturbation on the free oscillations of the Earth. *Geophysical Journal of the Royal Astronomical Society*, 53 (2):335–354, 1978.

J. H. Woodhouse and D. Giardini. Inversion for the splitting function of isolated low order normal mode multiplets. *EOS, Trans. Am. geophys. Un.*, 66:300, 1985.

H.-Y. Yang and J. Tromp. Synthetic free-oscillation spectra: an appraisal of various mode-coupling methods. *Geophysical Journal International*, 203(2):1179–1192, 2015.

Shi-Yu Zeng and Wen-Bin Shen. Stripping the narrowband coupled multiplets based on seismic records using the OSE. *Physics of the Earth and Planetary Interiors*, 272:58–67, 2017.

Shi-Yu Zeng and Wen-Bin Shen. Observations of the Singlets of Higher-Degree Modes Based on the OSE. *Journal of Earth Science*, pages 1–11, 2018.

C. Z. Zhou and P. F. Michelson. Spherical resonant-mass gravitational wave detectors. *Physical Review D*, 51(6), 1995.

R. L. Zimmerman and R. W. Hellings. Gravitational radiation dominated cosmologies. *The Astrophysical Journal*, 241:475–485, 1980.

W. Zürn and P. A. Rydelek. Revisiting the Phasor-Walkout method for detailed investigation of harmonic signals in time series. *Surveys in Geophysics*, 15(4):409–431, 1994.

W. Zürn and R. Widmer-Schnidrig. On noise reduction in vertical seismic records below 2 mHz using local barometric pressure. *Geophysical Research Letters*, 22(24):3537–3540, 1995.

Josipa MAJSTOROVIĆ

Influence des ondes gravitationnelles sur les modes propres de la Terre

Résumé

Nous avons révisé et développé une modélisation analytique de l'interaction des ondes gravitationnelles avec la Terre en termes d'excitation des modes propres. Nous avons, dans un premier temps, réévalué la réponse d'une Terre sphérique, sans rotation et radialement stratifiée à des sources d'ondes gravitationnelles monochromatiques en termes de déplacement radial induit à la surface. Nous avons ensuite développé une nouvelle solution pour une Terre en rotation, ellipsoïdale et latéralement hétérogène. Nous avons considéré comme sources d'ondes gravitationnelles les systèmes binaires de naines blanches. Dans les deux cas, les seuls modes propres qui sont excités sont les modes quadripolaires. La réponse finale dépend fortement de la fréquence de l'onde gravitationnelle, la plus grande excitation étant à résonance avec des modes propres. Cependant, la détection de ces faibles signaux dans des données gravimétriques ou sismologiques est très difficile de par la présence d'un bruit trop élevé dans ces observations et ce même après l'utilisation de techniques de traitement du signal, comme le filtrage adaptatif. La réponse de la Terre en termes d'excitation des modes propres est dix ordres de grandeur plus faible que le niveau de bruit ambiant sur Terre. Finalement, nous avons mis en évidence certaines limites d'outils de traitement du signal utilisés pour la recherche et l'analyse de petits signaux. En particulier, la distribution des stations à la surface du globe peut introduire des biais dans l'étude des modes propres.

Mots clés: ondes gravitationnelles, modes propres, filtrage adaptatif, traitement du signal

Abstract

We have revisited and developed an analytical model of the interaction between the gravitational waves and the Earth in terms of normal modes excitation. We have first reevaluated the induced response for a spherical, radially heterogeneous and non-rotating model to monochromatic gravitational wave sources in terms of radial displacement at the Earth's surface. Then we have developed a new analytical solution for a rotating elliptical model with lateral heterogeneities. We have considered sources of the gravitational waves that are the double white-dwarf binary systems. We have shown that for both models the only normal modes that are being excited are the quadrupole ones. The final responses highly depend on the gravitational wave frequencies, the largest response being at resonance with a normal mode. However, the detection of these elusive signals in gravimetric and seismological data is very difficult due to large environmental noise present in the data, even after using some signal processing techniques like the matched filtering. There are ten orders of magnitude difference between the calculated Earth's normal modes response and the ambient noise level. Finally, we have highlighted some limitation of the signal processing techniques used for the search and analysis of the weak signals. In particular, some biases can be introduced when using different station distributions at the surface of the globe in the frame of normal mode studies.

Keywords: gravitational waves, normal modes, matched filtering, signal processing techniques